UNIVERSIDADE FEDERAL DO RIO DE JANEIRO - UFRJ

CENTRO DE CIÊNCIAS DA SAÚDE - CCS

Programa de Pós-Graduação em Biotecnologia Vegetal e Bioprocessos - PBV

Elaboração de modelos preditivos da potencial atividade antiviral de espécies da biodiversidade brasileira frente ao SARS-CoV-2 através de métodos computacionais

Brendo Araujo Gomes

Orientadora: Profa. Dra. Suzana Guimarães Leitão

(Faculdade de Farmácia - FF/UFRJ)

Co-orientador: Prof. Dr. Marcus Tullius Scotti

(Departamento de Química – DQUI/UFPB)

Rio de Janeiro/2025

Elaboração de modelos preditivos da potencial atividade antiviral de espécies da biodiversidade brasileira frente ao SARS-CoV-2 através de métodos computacionais

Tese de Doutorado apresentada ao Programa de Pós-Graduação em Biotecnologia Vegetal e Bioprocessos da Universidade Federal do Rio de Janeiro como requisito final para a obtenção do grau de Doutor em Ciências, na Área de Concentração: Pesquisa e Desenvolvimento em Biotecnologia Vegetal.

Brendo Araujo Gomes

Orientadora: Profa. Dra. Suzana Guimarães Leitão

(Faculdade de Farmácia - FF/UFRJ)

Co-orientador: Prof. Dr. Marcus Tullius Scotti

(Departamento de Química – DQUI/UFPB)

Rio de Janeiro/2025

BANCA EXAMINADORA

Profa. Dra. Suzana Guimarães Leitão – ORIENTADORA
Universidade Federal do Rio de Janeiro (UFRJ)

Prof. Dr. Marcus Tullius Scotti – COORIENTADOR
Universidade Federal da Paraíba (UFPB)

Prof. Dr. Leandro Machado Rocha – Membro TITULAR
Universidade Federal Fluminense (UFF)

Profa. Dra. Alane Beatriz Vermelho – Membro TITULAR
Universidade Federal do Rio de Janeiro (UFRJ)

Prof. Dr. Lucas Silva Abreu – Membro TITULAR
Universidade Federal Fluminense (UFF)

Prof. Dr. Valdir Florencio da Veiga Junior– Membro TITULAR
Instituto Militar de Engenharia (IME)

Profa. Dra. Luana Beatriz dos Santos Nascimento – Membro SUPLENTE [REVISORA]
Universidade Federal do Rio de Janeiro (UFRJ)

CIP - Catalogação na Publicação

Gomes, Brendo Araujo

G633e Elaboração de modelos preditivos da potencial atividade antiviral de espécies da biodiversidade brasileira frente ao SARS-CoV-2 através de métodos computacionais / Brendo Araujo Gomes. -- Rio de Janeiro, 2025.
180 f.

Orientadora: Suzana Guimarães Leitão.
Coorientadora: Marcus Tullius Scotti.
Tese (mestrado) - Universidade Federal do Rio de Janeiro, Decania do Centro de Ciências da Saúde, Programa de Pós-Graduação em Biotecnologia Vegetal, 2025.

1. Bioprospecção. 2. UHPLC-MS/MS. 3. Quimiometria. 4. Quimioinformática. 5. Química Medicinal. I. Leitão, Suzana Guimarães, orient. II. Scotti, Marcus Tullius, coorient. III. Título.

Elaborado pelo Sistema de Geração Automática da UFRJ com os dados fornecidos pelo(a) autor(a), sob a responsabilidade de Miguel Romeu Amorim Neto - CRB-7/6283.

Dedico este trabalho a Ciência e a todos aqueles que a praticam,
pois mesmo frente ao pouco reconhecimento, banalização
e duros golpes, permanecem de pé desenvolvendo
suas pesquisas para o inteiro benefício
de tudo e todos.

AGRADECIMENTOS

Neste presente trabalho, gostaria de deixar explícito os meus sinceros agradecimentos às pessoas que contribuíram não só com a elaboração do estudo, mas também em minha formação, auxiliando no meu crescimento pessoal e profissional.

Agradeço aos meus pais Suely, Álvaro e Lourival que me concederam conselhos e ensinamentos, assim como zelaram pelo meu bem-estar e criação.

Agradeço à minha orientadora Profa. Dra. Suzana Leitão, a Tia Su, por ter me acolhido com tanto carinho em seu grupo de pesquisa e por me permitir fazer parte da grande família FitoFar. Sua generosidade, cuidado e dedicação foram fundamentais em cada etapa da minha trajetória. Sou imensamente grato, não apenas pelas orientações acadêmicas e científicas, mas também pelos inúmeros momentos de escuta, incentivo e apoio humano que marcaram essa caminhada. Tenha certeza, que levo comigo, além do aprendizado, a inspiração do seu exemplo como pesquisadora e como pessoa.

Agradeço ao meu orientador Prof. Dr. Marcus Scotti, pelos ensinamentos, apoio e capacitação em uma área de atuação completamente nova em minha formação.

Agradeço aos meus amigos: Aline Soares, Andrex da Veiga, Beatriz Ferreira, Daniel Simas, Diégina Araujo, Gabriel Martins, Marcos Toledo, Mariana Campos, Paulo Salles, Patrícia Jural, Simony Carvalho e Thamirys Fonseca, pela companhia, bons momentos e memórias, e disposição em me ensinar e ajudar no que fosse necessário.

Agradeço aos colaboradores Profa. Dra. Gilda Leitão, Prof. Dr. Diego Alonso e Dra. Milene Miranda, pelas ideias, aconselhamentos, auxílio em tomadas de decisão e treinamento técnico teórico-prático.

Agradeço aos meus eternos orientadores Prof. Dr. Rodrigo Leo e Profa. Dra. Rosy Simas. Há de se saber que não estaria onde estou, não chegaria aonde cheguei, sem o auxílio deles. Agradeço o tanto que cuidaram/am, zelaram/am, aconselharam/am, e ensinaram/am desde o início de minha jornada acadêmica.

Agradeço aos Professores Dr. Leandro Machado, Dra. Alane Vermelho, Dr. Lucas Abreu e Dr. Valdir da Veiga por comporem minha banca de defesa de tese contribuindo com sugestões e auxiliando no melhoramento do trabalho final.

Agradeço a Professora Dra. Luana Nascimento, revisora deste documento, que fez com toda excelência este trabalho minucioso e cuidadoso.

Agradeço aos órgãos de fomento CNPQ, CAPES e FAPERJ pela verba disponibilizada em forma de bolsa de estudos, e fomento para pesquisa.

“Não permaneça sempre na estrada principal, indo apenas aonde os outros já foram, seguindo um atrás do outro como um rebanho de ovelhas. Ocasionalmente, deixe a trilha já traçada e mergulhe na floresta. Cada vez que você fizer isso, certamente encontrará algo que nunca viu antes. Pode ser uma coisa simples, mas não a ignore. Explore em sua volta; uma descoberta leva a outra e, antes que você perceba, terá algo com o qual vale a pena ocupar sua mente. Todas as grandes descobertas são frutos do pensamento.”

[Artigo National Geographic, 1914]

— Alexander Graham Bell

“A exigência délfica “conhece-te a ti mesmo”, significava:
“reconhece que és um homem, não um Deus!”,
ela vale também para o homem, na época da ciência,
pois serve de advertência frente a todas as ilusões
de dominação e de domínio.”
Gadamer, Hans-Georg (1983).

APRESENTAÇÃO

A presente tese apresenta os resultados do projeto “Elaboração de modelos preditivos da potencial atividade antiviral de espécies da biodiversidade brasileira frente ao SARS-CoV-2 através de métodos computacionais”, desenvolvido no Programa de Pós-Graduação em Biotecnologia Vegetal e Bioprocessos, com início em 2021.

O projeto seguiu um *workflow* proposto pelo aluno e supervisionado pela Profa. Dra. Suzana Guimarães Leitão e pelo Prof. Dr. Marcus Tullius Scotti, focado em desenvolver alternativas computacionais, mais rápidas e com menores custos, na busca de potenciais agentes naturais anti-SARS-CoV-2 a partir de espécies vegetais da biodiversidade brasileira.

Durante o desenvolvimento deste projeto, a obtenção dos dados biológicos foi viabilizada por meio da colaboração com outros alunos e professores envolvidos na pesquisa. A participação do aluno nos ensaios biológicos foi parcial e com o objetivo principal de aprender e compreender as metodologias e técnicas empregadas. Em contrapartida, o aluno foi responsável pela obtenção de todos os dados químicos, conduzindo desde a preparação das amostras até as análises instrumentais. Além disso, atuou diretamente em todos os estudos computacionais do projeto, sendo responsável por sua conceituação, aplicação e integração. O aluno também realizou o processamento completo dos dados gerados, as análises computacionais e o desenvolvimento dos modelos preditivos relacionados à atividade biológica e à identificação de substâncias potencialmente ativas. Embora os dados *in silico* oriundos de estudos de *docking* e dinâmica molecular tenham sido realizados com o apoio de colaboradores experientes, houve participação ativa nesses processos, contribuindo com análises e interpretações dos resultados.

Este documento constitui na concretização da elaboração e resultados do projeto, sendo um dos requisitos obrigatórios para a obtenção do título de Doutor em Ciências e será apresentado em formato alternativo estabelecido pelo programa de pós-graduação. Nesse formato, a seção de "Resultados e Discussão" é substituída por artigos científicos, neste caso já publicados. O documento tem como organização a apresentação dos seguintes tópicos: "Introdução", "Fundamentação Teórica", "Justificativa" e "Objetivos", seguidos pela descrição detalhada das metodologias aplicadas. Na sequência, os artigos científicos são apresentados na íntegra, isto é, mantendo todas as seções conforme foram originalmente publicados, seguindo as normas estabelecidas pelo Programa. Após, os artigos são seguidos de uma conclusão geral do projeto, tópicos complementares (Perspectivas e Outras informações relevantes) e, por fim,

as referências essenciais que compõem os elementos iniciais. Também podem ser encontrados no documento, três anexos com informações suplementares do projeto, e dos artigos científicos publicados. Seguindo a formatação exigida pelo programa, figuras, quadros e tabelas, presentes nos artigos publicados, mantêm a numeração geral do documento, porém, preservam também os números originais da publicação para facilitar a compreensão e o acompanhamento pelos leitores.

Os dois artigos apresentados são: "*Myrtucommulones and Related Acylphloroglucinols from Myrtaceae as a Promising Source of Multitarget SARS-CoV-2 Cycle Inhibitors*", publicado em 2024 na revista *Pharmaceuticals* [Qualis A1/FI 4.3] e "*Predicting the Anti-SARS-CoV-2 Potential of Isoquinoline Alkaloids from Brazilian Siparunaceae Species Using Chemometric Tools*", publicado na revista *International Journal of Molecular Sciences* [Qualis A2/FI 4.9], em 2025.

LISTA DE SÍMBOLOS, SIGLAS E ABREVIATURAS

(+) Modo positivo de ionização

(−) Modo negativo de ionização

$3CL^{pro}$ *3-chymotrypsin like protease* - Protease similar à 3-quimiotripsina

ACE2 *Angiotensin-converting enzyme 2* - Enzima Conversora da Angiotensina 2

ANVISA Agência Nacional de Vigilância Sanitária

APCI *Atmospheric-pressure chemical ionization* - Ionização química a pressão atmosférica

BuCoV *Bovine Coronavirus* - Coronavírus Bovino

COVID-19 *Coronavirus disease of 2019* – doença por coronavírus 2019

DABCYL 4-(4-dimethyl-aminophenylazo)benzoyl

EDANS 5-[(2-aminoethyl)amino]naphtalene-1-sulfonic acid

EMA *European Medicines Agency*

ESI *Electrospray ionization* - Ionização por *electrospray*

FBMN *Feature-Based Molecular Networking* - Rede Molecular Baseada em Recursos

FDA *Food & Drug Administration*

FRET *Fluorescence Resonance Energy Transfer* - Transferência de energia fluorescente ressonante

GNPS *Global Natural Products Social Molecular Networking*

LC-MS/MS *Liquid chromatography tandem mass spectrometry* - Cromatografia em fase líquida acoplada a espectrometria de massas

M^{pro} Main Protease – Protease principal

MERS-CoV *Middle East Respiratory Syndrome Coronavirus* - Coronavírus da Síndrome Respiratória do Oriente Médio

MuCoV *Murine Coronavirus* - Coronavírus Murino

MS *Mass spectrometry* - Espectrometria de massas

MS^1 *Precursor ions mass spectrum* - Espectro de massas dos íons precursores

MS^2 *Fragment ions mass spectrum* - Espectro de massas dos íons fragmentos

MTT Brometo de 3-4,5-dimetil-tiazol-2-il-2,5-difeniltetrazólio

NIPALS *Nonlinear Interative Partial Least Squares* - Mínimos quadrados parciais interativos não lineares

NSP1–NSP16 Non-structural proteins 1 to 16 (Proteínas não estruturais 1 a 16, envolvidas em processos de replicação, transcrição e evasão imune dos coronavírus)

PL^{pro} *Papain-like Protease* - Protease semelhante à papaína

PLS *Partial least squares regression* - Mínimos quadrados parciais

PPL1a Polyprotein 1a (Poliproteína 1a, originada da tradução do genoma viral, precursora das nsps)

PPL1ab Polyprotein 1ab (Poliproteína 1ab, formada por tradução ribossômica com mudança de quadro de leitura, também precursora das nsps)

RBD *Receptor Binding Domain* - Domínio de ligação ao receptor

RdRp *RNA-dependent RNA polymerase* - Polimerase de RNA dependente de RNA

RMSE *Root mean-square error* - Raiz do erro quadrático médio

SARS-CoV-2 *Severe acute respiratory syndrome coronavirus 2* - Síndrome respiratória aguda grave do coronavírus 2

SARS-CoV *Severe Acute Respiratory Syndrome Coronavirus* - Coronavírus da Síndrome Respiratória Aguda Grave

SP *Spike Protein* - SP

TMPRSS2 *Transmembrane Protease, Serine 2* - Protease transmembranar do tipo serina

ThCoV *Turkey Coronavirus* - Coronavírus de Peru

ORF *Open Reading Frames* – Janelas abertas de leitura

VSV *Vesicular Stomatitis Virus* - Vírus da estomatite vesicular

LISTA DE FIGURAS

Figura 1. Média cumulativa do número de casos de infecção (superior), e mortes (inferior) confirmadas no mundo. Fonte: Our World in Data, 2025.

Figura 2. Mapa de calor da ocorrência de todas as espécies vegetais registradas no mundo, com destaque para a riqueza e abundância de plantas no Brasil. Fonte: adaptado de GBIF,2023; SIBBr, 2023.

Figura 3. Representação esquemática da taxonomia da ordem *Nidoviriales*. Fonte: Gupta *et al.*, 2022.

Figura 4. Representações esquemáticas da estrutura da partícula viral, e da arquitetura genômica do SARS-CoV-2. A: o nucleocapsídeo (N), a SP (S), a proteína de membrana (M) e a proteína de Envelope (E); B: o genoma viral (+)ssRNA completo de SARS-CoV-2. Fonte: Zhang *et al.*, 2021.

Figura 5. Representações esquemáticas da estrutura da SP de SARS-CoV-2. A: a estrutura geral do SARS-CoV-2 e posição da SP; B: a estrutura trimérica da SP; C: o protômero da SP; D: as principais regiões encontradas nas subunidades (S1 e S2).

Figura 6. Representação esquemática da estrutura da enzima $3CL^{pro}$ de SARS-CoV-2 (com destaque do sítio de ligação ativo). Fonte: Mengist; Dilnessa; Jin, 2021.

Figura 7. Representação esquemática da estrutura da enzima PL^{pro} de SARS-CoV-2. Fonte: Osipiuk *et al.*, 2021.

Figura 8. Esquema do processo de ligação ao receptor (SP:ACE2) e entrada do SARS-CoV-2 nas células hospedeiras. Fonte: Jackson *et al.*, 2021.

Figura 9. Esquema do processo de entrada, replicação e exocitose do SARS-CoV-2 nas células hospedeiras. Fonte: V'kovski *et al.*, 2021.

Figura 10. Média cumulativa do número de pessoas vacinadas, e destaque da porcentagem de indivíduos com esquema vacinal parcial e completo. Fonte: Our World in Data, 2025.

Figura 11. Exemplos de produtos naturais utilizados para prevenção, e atuação frente aos diferentes alvos no ciclo do SARS-CoV-2. Fonte: adaptado de Boozari e Hosseinzadeh, 2020; Xian *et al.*, 2020; Sharma *et al.*, 2021.

Figura 12. Resumos gráficos dos trabalhos de nosso grupo de pesquisa, exemplificando o potencial de espécies brasileiras (e suas moléculas) como potenciais agentes anti-SARS-CoV-2. A: extratos de espécies amazônicas de *Siparuna* e flavonoides isolados, como inibidores da replicação *in* vitro do SARS-CoV-2; B: triagem virtual de feniletanoides glicosilados como inibidores das proteases $3CL^{pro}$ e PL^{pro}; C: extratos da espécie *Ampelozizyphus amazonicus*, como inibidores da interação *Spike*(RBD):ACE2 e da replicação *in* vitro do SARS-CoV-2. Fonte: adaptado de Carla *et al.*, 2021; Cheohen *et al.*, 2023; Campos *et al.*, 2023.

Figura 13. Representação esquemática das etapas de processamento de dados oriundos de análises por LC-MS/MS. Fonte: GNPS, 2023.

Figura 14. Processo de construção das redes moleculares a partir dos dados oriundos de análises por LC-MS/MS. Fonte: Pilon *et al.*, 2021.

Figura 15. Diagrama representativo das faixas de polaridade de moléculas ionizadas por diferentes fontes de espectrometria de massas. GC-MS: cromatografia em fase gasosa acoplada a espectrometria de massas; LC-MS: cromatografia em fase liquida acoplada a espectrometria de massas. ESI: ionização por *electrospray*; APCI: ionização química a pressão atmosférica; APPI: ionização química por fotoionização; EI: ionização por elétrons; CI: ionização química. Fonte: adaptado de Wei; Xiang; Cai., 2020.

Figura 16. Princípios dos ensaios utilizando o *kit* comercial Lumit. Fonte: Promega *Website*, 2023.

Figura 17. Princípios dos ensaios utilizando o método de transferência ressonante de energia por fluorescência (FRET). Fonte: Biomol *Website*, 2023.

Figura 18. Parâmetros gerais de processamento de dados químicos obtidos por LC-MS/MS no *software* MZmine. Fonte: adaptado de Pilon *et al.*, 2021.

Figura 19. Princípios dos ensaios utilizando o método de redução do sal de tetrazólio em formazana. Fonte: Magalhães; Thá; Leme, 2018.

Figura 20. Princípios dos ensaios utilizando o *kit* comercial CytoTox 96® Non-Radioactive Colorimetric Assay. Fonte: Promega *Website*, 2025.

Figura 21. Figure 1. (A) Inhibition of Spike-pseudotyped VSV receptor-mediated cell entry after treatment with Myrtaceae extracts (*E. prasina*, *M. splendens*, *M. strigipes*, *E. mosenii*, and *E. brasiliensis*) in four dif- ferent concentrations (250, 125, 50, and 25 µg·mL−1), assessed by luciferase activity assay. Percent neutralization was determined by quantification of total luciferase signal resulting from successful pseudovirus infection, normalized to vehicle control (n = 3). (B) Vero E6-ACE2 cells viability after treatment with Myrtaceae extracts in different concentrations (500, 250, 125, 50, 25 and 12.5 µg·mL−1) was assessed with an MTT colorimetric test (5 mM, 1 × PBS). Total cell viability was determined by quantification of dye metabolization by untreated cells normalized to vehicle control (n = 3). Lines in the graphs mark, respectively, 90% and 50% of inhibition.

Figura 22. Figure 2. Scores (A), X-loadings weight (B) for the PLS model based on the LC-MS data obtained in the electrospray ionization in negative mode of the 15 samples of five species of Myrtaceae family, and the inhibition values of the extracts on the RBD:ACE2 interaction and the activity of the r3CL^{pro} and rPL^{pro} enzymes of SARS-CoV-2. The dashed line indicates the cutoff for contributions exceeding 0.05 (loadings weights).

Figura 23. Figure 3. Network 1 showing the oligomeric acylphloroglucinols type compounds, ions that most contribute to the anti-SARS-CoV-2 activity.

Figura 24. Figure 4. General structure of myrtucommulones and related acylphloroglucinols. Dashed lines denote characteristic fragmentation patterns observed in LC-ESI(-)MS/MS (adapted from [2]).

Figura 25. Figure 5. Structure and proposed fragmentation of annotated compounds (1–5). Compounds 1 and 2 (semimyrtucommulone and *nor*-semi myrtucommulone, respectively) were isolated as racemic mixtures [28,29].

Figura 26. Figure 6. Aligned chromatograms of Myrtaceae ethanol extracts by UHPLC-ESI(-)3D-IT-MS/MS highlighting the predicted ions.

Figura 27. Figure 7. Myrtaceae extracts inhibit virus replication in Calu-3 cells. Infected cells with SARS-CoV-2 at MOI (multiplicity of infection) 0.01 were treated with five different plant extracts at 50 µg·mL−1 for 24 h at 37 ◦C and 5% CO_2. After this period, the supernatants were harvested, and the virus titles were accessed by plaque-forming units (PFU/mL) assay. The percentage of inhibition was obtained by comparison with the infected/untreated group. *** $p \leq 0.001$ in relation to infected control (n = 4).

Figura 28. Figure 8. Effect of Myrtaceae species on the SARS-CoV-2 replication in Calu-3 cells. Calu-3 in- fected with SARS-CoV-2 (MOI: 0.01) for 1 h were treated with different concentrations (0.781, 1.563, 3.125, 6.25, 12.5, 25, 50, and 100 µg·mL−1) of the extracts at 37 ◦C and 5% CO2. The supernatants were harvested 24 h after infection for virus titration by a plaque-forming units (PFU/mL) assay. The percentage of inhibition was obtained by a comparison with infected/untreated cells and in- fected/treated cells. R2 values ranged from 0.77 to 0.97 (n = 4).

Figura 29. Figure 9. Cytotoxicity of plant extracts in Calu-3 cells. Uninfected cells were exposed to 200 µg·mL−1 for 72 h at 37 ◦C, 5% CO_2. Cell viability was determined using the LDH assay. * $p \leq 0.05$ and *** $p \leq 0.001$ in relation to DMSO-exposed cells (control) (n = 4).

Figura 30. Figure 10. Interaction of the PL^{pro}–compound **5** complex in the BL2loop. The protein is colored in pale cyan, the residues of BL2loop are colored in green (residues G266, N267, Y268, Q269, C270, and G271), and the ligand compound **5** is colored in orange (PDBid: 7JRN).

Figura 31. Figure 11. Interaction of the $3CL^{pro}$–compound **5** complex in the allosteric site. The A-chain of the homodimer is colored in grayish green, and the B-chain residues that interacted in the cavity are colored in magenta. A-Leu287 is represented by dark green sticks. Compound **5** is shown in orange within the alternative interaction groove (PDBid: 6XQT).

Figura 32. Figure 12. Results of the molecular dynamics of the PL^{pro}–compound 5 complex in 200 ns. (A) Pre- dicted h-bonds between the BL2loop residues and compound 5. (B) Calculated RMSD of the ligand compound 5 for the duration of the simulation. (C) Calculated RMSD of the BL2loop for the duration of the simulation. (D) Calculated RMSF for the residues of the PL^{pro}.

Figura 33. Figure 13. Results of the molecular dynamics of the $3CL^{pro}$-compound 5 complex in 200 ns. (A) Pre- dicted h-bonds between compound 5 and the residues CYS145, HIS41, GLU166, ARG188, and GLN189. (B) Calculated RMSD of the ligand compound 5 for the duration of the simulation. (C) Cal- culated RMSD of the catalytic site for the duration of the simulation. (D) Calculated RMSF for the residues of the $3CL^{pro}$.

Figura 34. Figure 14. Results of the molecular dynamics of the $3CL^{pro}$-compound 5 complex in 200 ns. (A Pre- dicted h-bonds between compound 5 and the residues GLY170. (B) Calculated RMSD of the ligand compound 5 for the duration of the simulation. (C) Calculated RMSD of the allosteric site for the duration of the simulation. (D) Calculated RMSF for the residues of the $3CL^{pro}$.

Figura 35. Figure 1. Effect of *Siparuna* extracts on spike protein-ACE2 interaction. C: crude ethanolic extract; H: hexane; D: dichloromethane; E: ethyl acetate; B: butanol. Data are expressed as means of three individual experiments ($n = 3$). Dotted lines indicate 70% and 90% inhibition.

Figura 36. Figure 2. Effect of *Siparuna* extracts on $3CL^{pro}$ activity. C: crude ethanolic extract; H: hexane; D: dichloromethane; E: ethyl acetate; B: butanol. Data are expressed as means of three individual experiments ($n = 3$). Dotted lines indicate 70% and 90% inhibition.

Figura 37. Figure 3. Effect of *Siparuna* extracts on PL^{pro} activity. C: crude ethanolic extract; H: hexane; D: dichloromethane; E: ethyl acetate; B: butanol. Data are expressed as means of three individual experiments ($n = 3$). Dotted lines indicate 70% and 90% inhibition.

Figura 38. Figure 4. Scores (A), X-loadings weight (B) for the PLS model based on the LC-MS data obtained in the low-level data matrix (concatenated ESI and APCI [+/−]) of the 75 samples of five species of the the Siparunaceae family, and the inhibition values of the extracts on the RBD:ACE2 interaction. C: crude ethanolic extract; H: hexane; D: dichloromethane; E: ethyl acetate; B: butanol.

Figura 39. Figure 5. Scores (A), X-loadings weight (B) for the PLS model based on the LC-MS data obtained in the low-level data matrix (concatenated ESI and APCI [+/−]) of the 75 samples of five species of Siparunaceae family, and the inhibition values of the extracts on the $r3CL^{pro}$ activity. C: crude ethanolic extract; H: hexane; D: dichloromethane; E: ethyl acetate; B: butanol.

Figura 40. Figure 6. Scores (A), X-loadings weight (B) for the PLS model based on the LC-MS data obtained in the low-level data matrix (concatenated ESI and APCI [+/−]) of the 75 samples of five species of Siparunaceae family, and the inhibition values of the extracts on the rPL^{pro} activity. C: crude ethanolic extract; H: hexane; D: dichloromethane; E: ethyl acetate; B: butanol.

Figura 41. Figure 7. Structure of the chemical compounds identified in *Siparuna* spp. Coclaurine (1), reticuline (2), boldine (3), laurolitsine (4), asimilobine (5), actinodaphnine (6), and bulbocapnine (7).

Figura 42. Figure 8. Calu-3 cells infected with SARS-CoV-2 at an MOI of 0.01, were treated with 25 extracts from *Siparuna* species at 50 µg·mL−1 for 24 h at 37 ◦C, 5% CO_2. C: crude ethanolic extract; H: hexane; D: dichloromethane; E: ethyl acetate; B: butanol. Viral titers were assessed by plaque assay in PFU/mL and compared to infected and untreated controls ($n = 4$). Dotted lines indicate 70% and 90% inhibition.

Figura 43. Figure 9. Calu-3 cells were treated with the 25 extracts of *Siparuna* species at 200 µg·mL−1 for 72 h at 37 ◦C and 5% CO_2. C: crude ethanolic extract; H: hexane; D: dichloromethane; E: ethyl acetate; B: butanol. Cell viability was assessed by analyzing the activity of the enzyme lactate dehydrogenase (LDH) and comparing it with that of the untreated controls. ($n = 3$). Dotted lines indicate 70% and 90% of inhibition.

Figura 44. Figure 10. Boiled egg diagram of the seven compounds under study. Points located in the yellow area indicate molecules predicted to passively permeate the blood−brain barrier (BBB). The white area represents the molecules passively absorbed by the human gastrointestinal tract (HIA). Blue points indicate molecules predicted to be effluxed from the central nervous system by P-glycoprotein.

Figura 45. Figure 11. 2D and 3D interactions among compound reticuline (2) (A), bulbocapnine (7) (B), positive control (PC), and targets of SARS-CoV-2 (PDBs 3SCI and 6M0J—Spike). Residues: Ala (Alanine), Arg (Arginine), Asn (Asparagine), Asp (Aspartic acid), Glu (Glutamic acid), Gly (Glycine), His (Histidine), Phe (Phenylalanine), and Tyr (Tyrosine). * Indicates the occurrence of similar residues in the interactions between compounds and PC.

Figura 46. Figure 12. 2D and 3D interactions among compound reticuline (2) (A), boldine (3) (B), positive control (PC), and targets of SARS-CoV-2 (PDBs 6MN2 and 7B3E—$3CL^{pro}$). Residues: Ala (Alanine), Arg (Arginine), Asn (Asparagine), Asp (Aspartic acid), Glu (Glutamic acid), Gly (Glycine), His (Histidine), Phe (Phenylalanine), and Tyr (Tyrosine). * Indicates the occurrence of similar residues in the interactions with the compounds and PC.

Figura 47. Figure 13. 2D and 3D interactions between compound actinodaphnine (6) (A), bulbocapnine (7) (B), positive control (PC), and targets of SARS-CoV-2 (PDBs 7LBR and 7TZJ). Residues: Ala (Alanine), Arg (Arginine), Asn (Asparagine), Asp (Aspartic acid), Glu (Glutamic acid), Gly (Glycine), His (Histidine), Phe (Phenylalanine), and Tyr (Tyrosine). * Indicates the occurrence of similar residues in the interactions with the compounds and PC.

Figura 48. Figure 14. Root mean square deviation (RMSD). (A) Spike (6M0J), (B) $3CL^{pro}$ (6M2N), and (C) PL^{pro} (7TZJ). bulbocapnine (**7**) (Pink), reticuline (**2**) (green), and inhibitor protein (yellow).

Figura 49. Figure 15. Root mean square fluctuation (RMSF). (A) Spike (6M0J), (B) $3CL^{pro}$ (6M2N), and (C) PL^{pro} (7TZJ). Complex protein bulbocapnine (**7**) (pink), complex protein reticuline (**2**) (green), complex protein inhibitor protein (yellow), and protein alone (black).

Figura 50. Figure 16. The radius of gyration (Rg). (A) Spike (6M0J); (B) 3CLpro (6M2N); and (C) PLpro (7TZJ). Complex protein bulbocapnine (**7**) (pink), complex protein reticuline (**2**) (green), complex protein inhibitor protein (yellow), and protein alone (black).

LISTA DE QUADROS E TABELAS

Quadro 1. Dados das principais vacinas aprovadas atualmente pela ANVISA – BRASIL, FDA – Estados Unidos e EMA – União Europeia para o enfrentamento da COVID-19.

Quadro 2. Dados dos principais medicamentos aprovados atualmente pela ANVISA – BRASIL, FDA – Estados Unidos e EMA – União Europeia para o enfrentamento da COVID-19.

Tabela 1. Gradiente cromatográfico utilizado nas análises por LC-MS/MS.

Tabela 2. Parâmetros da máquina utilizados nas análises de espectrometria de massas com as fontes de ionização química à pressão atmosférica (APCI) e de ionização por *electrospray* (ESI) operando nos modos positivo e negativo de ionização.

Tabela 3. Parâmetros para construção de redes moleculares quantitativas (FBMN) na plataforma GNPS.

Tabela 4. Table 1. Myrtaceae extracts and their effect on the entry and replication mechanisms associated with the Spike protein (250 $\mu g \cdot mL^{-1}$) in host cells and inhibition of $3CL^{pro}$ and PL^{pro} proteases (100 $\mu g \cdot mL^{-1}$) of SARS-CoV-2.

Tabela 5. Table 2. EC_{50} values for the five Myrtaceae extracts in Spike-pseudotyped VSV assay.

Tabela 6. Table 3. LC-MS/MS data of annotated and proposed compounds (undescribed) in the molecular network (MS/MS spectra in Supplementary Figures S5–S9).

Tabela 7. Table 4. Myrtaceae extract EC50 values.

Tabela 8. Table 5. Fitness of top-ranked individuals from GOLD docking.

Tabela 9. Table 6. *In silico* prediction of physicochemical properties of compounds **1**–**5**.

Tabela 10. Table 7. Toxicity prediction. Interpret the colors so that green means the substance is not toxic, yellow means it may be toxic, and red means toxic.

Tabela 11. Table 1. LC-MS/MS data of predicted ions and annotation of the proposed compounds.

Tabela 12. Table 2. Predicted interactions with cytochrome P450 (CYP) for the seven compounds.

Tabela 13. Table 3. Information about the target proteins of SARS-CoV-2, their respective ligands, and the RMSD values obtained from the redocking procedure.

Tabela 14. Table 4. Score values and probability of activity of the test compounds on the targets of SARS-CoV-2.

RESUMO

O SARS-CoV-2 pode causar danos multissistêmicos com risco de morte, sendo responsável por altos índices de infecção e mortalidade, muitas vezes subnotificados. Metabólitos secundários de plantas têm se mostrado promissores como antivirais, atuando no fortalecimento do sistema imunológico, na proteção contra infecções e na inibição da replicação viral, especialmente contra alvos como a SP e as proteases $3CL^{pro}$ e PL^{pro}. A biodiversidade brasileira oferece vasto potencial para a descoberta de novas moléculas bioativas. Além disso, ferramentas computacionais como modelos preditivos e redes moleculares aceleram a triagem e identificação de compostos com atividade contra a COVID-19, otimizando recursos e ampliando as possibilidades terapêuticas. Diante desse cenário, este estudo teve como objetivo desenvolver modelos preditivos capazes de identificar potenciais espécies vegetais e suas substâncias bioativas, utilizando triagens químicas e biológicas de extratos da Fito-Extractoteca com possível ação antiviral contra o SARS-CoV-2. Os dados dessas triagens foram empregados na construção de modelos preditivos por meio de métodos quimiométricos, bem como na criação de redes moleculares para investigação qualitativa e anotação das substâncias preditas. As etapas de triagem química e biológica apresentaram resultados promissores na indicação de espécies vegetais com potencial inibitório anti-SARS-CoV-2. Além disso, abordagens de mineração de dados (*data mining*) e *molecular networking* demostraram ser contribuintes essenciais para o ajuste dos modelos desenvolvidos e análises complementares. Os resultados obtidos demonstram o potencial da biodiversidade brasileira como fonte de agentes anti-SARS-CoV-2, e a sua capacidade de ação através de mecanismos distintos de forma *multitarget*. Os modelos preditivos otimizaram o processo de busca por substâncias anti-SARS-CoV-2, além de fornecer *insights* significativos para o refinamento dos ensaios subsequentes. Além disso, demonstram que os modelos preditivos baseados em triagens experimentais facilitam o estudo de matrizes complexas, configurando-se como alternativas promissoras frente a ensaios de menor precisão, como o *docking molecular*, ou de custos mais elevados, como o fracionamento bioguiado e a desreplicação. Esses avanços representam um progresso significativo na busca por novos candidatos a fármacos contra a COVID-19, aproveitando a diversidade vegetal do Brasil e empregando métodos computacionais para otimizar o processo de triagem e identificação de substâncias com atividade antiviral.

Palavras-chave: metabólitos vegetais, LUMIT, FRET, LC-MS/MS, quimioinformática

ABSTRACT

SARS-CoV-2 can cause multisystemic damage with a risk of death and has been responsible for high infection and mortality rates, often underreported. Plant secondary metabolites have shown promise as antiviral agents by strengthening the immune system, protecting against infections, and inhibiting viral replication—particularly through interaction with targets such as the Spike protein and viral proteases 3CLpro and PLpro. Brazil's vast biodiversity offers great potential for the discovery of new bioactive molecules. Additionally, computational tools such as predictive models and molecular networks accelerate the screening and identification of compounds with activity against COVID-19, optimizing resources and expanding therapeutic possibilities. In this context, the present study aimed to develop predictive models capable of identifying potential plant species and their bioactive compounds by using chemical and biological screenings of extracts from the Fito-Extractoteca, with possible antiviral activity against SARS-CoV-2. The data from these screenings were used to construct predictive models through chemometric methods, as well as to generate molecular networks for qualitative investigation and annotation of the predicted substances. The chemical and biological screening steps yielded promising results in identifying plant species with anti-SARS-CoV-2 inhibitory potential. Moreover, data mining and molecular networking approaches proved to be essential contributors to the refinement of the developed models and to complementary analyses. The results highlight the potential of Brazilian biodiversity as a source of anti-SARS-CoV-2 agents, with multitarget activity through distinct mechanisms. The predictive models optimized the search for anti-SARS-CoV-2 substances and provided meaningful insights for the improvement of subsequent assays. Furthermore, these models—based on experimental screenings—facilitated the study of complex matrices and emerged as promising alternatives to less precise assays, such as molecular docking, or more costly strategies like bioassay-guided fractionation and dereplication. These advances represent significant progress in the search for new drug candidates against COVID-19, by leveraging Brazil's plant diversity and applying computational methods to streamline the screening and identification of antiviral compounds.

Keywords: plant metabolites, LUMIT, FRET, LC-MS/MS, cheminformatics

SUMÁRIO

1. INTRODUÇÃO 24

2. FUNDAMENTAÇÃO TEÓRICA 28

2.1. A COVID-19 e o vírus SARS-CoV-2 28

2.2. A SP de SARS-CoV-2 30

2.3. As proteases $3CL^{pro}$ e PL^{pro} de SARS-CoV-2 31

2.4. Mecanismos de entrada e replicação associados à SP e às enzimas $3CL^{pro}$ e PL^{pro} do SARS-CoV-2 nas células hospedeiras 33

2.5. Tratamentos: vacinas e medicamentos frente à COVID-19 36

2.6. Produtos Naturais no enfrentamento do SARS-CoV-2 e da COVID-19 40

2.7. Processamento de dados químicos 45

2.8. Quimiometria 46

2.9. Modelos quimiométricos de predição químico-biológicos 47

2.10. Construção de Redes Moleculares 48

3. JUSTIFICATIVA 51

4. OBJETIVOS 52

4.1. Objetivo Geral 52

4.2. Objetivos específicos 52

5. MATERIAIS E MÉTODOS 53

5.1. Biblioteca de Extratos/ Fito-Extractoteca 53

5.2. Obtenção de *fingerprintings* por LC-MS/MS 54

5.3. Triagem biológica por ensaios da inibição da interação *Spike* (RBD):ACE2 56

5.4. Triagem biológica por ensaios da inibição da atividade de $3CL^{pro}$ e PL^{pro} 57

5.5. Processamento dos dados químicos 59

5.6. Ensaios quimiométricos 60

5.7. Construção de redes moleculares 60

5.8. Ensaios de citotoxidez em células Vero E6 e Calu-3 61

5.8.1. Citotoxidez em Células Vero E6 61

5.8.2. Citotoxidez em células Calu-3 62

5.9. Ensaio de neutralização *in vitro* de vírus da estomatite vesicular (VSV) pseudotipado com a SP de SARS-CoV-2 63

5.9.1. Construção e produção dos pseudovírus 64

5.9.2. Ensaios de neutralização dos pseudovírus 64

5.10. Ensaios antivirais frente aos SARS-CoV-2 65

5.10.1. Ensaio antiviral 65

5.11. Ensaios e estudos *in silico* 67
5.11.1. *Docking* molecular 67
5.11.2. Dinâmica molecular 68
5.11.3. Predição de características farmacocinéticas (ADMET) 70
6. RESULTADOS E DISCUSSÃO 71
6.1. Artigo 1: *Myrtucommulones and Related Acylphloroglucinols from Myrtaceae as a Promising Source of Multitarget SARS-CoV-2 Cycle Inhibitors* 71
6.2. Artigo 2: *Predicting the Anti-SARS-CoV-2 Potential of Isoquinoline Alkaloids from Brazilian Siparunaceae Species Using Chemometric Tools* 86
7. CONCLUSÃO 132
8. PERSPECTIVAS 134
9. REFERÊNCIAS BIBLIOGRÁFICAS 136

1. INTRODUÇÃO

A doença causada por coronavírus 2019 (COVID-19) foi identificada, inicialmente, em habitantes da cidade de Wuhan (China) nos meses finais de 2019 (Spiteri *et al.,* 2020). Segundo Andersen *et al.* (2020) e Zhou *et al.* (2020a), a síndrome respiratória aguda grave causadora do coronavírus 2 (SARS-CoV-2) se assemelha bastante ao primeiro SARS-CoV, afetando múltiplos órgãos, causando, principalmente, danos alveolares e cardíacos, podendo culminar na morte do paciente infectado. Somente no Brasil há cerca de 39 milhões de casos confirmados e 715 mil mortes desde o aparecimento da doença. Já no mundo, atualmente, o número é de cerca de 777 milhões de casos registrados com mais de sete milhões de mortes (OMS, 2025) (Figura 1). Além disso, acredita-se que houve diversos casos subnotificados.

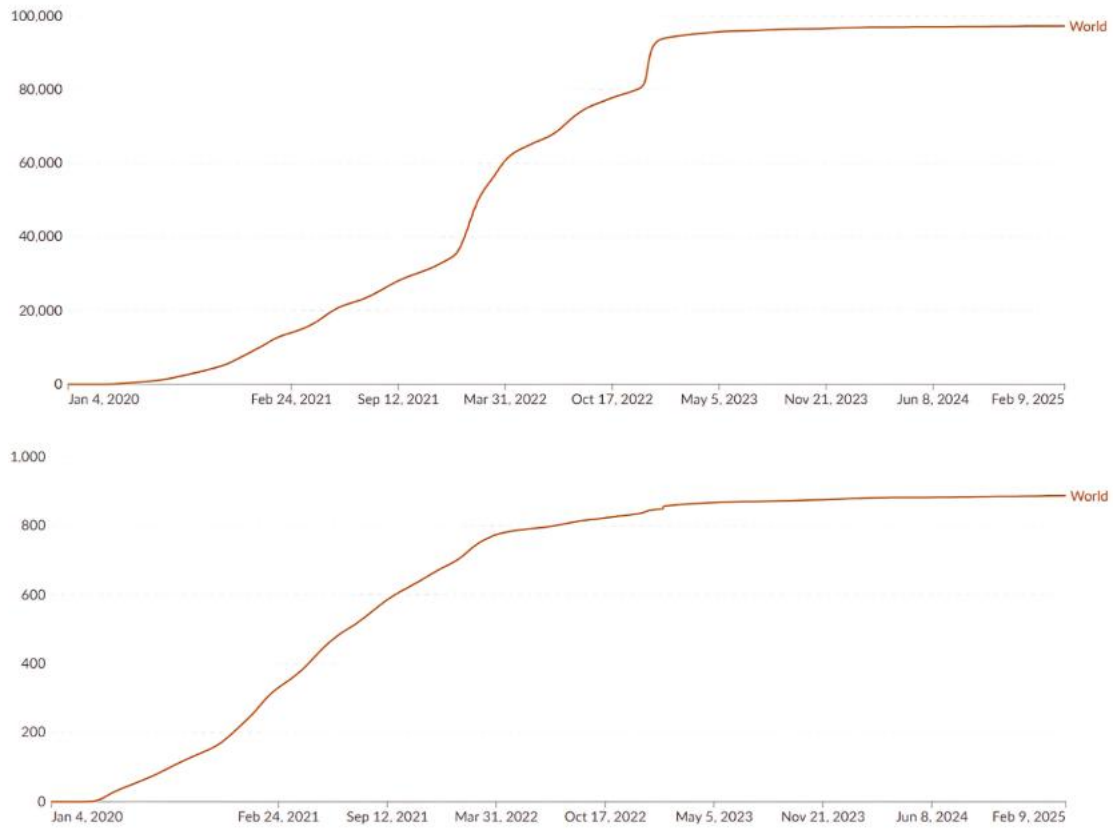

Figura 1. Média cumulativa do número de casos de infecção (superior) e mortes (inferior) confirmadas no mundo. Fonte: Our World in Data, 2025.

Os metabólitos secundários vegetais são alternativas relevantes na busca de substâncias com potencial atividade farmacológica, e diversas plantas já se destacam no cenário de desenvolvimento de novos medicamentos antivirais (Martinez *et al.,*2015; Newman & Cragg, 2020). Apesar do progresso da vacinação e de já existirem alternativas terapêuticas aprovadas

e estabelecidas contra o SARS-CoV-2, o desenvolvimento de novos medicamentos que auxiliem na prevenção e tratamento da COVID-19 ainda é uma questão de prioridade global.

Segundo Bhuiyan *et al.* (2020) diversas famílias botânicas são alvos promissores na busca de moléculas naturais com potencial anti-SARS-CoV-2. Até o momento, as espécies vegetais investigadas demostraram que podem auxiliar no fortalecimento do sistema imunológico, na proteção contra a infecção viral e ter ação direta sobre o ciclo de replicação e sobre a própria estrutura (viral) do SARS-CoV-2 (Boozari & Hosseinzadeh, 2020; Yadav *et al.*, 2021). As buscas se baseiam em diversos alvos - proteínas estruturais e não-estruturais, tais como: o gene da RNA polimerase dependente de RNA (RdRp), a 2'-*O*-metil-transferase (MTase), a protease serina transmembranar tipo II (TMPRSS2), mas principalmente, a proteína *spike* (SP) e as proteases virais de replicação 3-quimiotripsina-*like* ($3CL^{pro}$) e papaína-*like* (PL^{pro}) (Verma *et al.,* 2020; Yadav *et al.*, 2021). Chapman e Andurkar (2022), e Al-Harrasi *et al.* (2022) em suas revisões mostraram que diversas moléculas de origem vegetal são relevantes como potenciais agentes anti-SARS-CoV-2, com resultados promissores para terpenoides, substâncias fenólicas e alcaloides.

O Brasil detém a maior biodiversidade do mundo, com cerca de 15% das espécies viventes do planeta e mais de 60% da biodiversidade mundial. Ao avaliar somente os vegetais, o Brasil é o país com o maior número de espécies no mundo, e ocupa os primeiros lugares entre os países mais megadiversos (The Brazil Flora Group, 2018) (Figura 2). Logo, a flora brasileira é detentora de diversos alvos promissores na busca de substâncias com potencial anti-SARS-CoV-2. Uma vez que a bioprospecção se apresenta como uma das mais importantes ferramentas para desenvolvimento de medicamentos a partir da biodiversidade (Newman & Cragg, 2020), a flora do país se torna uma potência para a descoberta de novos candidatos a fármacos no enfrentamento à COVID-19.

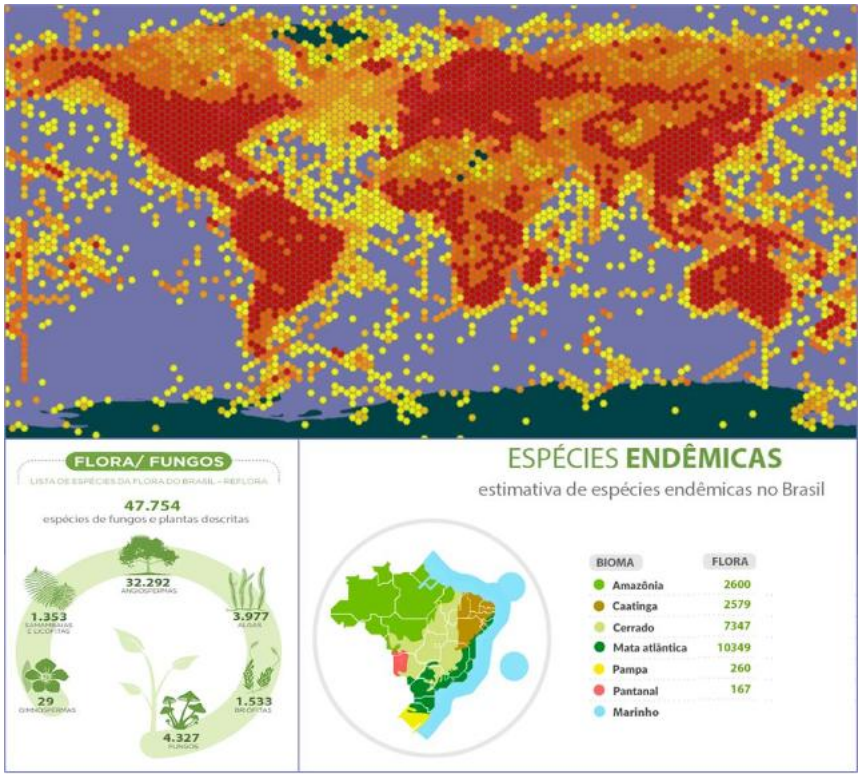

Figura 2. Mapa de calor (verde < amarelo < laranja < vermelho) da ocorrência de todas as espécies vegetais registradas no mundo, com destaque para a riqueza e abundância de plantas no Brasil. Fonte: adaptado de GBIF, 2025; SIBBr, 2025.

As abordagens tradicionais que podem vir a ser utilizadas na descoberta de substâncias com atividade potencial anti-SARS-CoV-2 englobam rotineiramente a desreplicação de extratos e isolamento de moléculas ativas em fracionamentos bioguiados. Cabe ressaltar, porém, que estes ensaios geram conjuntos de dados complexos, dificultando as intepretações de resultados relevantes, além de demandar elevados gastos com tempo, materiais e outros custos associados.

Dessa forma, os métodos computacionais se apresentam como alternativas pertinentes nesta busca. Os modelos quimiométricos de predição permitem a triagem de grande número de amostras de matrizes biológicas complexas, assim como bibliotecas inteiras de substâncias, identificando aquelas com a maior probabilidade de exibirem as atividades biológicas investigadas (Ferreira, 2015; Xu *et al.*, 2022). Uma alternativa computacional é a construção de redes moleculares, uma vez que estas permitem uma avaliação visual qualitativa dos dados e a facilitação nas interpretações de relações químico-biológicas existentes (Pilon *et al.*, 2021). Também, pode-se observar o avanço cada vez maior de técnicas como o aprendizado de máquina (*machine learning*), integrado à metabolômica baseada em LC-MS/MS, que têm permitido a caracterização rápida e precisa da bioatividade de produtos naturais, impulsionando

a identificação de novos alvos terapêuticos e reduzindo as barreiras associadas à redescoberta de substâncias já conhecidas (Brittin *et al*., 2025). Além destas, diversas outras abordagens emergem continuamente, e se solidificam no *workflow* adotado pela comunidade científica, se consolidando como ferramentas indispensáveis na busca de novos fármacos a partir de produtos naturais. Essas ferramentas economizam tempo, esforços, recursos e custos, uma vez que reduzem a necessidade de avaliar todo o perfil químico do extrato vegetal e o teste de todas as substâncias experimentalmente, direcionando o foco para os alvos mais promissores.

2. FUNDAMENTAÇÃO TEÓRICA

2.1. A COVID-19 e o vírus SARS-CoV-2

A COVID-19 se disseminou rapidamente pelo mundo, levando a Organização Mundial da Saúde (OMS) a declarar estado de pandemia global em março de 2020. Desde então, o combate à doença se tornou um desafio significativo para as políticas de saúde pública mundiais, ultrapassando até mesmo surtos anteriores de síndromes respiratórias, como o MERS-CoV em 2012 (Hu *et al.*, 2021). Neste período houve falta de espaço, materiais, aparelhagens, capacidade e/ou conhecimento técnico para o enfrentamento desta doença (Akay *et al.*, 2022), acarretando milhares de óbitos. E apesar da intensa busca por medicamentos que auxiliassem no tratamento da doença, ainda não havia alternativas aprovadas e estabelecidas, uma vez que não era não era possível realizar ensaios pré-clínicos e clínicos de substâncias relevantes (Verma *et al.*, 2020). Cabe ressaltar, que no intervalo de março de 2020 até os dias atuais, um dos maiores empecilhos no estudo e desenvolvimento de alternativas contra a COVID-19 é o aparecimento de variantes do vírus (OMS, 2023). O desenvolvimento das primeiras vacinas foi concluído em meados de 2020 e, o primeiro lote, disponibilizado apenas em dezembro desse mesmo ano. Com o progresso da vacinação e das medidas protetivas recomendadas pelos sistemas governamentais, houve a redução das taxas de transmissão e mortalidade, levando a OMS a declarar o fim da Emergência de Saúde Pública de Importância Internacional (ESPII) referente à COVID-19 em maio de 2023.

O novo coronavírus (SARS-CoV-2) pertence à ordem *Nidoviriales*, família *Coronaviridae* – gênero *Betacoronavirus*, grupo no qual também se encontram dois já reconhecidos representantes, o coronavírus causador da síndrome respiratória aguda grave (SARS-CoV) e o coronavírus causador da síndrome respiratória do oriente médio (MERS-CoV) (Gupta *et al.*, 2022). Os coronavírus integram quatro gêneros que podem vir a infectar diferentes animais, como pássaros (coronavírus aviário e BuCoV/MuCoV/ThCoV) e mamíferos, incluindo os seres humanos, como os coronavírus humanos (HCoV) e os causadores das síndromes respiratórias (SARS-CoV e MERS-CoV) (Jeong *et al.*, 2020) (Figura 3).

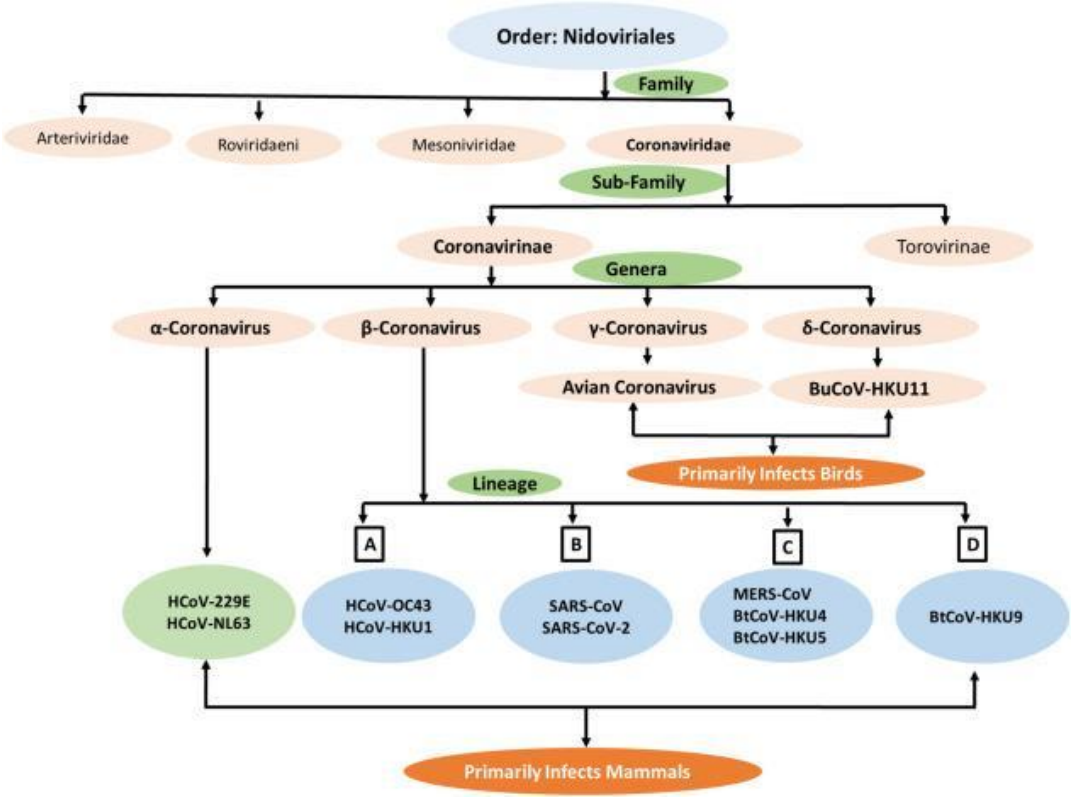

Figura 3. Representação esquemática da taxonomia da ordem *Nidoviriales*. Fonte: Gupta *et al.*, 2022.

A partícula viral do SARS-CoV-2 é arredondada, com cerca de 80 a 120 nm de diâmetro, e projeções em forma de "coroa" na superfície (Bolcato *et al.,* 2020 e Gupta, *et al.*, 2022). O seu material genômico é envelopado e constituído por RNA de fita simples e de polaridade positiva. O genoma completo é de cerca 30 kb, sendo dividido em regiões que irão originar: dezesseis proteínas não estruturais (nsp1-16) originadas a partir das poliproteínas ppla e pplb, codificadas pelas "janelas abertas de leitura" ORF1a e ORF1b. Além disso, há regiões que originarão proteínas estruturais codificadas pelo RNA subgenômico: a SP, a proteína do envelope viral, a proteína de membrana e o nucleocapsídeo. Também estão presentes na estrutura do genoma viral de SARS-CoV-2 as regiões de cinco proteínas acessórias, ORFs 6, 7a-b, 8 e 9 (Jeong *et al.*, 2020; Zhang *et al.*, 2021.; Gupta, *et al.*, 2022) (Figura 4).

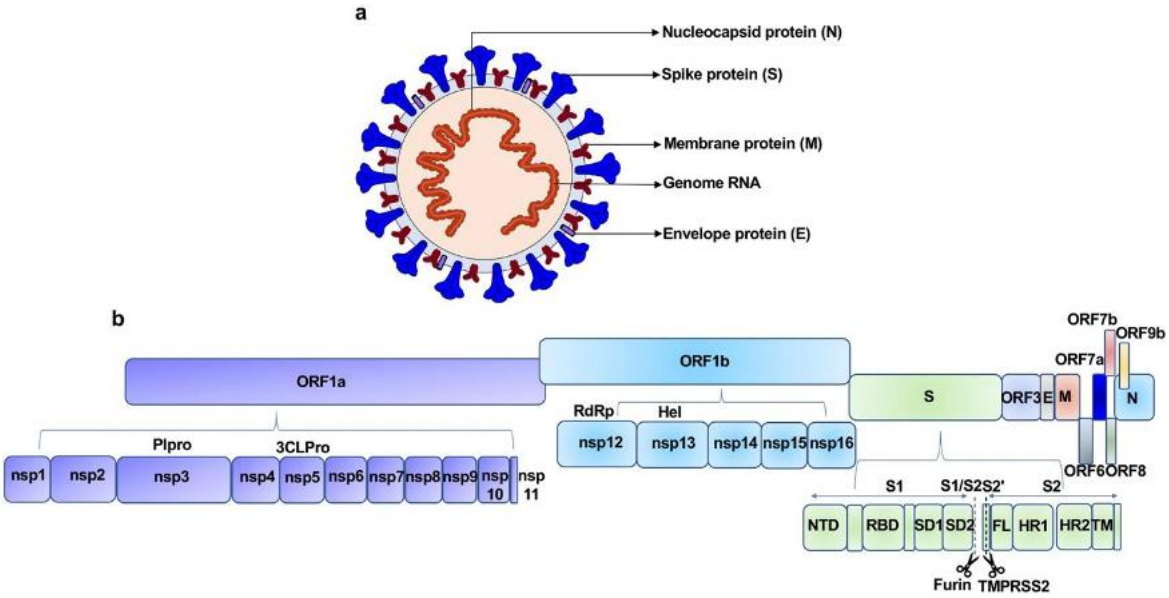

Figura 4. Representações esquemáticas da estrutura da partícula viral, e da arquitetura genômica do SARS-CoV-2. **A:** nucleocapsídeo (N), SP (S), proteína de membrana (M) e proteína de Envelope (E); **B:** genoma viral (+)ssRNA completo de SARS-CoV-2. Fonte: Zhang *et al.*, 2021.

O SARS-CoV-2 demonstrou uma capacidade de transmissão elevada, superando até mesmo os outros membros do gênero *Betacoronavirus* (Hu *et al.*, 2021). Sua alta capacidade de infectar seres humanos, atrelada à sua transmissibilidade através de contato com gotículas e secreções de pessoas infectadas, resultou em uma grande quantidade de pessoas infectadas em um curto espaço de tempo (Antonio *et al.*, 2020), originando, dessa forma, uma nova doença, chamada COVID-19 (doença do coronavírus 2019).

2.2. A SP de SARS-CoV-2

Os coronavírus, assim como outros vírus patogênicos humanos, possuem proteínas específicas responsáveis pelo reconhecimento e ligação aos receptores das células hospedeiras. No caso do SARS-CoV-2, a SP desempenha um papel crucial ao interagir com os receptores presentes na superfície das células-alvo, desencadeando o processo de endocitose mediada por clatrina. A enzima conversora de angiotensina II (ACE2) é um receptor-chave para a ligação da SP (Lan *et al.*, 2020; Zhou *et al.*, 2020b).

A SP do SARS-CoV-2, fundamental para a montagem e infecção viral, é composta por duas subunidades distintas: S1 e S2. A subunidade S1 contém o domínio de ligação ao receptor (RBD), responsável por se ligar ao receptor ACE2 presente nas célula-alvo. Por sua vez, a subunidade S2 facilita o processo de fusão, entrada e transporte intracelular do vírus na célula hospedeira (Tortorici & Veesler, 2019; Zhou *et al.*, 2020b). Esta proteína possui cerca de 200

kDa e é composta por 1273 aminoácidos. Em sua estrutura podem ser encontradas uma porção N-terminal localizada na região extracelular do envelope viral, um domínio transmembrana que está ancorado à membrana viral, e um segmento C-terminal intracelular (Huang *et al.*, 2020) (Figura 5).

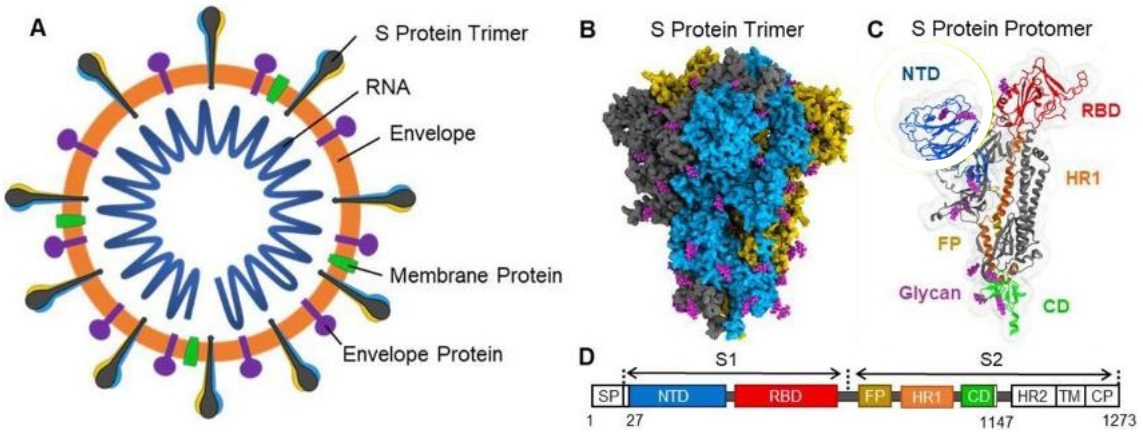

Figura 5. Representações esquemáticas da estrutura da proteína *spike* (SP) de SARS-CoV-2. **A:** a estrutura geral do SARS-CoV-2 e posição da SP; **B:** a estrutura trimérica da SP; **C:** o protômero da SP; **D:** as principais regiões encontradas nas subunidades (S1 e S2). Fonte: criada no Biorrender por Mellanie Fontes-Dutra.

2.3. As proteases $3CL^{pro}$ e PL^{pro} de SARS-CoV-2

A $3CL^{pro}$, também conhecida como protease principal (do ingês, *main protease* MP) é uma enzima essencial para a replicação do SARS-CoV-2. Ela desempenha um papel crucial na clivagem de algumas poliproteínas virais, permitindo a formação de proteínas funcionais necessárias para a montagem e replicação do vírus (Dömling & Gao, 2020).

A MP do SARS-CoV-2 é uma proteína monomérica com três domínios: I, II e III (Figura 6). O domínio I é uma folha-beta antiparalela, enquanto os domínios II e III são compostos principalmente por α-hélices. O sítio ativo da $3CL^{pro}$ está localizado entre os domínios I e II. Essa proteína é uma enzima homodimérica, formada por dois monômeros idênticos dispostos perpendicularmente um em relação ao outro, o que pode vir a aumentar sua atividade enzimática, uma vez que o monômero é praticamente inativo (Mengist *et al.*, 2021).

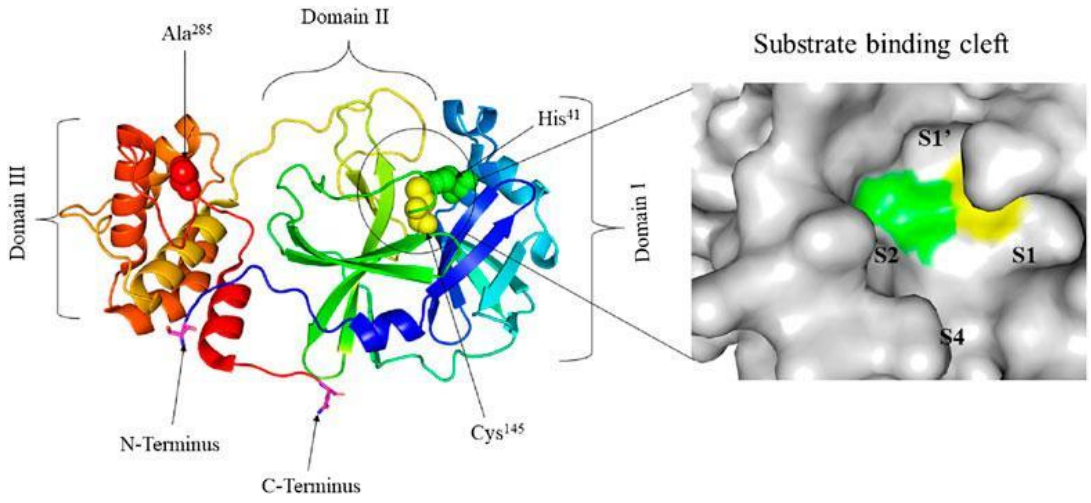

Figura 6. Representação esquemática da estrutura da enzima $3CL^{pro}$ de SARS-CoV-2 (com destaque do sítio de ligação ativo). Fonte: Mengist *et al.* (2021).

A PL^{pro} do SARS-CoV-2 também é uma enzima com papel importante na replicação viral, uma vez que sua atividade é essencial para a formação do complexo de replicação/transcrição do vírus (Dömling & Gao, 2020).

A protease semelhante a papaína possui três domínios principais denominados polegar (*thumb*), palma (*palm*) e dedos (*fingers*) (Figura 7). O domínio *thumb* é uma estrutura de folha-beta antiparalela localizada na região N-terminal; enquanto o domínio *palm* é o maior e contém o sítio catalítico responsável pela atividade enzimática da PL^{pro}, apresentando uma estrutura dobrada semelhante a uma mão, com uma conformação tridimensional bem característica. Por fim, o domínio *fingers*, localizado na região C-terminal, é composto principalmente por α-hélices e desempenha um papel crucial na interação com outros componentes da replicação viral, além de modular a atividade enzimática (Gao *et al.*, 2021; Osipiuk *et al.*, 2021).

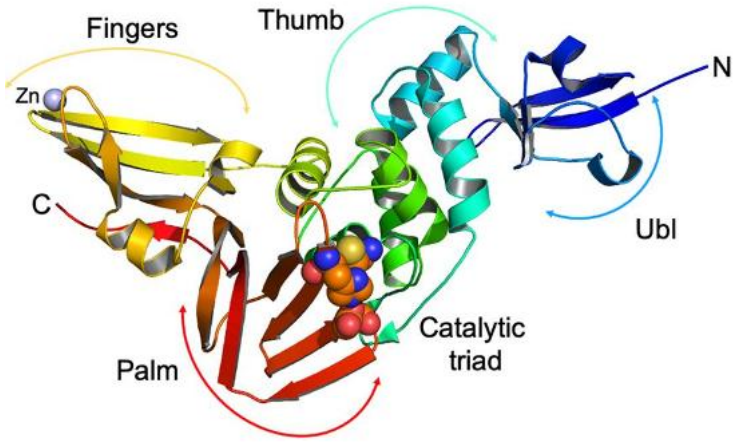

Figura 7. Representação esquemática da estrutura da enzima PL^{pro} de SARS-CoV-2. Fonte: Osipiuk *et al.* (2021).

2.4. Mecanismos de entrada e replicação associados à SP e às enzimas $3CL^{pro}$ e PL^{pro} do SARS-CoV-2 nas células hospedeiras

A SP interage com o receptor ACE2 na superfície das células hospedeiras, o que desencadeia a entrada do vírus, e essa entrada pode ocorrer de duas maneiras: através da endocitose mediada por clatrina, ou por meio da clivagem da subunidade S2 da SP na presença da protease TMPRSS2 (Jackson *et al.*, 2021) (Figura 8). No processo de endocitose mediada por clatrina, o complexo vírus-ACE2 é internalizado pela célula em uma vesícula. Em seguida, a clivagem da subunidade S2 da SP ocorre no endossomo por meio de catepsinas, permitindo a fusão da membrana viral com a membrana endossomal e liberando o material genético viral no citoplasma (Huang *et al.*, 2020; Jackson *et al.*, 2021). Na presença da protease TMPRSS2, a clivagem da subunidade S2 ocorre na superfície da célula hospedeira. Esse evento ativa a SP e facilita a fusão direta entre a membrana viral e a membrana celular (Huang *et al.*, 2020; Jackson *et al.*, 2021).

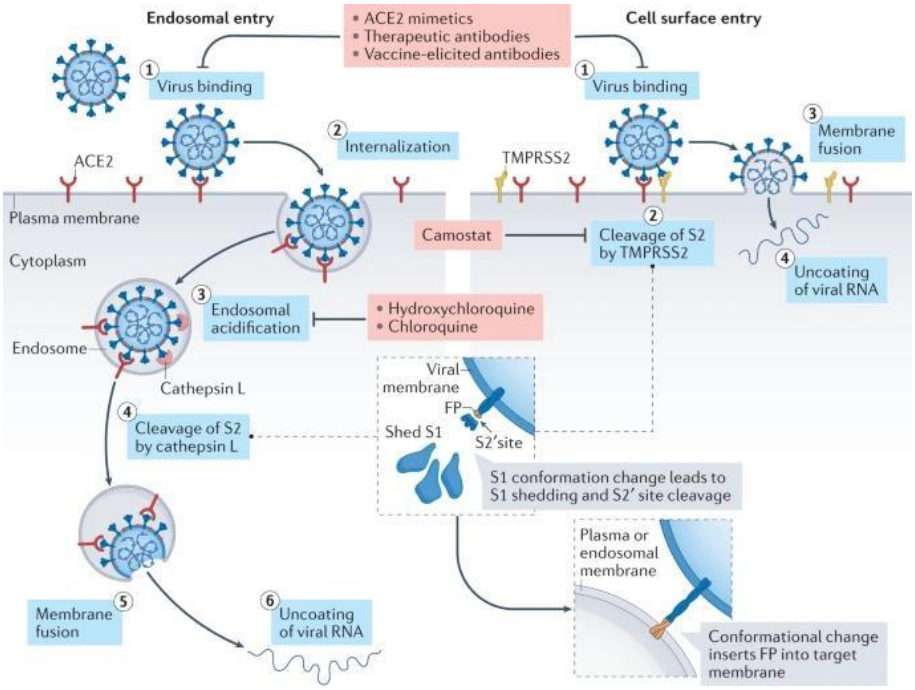

Figura 8. Esquema do processo de ligação ao receptor (SP:ACE2) e entrada do SARS-CoV-2 nas células hospedeiras. Fonte: Jackson *et al.* (2021).

Após a entrada do SARS-CoV-2 na célula hospedeira (Figura 9), inicia-se o processo de replicação viral, que envolve várias etapas cruciais. Resumidamente, a primeira etapa é a transcrição e tradução do RNA viral. Após a liberação do RNA viral no citoplasma, a RNA polimerase viral transcreve o RNA viral em moléculas de RNA mensageiro (mRNA), que são então traduzidos pelos ribossomos da célula hospedeira para produzir as proteínas virais (Zhang *et al.*, 2021.; Gupta, *et al.*, 2022).

Durante a tradução, dependente da codificação das ORFs 1a e 1b, são produzidas poliproteínas virais (ppla e pplb) que contêm 16 proteínas virais (nsp) em uma única cadeia polipeptídica. Essas poliproteínas são clivadas em proteínas funcionais individuais por proteases virais específicas, como a $3CL^{pro}$ e a PL^{pro} (Malik *et al.*, 2020; Shajahan *et al.*, 2021; V'kovski *et al.*, 2021). Essas proteases são essenciais para a replicação e montagem do vírus, o que permite a conclusão do ciclo viral

A replicação ocorre com auxílio da RdRp, que utiliza o RNA viral como molde para sintetizar cópias adicionais do genoma viral. Esse processo ocorre principalmente no retículo endoplasmático rugoso envolve a produção de cópias complementares de RNA (RNA de sentido negativo) e a subsequente síntese de múltiplas cópias positivas do RNA viral (Shajahan *et al.*, 2021; V'kovski *et al.*, 2021; Gupta, *et al.*, 2022).

Após a síntese de proteínas virais e replicação do RNA viral, os componentes virais são montados no compartimento intermediário - retículo endoplasmático rugoso - complexo de Golgi. A SP é incorporada na superfície viral, e as proteínas da matriz viral (membrana) envolvem o genoma viral, enquanto as proteínas do envelope são incorporadas nessa membrana (V'kovski *et al.*, 2021).

Finalmente, as novas partículas virais são liberadas da célula hospedeira por meio de exocitose ou lise celular. Na exocitose, os vírus são transportados para a superfície celular e liberados para o ambiente extracelular. Na lise celular, a célula hospedeira é "rompida", liberando os vírus para o meio extracelular (Malik *et al.*, 2020; Shajahan *et al.*, 2021; V'kovski *et al.*, 2021).

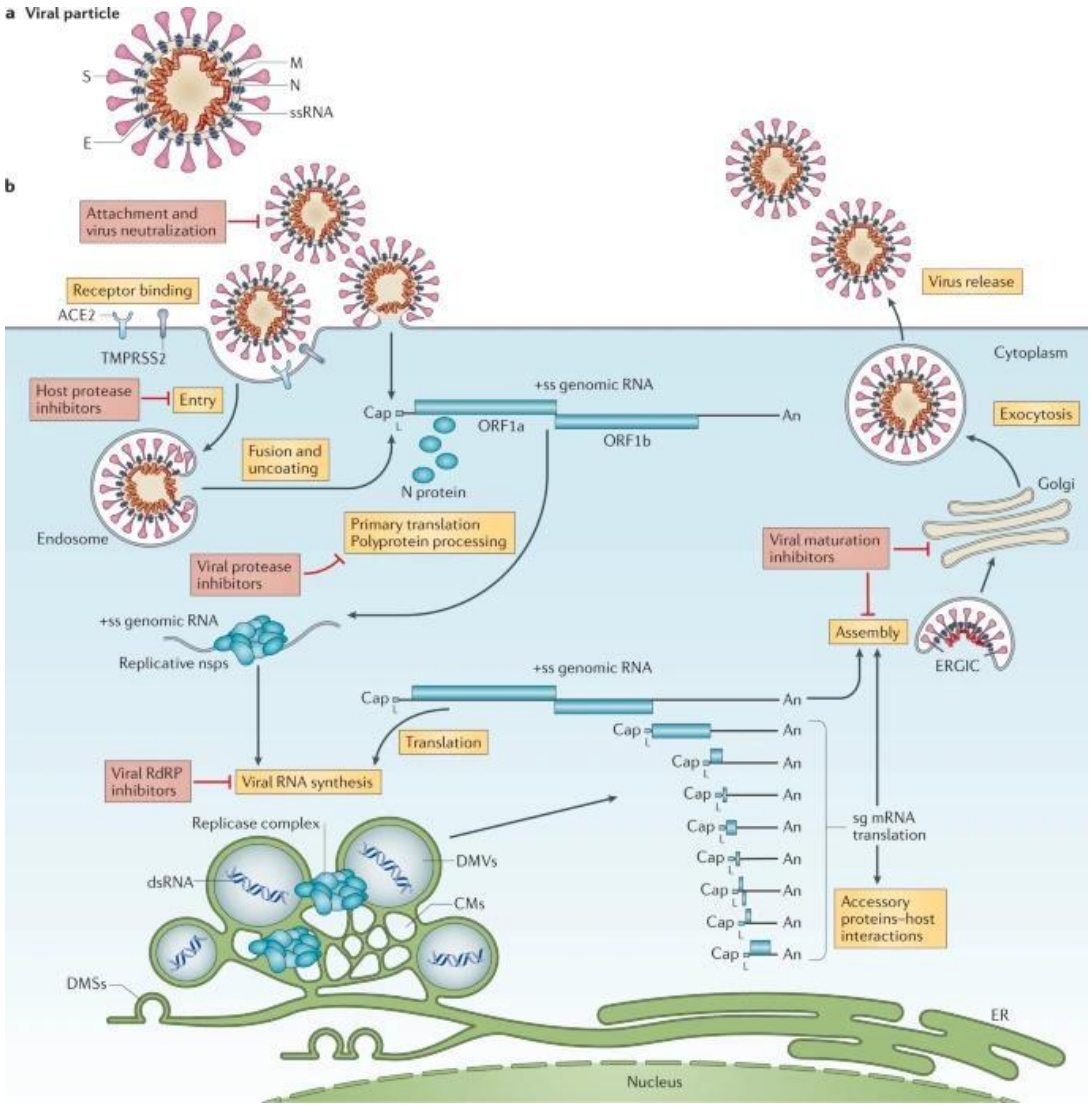

Figura 9. Esquema do processo de entrada, replicação e exocitose do SARS-CoV-2 nas células hospedeiras. Fonte: V'kovski *et al.* (2021).

2.5. Tratamentos: vacinas e medicamentos frente à COVID-19

As vacinas contra o SARS-CoV-2 foram desenvolvidas com o objetivo de prevenir a infecção pelo vírus e reduzir a gravidade da COVID-19, minimizando os efeitos graves e a alta taxa de letalidade da doença. Desde o surgimento da pandemia, várias vacinas foram desenvolvidas e aprovadas para uso em diferentes países.

Existem diferentes tipos de vacinas contra o SARS-CoV-2: as vacinas de RNA mensageiro (mRNA), as vacinas de vetor viral, as vacinas de subunidade proteica e as vacinas de vírus inativado. Cada um desses tipos utiliza uma estratégia diferente para induzir uma resposta imunológica protetora, sendo estas:

- Vacinas de RNA mensageiro sintético (mRNA): utilizam uma molécula de RNA mensageiro para instruir as células a produzirem uma proteína viral específica, desencadeando uma resposta imunológica.

- Vacinas de vetor viral: utilizam um vetor viral modificado para transportar material genético do SARS-CoV-2 para as células, estimulando uma resposta imunológica.

- Vacinas de subunidade proteica: utilizam uma proteína viral purificada ou sintética para estimular uma resposta imunológica.

- Vacinas de vírus inativado: utilizam o SARS-CoV-2 inativado para estimular a resposta imunológica, sem causar a doença.

De acordo com a Agência Nacional de Vigilância Sanitária (ANVISA) (2025a), no Brasil, já circularam diversas vacinas, com diferentes tecnologias, níveis de segurança e eficiência, que compuseram o esquema vacinal determinado pelo Ministério da Saúde. Apesar disso, também houve algumas outras que sequer chegaram ao país, que ainda estão em processo de aprovação, ou que tiveram seu uso desaprovado ou suspenso, mas que circulam ou já circularam em outros países (FDA, 2025a; EMA, 2025a) (Quadro 1).

Quadro 1. Dados das principais vacinas para o enfrentamento da COVID-19 aprovadas atualmente pelas agências ANVISA – Brasil, FDA – Estados Unidos e EMA – União Europeia.

Vacina	**Empresa Fabricante**	**Tecnologia**	**Agências - Aprovação**
Comirnaty®	BioNtech - Pfizer/Wyeth	RNA mensageiro sintético	ANVISA; FDA; EMA
Comirnaty® bivalente	BioNtech - Pfizer/Wyeth	RNA mensageiro sintético	ANVISA; FDA; EMA
Spikevax®	Moderna	RNA mensageiro sintético	ANVISA; FDA; EMA
Spikevax® Bivalente	Moderna	RNA mensageiro sintético	ANVISA; FDA; EMA
Sputnik V®	Bthek Biotecnologia	Vetor adenovírus D-26 e D-5	---------- ---
Jcovden®	Janssen-Cilag Johnson & Johnson	Vetor adenovírus D-26	ANVISA; FDA; EMA
Covishield®/ Vaxzevria®	Fiocruz e Astrazeneca	Vetor adenovírus recombinante	ANVISA; EMA
VidPrevtyn Beta®	Sanofi-GSK	Proteína viral	EMA
BIMERVAX®	HIPRA -Human Health	Proteína viral	EMA
Nuvaxovid®	Novavax	Proteína viral	FDA; EMA
VLA2001®	Valneva	Vírus inativado	EMA
Coronavac®	Butantan e Sinovac	Vírus inativado	---------- ---
BBIBP-CorV®	Sinopharm	Vírus inativado	---------- ---
Covaxin®	Bharat Biotech	Vírus inativado	---------- ---
Vacina Covid-19 (recombinante)	Zalika	Proteína recombinante	ANVISA

Fonte: ANVISA (2025); FDA (2025); EMA (2025)

Contudo, a evolução de novas variantes de SARS-CoV-2 tem se tornado um desafio significativo no contexto da pandemia de COVID-19. Essas variantes apresentam uma maior adaptação e virulência em comparação às cepas iniciais, resultando em grandes surtos de infecções com um aumento significativo no número de casos e óbitos (Dhar *et al.*, 2021).

Com o avanço da vacinação (Figura 10), a eficácia das vacinas tem sido mantida contra as principais variantes (Bernal *et al.*, 2021), embora já tenha sido demonstrado que a efetividade da proteção diminui com o passar do tempo, tornando-se necessárias doses de reforço e modificações na tecnologia para garantir a proteção adequada (Bar-On *et al.*, 2021).

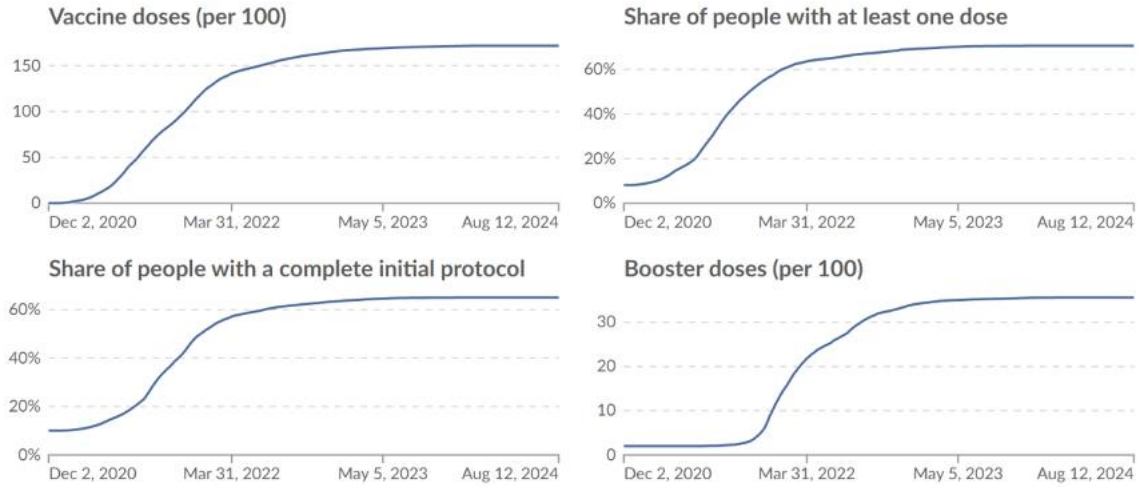

Figura 10. Média cumulativa do número de pessoas vacinadas, e destaque da porcentagem de indivíduos com esquema vacinal parcial e completo. Fonte: Our World in Data (2025).

Diante do cenário do surgimento constante de novas variantes, com possibilidade do aparecimento de cepas mais transmissíveis e virulentas, e das dificuldades em se completar o processo de vacinação de forma global, é de suma importância que sejam desenvolvidos e disponibilizados medicamentos capazes de controlar a infecção pelo SARS-CoV-2. Além de contribuir para a redução de casos graves e óbitos, as substâncias anti-SARS-CoV-2 podem desempenhar um papel crucial na contenção e/ou erradicação desse vírus (Zhou *et al.*, 2022).

Há diversos medicamentos antivirais que vêm sendo avaliados. É fundamental ressaltar que a eficácia desses medicamentos pode variar, uma vez que grande parte destes está sendo adaptado ao tratamento desta doença, não tendo sido originalmente desenvolvidos necessariamente para tal (ANVISA, 2025b; FDA, 2025b; EMA, 2025b). A pesquisa e o desenvolvimento de novos medicamentos antivirais específicos para o SARS-CoV-2 estão em andamento, e já existem diversas patentes registradas, mas nenhum novo fármaco de origem natural foi aprovado e/ou está sendo comercializado para tal fim. Os principais tipos de

medicamentos atualmente aprovados e empregados pelas principais agências de regulamentação mundiais (Quadro 2) incluem anticorpos monoclonais, antivirais de amplo espectro, inibidores de proteases e moduladores do sistema imunológico, sendo as principais classes:

- Anticorpos monoclonais: proteínas que se ligam e neutralizam o vírus SARS-CoV-2, reduzindo sua replicação e a gravidade da doença.

- Antivirais de amplo espectro: medicamentos que inibem a replicação viral de forma geral, normalmente não limitados ao SARS-CoV-2.

- Inibidores de proteases: medicamentos que têm como alvo as proteases do vírus, essenciais para sua replicação.

- Moduladores do sistema imunológico: medicamentos que auxiliam no controle da resposta imunológica exagerada em casos graves, reduzindo a inflamação e os danos aos órgãos afetados.

Quadro 2. Dados dos principais medicamentos para o enfrentamento da COVID-19 aprovados atualmente pelas agências ANVISA – Brasil, FDA – Estados Unidos e EMA – União Europeia.

Medicamentos	**Classe**	**Alvos/Atividades**	**Agência - Aprovação**
Remdesivir	Antiviral de amplo espectro	Ciclo viral/ impedir a replicação viral no organismo	ANVISA; FDA; EMA
Sotrovimabe	Anticorpo monoclonal	SP/ bloquear a interação e entrada do vírus na célula hospedeira	FDA; EMA
Baricitinibe	Inibidor de proteases/ Imunomodulador	Proteases Janus Quinases (JAKs 1 e 2)/ inibir os processos de defesa do sistema imune	ANVISA; FDA
Molnupiravir	Antiviral de amplo espectro	Ciclo viral/ impedir a replicação viral no organismo	ANVISA; FDA; EMA
Tocilizumabe	Anticorpo monoclonal/ Imunomodulador	Interleucina 6/ reduzir os níveis do receptor IL-6 humana	ANVISA; FDA; EMA
Paxlovid® (nirmatrelvir + ritonavir)	Antiviral de amplo espectro	Ciclo viral/ impedir a replicação viral no organismo	ANVISA; FDA; EMA
Anakinra	Imunomodulador	Interleucina 1/ reduzir os níveis do receptor IL-1 humana	FDA; EMA
Vilobelimabe	Anticorpo monoclonal/ Imunomodulador	Receptor C5a/ reduzir os níveis do receptor C5a humano	FDA
REGEN-COV® (Casirivimab + Imdevimab)	Anticorpo monoclonal	SP/ bloquear a interação e entrada do vírus na célula hospedeira	FDA; EMA
Bamlanivimab + Etesevimab	Anticorpo monoclonal	SP/ bloquear a interação e entrada do vírus na célula hospedeira	FDA
Bebtelovimabe	Anticorpo monoclonal	SP/ bloquear a interação e entrada do vírus na célula hospedeira	FDA
Evusheld® (tixagevimab + cilgavimab)	Anticorpo monoclonal	SP/ bloquear a interação e entrada do vírus na célula hospedeira	FDA; EMA
Regdanvimabe	Anticorpo monoclonal	SP/ bloquear a interação e entrada do vírus na célula hospedeira	EMA

Fonte: ANVISA (2025); FDA (2025); EMA (2025)

2.6. Produtos Naturais no enfrentamento do SARS-CoV-2 e da COVID-19

As plantas possuem um longo histórico como recurso terapêutico, e práticas de saúde baseadas em produtos naturais são encontradas em diversas culturas ao redor do mundo. Mesmo

atualmente, as plantas continuam sendo uma fonte importante de substâncias ativas e alvos de inspiração para o desenvolvimento de diversos medicamentos (Newman & Cragg, 2020).

Os produtos naturais são conhecidos por apresentarem diversas atividades, tais como: imunomoduladores, anti-inflamatórios, antivirais, antioxidantes, antimicrobianos, entre outros, sendo alvo de pesquisas em diversas áreas, para o desenvolvimento de medicamentos, cosméticos, suplementos alimentares e defensivos agrícolas, por exemplo (Ekiert *et al.*, 2020).

Com a pandemia de COVID-19, uma das atividades mais investigadas no mundo foi a antiviral, uma vez que a demanda por medicamentos anti-SARS-CoV-2 foi e ainda é crescente. Existem, na literatura, diversas evidências promissoras de atividades de produtos naturais identificadas por triagem computacional (Silva *et al.*, 2021; Verma *et al.*, 2021). Também existem relatos de estudos *in vitro* para o SARS-CoV-2, apesar de em menor quantidade (Sharma *et al.*, 2021; Iqhrammullah *et al.*, 2023). Por fim, há uma parcela de estudos encontrados que tratam do reposicionamento de fármacos, e do conhecimento advindo de práticas medicinais tradicionais para combater a doença (Xian *et al.*, 2020; Chapman & Andurkar, 2022).

Dentre os metabólitos secundários encontrados em plantas, flavonoides, terpenoides, alcaloides, saponinas, lignanas, entre outros, são conhecidos por influenciarem nas funções celulares, na permeabilidade da membrana e na replicação viral (Chapman & Andurkar, 2022; Al-Harrasi *et al.,* 2022). Dessa forma, pode-se esperar que estes possam atuar em diferentes alvos da infecção pelo SARS-CoV-2, como, por exemplo, na inibição da fixação e penetração viral, inibição do RNA viral e da síntese de proteínas, além de afetar proteínas-chave do vírus (Xian *et al.,* 2020; Sharma *et al.*, 2021). Além disso, algumas substâncias também podem atuar por meio de mecanismos de inibição da liberação de novas partículas virais, e do aumento da imunidade do hospedeiro (Figura 11).

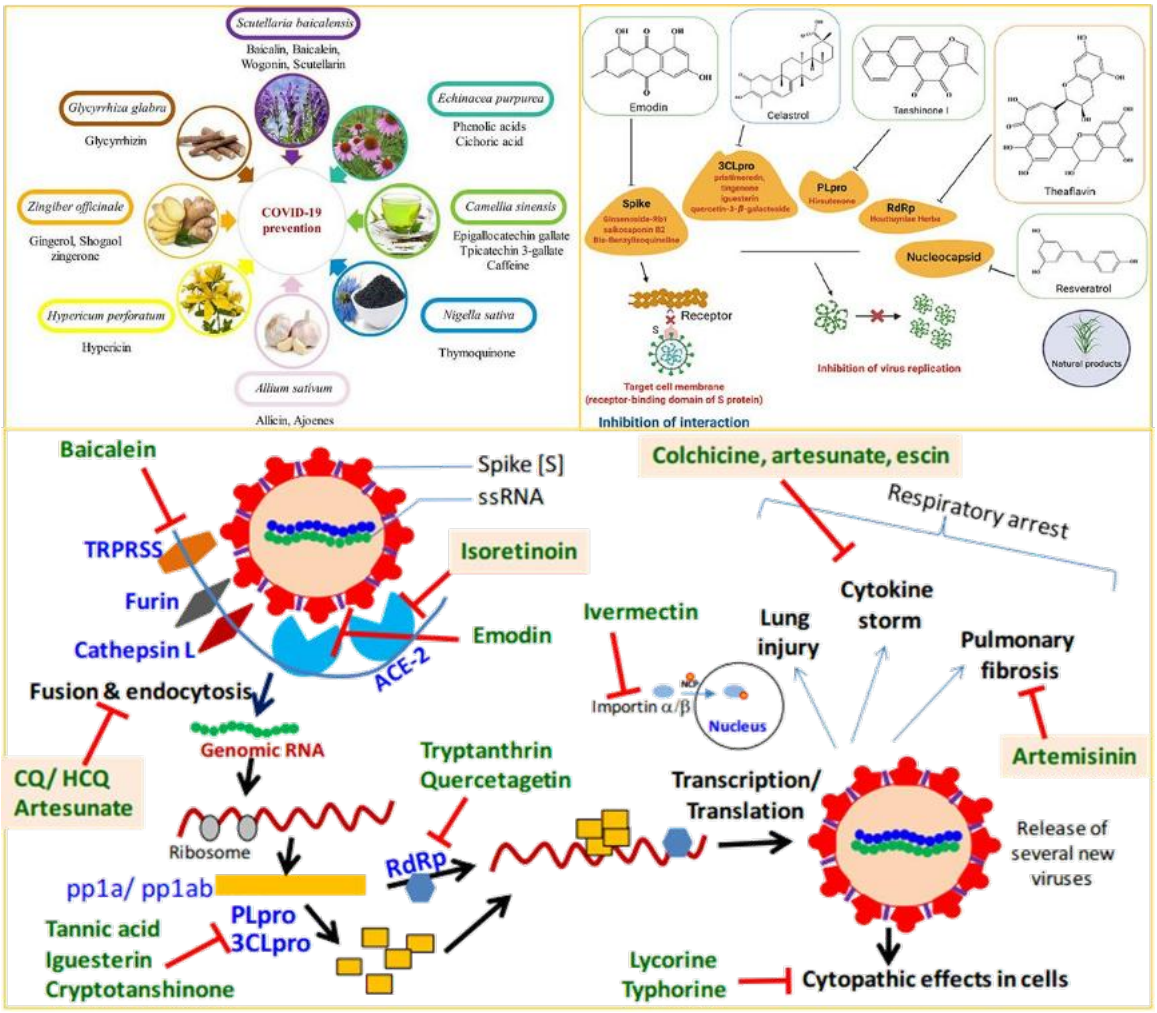

Figura 11. Exemplos de produtos naturais utilizados para prevenção, e atuação frente aos diferentes alvos no ciclo do SARS-CoV-2. Fonte: adaptado de Boozari & Hosseinzadeh (2020); Xian *et al.* (2020); Sharma *et al.* (2021).

Buscando ratificar a assertiva que os metabólitos vegetais são amplamente reconhecidos por sua diversidade estrutural e atividade biológica, tornando-se fontes promissoras para o desenvolvimento de inibidores contra alvos do SARS-CoV-2, nosso grupo realizou uma revisão sistemática baseada nas diretrizes PRISMA* (*Preferred Reporting Items for Systematic Reviews and Meta-Analyses*) avaliando o potencial de substâncias derivadas de plantas na inibição *in vitro* de alvos virais essenciais, incluindo a interação Spike:ACE2, as proteases $3CL^{pro}$ e PL^{pro}, e a RNA polimerase dependente de RNA (RdRp) (Dados não publicados [Artigo submetido – Em revisão]).

*O método PRISMA (*Preferred Reporting Items for Systematic Reviews and Meta-Analyses*) é uma diretriz internacional para a condução e apresentação de revisões sistemáticas e meta-análises, que visa garantir transparência, reprodutibilidade e qualidade na seleção, extração e síntese dos estudos incluídos.

A revisão analisou estudos disponíveis em seis bases de dados eletrônicas (PubMed, Scielo, Science Direct, Scopus, Springer e Web of Science) no período de janeiro de 2020 a fevereiro de 2024. Foram utilizadas palavras-chave relacionadas a produtos naturais e aos principais alvos moleculares do SARS-CoV-2. Apenas artigos completos publicados em inglês foram incluídos, enquanto revisões, livros, teses e estudos de caso foram excluídos. Para garantir a abrangência da busca, também foram examinadas referências adicionais dos estudos selecionados.

A extração de dados revelou 334 substâncias derivadas de plantas com potencial atividade antiviral. Esses metabólitos pertencem a 19 classes químicas, destacando-se os flavonoides (n=145), terpenoides (n=41), feniletanoides (n=20) e ácidos fenólicos (n=19). A maioria dos ensaios experimentais concentrou-se na inibição da $3CL^{pro}$ (n=301), seguida por PL^{pro} (n=33), interação Spike-ACE2 (n=25) e RNA polimerase (n=2). No total, 21 substâncias (6%) demonstraram forte atividade antiviral, com valores de IC_{50} inferiores aos dos fármacos e/ou produtos de referência. Os compostos *multitarget* mais promissores incluíram kaempferitrina, kuwanon A, luteolina, miricetina, quercetina e glicirrizina (ação sobre Spike e 3CLpro), além de honokiol (Spike e PL^{pro}) e silibinina, que demonstraram atividade contra todos os quatro alvos estudados.

Esses achados reforçam o potencial dos produtos naturais como fontes de moléculas bioativas para o desenvolvimento de novas estratégias terapêuticas contra o SARS-CoV-2, destacando a importância da continuidade das investigações nesse campo.

A diversidade de espécies vegetais no Brasil contribui para uma ampla variedade de metabólitos secundários disponíveis. Dessa forma, os biomas brasileiros se apresentam como reservatórios de substâncias naturais potencialmente bioativas e farmacologicamente promissoras (Ekiert *et al.*, 2020). De acordo com Amparo *et al.* (2021) diversos metabólitos constituintes de óleos essenciais de plantas brasileiras tiveram resultados relevantes em triagens virtuais frente a proteínas-chave do vírus responsável pela COVID-19, com destaque para α-calacoreno e o α-muuroleno oriundos de plantas presentes em *hotspots* brasileiros de biodiversidade com potencial farmacológico, demonstrando o valor da flora do país como fonte de moléculas anti-SARS-CoV-2.

Ainda demonstrando a relevância da flora brasileira, alguns trabalhos de nosso grupo de pesquisa investigaram o potencial de plantas, em estudos *in silico* e *in vitro*, para o enfrentamento da COVID-19 (Figura 12). O estudo de Leal *et al.* (2021a) demonstrou a capacidade de inibição da replicação viral *in vitro* do SARS-CoV-2 por flavonoides isolados da espécie *Siparuna cristata* (Poepp. & Endl.) A.DC. No trabalho de Cheohen *et al.* (2023)

investigou-se a capacidade *in silico* dos feniletanoides glicosilados como inibidores das proteases $3CL^{pro}$ e PL^{pro}. Dentre as substâncias *multitarget* mais promissoras se pode destacar o forsitosídeo e o verbascosídeo, feniletanoides abundantes em plantas brasileiras. Por fim, o grupo também investigou o potencial dos extratos das cascas da espécie *Ampelozizyphus amazonicus* Ducke frente ao SARS-CoV-2. Estes extratos, utilizados tradicionalmente por quilombolas, demonstraram a capacidade *in vitro* de inibição da interação Spike (RBD):ACE2, e da replicação viral em linhagem de células epiteliais humanas derivadas de adenocarcinoma de pulmão [Calu-3] . Dessa forma, os fenólicos encontrados nestes extratos destacaram-se como potenciais agentes *multitarget* anti-SAR-CoV-2 (Campos *et al.*, 2023).

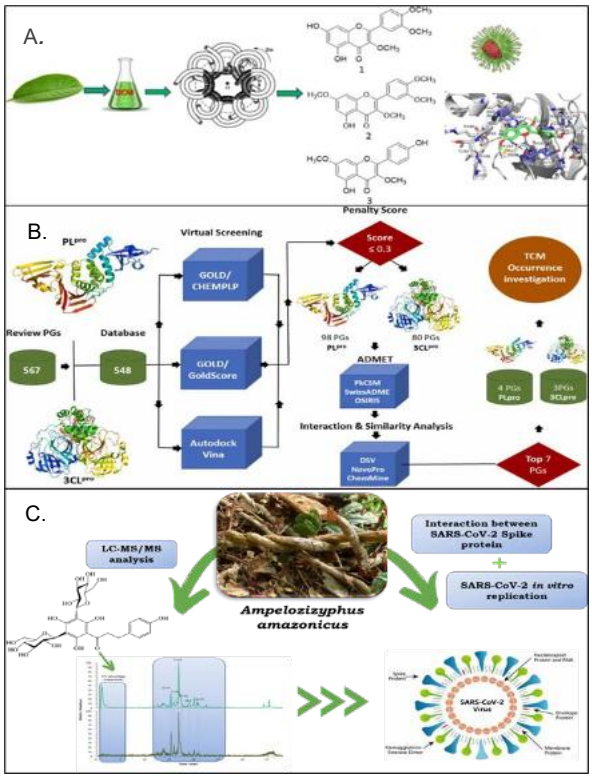

Figura 12. Resumos gráficos dos trabalhos de nosso grupo de pesquisa, exemplificando o potencial de espécies brasileiras (e suas moléculas) como potenciais agentes anti-SARS-CoV-2. **A**: extratos de espécies amazônicas do gênero *Siparuna*, e flavonoides isolados, como inibidora da replicação *in* vitro do SARS-CoV-2; **B**: triagem virtual de feniletanoides glicosilados como inibidores das proteases $3CL^{pro}$ e PL^{pro}; **C**: extratos da espécie *Ampelozizyphus amazonicus*, como inibidores da interação *Spike*(RBD):ACE2 e da replicação *in* vitro do SARS-CoV-2. Fonte: adaptado de Leal *et al.* (2021a); Cheohen *et al.* (2023); Campos *et al.* (2023).

A expressiva diversidade de substâncias bioativas derivadas da flora brasileira, revelada por estudos *in vitro* e *in silico*, reforça o papel estratégico dos produtos naturais na busca por terapias antivirais contra o SARS-CoV-2. Entretanto, a triagem realizada por meio destes

ensaios biológicos e/ou métodos em química medicinal, aliada às análises químicas das substâncias investigadas, pode gerar um volume expressivo de dados, cuja complexidade demanda abordagens analíticas integradas e multidisciplinares. Dessa forma, a utilização de métodos computacionais para o processamento dos dados, desenvolvimento de modelos preditivos e realização de análises complementares, como *docking* e dinâmica molecular, torna-se essencial para a interpretação, compreensão e otimização do conjunto de informação obtidas. Assim, o uso de ferramentas matemáticas e estatísticas possibilitam a construção de modelos robustos que correlacionem perfis químicos com atividades biológicas, agilizando e barateamento a pesquisa de moléculas potencialmente ativas frente ao SARS-CoV-2.

2.7. Processamento de dados químicos

É possível obter um extenso conjunto de dados a partir de análises por cromatografia em fase líquida ou gasosa acopladas a espectrometria de massas de resolução unitária ou alta resolução, principalmente ao se avaliar matrizes biológicas complexas, como os extratos vegetais. Neste tipo de análise, centenas, ou até milhares de metabólitos podem ser detectados, e a anotação dessas substâncias está diretamente relacionada à qualidade dos resultados analíticos e à eficiência das ferramentas de processamento e análise de dados (Rathahao-Paris *et al.*, 2015). Para inferências qualitativas, como a anotação dos íons encontrados nestas análises, se utilizam como critérios: valores de *m/z*, tempo de retenção e padrões de fragmentação (Chaleckis *et al.*, 2019). Entretanto, para outras interpretações e inferências quantitativas, os valores de área e intensidade, absolutos e relativos, também são necessários.

Para extrair de forma seletiva as informações necessárias dos arquivos brutos de análise, as ferramentas de processamento de dados são essenciais. O processamento permite a redução da complexidade e a correção da variação experimental intrínseca, simplificando as informações e facilitando a interpretação dos resultados (Rathahao-Paris *et al.*, 2015). Existem diversos *softwares* disponíveis para a visualização e processamento dos dados, tanto de código aberto, como o MZmine, XCMS, MS-Dial e MetAlign, quanto comerciais, como o MarkerView, Compound Discoverer e MarkerLynx (Li *et al.*, 2018; Borges *et al.*, 2021).

De acordo com a documentação orientativa encontrada na plataforma GNPS, as principais etapas para um processamento de dados completo são: importação dos dados (em extensão aberta) para o software/plataforma selecionada; detecção (determinação do "corte") das massas (MS^1 e MS^2) dos dados brutos; construção dos cromatogramas para cada amostra carregada; deconvolução; agrupamento dos isótopos; alinhamento dos dados; validação

manual; e exportação das informações relevantes para o estudo (Figura 13) (GNPS, 2023). Além disso, também podem ser realizadas algumas etapas complementares, como: a filtragem de massas e isótopos; a reavaliação automatizada dos dados brutos para resgate de informações excluídas pelos demais parâmetros; a normalização dos dados, entre outras (Borges *et al.*, 2021).

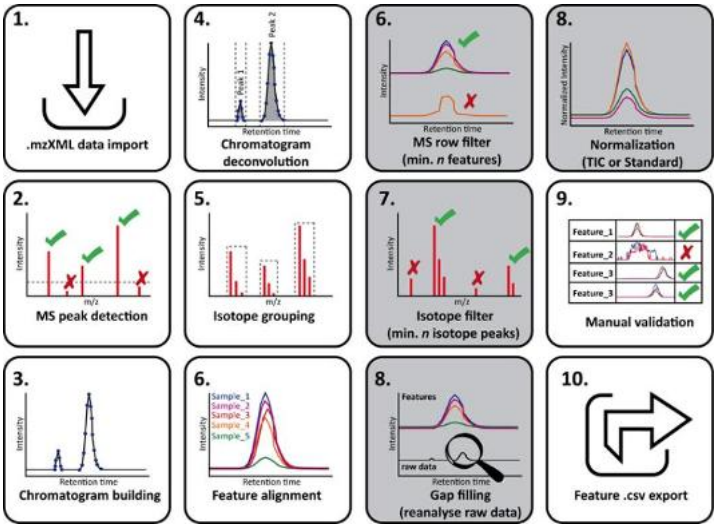

Figura 13. Representação esquemática das etapas de processamento de dados oriundos de análises por LC-MS/MS. Fonte: GNPS (2023).

2.8. Quimiometria

As diferentes técnicas instrumentais geram conjuntos de dados complexos, o que pode dificultar o trabalho com essa carga de informação e levar a erros de análise e de interpretação. Nesse contexto, a metodologia de avaliação manual dos dados torna-se obsoleta, uma vez que são necessários estudos em sistemas múltiplos que exigem procedimentos matemáticos e estatísticos mais complexos para o tratamento dos dados.

Os dados obtidos, de natureza química ou não, podem ser avaliados por ensaios univariados ou multivariados. Análises univariadas mensuram de forma sistemática questões acerca de uma única variável em várias amostras, enquanto as multivariadas tratam de um grupo de variáveis de uma determinada amostra (ou grupo de amostras) em interpretações relacionadas ao conjunto total de dados (Barros Neto *et al.*, 2006; Correia & Ferreira, 2007). A utilização desses procedimentos possibilita a ampliação do número de parâmetros avaliados e facilita a interpretação dos resultados (Correia & Ferreira, 2007).

Assim como na estatística convencional, a quimiometria visa extrair informações de um conjunto complexo de dados adquiridos em diversas análises, fornecendo concepções

relevantes sobre os resultados. Dentre as ferramentas mais utilizadas na quimiometria, destacam-se os modelos de análise exploratória e classificatória – não-supervisionados, e os métodos supervisionados de classificação e predição (Ferreira, 2015; Pilon *et al.*, 2020).

Dentre as ferramentas exploratórias mais usuais, temos: a análise de componentes principais (PCA) e a análise de agrupamentos hierárquicos (HCA), por exemplo, que determinam a distribuição natural dos dados, assim como sua similaridade interna (tendência de grupos), sem a designação de fatores determinantes (Ferreira, 2015; Maraschin *et al.*, 2017). Nos modelos supervisionados, pode-se destacar as análises por quadrados mínimos parciais (PLS), que insere fatores determinantes/preditores nas análises, visando maximizar a separação em grupos pré-determinados, e possibilitar inferências (predições) de classificação, regressão e agrupamentos (comportamento do conjunto de dados) (Ferreira, 2015; Maraschin *et al.*, 2017).

2.9. Modelos quimiométricos de predição químico-biológicos

Em produtos naturais, os modelos preditivos são utilizados para indicar relações intrínsecas entre substâncias e atividades biológicas. Nestes modelos, a presença de atividade e sua mensuração podem ser correlacionadas aos perfis químicos das matrizes biológicas avaliadas. Dessa forma, estes modelos são capazes de gerar indicações das substâncias potencialmente associadas às atividades investigadas, indicando os alvos mais relevantes a serem estudados, confirmando as atividades preditas.

Diversas técnicas estatísticas podem ser empregadas na construção desses modelos, tais como métodos de regressão, análise discriminante, árvores de decisão, redes neurais, entre outras (Xue *et al.*, 2022).

Para a construção destes modelos, é necessário um conjunto de dados que contenha informações acerca do perfil químico e/ou da estrutura molecular de substâncias (Ferreira, 2015; Pilon *et al.*, 2020), e suas atividades biológicas correspondentes. Esse conjunto de dados é normalmente dividido em um grupo de treinamento, utilizado para desenvolver o modelo, e um grupo de teste, utilizado para avaliar a capacidade preditiva do modelo (Ferreira, 2015; Xue *et al.*, 2022). Durante a construção dos modelos, os dados passam por diversas modificações, uma vez que é necessário avaliar o uso de pré-processamentos (transformação, normalização e escalonamento), escolher os algoritmos mais promissores e selecionar as variáveis mais relevantes para a predição (Pilon *et al.*, 2020; Xue *et al.*, 2022).

Após o modelo ser desenvolvido e validado, este possuirá capacidade de predizer a atividade biológica de amostras e substâncias que não foram utilizadas em sua construção e

treino. Dessa forma, poderão ser aplicados na área da saúde, como no desenvolvimento de novos fármacos, ou na identificação de marcadores de diversas doenças (Mocák, 2012).

Em alguns trabalhos como o de Ali *et al.* (2012), métodos supervisionados foram utilizados para avaliar o potencial de uvas e outras bagas na busca de substâncias com potencial de inibição do fator de necrose tumoral alfa [TNF-α]. Os resultados a partir dos ensaios quimiométricos contribuíram para a classificação dos grupos de amostras com a presença de ácidos orgânicos e fenólicos semelhantes como alvos promissores. Em outro estudo, nove extratos de menta foram avaliados na busca do perfil químico com a maior capacidade antioxidante. Os métodos discriminantes utilizados contribuíram apara a determinação de cinco amostras, e seus principais componentes potencialmente relevantes (Park *et al.*, 2019).

2.10. Construção de Redes Moleculares

Redes moleculares são ferramentas poderosas utilizadas na área da química, uma vez que permitem visualizar e analisar dados químicos complexos. O principal objetivo da construção destas redes é a representação de relações estruturais e funcionais entre diferentes moléculas com base em suas características químicas.

As redes moleculares têm uma ampla gama de aplicações. Na área da saúde podem ser utilizadas na descoberta de novas substâncias candidatas a medicamentos com base em suas similaridades estruturais com moléculas conhecidas, e atividades biológicas desejadas (Moura *et al.*, 2022). Além disso, as redes moleculares são utilizadas na análise de dados de química combinatória, na predição de propriedades físico-químicas, na seleção de grupos para síntese, na identificação de fragmentos e subestruturas químicas relevantes, entre outras (Pilon *et al.*, 2021).

A plataforma *Global Natural Products Social Molecular Networking* (GNPS) é amplamente utilizada para organizar, visualizar e analisar conjuntos de dados de espectrometria de massas, com base nos fragmentos dos íons adquiridos Uma das principais ferramentas disponíveis na plataforma é a *Molecular Networking*, que permite a construção de redes moleculares a partir da similaridade estrutural entre as substâncias avaliadas (GNPS, 2023).

Nessa abordagem, os espectros de MS^2 (fragmentação) são organizados e classificados de acordo com um valor de similaridade calculado a partir do cosseno de sobreposição entre os espectros presentes nas amostras e os espectros de referência disponíveis em bancos de dados, onde, o cosseno igual a 0 indica diferença total, e 1 indica similaridade completa entre os espectros (Pilon *et al.*, 2021; Moura *et al.*, 2022).

Os espectros de consenso das moléculas são representados por um nó (*node*), onde os espectros de MS^2 correspondentes a uma mesma substância são agrupados, podendo estar conectados a outros nós por meio de arestas (*edges*), representando as correlações existentes (Pilon *et al.*, 2021; Afoullouss *et al.*, 2022; Moura *et al.*, 2022) (Figura 14). Cabe ressaltar que, na plataforma GNPS as arestas são estabelecidas pelas similaridades estruturais e os valores atribuídos são os resultados dos cossenos calculados (GNPS, 2023). Contudo, em outras plataformas podem ser consideradas as similaridades de propriedades físico-químicas, as interações moleculares, entre outras. Além disso, outros parâmetros são utilizados, como índices de similaridade molecular, coeficientes de correlação e distâncias euclidianas.

Uma vez construídas, as redes moleculares podem ser visualizadas, processadas e analisadas usando técnicas de visualização gráfica, como no *software* livre Cytoscape. Essa representação visual permite identificar agrupamentos de moléculas semelhantes, bem como determinar moléculas-chave ou centrais que desempenham papéis importantes na rede (Pilon *et al.*, 2021; Afoullouss *et al.*, 2022; Moura *et al.*, 2022). Além disso, as redes moleculares podem ser enriquecidas com informações adicionais, como anotações de origem, propriedades físico-químicas e atividades biológicas, fornecendo uma visão abrangente e integrada dos dados químicos.

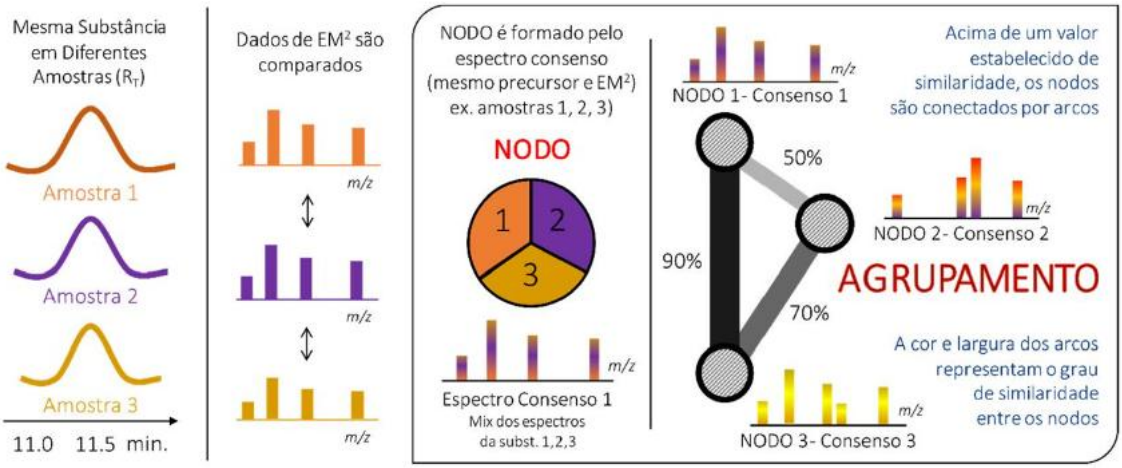

Figura 14. Processo de construção das redes moleculares a partir dos dados oriundos de análises por LC-MS/MS. Fonte: Pilon *et al.* (2021).

Diante do exposto, observa-se que o enfrentamento da COVID-19 requer uma abordagem integrada que una conhecimento biológico e químico com estratégias computacionais e quimiométricas avançadas. A compreensão aprofundada da biologia do SARS-CoV-2, incluindo seus mecanismos de entrada, replicação e principais alvos moleculares, associada à

capacidade da flora brasileira de fornecer substâncias bioativas promissoras, constitui um arcabouço estratégico essencial para o desenvolvimento de novos fármacos antivirais. Nesse contexto, a aplicação de ferramentas de processamento de dados, modelagem preditiva e construção de redes moleculares permite não apenas acelerar o processo de descoberta e triagem de produtos naturais, como também otimizar a seleção de candidatos com maior potencial terapêutico. Assim, a conjugação entre a biodiversidade brasileira, a expertise em produtos naturais e o uso de metodologias computacionais robustas desponta como uma via promissora e necessária para o desenvolvimento de alternativas eficazes e acessíveis no combate à COVID-19 e a futuras emergências virais.

3. JUSTIFICATIVA

A pesquisa para encontrar alternativas terapêuticas a partir de produtos naturais contra a COVID-19 enfrenta diversos desafios. O gasto elevado com recursos como tempo, consumíveis e maquinários, retardam o avanço dos estudos. A escassez de medicamentos comprovadamente eficazes e de baixos efeitos colaterais também têm sido um desafio. Além disso, a baixa adesão da população de alguns países pelo protocolo vacinal completo, possibilitando novos surgimentos e rápida disseminação de variantes, destaca a importância de prosseguir e avançar nas pesquisas em busca de soluções para combater a COVID-19.

Algumas abordagens alternativas aos ensaios com o SARS-CoV-2 já foram desenvolvidas, como os ensaios *in vitro* utilizando proteínas estruturais e enzimas essenciais no ciclo de entrada e replicação do vírus. Contudo, estes métodos também possuem custos financeiros elevados.

Apesar de a triagem virtual com técnicas como o *docking molecular* se mostrarem alternativas viáveis, os ensaios *in silico* com matrizes complexas (extratos) não são possíveis. Ensaios de maior complexidade demandam alta capacidade computacional, ou seja, máquinas de custo bastante elevado.

Os estudos de desreplicação, metabolômica ou fracionamento bioguiado, metodologias de famacognosia tradicional e moderna, também são custosas quanto ao tempo de realização, materiais consumidos e maquinários necessários.

Baseando-se no acima exposto, o desenvolvimento de modelos quimiométricos de predição podem vir a resolver tais questões, sendo abordagens mais promissoras para a busca de moléculas anti-SARS-CoV-2. Nestes ensaios, conjuntos complexos de dados experimentais e computacionais se complementam gerando modelos acurados de predição.

Estudos presentes na literatura, e resultados anteriores do grupo, confirmam o potencial de substâncias de origem vegetal como agentes anti-Sars-CoV-2, com enfoque para moléculas oriundas de plantas da biodiversidade brasileira. Dessa forma, justifica-se o estudo de outras espécies da biodiversidade do Brasil, buscando extratos e/ou substâncias com potencial ação antiviral.

Deste modo, os recursos da comunidade científica poderão ser focados em ensaios com maior robustez, utilizando as substâncias preditas mais promissoras em ensaios de inibição da entrada e replicação *in vitro* e *in vivo* do SARS-CoV-2 nas células hospedeiras. Diante do exposto, o presente trabalho poderá acarretar o aumento de informações acerca de substâncias-

alvo para estudos aprofundados da ação antiviral frente ao SARS-CoV-2, assim como desenvolver métodos inovadores na busca de substâncias anti-COVID-19.

4. OBJETIVOS

4.1. Objetivo Geral

Este trabalho tem como objetivo principal desenvolver modelos preditivos capazes de indicar espécies (e suas substâncias) da biodiversidade brasileira presentes na Fito-Extractoteca com potencial ação antiviral frente ao SARS-CoV-2 a partir de triagens experimentais e métodos computacionais.

4.2. Objetivos específicos

Os objetivos detalhados a serem alcançados são:

- Realizar a triagem química por LC-MS/MS de todos os extratos presentes na Fito-Extractoteca (banco de extratos de acesso do laboratório);
- Realizar a triagem biológica de todos os extratos da Fito-Extractoteca no modelo de inibição da interação RBD:ACE2;
- Realizar a triagem biológica de todos os extratos da Fito-Extractoteca no modelo de inibição das proteases $3CL^{pro}$ e PL^{pro};
- Avaliar quais os métodos computacionais e os melhores parâmetros matemáticos que serão utilizados para a construção dos modelos de predição;
- Construir redes moleculares para avaliação qualitativa dos dados, assim como anotação das substâncias preditas e suas correlatas (semelhança MS^2);
- Desenvolver modelos de predição *onetarget* e *multitarget* com alta robustez.

5. MATERIAIS E MÉTODOS

5.1. Biblioteca de Extratos/ Fito-Extractoteca

A Fito-Extractoteca é uma biblioteca de extratos registrada no Sistema Nacional de Gestão do Patrimônio Genético e do Conhecimento Tradicional (SisGen) sob o código de cadastro CAB8693, e o acesso ao patrimônio genético e ao conhecimento tradicional das plantas que a compõe é autorizada sob o código AEAC3E9 e A5A49CA. Esta biblioteca é composta por mais de 300 amostras, sendo extratos, frações e substâncias isoladas de espécies com ocorrências, principalmente, nas florestas Amazônica e Mata Atlântica. O banco de extratos foi construído por alunos de graduação e pós-graduação ao longo do histórico de existência do Laboratório de Fitoquímica e Farmacognosia – LabFitoFar, coordenado pela professora Suzana G. Leitão, da Faculdade de Farmácia, UFRJ, e do Laboratório de Fitoquímica e Cromatografia Contracorrente – FitoCCC, coordenado pela professora Gilda G. Leitão, do IPPN, UFRJ.

Para este estudo, apenas uma parcela da Fito-Extractoteca foi considerada, uma vez que algumas amostras não atendiam ao escopo do projeto proposto. Os extratos originados de mais de uma espécie vegetal brasileira de uma mesma família botânica atendiam o critério de seleção das amostras. Os extratos foram selecionados independente de pertenceram ao mesmo gênero e/ou da polaridade dos extratos existentes. Dessa forma, o banco de amostras utilizado neste estudo foi composto por 160 extratos de diversas polaridades (hidroalcóolico, hexano, diclorometano, acetato de etila, butanol e água), oriundos de 37 espécies pertencentes a 17 gêneros e sete famílias botânicas diferentes (Anexo 1).

De forma geral, o material vegetal seco, utilizado nas diferentes amostras, passou por um processo de extração hidroalcóolica, empregando os métodos de maceração ou percolação. O extrato hidroalcóolico obtido foi concentrado sob pressão reduzida em evaporador rotatório. Em seguida, o extrato etanólico seco foi dissolvido em uma solução de água e metanol (9:1) e submetido à partição líquido-líquido, utilizando solventes de polaridade crescente, incluindo hexano, diclorometano, acetato de etila e butanol. Para algumas amostras foram mantidos e analisados os resíduos aquosos, os demais foram descartados. As amostras de *A. amazonicus* (saracura-mirá) seguiram protocolos distintos. O material vegetal foi submetido a extrações por decocção ou percolação, e/ou de acordo com o método tradicional utilizado pelos quilombolas de Oriximiná – PA, com água fervente ou etanol seguido de secagem em evaporador rotativo sob pressão reduzida e/ou liofilização e/ou *spray-dryer*.

5.2. Obtenção de *fingerprintings* por LC-MS/MS

Todos os extratos investigados seguiram os mesmos métodos padronizados de preparo e análise. As amostras foram solubilizadas em acetonitrila até atingir a concentração final de 2 $mg.mL^{-1}$. Visando a exclusão de possíveis partículas em suspensão e material não solubilizado, todas as amostras foram submetidas a ultracentrifugação (10.000 rpm) durante 10 minutos. O sobrenadante foi recolhido e transferido para *vials* de injeção.

Em seguida, 2 µL de cada amostra foram analisados em cromatógrafo de fase líquida de ultra/alta eficiência (UHPLC) Dionex Ultimate 3000 (ThermoFischer Scientific, Waltham, MA, EUA) acoplado ao espectrômetro de massas (MS) de resolução unitária LCQfleet (ThermoFischer Scientific, Waltham, MA, EUA) com analisador principal Ion Trap 3D.

A fase móvel utilizada foi A: água com adição de 0,1% de ácido fórmico e 0,1% de formiato de amônio, e B: acetonitrila. As análises foram realizadas utilizando uma coluna Acquity BEH C18 (1,7 µL, 2,1 x 100 mm, 100Å) com vazão de 0,45 $mL.min^{-1}$, de acordo com o gradiente de eluição descrito na Tabela 1.

Tabela 1. Gradiente cromatográfico utilizado nas análises por LC-MS/MS.

Tempo (minutos)	Solvente A (%)	Solvente B (%)
0	95	5
5	95	5
25	-	100
30	-	100
31	95	5
36	95	5

As fontes de ionização possibilitam avaliar substâncias com polaridades distintas (Figura 20). Para cromatografia em fase liquida, rotineiramente se investiga moléculas de média-alta polaridade, já as análises em fase gasosa têm como foco as substâncias de menor polaridade e menor peso molecular (Lanças, 2019).

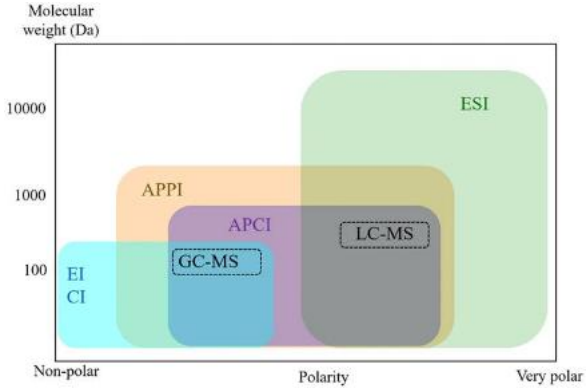

Figura 15. Diagrama representativo das faixas de polaridade de moléculas ionizadas por diferentes fontes em espectrômetros de massas. GC-MS: cromatografia em fase gasosa acoplada a espectrometria de massas; LC-MS: cromatografia em fase liquida acoplada a espectrometria de massas. ESI: ionização por *electrospray*; APCI: ionização química a pressão atmosférica; APPI: ionização química por fotoionização; EI: ionização por impacto de elétrons; CI: ionização química. Fonte: adaptado de Wei *et al*., 2020.

A fonte APCI, utilizada em análises por LC-MS, possibilita a ionização de moléculas na faixa de média polaridade, enquanto a fonte ESI favorece a ionização de substâncias mais polares. Além disso, cabe ressaltar que os modos de ionização (positivo e negativo) também propiciam a ionização de moléculas com características distintas. No modo positivo, moléculas de caráter básico são favorecidas, já no modo negativo as substâncias ácidas são ionizadas mais facilmente.

As amostras foram analisadas utilizando as duas fontes de ionização disponíveis: a fonte de ionização química à pressão atmosférica (APCI), e a de ionização por *electrospray* (ESI), ambas operandas nos modos positivo e negativo de ionização. Os espectros de MS foram adquiridos com faixa de aquisição *m/z* 100-1000, com quatro eventos de *scan*, onde foram obtidos os sinais de MS^1, seguidos de três eventos de fragmentação dos três íons mais intensos acima de 200 cps. A energia de colisão na célula de dissociação induzida por colisão (CID) foi normalizada em 35 eV. Nitrogênio de alta pureza (N_2) foi utilizado como gás de dispersão e auxiliar. Hélio de alta pureza (He) foi utilizado como gás de colisão. Os demais parâmetros utilizados nas análises de MS estão descritos na Tabela 2. As análises foram realizadas em triplicata.

Tabela 2. Parâmetros da máquina utilizados nas análises por espectrometria de massas com as fontes de ionização química à pressão atmosférica (APCI) e de ionização por *electrospray* (ESI) operando nos modos positivo e negativo de ionização.

ESI (+)	ESI (-)	Parâmetros	APCI (+)	APCI (-)
450	450	Temperatura da fonte (°C)	450	450
4	5.5	Voltagem da fonte (kV)	5	6
100	100	Corrente da fonte (µA)	20	20
350	350	Temperatura do capilar (°C)	350	350
10	12	Voltagem do capilar (V)	27	25
20	20	Fluxo *sheat gas* (U.A)	20	20
10	10	Fluxo *aux gas* (U.A)	10	10
10	10	Fluxo *sweep gas* (U.A)	0	0

Fonte: o Autor.

Todos as análises por UHPLC-MS/MS foram realizadas na Central Analítica do Departamento de Produtos Naturais e Alimentos (CA-DPNA) da Faculdade de Farmácia (FF) – Universidade Federal do Rio de Janeiro (UFRJ).

5.3. Triagem biológica por ensaios da inibição da interação *Spike* (RBD):ACE2

Os ensaios de triagem da inibição da interação RBD:ACE2 foram realizados pela doutoranda Mariana F. Campos e pela discente de iniciação científica Beatriz A. C. de Oliveira no laboratório de biotecnologia e bioengenharia estrutural (LABGENEST), em colaboração com o Professor Dr. Diego Alonso – Faculdade de Farmácia, UFRJ.

Para este ensaio, o kit Lumit™ SARS-CoV-2 Spike RBD:hACE2 *Immunoassay* da Promega foi utilizado de acordo com as instruções do fabricante. As soluções do *kit* foram preparadas seguindo o protocolo fornecido, que envolve a adição dos extratos (250 $\mu g.mL^{-1}$) - concentração definida com base em triagens e testes prévios, seguida pela adição do RBD e do receptor ACE2. A detecção é realizada usando anticorpos secundários ligados a partículas luminosas e um substrato reativo (Figura 15). A ligação dos anticorpos secundários às proteínas

resulta na reconstituição das partículas de NanoBiT®, uma tecnologia desenvolvida pela Promega, gerando bioluminescência. Dessa forma, a presença de um inibidor que interrompa a interação entre RBD e hACE2 reduz o sinal bioluminescente, impedindo a complementação das partículas luminosas. Os ensaios foram realizados em duplicata amostral.

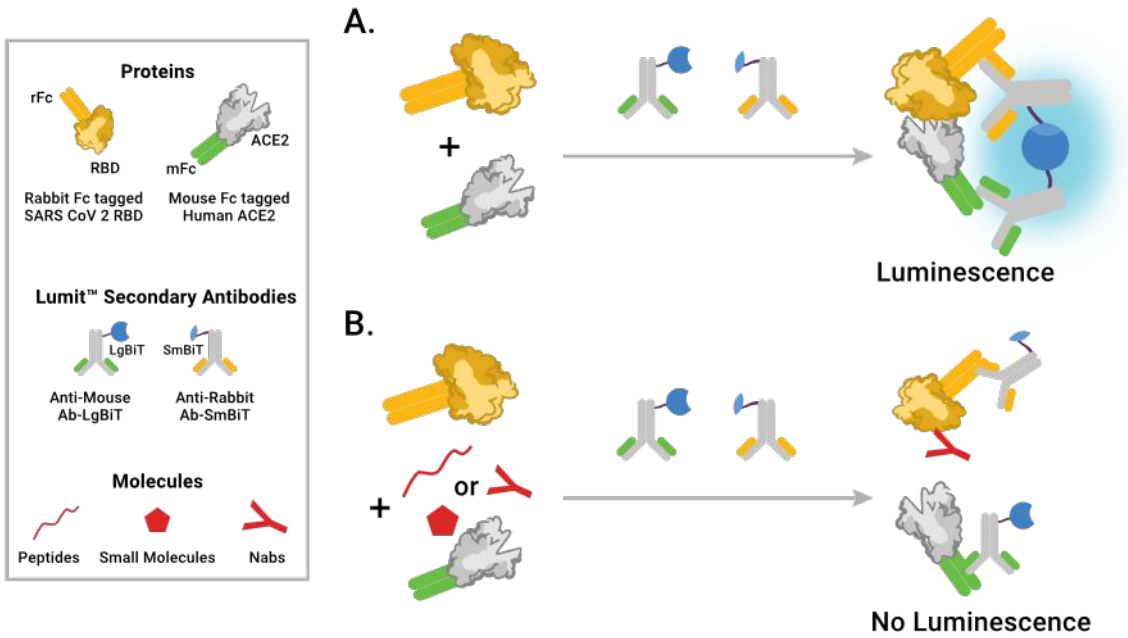

Figura 16. Princípios dos ensaios utilizando o *kit* comercial Lumit®. Fonte: Promega *Website*, 2025.

5.4. Triagem biológica por ensaios da inibição da atividade de $3CL^{pro}$ e PL^{pro}

Os ensaios de triagem da inibição da atividade das proteases de SARS-CoV-2 foram realizados no laboratório de biotecnologia e bioengenharia estrutural (LABGENEST), em colaboração com o Professor Dr. Diego Alonso – Faculdade de Farmácia, UFRJ. O protocolo de expressão e purificação das enzimas recombinantes foi desenvolvido pela doutoranda Larissa E. C. Constant em sua dissertação de mestrado (Constant, 2022). Os ensaios foram realizados pelos doutorandos Larissa E. C. Constant, Thamirys S. Fonseca e Brendo A. Gomes, e pela equipe de discentes de iniciação científica dos laboratórios LABGENEST e FitoFar.

Para este ensaio, os substratos específicos das enzimas $3CL^{pro}$ e PL^{pro} contendo os fluoróforos - 4-(4-dimethyl-aminophenylazo)benzoyl (DABCYL) e 5-[(2-aminoethyl)amino]naphtalene-1-sulfonic acid (EDANS) foram sintetizados pelas empresas GenScript e FastBio, respectivamente. Estes substratos possuíam as seguintes sequências:

- Para o sítio de clivagem nsp4-nsp5 da $3CL^{pro}$:

  DABCYL - Ala-Val-Leu-Gln ↓ Ser-Gly-Phe-Arg-Lys - **EDANS**

- Para o sítio de clivagem nsp3-nsp4 da PL^{pro}:

  DABCYL - Ala-Leu-Lys-Gly ↓ Gly-Lys-Iso-Val - **EDANS**

Dessa forma, os ensaios foram realizados em placas de 96 poços próprias para fluorimetria, utilizando o método de transferência ressonante de energia por fluorescência (FRET - *Fluorescent Ressonance Energy Transfer*) (Figura 16). Após a adição de enzima, substrato específico e extratos (100 $\mu g.mL^{-1}$) - concentração foi definida com base em triagens e testes prévios, em cada poço, a placa foi incubada a 37°C durante 15 minutos no tampão de ensaio. Em seguida, a reação foi desenvolvida a 37°C por 45 minutos utilizando um espectrofluorímetro Spectra Max M5. A taxa de hidrólise foi determinada monitorando a fluorescência ao longo do tempo (excitação $\lambda = 330$ nm; emissão $\lambda = 490$ nm). Os ensaios foram realizados em duplicata amostral.

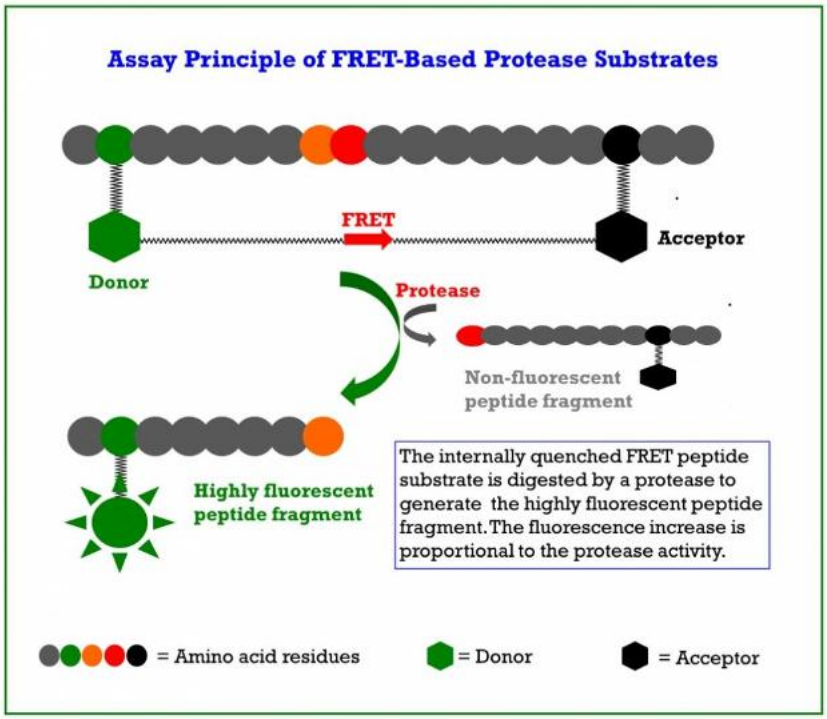

Figura 17. Princípios dos ensaios utilizando o método de transferência ressonante de energia por fluorescência (FRET). Fonte: Biomol *Website* (2025).

5.5. Processamento dos dados químicos

Os dados obtidos nas análises por LC-MS/MS foram convertidos em arquivos abertos de extensão ".mzML" no *software* MSConvertGUI versão 3.0 - ProteoWizard. Em seguida, os arquivos convertidos foram importados para o *software* MZmine versão 2.53, onde foram visualizados e processados, utilizando os parâmetros gerais descritos na Figura 18. Cabe ressaltar que os parâmetros de processamento foram adaptados de acordo com o conjunto de amostras analisadas. As planilhas ".csv" exportadas continham o sinal ID, valor de MS^1, tempo de retenção e a área sinal. As informações de MS^2 foram exportadas em arquivos com extensão ".mgf".

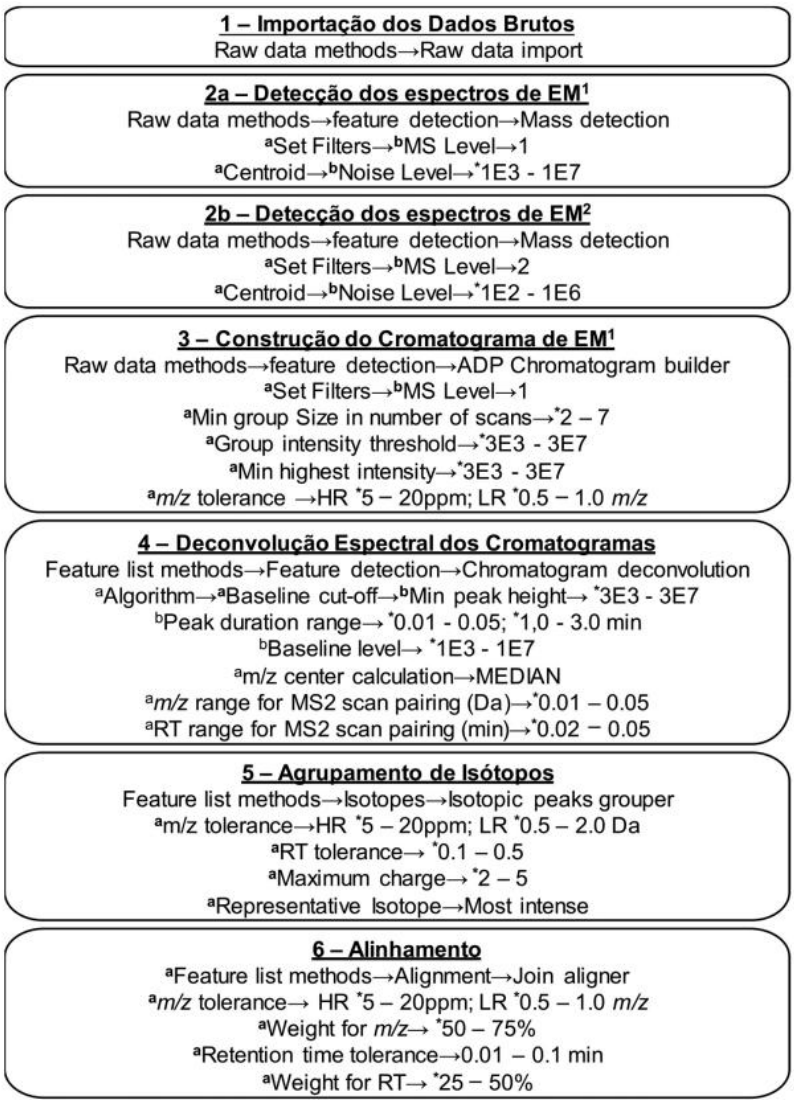

Figura 18. Parâmetros gerais de processamento de dados químicos obtidos por LC-MS/MS no *software* MZmine. Fonte: adaptado de Pilon *et al.* (2021).

5.6. Ensaios quimiométricos

Os arquivos ".csv" exportados pelo software MZmine, juntamente com os metadados dos valores de atividade obtidos nas triagens biológicas, foram carregados como arquivos ASCII no *software* The Unscrambler X, versão 10.4 (CAMO Software, Oslo, Noruega). A partir desses dados, foram aplicadas duas técnicas estatísticas multivariadas: Análise de Componentes Principais (PCA) e Regressão por Mínimos Quadrados Parciais (PLS-*Regression*).

O algoritmo PLS combina conceitos da PCA e da regressão linear, identificando variáveis latentes que maximizam a correlação entre os preditores, neste caso, os íons (*m/z*), e a atividade biológica.

Os valores de porcentagem de inibição e IC_{50} obtidos nos ensaios de triagem biológica foram utilizados como variáveis dependentes contínuas. Além disso, foram testadas variáveis dependentes binárias para classificação dos compostos quanto à inibição, considerando ativo ($\geq 50\%$) e inativo ($< 50\%$).

Para a construção dos modelos PLS, foi utilizado o algoritmo NIPALS e o método de validação cruzada utilizado foi o *Leave-One-Out*.

5.7. Construção de redes moleculares

Os arquivos ".mzML" convertidos no *software* MSconvertGUI, assim como os arquivos com extensão ".csv" e ".mgf" exportados pelo *software* MZmine foram carregados através do *software* WinSCP em área de trabalho própria existente dentro do *host* da plataforma GNPS. Também foi incluído neste espaço de trabalho um arquivo *metadata* ".tsv" contendo os dados de ID das amostras, correlacionando-as com as informações binárias (ativo-inativo; citotóxico-não citotóxico) e contínuas (valores de porcentagem de inibição e IC_{50}) obtidas em todos os ensaios de triagem biológica.

Para a construção das redes moleculares foi utilizada a ferramenta *Feature Networking* disponível na Plataforma GNPS. Todos os arquivos disponíveis no espaço de trabalho próprio foram utilizados para a elaboração das redes quantitativas (FBMN - *Feature-Based Molecular Networking*) de acordo com os parâmetros básicos descritos na Tabela 3.

Os parâmetros utilizados foram aqueles recomendados na documentação do GNPS para dados com resolução unitária. Os dados gerados pelo GNPS foram baixados e processados no *software* Cytoscape 3.9.1 para a obtenção dos resultados da análise de redes moleculares.

Esses arquivos foram utilizados para a desreplicação das substâncias indicadas pelos modelos preditivos como potencialmente associadas à atividade anti-SARS-CoV-2. Além da anotação pelo GNPS, uma base de dados personalizada também foi utilizada.

Tabela 3. Parâmetros para construção de redes moleculares quantitativas (FBMN) na plataforma GNPS.

Parâmetros	**Configurações utilizadas**
Precursor Ion Mass Tolerance	2.0 Da
Fragment Ion Mass Tolerance	0.5 Da
Min Pairs Cos	0.7
Min Matched Peaks	6
Max shift between precursors	500
Network TopK	20
Max connected componente size	0

Fonte: o Autor.

5.8. Ensaios de citotoxidez em células Vero E6 e Calu-3

Os ensaios citotoxidez em Vero E6 foram realizados pela doutoranda Mariana F. Campos e pela discente de iniciação científica Beatriz A. C. de Oliveira no laboratório de biotecnologia e bioengenharia estrutural (LABGENEST) em colaboração com o Professor Dr. Diego Alonso, Faculdade de Farmácia – UFRJ. Já os ensaios com a linhagem Calu-3 foram executados pelos discentes de gradução e pós-gradução Alice Santos Rosa, Thamara Kelcya Fonseca Oliveira, Amanda Resende Tucci, Júlia Nilo Henrique Lima e Vivian Neuza Santos Ferreira, em colaboração com a Dra. Milene Dias Miranda, Laboratório de Morfologia e Morfogênese Viral (LMMV) - FIOCRUZ. Os gráficos foram construídos e analisados utilizando o *software* GraphPad Prism, versão 8 e 10 (GraphPad Software, San Diego, CA, EUA), representando a média dos dados obtidos em pelo menos três réplicas técnicas.

5.8.1. Citotoxidez em Células Vero E6

Para este ensaio, foi realizada a avalição da redução do sal de tetrazólio (MTT) em formazana, visando avaliar a viabilidade mitocondrial das células epiteliais de rim de macaco verde africano (Vero E6). Neste ensaio, o MTT, substância amarelada, é reduzido em células metabolicamente ativas pela enzima mitocondrial NADH, formando cristais violáceos de formazana (Figura 17).

As células Vero E6 foram cultivadas em meio de cultura F-12 e posteriormente semeadas em placas de 96 poços, sendo incubadas por 24 horas. As soluções de estoque e os tratamentos foram preparados a partir dos extratos solubilizados em dimetilsulfóxido (DMSO). As concentrações dos tratamentos foram determinadas com base em ensaios preliminares de triagem, e as células foram tratadas por 48 horas em duplicata. Como controles, foram incluídos grupos com meio de cultura e DMSO.

Após o período de tratamento, 500 µL de meio de cultura fresco contendo 10 µL de MTT foi adicionado a cada poço, e as placas foram incubadas em estufa úmida a 5% de CO_2 por 4 horas. Os cristais de formazana formados foram dissolvidos em 50 µL de DMSO, e a absorbância foi medida a 540 nm utilizando um leitor de microplacas Spectra Max M5. Os ensaios foram realizados em triplicata experimental, seguindo rigorosos procedimentos estéreis e condições controladas de incubação.

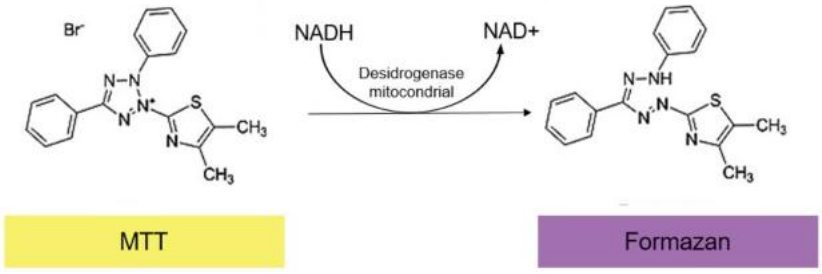

Figura 19. Princípios dos ensaios utilizando o método de redução do sal de tetrazólio em formazana. Fonte: Magalhães; Thá; Leme (2018).

5.8.2. Citotoxidez em células Calu-3

A linhagem celular Calu-3, derivada de um adenocarcinoma brônquico humano e fornecida pela plataforma Farmanguinhos RPT11M, foi cultivada em placas de 96 poços ($1,5 \times 10^4$ células/poço).

Para a avaliação da citotoxidez, as células foram expostas a 25 extratos diferentes na concentração de 200 $\mu g \cdot mL^{-1}$ por 72 horas, utilizando o ensaio CytoTox 96® Non-Radioactive Colorimetric Assay (Promega, Madison, WI, EUA). Este ensaio quantifica a atividade da enzima Lactato Desidrogenase (LDH) conforme as diretrizes do fabricante (Figura 18).

Para este ensaio, os extratos foram inicialmente dissolvidos em dimetilsulfóxido (DMSO) 100% e posteriormente diluídos em Dulbecco's Modified Eagle Medium (DMEM—Gibco,

Waltham, MA, EUA). As concentrações de DMSO foram mantidas abaixo de 1% (v/v) para evitar interferências na proliferação e viabilidade celular

As células do grupo controle (não tratado) foram lisadas utilizando a Solução de Lise do kit. Em seguida, a placa foi centrifugada a 400× g por três minutos, e 50 µL do sobrenadante foi cuidadosamente transferido para outra placa. O reagente CytoTox 96® foi adicionado, e a mistura foi incubada por 30 minutos à temperatura ambiente, protegida da luz. Após a incubação, a Solução de Interrupção (Stop Solution) foi adicionada, e a absorbância foi registrada a 490 nm utilizando um espectrofotômetro (Loccus, São Paulo, Brasil).

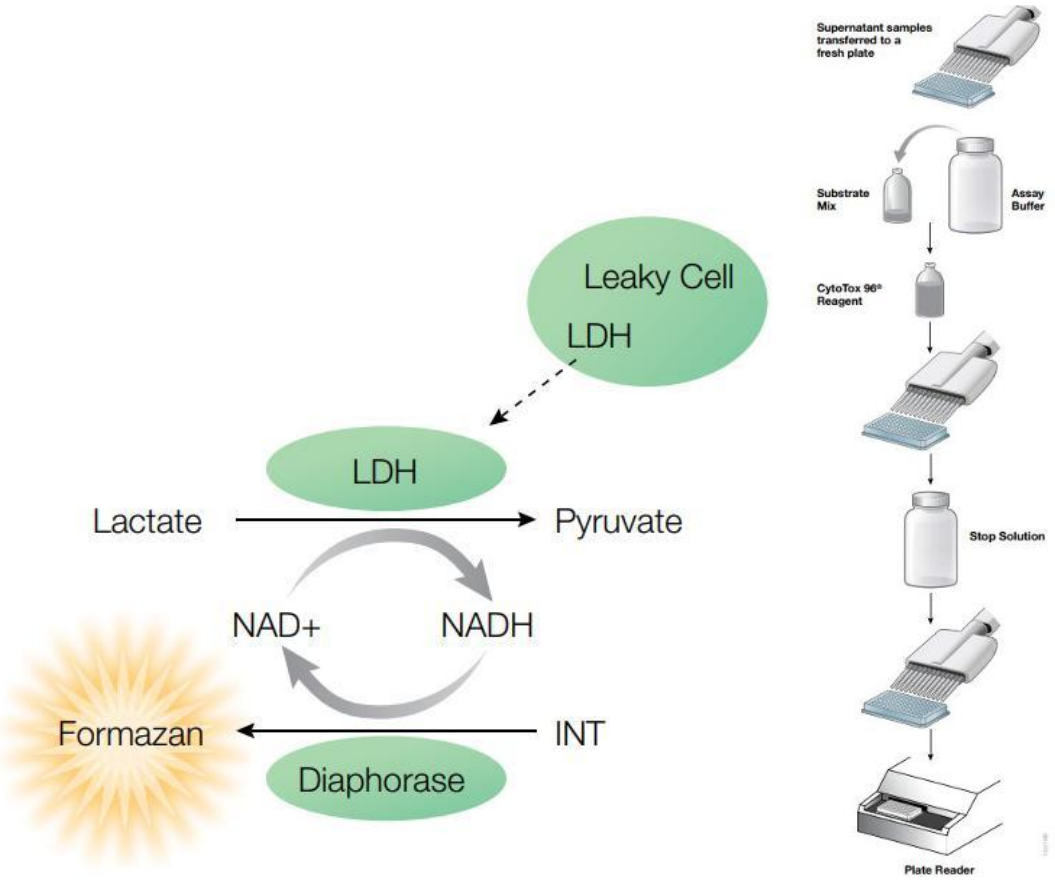

Figura 20. Princípios dos ensaios utilizando o *kit* comercial CytoTox 96® Non-Radioactive Colorimetric Assay. Fonte: Promega *Website* (2025).

5.9. Ensaio de neutralização *in vitro* de vírus da estomatite vesicular (VSV) pseudotipado com a SP de SARS-CoV-2

Os ensaios de neutralização de VSV (*Vesicular Stomatitis Virus*) pseudotipado com a SP de SARS-CoV-2 foi realizado pela doutoranda Mariana F. Campos, em colaboração com o Professor Dr. Diego Alonso (LABGENEST) – Faculdade de Farmácia, UFRJ.

5.9.1. Construção e produção dos pseudovírus

A construção do vírus pseudotipado com a SP do SARS-CoV-2 foi realizada utilizando um sistema baseado no VSV humano. Os plasmídeos necessários para essa construção foram gentilmente cedidos pela Profª. Dra. Luciana de Jesus Costa, do Laboratório de Genética e Imunologia das Infecções Virais, Instituto de Microbiologia Paulo de Góes, UFRJ.

Os pseudovírus foram gerados em linhagem de células humanas de rim embrionário 293 transformadas com o antígeno T do vírus SV40 transduzidas para expressão estável do receptor humano ACE2 [HEK293-T/ACE2] (3×10^6 células/garrafa), carregando o gene da luciferase como repórter. Para a produção do vírus VSV-Luciferase (VSV-Luc), as células foram transfectadas com o plasmídeo VSV-G utilizando o reagente Lipofectamine 3000 (Invitrogen, ThermoFisher Scientific, Waltham, MA, EUA), seguindo as instruções do fabricante.

Em seguida, o VSV-Luc foi utilizado para infectar células HEK293-T ($4{,}5 \times 10^6$ células/placa de Petri) previamente transfectadas com os plasmídeos de expressão da SP do SARS-CoV-2, tanto da variante original quanto da subvariante Ômicron BA.2, também empregando o reagente Lipofectamine 3000. Após incubação por 24 horas a 37 °C e 5% de CO_2, o sobrenadante das placas foi coletado, centrifugado a 1.500 rpm por 10 minutos para remoção de células mortas e debris, e filtrado através de filtros de seringa de 0,22 nm (Merck, Darmstadt, Alemanha). O pseudovírus purificado foi então aliquotado e armazenado em ultrafreezer para uso nos ensaios subsequentes.

5.9.2. Ensaios de neutralização dos pseudovírus

Os ensaios de neutralização foram realizados utilizando a linhagem celular VERO E6/ACE2, que corresponde a células do epitélio renal de macaco-verde africano geneticamente modificadas para superexpressar o receptor ACE2. Essas células foram cultivadas em placas de 96 poços (Costar, Nova York, NY, EUA) a uma densidade de 5×10^4 células/poço em meio completo (10% de soro fetal bovino – FBS, 1% de penicilina/estreptomicina).

Os pseudovírus contendo as proteínas *Spike* das linhagens original e Ômicron BA.2 foram pré-incubados com os extratos testados em diferentes concentrações (12,5, 25, 50, 125 e 250 μg/mL) por 1 hora, em meio de cultura sem FBS. Após esse período de incubação, 80 μL da mistura foram adicionados às monocamadas de células VERO E6/ACE2, e as placas foram mantidas por 1 hora a 37 °C e 5% de CO_2.

Em seguida, 120 µL de meio completo contendo 10% de FBS foram adicionados a cada poço, e as placas foram incubadas por 48 horas sob as mesmas condições. Após esse período, os poços foram cuidadosamente lavados duas vezes com PBS 1× (137 mM NaCl, 2,7 mM KCl, 8 mM Na_2HPO_4 e 2 mM KH_2PO_4). Para quantificação da neutralização, 60 µL de um agente lisante diluído 5× (Promega, Madison, WI, EUA) foram adicionados a cada poço, e a placa foi manualmente agitada por 15 segundos.

Do sobrenadante das células lisadas, 50 µL foram transferidos para uma placa de 96 poços branca de fundo chato (Costar, Nova York, NY, EUA). Posteriormente, 100 µL do substrato de luciferase (Luciferase Assay System, Promega, Madison, WI, EUA) foram adicionados, conforme as instruções do fabricante. A leitura da luminescência foi realizada imediatamente após a adição do reagente, utilizando um leitor de microplacas SpectraMax M5 (Molecular Devices, San Jose, CA, EUA), com um tempo de exposição de 500 ms.

A porcentagem de neutralização viral foi determinada com base na quantificação do sinal de luciferase, refletindo o grau de infecção bem-sucedida pelos pseudovírus. Os resultados foram normalizados em relação ao controle do veículo e células não infectadas (n = 3), permitindo a avaliação da eficácia dos extratos testados na inibição da entrada do SARS-CoV-2 nas células-alvo.

5.10. Ensaios antivirais frente aos SARS-CoV-2

Os ensaios antivirais frente ao SARS-CoV-2 foram executados em instalação multiusuário de nível de biossegurança 3 (BSL3) pelos discentes de graduação e pós-graduação Alice Santos Rosa, Thamara Kelcya Fonseca Oliveira, Amanda Resende Tucci, Júlia Nilo Henrique Lima e Vivian Neuza Santos Ferreira, em colaboração com a Dra. Milene Dias Miranda, Laboratório de Morfologia e Morfogênese Viral (LMMV) - FIOCRUZ.

5.10.1. Ensaio antiviral

Para avaliar as atividades antivirais dos 25 extratos testados, monocamadas de células Calu-3 (linhagem derivada de adenocarcinoma brônquico humano) foram cultivadas em placas de 96 poços ($1,5 \times 10^4$ células/poço) e infectadas com o vírus SARS-CoV-2, linhagem B.1 (GenBank MT710714, SisGen AC58AE2), utilizando uma multiplicidade de infecção (MOI) de 0,01. O processo de infecção envolveu a incubação das células a 37 °C e 5% de CO_2 por 1 hora, permitindo a adsorção e entrada viral.

Após esse período, os sobrenadantes foram removidos e as células foram tratadas por 24 horas com uma curva de concentração dos extratos (0,781 a 200 $\mu g \cdot mL^{-1}$). Em seguida, os sobrenadantes foram coletados e submetidos ao ensaio de titulação viral utilizando a técnica de unidades formadoras de placa (Plaque-Forming Unit Assay – PFU/mL) para determinar o crescimento viral. A concentração do extrato necessária para inibir 50% da replicação viral máxima (EC_{50}) foi determinada por comparação com o controle positivo (células infectadas e não tratadas).

5.10.2. Titulação viral

Para a determinação dos títulos virais, foi utilizada a linhagem Vero E6 (células epiteliais de rim de macaco-verde africano, ATCC CRL-1586), cultivada em placas de 96 poços (1×10^4 células/poço). As células foram expostas a diluições seriadas dos sobrenadantes virais (1:200 a 1:25.600) e incubadas por 1 hora a 37 °C e 5% de CO_2. Após esse período, 50 µL de meio semissólido contendo DMEM-high Glucose 10×, 2,4% de carboximetilcelulose (CMC), 2% de soro fetal bovino (FBS), 1% de penicilina/estreptomicina e 4,4% de bicarbonato de sódio foi adicionado a cada poço, e as culturas foram mantidas em incubação por 72 horas sob as mesmas condições.

Após a incubação, as células foram fixadas com formalina 4% por 3 horas à temperatura ambiente e posteriormente coradas com cristal violeta 0,04% por 1 hora. As placas virais foram contadas, e os títulos virais foram expressos em PFU/mL.

Os títulos virais nos sobrenadantes das células infectadas e tratadas foram comparados com os das células infectadas não tratadas, expressando-se a inibição da replicação viral em porcentagem. Todos os experimentos envolvendo SARS-CoV-2 foram realizados em laboratório de nível de biossegurança 3 (BSL-3), seguindo rigorosamente as diretrizes da Organização Mundial da Saúde (OMS).

Os dados foram analisados e os gráficos gerados utilizando o software GraphPad Prism, versão 10.2.1 (GraphPad Software, San Diego, CA, EUA), representando a média dos valores obtidos em pelo menos três réplicas técnicas.

5.11. Ensaios e estudos *in silico*

Os ensaios computacionais de ancoragem molecular, dinâmica molecular e predição de características farmacocinéticas (ADMET) foram conduzidos pelos discentes de pós-graduação Maria Eduarda Alves Esteves, Bruce Veiga Andriolo e Caio Felipe de Araujo Ribas Cheohen, em colaboração com a Profa. Dra. Manuela Leal da Silva, coordenadora do Laboratório de Modelagem e Dinâmica Molecular (LMDM), vinculado ao Instituto de Biodiversidade e Sustentabilidade (NUPEM) – UFRJ. Adicionalmente, as discentes de pós-graduação Natalia Ferreira de Sousa e Renata Priscila Barros de Menezes também contribuíram com as análises deste tipo, colaboração com o Prof. Dr. Marcus Scotti, coordenador do Cheminformatics Lab, pertencente ao Departamento de Química – UFPA.

5.11.1. *Docking* molecular

Os estudos de *docking* molecular foram realizados para avaliar a interação entre proteínas virais do SARS-CoV-2 e compostos de interesse. Diferentes abordagens e softwares foram empregados para garantir a confiabilidade dos resultados.

As proteínas virais foram obtidas a partir de bancos de dados estruturais e preparadas para o docking molecular utilizando Discovery Studio Visualizer v20.1 (BIOVIA, Dassault Systèmes, San Diego, CA, EUA). Os sítios ativos foram definidos com base nas informações disponíveis na literatura e na presença de ligantes co-cristalizados. Para proteínas que não apresentavam ligantes associados, os sítios de interação foram preditos por meio de ferramentas como BiteNet Platform – Skoltech iMolecule (Skolkovo Institute of Science and Technology, Moscou, Rússia).

Os compostos de interesse foram desenhados e padronizados utilizando Marvin Sketch v19.18 e Standardizer v21.2.0 (ChemAxon, Budapeste, Hungria). O processo incluiu a adição de hidrogênios, padronização de anéis aromáticos, remoção de sais e conversão para modelos tridimensionais em formato ".sdf".

Os ensaios de docking molecular foram conduzidos utilizando três softwares distintos: Molegro Virtual Docker v6.0.1 (MVD) (CLC bio, QIAGEN, Aarhus, Dinamarca); GOLD Suite (Cambridge Crystallographic Data Centre – CCDC, Cambridge, Reino Unido); PLANTS (Simplex Evolution Algorithm). Dependendo do software empregado, o *docking* foi realizado de forma direcionada, com base na posição de ligantes co-cristalizados, ou cego, avaliando toda a superfície da proteína para identificação de potenciais sítios de ligação. Foram definidas

esferas de busca com raios variáveis para cada proteína-alvo, permitindo simulações específicas ou de amplo espectro. Para cada simulação, foram aplicadas diferentes funções de pontuação (MolDock Score, PLANTS Score e Rerank Score) para estimar a energia de ligação dos complexos. Além disso, a análise de interações incluiu cálculos de energia interna, interações eletrostáticas e hidrogênios, além da avaliação da estabilidade conformacional dos compostos no sítio ativo da proteína.

A análise das interações entre os compostos e os resíduos das proteínas foi realizada utilizando Maestro (Schrödinger Release 2023-3, Schrödinger, LLC, Nova York, EUA) e Protein-Ligand Interaction Profiler. Os complexos foram visualizados e analisados no Discovery Studio Visualizer v20.1 para identificar interações moleculares relevantes.

Para minimizar falsos positivos, foi realizada uma abordagem de *docking* consensual, combinando os resultados de diferentes funções de pontuação. A probabilidade de atividade de cada composto foi calculada a partir dos valores energéticos obtidos nas simulações, permitindo uma normalização entre os alvos proteicos estudados.

Os resultados foram expressos em termos de afinidade dos compostos pelos alvos virais, utilizando valores de energia de ligação e frequência de interações em múltiplas simulações. O modelo foi validado por meio de compostos controle previamente descritos na literatura, garantindo maior confiabilidade nas predições. A abordagem utilizada permitiu uma análise abrangente do potencial dos compostos testados para a interação com proteínas-chave do SARS-CoV-2.

5.11.2. Dinâmica molecular

As simulações de Dinâmica Molecular (DM) foram realizadas para avaliar a estabilidade das interações entre proteínas virais do SARS-CoV-2 e os compostos de interesse. Diferentes softwares e metodologias foram empregados para garantir a precisão das análises.

Os arquivos de proteína foram preparados com protonação ajustada para pH 8.0 utilizando o servidor web H++. A preparação dos ligantes foi realizada por meio da ferramenta Antechamber, garantindo a parametrização correta para os cálculos de dinâmica molecular. Para complexos contendo íons metálicos, a modelagem foi feita utilizando o MCPB.py e o software GAMESS-US, permitindo a simulação adequada das interações entre os cofatores metálicos e a proteína.

Os sistemas foram solvatados em caixas de simulação do tipo Octaedro Truncado ou Dodecaédrica, com uma distância de 12,0 Å entre a proteína e as bordas da caixa. A neutralização da carga elétrica do sistema foi realizada com a adição de íons cloreto e sódio, ajustando a força iônica para 0,15 M.

As simulações de dinâmica molecular foram conduzidas utilizando os softwares: AMBER 2022 e AmberTools 2022 (University of California, San Francisco, CA, EUA); GROMACS 5.0 (Royal Institute of Technology, Estocolmo, Suécia). Diferentes campos de força foram aplicados conforme a metodologia adotada: ff19SB, gaff2 e OPC para AMBER; GROMOS43a1 para GROMACS.

O modelo de solvatização utilizado foi SPC/E (Extended Point Charge). A minimização de energia foi realizada com 1.000 ciclos do método Steepest Descent, seguida por uma etapa de equilíbrio térmico a 300 K, utilizando o algoritmo V-rescale no conjunto NVT (número de partículas, volume e temperatura) por 100 ps. Posteriormente, a pressão foi equilibrada a 1 atm com o algoritmo Parrinello-Rahman no conjunto NPT (número de partículas, pressão e temperatura) por 100 ps.

As simulações de produção foram conduzidas por períodos de 50 a 200 ns, dependendo da abordagem adotada, com controle de pressão utilizando o Monte Carlo Barostat e restrição das ligações de hidrogênio pelo algoritmo SHAKE. O passo de integração foi definido em 1 fs (0,001 ps) para garantir a precisão dos cálculos.

Para avaliar a estabilidade estrutural e conformacional dos complexos proteína-ligante, foram calculados: Desvio Quadrático Médio (RMSD, Root Mean Square Deviation) de todos os átomos pesados em relação à estrutura inicial e a Flutuação Quadrática Média dos Resíduos (RMSF, Root Mean Square Fluctuation) para determinar a flexibilidade dos resíduos próximos ao sítio de ligação.

A energia de interação proteína-ligante foi determinada por meio do cálculo das energias Coulômbica de curto alcance e Lennard-Jones de curto alcance, considerando a estabilidade do complexo ao longo da simulação.

Os gráficos de RMSD e RMSF foram gerados utilizando o software Grace, e a visualização das interações moleculares foi realizada com o UCSF Chimera (University of California, San Francisco, CA, EUA).

5.11.3. Predição de características farmacocinéticas (ADMET)

A predição das propriedades de absorção, distribuição, metabolismo, excreção e toxicidade (ADMET) foi realizada utilizando diferentes ferramentas computacionais, permitindo a avaliação do perfil farmacocinético e toxicológico dos compostos estudados.

A predição das propriedades farmacocinéticas foi conduzida utilizando as plataformas *online* SwissADME ou ADMETlab 2.0, permitindo a análise de: Peso molecular (MW); Número de aceitadores (nHA) e doadores (nHD) de ligações de hidrogênio; Número de ligações rotativas (nRot); Área de superfície polar topológica (TPSA); Coeficiente de partição octanol/água (LogP);

Predição de absorção celular intestinal (permeabilidade Caco-2); Capacidade de atuar como substrato (Pgp-sub) ou inibidor (Pgp-inh) da P-glicoproteína; Absorção intestinal humana (HIA); Penetração na barreira hematoencefálica (BBB); Fração não ligada às proteínas plasmáticas (Fu); Predição se as moléculas atuam como substratos ou inibidores das isoenzimas do citocromo P450 (CYP).

Adicionalmente, o software DataWarrior v. 4.7.2 – OpenMolecules (Actelion Pharmaceuticals Ltd., Allschwil, Suíça) foi empregado para análises complementares de toxicidade preditiva, como Hepatotoxicidade humana (H-HT); Danos hepáticos induzidos por fármacos (DILI); Teste de Ames para mutagenicidade; Carcinogenicidade; Toxicidade respiratória.

Os resultados dessas predições foram analisados para identificar potenciais riscos toxicológicos e limitações na absorção e metabolismo dos compostos, fornecendo suporte para futuras otimizações estruturais.

6. RESULTADOS E DISCUSSÃO

Esta seção apresentará os resultados e discussões obtidos nos ensaios realizados no formato de artigos científicos já publicados, adotando uma alternativa à apresentação tradicional de teses. Tal apresentação é estabelecida e aceita pelo programa de pós-graduação em Biotecnologia Vegetal e Bioprocessos. Os artigos serão dispostos integralmente e em sequência, precedidos por informações gerais. Os materiais suplementares destes artigos, encontram-se nos anexos 2 e 3 deste documento.

6.1. Artigo 1: *Myrtucommulones and Related Acylphloroglucinols from Myrtaceae as a Promising Source of Multitarget SARS-CoV-2 Cycle Inhibitors*

O artigo "*Myrtucommulones and Related Acylphloroglucinols from Myrtaceae as a Promising Source of Multitarget SARS-CoV-2 Cycle Inhibitors*" foi publicado na revista *Pharmaceuticals* em março de 2024 (Volume 17, artigo 436). A *Pharmaceuticals* é uma revista científica de relevância, classificada como Qualis A1 e com um fator de impacto de 4.3.

O estudo aborda a construção de modelos preditivos de substâncias naturais provenientes de diferentes espécies da família Myrtaceae, com foco nas myrtucommulonas e acilfloroglucinóis, e seu potencial antiviral frente ao SARS-CoV-2. A pesquisa combina abordagens *in vitro* e *in silico*, demonstrando que determinados extratos e substâncias possuem atividade *multitarget*, inibindo proteínas essenciais para o ciclo viral, como *Spike*, $3CL^{pro}$ e PL^{pro}. O trabalho reforça a importância da bioprospecção de produtos naturais como alternativa para novas terapias antivirais. Além disso, destaca a relevância da biodiversidade brasileira para a inovação no campo da pesquisa e desenvolvimento de novos medicamentos.

Neste estudo, o aluno teve uma participação ativa e fundamental, sendo responsável pela proposta do *workflow* experimental, colaborando na investigação dos extratos frente às proteases $3CL^{pro}$ e PL^{pro}, e encabeçando o processamento dos dados químicos e o desenvolvimento dos modelos preditivos. Além disso, contribuiu significativamente para a construção e análise das redes moleculares e para a anotação das substâncias preditas. Também teve uma atuação destacada na redação do manuscrito e na revisão dos dados.

pharmaceuticals

MDPI

Article

Myrtucommulones and Related Acylphloroglucinols from Myrtaceae as a Promising Source of Multitarget SARS-CoV-2 Cycle Inhibitors

Simony Carvalho Mendonça[1,†], Brendo Araujo Gomes [1,2,†], Mariana Freire Campos [1,2], Thamirys Silva da Fonseca[3], Maria Eduarda Alves Esteves[4], Bruce Veiga Andriolo[5], Caio Felipe de Araujo Ribas Cheohen[6], Larissa Esteves Carvalho Constant[7], Stephany da Silva Costa[7], Pedro Telles Calil[8], Amanda Resende Tucci[9,10], Thamara Kelcya Fonseca de Oliveira[9,10], Alice dos Santos Rosa[9,10] , Vivian Neuza dos Santos Ferreira[9], Julia Nilo Henrique Lima[9], Milene Dias Miranda[9,10], Luciana Jesus da Costa[8], Manuela Leal da Silva[4,5,6], Marcus Tullius Scotti[11], Diego Allonso[7,12], Gilda Guimarães Leitão[13,*] and Suzana Guimarães Leitão[1,2,3,*]

1 Departamento de Produtos Naturais e Alimentos, Faculdade de Farmácia, Universidade Federal do Rio de Janeiro, Rio de Janeiro 21941-902, RJ, Brazil; sy2802@ufrj.br (S.C.M.); brendoo.bc@ufrj.br (B.A.G.); camposmariana@biof.ufrj.br (M.F.C.)
2 Programa de Pós-Graduação em Biotecnologia Vegetal e Bioprocessos, Centro de Ciências da Saúde, Universidade Federal do Rio de Janeiro, Rio de Janeiro 21941-902, RJ, Brazil
3 Programa de Pós-Graduação em Ciências Farmacêuticas, Faculdade de Farmácia, Universidade Federal do Rio de Janeiro, Rio de Janeiro 21941-902, RJ, Brazil; thamirysfonseca@ufrj.br
4 Programa de Pós-Graduação em Biologia Computacional e Sistemas, Instituto Oswaldo Cruz, Rio de Janeiro 21040-900, RJ, Brazil; mariaesteves@aluno.fiocruz.br (M.E.A.E.); manuela@macae.ufrj.br (M.L.d.S.)
5 Programa de Pós-Graduação em Biotecnologia, Instituto Nacional de Metrologia, Qualidade e Tecnologia, Duque de Caxias 25250-020, RJ, Brazil; bruceandriolo@ufrj.br
6 Programa de Pós-Graduação Multicêntrico em Ciências Fisiológicas, Centro de Ciências da Saúde, Instituto de Biodiversidade e Sustentabilidade NUPEM, Universidade Federal do Rio de Janeiro, Macaé 27965-045, RJ, Brazil; caiocheohen@ufrj.br
7 Programa de Pós-Graduação em Ciências Biológicas, Instituto de Biofísica Carlos Chagas Filho, Universidade Federal do Rio de Janeiro, Rio de Janeiro 21941-590, RJ, Brazil; larissaconstant@biof.ufrj.br (L.E.C.C.); stephanycosta@biof.ufrj.br (S.d.S.C.); diegoallonso@pharma.ufrj.br (D.A.)
8 Departamento de Virologia, Instituto de Microbiologia Paulo de Góes, Universidade Federal do Rio de Janeiro, Rio de Janeiro 21941-590, RJ, Brazil; ptcalil@micro.ufrj.br (P.T.C.); ljcosta@micro.ufrj.br (L.J.d.C.)
9 Laboratory of Morphology and Viral Morphogenesis, Oswaldo Cruz Institute, Oswaldo Cruz Foundation, Rio de Janeiro 21041-250, RJ, Brazil; amanda.tucci@ioc.fiocruz.br (A.R.T.); thamara.oliveira@ioc.fiocruz.br (T.K.F.d.O.); alicerosa@aluno.fiocruz.br (A.d.S.R.); vivian.ferreira@ioc.fiocruz.br (V.N.d.S.F.); julianilo@ufrj.br (J.N.H.L.); mmiranda@ioc.fiocruz.br (M.D.M.)
10 Programa de Pós-Graduação em Biologia Celular e Molecular, Instituto Oswaldo Cruz, Fundação Oswaldo Cruz, Rio de Janeiro 21041-250, RJ, Brazil
11 Departamento de Química, Universidade Federal da Paraíba, João Pessoa 58033-455, PB, Brazil; mtscotti@ccae.ufpb.br
12 Departamento de Biotecnologia Farmacêutica, Faculdade de Farmácia, Universidade Federal do Rio de Janeiro, Rio de Janeiro 21941-902, RJ, Brazil
13 Instituto de Pesquisas de Produtos Naturais, Universidade Federal do Rio de Janeiro, Rio de Janeiro 21941-902, RJ, Brazil
* Correspondence: ggleitao@ippn.ufrj.br (G.G.L.); sgleitao@pharma.ufrj.br (S.G.L.); Tel.: +55-21-3938-6513 (G.G.L.); +55-21-3938-6414 (S.G.L.)
† These authors contributed equally to this work.

check for updates

Citation: Mendonça, S.C.; Gomes, B.A.; Campos, M.F.; da Fonseca, T.S.; Esteves, M.E.A.; Andriolo, B.V.; Cheohen, C.F.d.A.R.; Constant, L.E.C.; da Silva Costa, S.; Calil, P.T.; et al. Myrtucommulones and Related Acylphloroglucinols from Myrtaceae as a Promising Source of Multitarget SARS-CoV-2 Cycle Inhibitors. *Pharmaceuticals* **2024**, *17*, 436. https://doi.org/10.3390/ph17040436

Academic Editor: Sabina Lachowicz-Wis´niewska

Received: 11 March 2024
Accepted: 22 March 2024
Published: 28 March 2024

Copyright: © 2024 by the authors. Licensee MDPI, Basel, Switzerland. This article is an open access article distributed under the terms and conditions of the Creative Commons Attribution (CC BY) license (https://creativecommons.org/licenses/by/4.0/).

Abstract: The LABEXTRACT plant extract bank, featuring diverse members of the Myrtaceae family from Brazilian hot spot regions, provides a promising avenue for bioprospection. Given the pivotal roles of the Spike protein and $3CL^{pro}$ and PL^{pro} proteases in SARS-CoV-2 infection, this study delves into the correlations between the Myrtaceae species from the Atlantic Forest and these targets, as well as an antiviral activity through both *in vitro* and *in silico* analyses. The results uncovered notable inhibitory effects, with *Eugenia prasina* and *E. mosenii* standing out, while *E. mosenii* proved to be multitarget, presenting inhibition values above 72% in the three targets analyzed. All

extracts inhibited viral replication in Calu-3 cells (EC_{50} was lower than 8.3 μg·mL^{-1}). Chemometric analyses, through LC-MS/MS, encompassing prediction models and molecular networking, identified potential active compounds, such as myrtucommulones, described in the literature for their antiviral activity. Docking analyses showed that one undescribed myrtucommulone (m/z 841 [M − H]$^-$) had a higher fitness score when interacting with the targets of this study, including ACE2, Spike, PL^{pro} and $3CL^{pro}$ of SARS-CoV-2. Also, the study concludes that Myrtaceae extracts, particularly from *E. mosenii* and *E. prasina*, exhibit promising inhibitory effects against crucial stages in SARS-CoV-2 infection. Compounds like myrtucommulones emerge as potential anti-SARS-CoV-2 agents, warranting further exploration.

Keywords: COVID-19; FRET; pseudotyped virus; PLS regression

1. Introduction

Brazil holds areas of high natural wealth in terms of plant biodiversity, including two out of the thirty-four hotspots spread across the world: Cerrado and the Atlantic Forest. These ecoregions remain highly threatened, subject to rapid urbanization and high levels of resource exploitation [1].

The Myrtaceae family is commonly found in many of these biodiversity hotspots, such as southwestern Australia, as well as in the Brazilian Cerrado and Atlantic Forest [2], where Myrtaceae stands out as one of the most diverse families of woody plants [1]. The LABEX-TRACT from the Federal University of Rio de Janeiro is a plant extract bank that holds a representative number of samples, containing species from the Atlantic Forest and the Amazon regions, which represent an outstanding source of potentially pharmacologically active compounds, as well as new chemical entities.

Several studies, by using both *in silico* and *in vitro* approaches, have demonstrated the relevance of the Brazilian flora in tackling SARS-CoV-2 infection and, therefore, the COVID- 19 pandemic. Previous studies from our group have shown the capacity of flavonoids isolated from *Siparuna cristata* (Poepp. & Endl.) A. DC. to inhibit SARS-CoV-2 *in vitro* replication [3], as well as the capability of glycosylated phenylethanoid glycosides to act as 3-Quimiotripsin-like protease ($3CL^{pro}$) and Papain-like protease (PL^{pro}) inhibitors, of which forsythoside and verbascoside (abundant phenylpropanoids in Brazilian plants) were the most promising multitarget compounds [4]. The potential of *Ampelozizyphus amazonicus* Ducke bark extracts against SARS-CoV-2, which is a plant traditionally used by Brazil- ian *quilombola* Amazonian riverine communities to treat COVID, has been demonstrated by their capacity to inhibit the interaction between the SARS-CoV-2 Spike protein and angiotensin-converting enzyme 2 (ACE2) receptor and, therefore, reduce viral replication in Calu-3 cells. This effect was attributed to phenolic compounds found in these extracts [5]. SARS-CoV-2's Spike protein, $3CL^{pro}$, and PL^{pro} are significant viral targets for devel- oping multitarget compounds to combat the virus [6]. The Spike protein, responsible for viral-host cell fusion, is crucial for the virus's entry into the host cell [7]. By targeting this protein, the interaction with the host's ACE2 receptor can be prevented, thereby inhibiting the entry of the virus [8]. $3CL^{pro}$, a homodimeric protease, is vital for the viral replication process. Its unique structure, comprising three domains and an active site with a catalytic dyad (HIS 41 and CYS 145), makes it an ideal target for antiviral drugs [9–11]. PL^{pro}, on the other hand, is a monomeric protease with a distinct active site formed by a catalytic triad (CYS 111, HIS 272, and ASP 286). Its enzymatic activity is integral for viral maturation and replication [12–14].

The Myrtaceae family has economic importance, as its species are commonly used as condiments, for essential oil extraction, and for wood and fruit production [15]. Moreover, their valuable therapeutic properties, such as antibacterial, antifungal, antiviral, antioxi- dant, anti-inflammatory, cytotoxic, and antiproliferative activities, have stimulated research efforts to identify bioactive compounds in their extracts. These extracts are known to be

rich in terpenes, polyphenols, and other unique acylphloroglucinol compounds named myrtucommulones [2,16–18]. These phloroglucinol derivatives can be chemically divided into two main subclasses: oligomeric acylphloroglucinols and phloroglucinol–terpene adducts [2], with a very large structural diversity. Among these compounds, the myrtucommulones are related to various biological activities. Several have shown significant activities against Epstein–Barr virus (EBV), herpes simplex virus (HSV), respiratory syncytial virus (RSV), and human immunodeficiency virus (HIV), and more recently, docking analysis have suggested that they can be effective against SARS-CoV-2 [19–22].

In this context, the objective of this work was to investigate through chemometric analyses correlations between the bioactive compounds present in extracts of the Myrtaceae family on the entry and replication mechanisms associated with the Spike protein, ACE2, and $3CL^{pro}$ and PL^{pro} proteases of SARS-CoV-2 in host cells through *in vitro* and *in silico* analysis. The species studied included *Eugenia brasiliensis* Lam., *Eugenia prasina* O. Berg., *Eugenia mosenii* (Kausel) Sobral, *Myrcia strigipes* Mart., and *Myrcia splendens* Sw. DC., all from Atlantic Forest and available in the LABEXTRACT.

2. Results and Discussion

2.1. Myrtaceae Extracts Inhibit RBD:ACE2 Complex Formation and SARS-CoV-2 Proteases Activity In Vitro

The ability of the extracts to inhibit the formation of RBD:ACE2 complex was assessed by Lumit™ kit (Promega), a bioluminescence-based kit suitable for the trial of potential inhibitory samples [23]. At 250 $\mu g \cdot mL^{-1}$, only the *E. brasiliensis* (12%) extract was not able to inhibit RBD:ACE2 interaction above 70% (Table 1). The extract of *E. prasina* stood out as the most active, showing an inhibitory rate of 96%, followed by *E. mosenii* extract (84%).

Table 1. Myrtaceae extracts and their effect on the entry and replication mechanisms associated with the Spike protein (250 $\mu g \cdot mL^{-1}$) in host cells and inhibition of $3CL^{pro}$ and PL^{pro} proteases (100 $\mu g \cdot mL^{-1}$) of SARS-CoV-2.

	Inhibition (%)		
Extracts	**Spike:ACE2**	**$3CL^{pro}$**	**PL^{pro}**
Eugenia brasiliensis	12	69	34
Myrcia splendens	81	58	52
Eugenia mosenii	84	100	72
Myrcia strigipes	79	46	43
Eugenia prasina	96	53	57

The FRET-based assay was employed to measure SARS-CoV-2 $3CL^{pro}$ and PL^{pro} proteolytic activities by using the fluorescence resonance energy transfer (FRET) approach. This assay has been applied to investigate potential enzyme activity inhibitors from both synthetic and natural sources [24].

As presented in Table 1, only the extract from *M. strigipes* exhibits inhibitory activity below 50% against SARS-CoV-2 $r3CL^{pro}$. Notably, the *E. mosenii* extract displays inhibitory activity exceeding 80%. Regarding activity against SARS-CoV-2 rPL^{pro}, the extracts from *E. brasiliensis* and *M. strigipes* demonstrated inhibitory activities below 50%, while *E. mosenii* displayed the highest inhibition value (72%).

2.2. Myrtaceae Extracts Inhibit SARS-CoV-2 Spike-Pseudotyped VSV Entry into VERO ACE2 Cells

Since most Myrtaceae extracts showed good inhibition of the RBD:ACE2 complex formation, a SARS-CoV-2 Spike-pseudotyped VSV that contains in the envelope the SARS-CoV-2 Spike protein and a VSV replication machinery with a luciferase reporter gene was used to measure the potential of Myrtaceae extracts to block SARS-CoV-2 Spike-mediated cell entry. For this assay, Vero E6 cells that overexpress ACE2 (Vero E6/ACE2) were used. When the Spike pseudotyped viruses are incubated with cells containing the ACE2, it is possible for them to recognize the receptor and attach and enter the cells through

the binding between the Spike protein and the receptors on the cell surface. It had been previously shown using RBD:ACE2 complex formation assays that Myrtaceae extracts present the ability to inhibit the protein–protein interaction, suggesting that substances in the extracts could act as blockers of virus cell entry. In follow-up neutralization assays, using Spike-pseudotyped VSV, extracts were able to significantly block receptor-mediated cell entry (Figure 1A) at the highest tested concentration (250 μg·mL^{-1}). The extract from *E. mosenii* seemed to be the most active, inhibiting cell entry up to 80% even at the lowest tested concentration (25 μg·mL^{-1}) and presenting the lowest EC_{50} value (<25 μg·mL^{-1}) (Table 2). The extracts only induced cell toxicity in concentrations above 500 μg·mL^{-1} (Figure 1B).

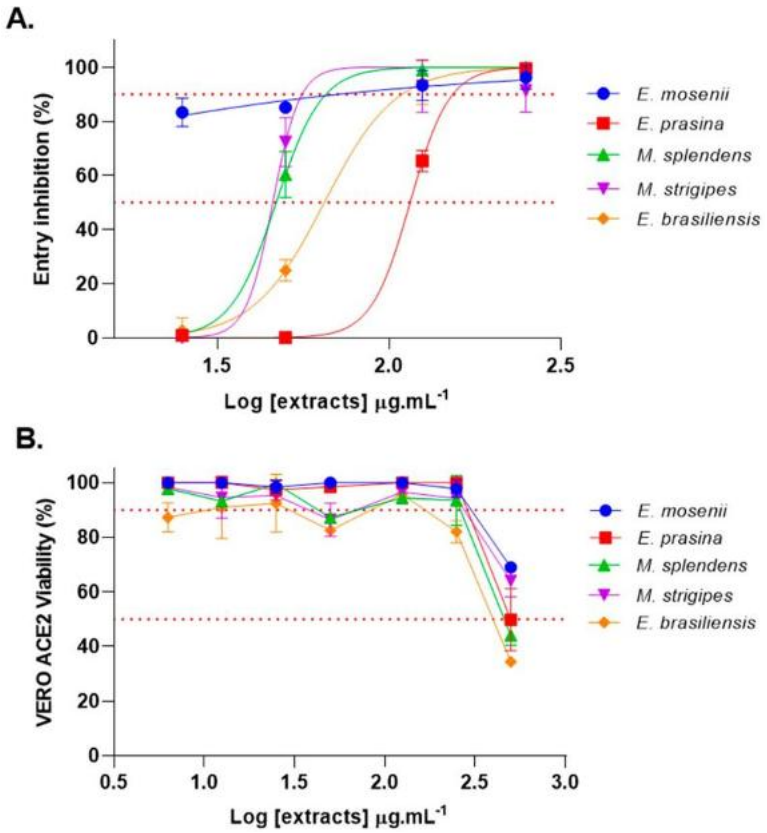

Figure 1. (**A**) Inhibition of Spike-pseudotyped VSV receptor-mediated cell entry after treatment with Myrtaceae extracts (*E. prasina*, *M. splendens*, *M. strigipes*, *E. mosenii*, and *E. brasiliensis*) in four dif- ferent concentrations (250, 125, 50, and 25 μg·mL^{-1}), assessed by luciferase activity assay. Percent neutralization was determined by quantification of total luciferase signal resulting from successful pseudovirus infection, normalized to vehicle control (n = 3). (**B**) Vero E6-ACE2 cells viability after treatment with Myrtaceae extracts in different concentrations (500, 250, 125, 50, 25 and 12.5 μg·mL^{-1}) was assessed with an MTT colorimetric test (5 mM, 1× PBS). Total cell viability was determined by quantification of dye metabolization by untreated cells normalized to vehicle control (n = 3). Lines in the graphs mark, respectively, 90% and 50% of inhibition.

Table 2. EC_{50} values for the five Myrtaceae extracts in Spike-pseudotyped VSV assay.

	E. mosenii	*E. prasina*	*M. splendens*	*M. strigipes*	*E. brasiliensis*
EC_{50} (μg·mL^{-1})	<25	115	47	45	65

2.3. Chemometric Analyses Using Partial Least Squares Regression Prediction Model

To predict the potential active compounds that inhibit all the Spike:ACE2 interactions (Lumit™ kit) and r3CL^{pro} and rPL^{pro} proteolytic activities (FRET), the 15 ethanol extracts

from the five species of the Myrtaceae family underwent liquid chromatography coupled to tandem mass spectrometry (LC-MS/MS) analysis using two ionization sources in both positive and negative modes (LC-ESI/APCI-(+/−)-MS/MS). Chemometric analyses were performed alongside binary values of activities in the three target models (excluding SARS-CoV-2 Spike-pseudotyped VSV entry assay). A Partial Least Squares (PLS) regression analysis model was constructed to correlate the LC-MS data with the inhibitory activity of the extracts.

The PLS regression used the LC-MS dataset of the 15 samples as independent variables (X), encompassing a total of 170 parameters (m/z ions), with the dependent variable (Y) being the inhibition activities against the three target models. This algorithm combines principal component analysis (PCA) and linear regression, seeking latent variables that maximize the correlation between predictors (m/z ions) and biological activity. Based on the PLS analyses, patterns in the sample distribution were identified, allowing classification into two groups based on average activity values across the three target models: more active samples (≥50% inhibition; active) and less active samples (<50% inhibition; non-active).

All four chemical datasets (ESI+/− and APCI+/−) for each plant extract were modeled, and the data obtained from negative electrospray ionization (ESI) showed the highest explained variance, R^2 and Q^2 values, and the lowest Root Mean Square Error (RMSE) in the four constructed models. Therefore, data from this ionization mode were selected to proceed with prediction analyses. At the outset, three models were developed to individually evaluate the Spike:ACE2, r3CL^{pro}, and rPL^{pro} targets. Within these models, our goal was to assess the influence of ions obtained through LC-MS/MS analyses in explaining the inhibitory activity response. Consequently, this approach enabled us to identify ions exhibiting the strongest correlation with the target under investigation, thereby providing insights into their potential roles in the conducted experimental assays.

In the investigation model of Spike:ACE2 interaction inhibitors, the explained variance was 99.7% utilizing five factors, which is higher than the values observed in the models for investigating r3CL^{pro} inhibition (81% with six factors) and rPL^{pro} inhibition (85% with four factors). Similar trends were observed in terms of accuracy and reproducibility parameters: R2/Q2 values of 0.95/0.91, 0.77/0.65, and 0.85/0.74 for Spike:ACE2, r3CL^{pro}, and rPL^{pro}, respectively (Supplementary Figures S1–S3). In all cases, the Root Mean Square Error of Calibration (RMSEC) was below 0.2, and the Root Mean Square Error of Cross-Validation (RMSECV) was under 0.3. These parameters collectively indicate a robust fit for the constructed models.

In the investigation of potential inhibitors for the Spike:ACE2 interaction (Supplementary Figure S1), ten ions with contributions exceeding 0.1 (loadings weights) were identified: m/z 996.4, 911.5, 841.3, 826.6, 741.6, 661.4, 453.4, 445.1, 439.4, and 431.1. In the other models, ten and seven ions were found with the same contribution threshold: m/z 841.3, 661.4, 611.1, 555.0, 453.4, 445.1, 439.4, 431.1, 341.3, and 271.1 for r3CL^{pro} (Supplementary Figure S2) and m/z 841.3, 661.4, 457.4, 453.4, 445.1, 439.4, and 431.1, for rPL^{pro} (Supplementary Figure S3). When examining the one-target models that were created, it becomes evident that there are certain ions displaying contributions exceeding the established threshold, and some ions are similar across all three evaluated targets. As a result, the decision was made to develop a fourth model, a multitarget model. This choice was based on the premise that molecules capable of affecting more than one target hold greater promise in the quest for compounds with anti-SARS-CoV-2 potential. To construct this model, the same data matrix and normalization techniques employed in the one-target models were used, with the sole distinction lying in the assessed response. The response (Y) for this model was formulated following this logic: samples exibiting activity in all three targets were categorized as multitarget active (1, Active), whereas samples demonstrating activity in only one or two targets were designated as one-target active (−1, Non-active) (Figure 2A,B).

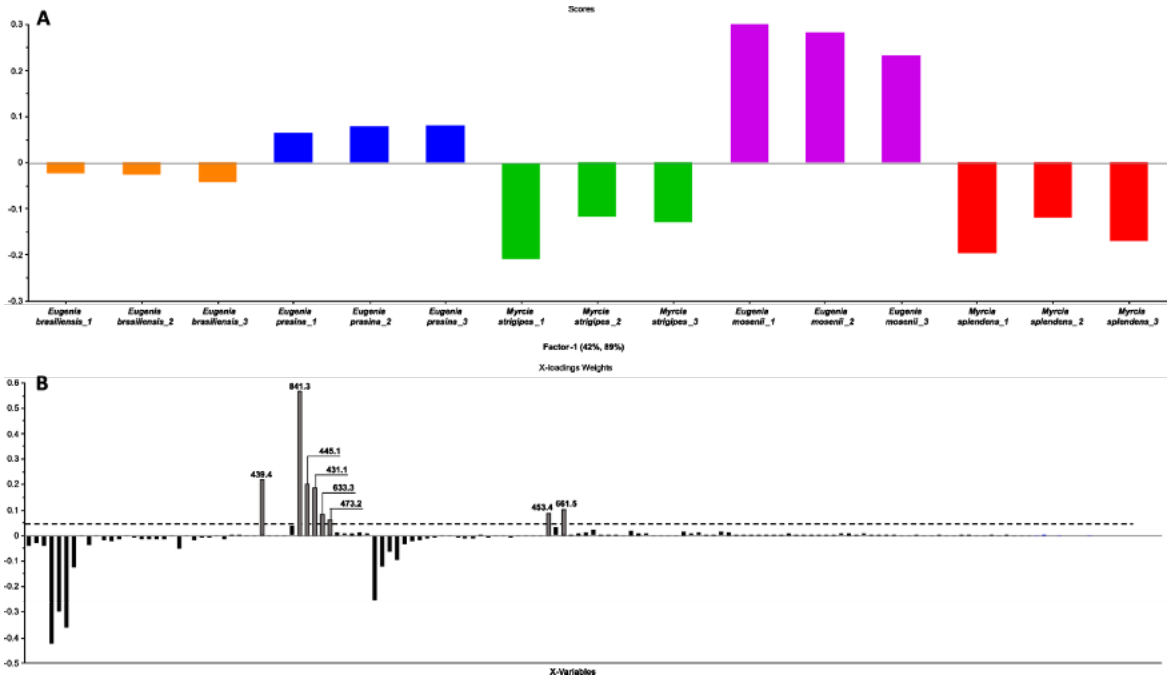

Figure 2. Scores (**A**), X-loadings weight (**B**) for the PLS model based on the LC-MS data obtained in the electrospray ionization in negative mode of the 15 samples of five species of Myrtaceae family, and the inhibition values of the extracts on the RBD:ACE2 interaction and the activity of the r3CL^{pro} and rPL^{pro} enzymes of SARS-CoV-2. The dashed line indicates the cutoff for contributions exceeding 0.05 (loadings weights).

The multitarget PLS model achieved an explained variance of 98.1% during calibration, employing seven factors and 96.9% during internal validation. The model presented an R^2 of 0.98 and a Q^2 of 0.96, indicating a reliable fit. Additionally, it had low RMSE values, with RMSECV (validation error) at 0.15, higher than RMSEC (calibration error) at 0.11. An expected RMSECV > RMSEC relationship confirmed the representativeness of the calibration data and the absence of overfitting in the model.

In the score plot of the PLS model (Figure 2A), the separation between the two distinct groups is evident (active and non-active). The X-loadings weights plot (Figure 2B) reveals the ions that make the most positive contribution in explaining the desired activity, specifi- cally, ions that are found exclusively and/or in greater abundance in extracts with higher activity. This process identified eight ions with m/z values of $[M - H]^-$ 431.1, 439.4, 445.1, 453.4, 473.2, 633.3, 661.5, and 841.3.

2.4. Annotated Compounds for the Predicted Ions in the Multitarget Model Using Molecular Networking Analyses

Molecular networks are now widely used in the natural products chemistry area since the creation of the open-source Global Natural Products Social Molecular Networking (GNPS) online platform [25]. This tool allows the visualization of tandem mass spectrome- try data (MS^2) to highlight structural similarities between metabolites of complex matrices and to help in the annotation of the detected metabolites [26].

The clusters formed can be considered "molecular families" since the compounds should share key chemical characteristics for the node's connection. The predicted ions in the chemometric analysis formed a network whose compounds did not match the GNPS library search. However, through this concept of molecular networks, they could belong to the same class of compounds. The ions that most contribute to the anti-SARS-CoV-2 activity were grouped into Network 1 (Figure 3).

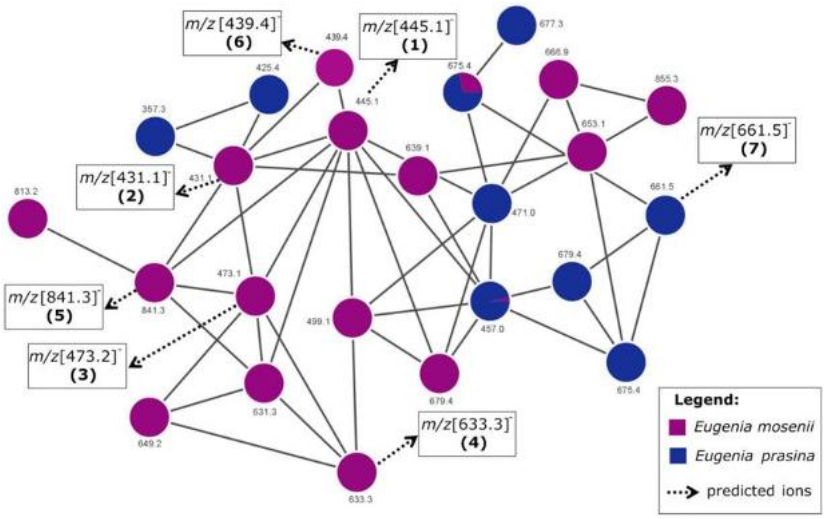

Figure 3. Network 1 showing the oligomeric acylphloroglucinols type compounds, ions that most contribute to the anti-SARS-CoV-2 activity.

The molecular networks 1 and 2 (Figure 3 and Supplementary Figure S4) display the nodes of the predicted ions with *m/z* [445.1]⁻ (**1**), *m/z* [431.1]⁻ (**2**), *m/z* [473.2]⁻ (**3**), *m/z* [633.3]⁻ (**4**), *m/z* [841.3]⁻ (**5**), *m/z* [439.4]⁻ (**6**), *m/z* [661.5]⁻ (**7**), and *m/z* [453.4]⁻ (**8**). It is interesting to note that these ions were more prevalent in *E. mosenii*, which was the most active and multitarget species among the analyzed anti-SARS-CoV-2 targets. However, the species *E. prasina* also presents compounds contained in Networks 1 and 2, which could partially explain the separation of these two species from the others as being the most active in the multitarget PLS model (Figure 2).

The parent masses and MS^2 fragments of these compounds strongly suggest they are myrtucommulones, a class of oligomeric acylphloroglucinols commonly found in the Myrtaceae species (Figure 4). These compounds have attracted the attention due to their diverse molecular architectures that, in general, are composed of an acylphloroglucinol nucleus attached to one or more syncarpic acid residues via an *iso*-butyl or *iso*-pentyl bridge(s) [2,17].

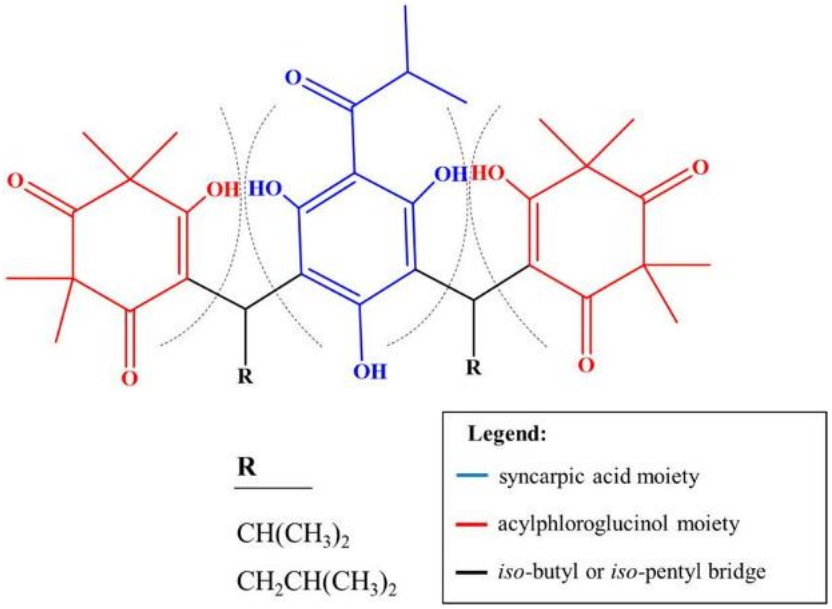

Figure 4. General structure of myrtucommulones and related acylphloroglucinols. Dashed lines denote characteristic fragmentation patterns observed in LC-ESI(-)MS/MS (adapted from [2]).

Assignments were made based on the presence of characteristic ions from the portions of syncarpic acid and acylphloroglucinol, resulting from the cleavage of these molecules on both sides of the iso-butyl or iso-pentyl bridge (Figure 4 and Table 3). This mechanism was previously described for β-triketone heterodimers linked by an iso-pentyl moiety found in the acetonitrile extract of *Eucalyptus gregsoniana*, a species from the Myrtaceae family [27]. Of the eight predicted ions, two compounds were annotated based on previously described fragmentation patterns [17], and three were proposed as undescribed compounds (Table 3). The remaining ions m/z [439.4]$^-$ and m/z [661.5]$^-$ have the same fragmentation pattern and are present in Network 1 of the myrtucommulone class (Figure 3). The ion at m/z of [453.4]$^-$ exhibits a comparable fragmentation pattern and is found within Network 2 of other acylphloroglucinol derivatives. It displays the mass corresponding to the acylphloroglucinol monomer in the MS/MS spectrum (Supplementary Figure S4).

Table 3. LC-MS/MS data of annotated and proposed compounds (undescribed) in the molecular network (MS/MS spectra in Supplementary Figures S5–S9).

Compound	Rt (min)	Molecular Formula	[M − H]$^-$ (*m*/*z*)	MS/MS (MS^2)	Proposed/Annotated Compound	Relative Content (%)	Ref.
Network 1							
1	21.86	$C_{25}H_{34}O_7$	445.1	235, 209, 181	semimyrtucommulone	*E. mosenii* (6.2)	[17,28]
2	23.78	$C_{24}H_{32}O_7$	431.1	221, 209, 165, 151	*nor*-semimyrtucommulone	*E. mosenii* (7.9)	[17,29]
3	25.24	$C_{27}H_{38}O_7$	473.2	263, 209, 151	undescribed	*E. mosenii* (4.2)	-
4	27.76	$C_{36}H_{42}O_1$	633.3	423, 219, 205, 209, 165	undescribed	*E. mosenii* (0.9)	-
5	28.54	$C_{47}H_{54}O_1$	841.3	631, 577, 421, 367	undescribed	*E. mosenii* (26)	-

Compounds **1** (semimyrtucommulone) and **2** (*nor*-semimyrtucommulone) were previously described in *Myrtus communis* and have acylphloglucinol and syncarpic acid residues linked by an iso-butyl bridge [17], as well as compound 3, not yet reported in the literature. These structures are classified as dimeric type myrtucommulones [2].

The fragmentations follow the aforementioned patterns (Figure 5), which means that cleavage on one side of the iso-butyl bridge creates the pairs of fragments at m/z [209]$^-$ and m/z [235]$^-$ for compound **1**, m/z [209]$^-$, m/z [221]$^-$ for compound **2**, and m/z [209]$^-$ and m/z [263]$^-$ for compound **3**. The ion at m/z [209]$^-$ is characteristic of the acylphloroglucinol residue [2]. The subsequent cleavage on the other side of the iso-butyl bridge generates the fragments at m/z [181]$^-$, m/z [165]$^-$, and m/z [209]$^-$ for compounds **1**, **2**, and **3**, respectively. These ions are characteristic of the syncarpic acid residue (Supplementary Figures S5–S7).

Compounds **4** and **5** present the same fragmentation pattern but are characteristic of trimeric and tetrameric molecules, respectively, meaning that they contain more than two residues of acylphloroglucinol and/or syncarpic acid (Figure 5, Supplementary Figures S8 and S9). Similarly to compounds **3**, **4** and **5**, several unknown compounds with a similar fragmentation pattern were observed in Network 1, suggesting that new compounds of this class may be present in *E. mosenii* and *E. prasina*.

Phloroglucinols and their derivatives, in particular myrtucommulones, display diverse molecular architectures and a wide range of biological profiles, such as antimicrobial, antiviral, anti-inflammatory, antiproliferative, and cytotoxic properties [2].

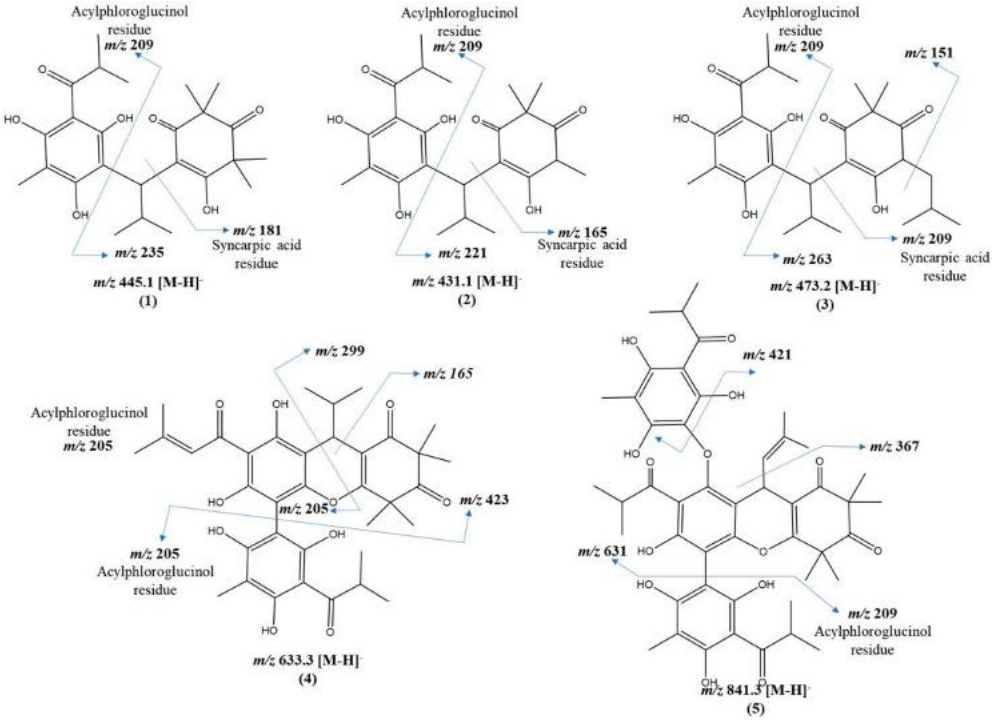

Figure 5. Structure and proposed fragmentation of annotated compounds (**1**–**5**). Compounds **1** and **2** (semimyrtucommulone and *nor*-semi myrtucommulone, respectively) were isolated as racemic mixtures [28,29].

The antiviral activity of the hydroalcoholic leaf extracts of *Myrtus communis* L. was investigated by Moradi et al. [19] against herpes simplex virus-1 (HSV-1), who observed an inhibitory effect on the virus both before and after entering the cell. In the review study conducted by Nicoletti et al. [17], myrtucommulones extracted from species of the genus *Kunzea* and *Melaleuca* also showed moderate effects against HSV-1.

Myrtucommulones and related acylphloroglucinols from Myrtaceae were evaluated for their *in vitro* activity against the respiratory syncytial virus (RSV), showing promising effects compared with the ribavirin control. Studies suggested that the antiviral activ- ity of these compounds might be influenced by the side chains of the phloroglucinol moiety [20,21]. Phloroglucinols have also been shown to be effective against other viruses, such as human immunodeficiency virus (HIV), herpes or enterovirus, and preliminary docking analysis data suggest that they can be effective against SARS-CoV-2 [22]. In addi- tion, macrocarpals A-E (phloroglucinol dialdehyde diterpene derivatives) were isolated from *Eucalyptus globulus* Labill. (Myrtaceae) showed pronounced anti-HIV activity [2].

Liquid chromatography coupled with tandem mass spectrometry (UHPLC-MS/MS) analysis of the five Myrtaceae ethanol extracts showed chemical differences in their profiles (Figure 6), evidencing the more significant presence of myrtucommulones in the multitarget extracts (*E. prasina* and *E. mosenii*). Through the Feature Based Molec- ular Network (FBMN) workflow, other molecular networks were constructed (Supple- mentary Figure S4). For the unpredicted ions, there was a match in the GNPS library for 2′,6′-dihydroxy-4′-methoxydihydrochalcone (m/z 271.1 $[M - H]^-$) in *E. brasiliensis* (Supplementary Figure S10) [30] and myricitrin for *E. prasina* [31], as well as the presence of quinic and ellagic acids for *M. splendens* [32], confirmed by their fragmentation profiles. In addition, *M. splendens* and *M. strigipes* show chemical similarities in the range of 24 to 28 min, with evidence of the presence of tannins already reported in the literature for species of the Myrtaceae family [32].

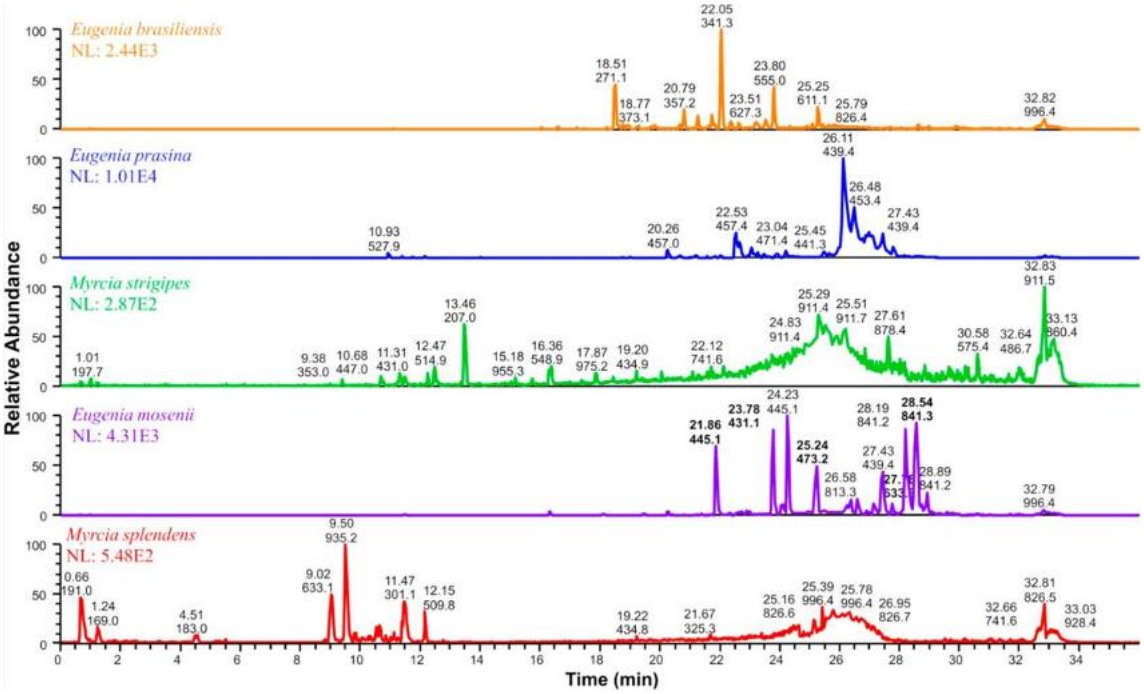

Figure 6. Aligned chromatograms of Myrtaceae ethanol extracts by UHPLC-ESI(-)3D-IT-MS/MS highlighting the predicted ions.

The recognition that Myrtaceae extracts act as blockers of the ACE2:RBD interaction in Vero E6/ACE2 cells infected with Spike-pseudotyped VSV and as inhibitors of the SARS-CoV-2 r3CLpro and rPLpro proteolytic activities led us to investigate the Myrtaceae extracts as inhibitors of the SARS-CoV-2 replication in infected Calu-3 cells, a model of human lung epithelial cells (human pneumocytes type II model).

2.5. Myrtaceae Extracts Inhibit SARS-CoV-2 Replication in Infected Lung Cells

Despite Vero E6 cells being recognized as an important lineage for SARS-CoV-2 replication [33], they may not adequately mimic the infection event in human cells [34,35]. Therefore, in a second phase, we conducted experimental assays with the human pneumocyte lineage, widely recognized as the most effective model for *in vitro* infection and screening of anti-coronavirus drugs due to its high permissibility to SARS-CoV-2 through a transmembrane serine protease 2 (TMPRSS2)-dependent mechanism viral entry [36–38].

Firstly, Calu-3 cells were infected at a multiplicity of infection (MOI) of 0.01, and the extracts were evaluated for their antiviral activity at a single concentration (50 μg·mL^{-1}) for 24 h of treatment, aiming to select the plant species with the best antiviral performance. However, the data indicated that all extracts exhibited high potential as inhibitors of SARS-CoV-2 replication, reducing viral infection by more than 80% (Figure 7).

Based on the initial screening, we further investigated whether the anti-SARS-CoV-2 activity of the studied species would remain effective in Calu-3 cells that were infected and exposed to different extract concentrations (curve: 0.781, 1.563, 3.125, 6.25, 12.5, 25, 50, and 100 μg·mL^{-1}) for 24 h. *In vitro* analysis demonstrated that the five Myrtaceae extracts were able to inhibit approximately 100% of SARS-CoV-2 replication when treated with a high tested concentration (100 μg·mL^{-1}). Remarkably, it was observed that the high antiviral effect was maintained in treatments until 12.5 μg·mL^{-1} (100–60%) (Figure 8). We highlight that all extracts presented lower EC_{50} values in Calu-3 cells, with a concentration below 8.15 μg·mL^{-1} (Table 4). These data indicate that the concentration required to obtain 50% of maximum inhibition in SARS-CoV-2-Calu-3 cells is lower than in VSV-Vero E6/ACE2 cells.

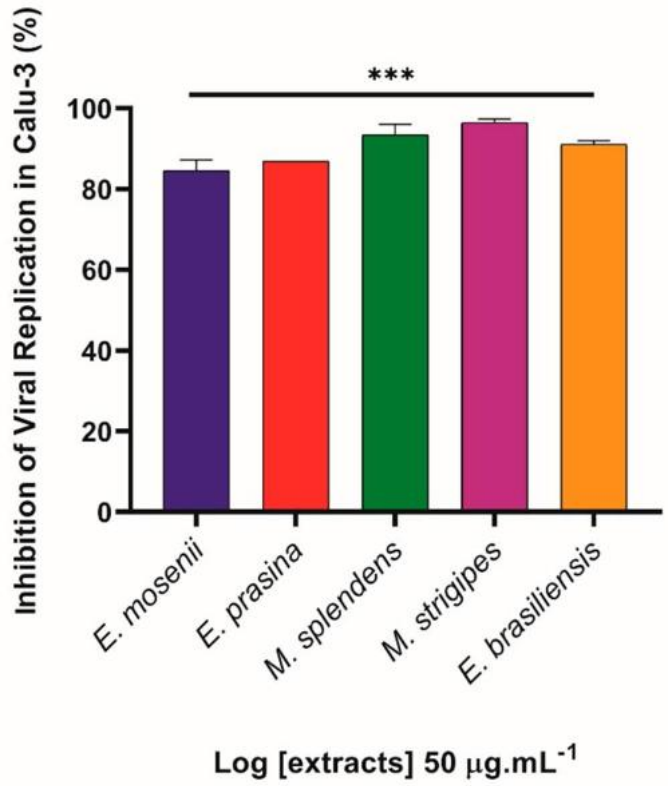

Figure 7. Myrtaceae extracts inhibit virus replication in Calu-3 cells. Infected cells with SARS-CoV-2 at MOI (multiplicity of infection) 0.01 were treated with five different plant extracts at 50 μg·mL^{-1} for 24 h at 37 °C and 5% CO_2. After this period, the supernatants were harvested, and the virus titles were accessed by plaque-forming units (PFU/mL) assay. The percentage of inhibition was obtained by comparison with the infected/untreated group. *** $p \leq 0.001$ in relation to infected control (n = 4).

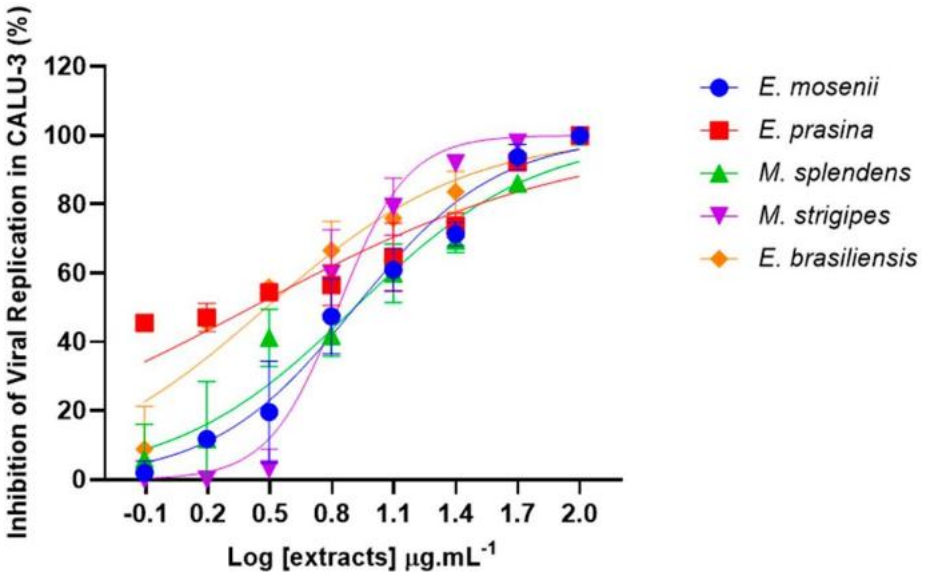

Figure 8. Effect of Myrtaceae species on the SARS-CoV-2 replication in Calu-3 cells. Calu-3 infected with SARS-CoV-2 (MOI: 0.01) for 1 h were treated with different concentrations (0.781, 1.563, 3.125, 6.25, 12.5, 25, 50, and 100 μg·mL^{-1}) of the extracts at 37 °C and 5% CO_2. The supernatants were harvested 24 h after infection for virus titration by a plaque-forming units (PFU/mL) assay. The percentage of inhibition was obtained by a comparison with infected/untreated cells and infected/treated cells. R^2 values ranged from 0.77 to 0.97 (n = 4).

Table 4. Myrtaceae extract EC_{50} values.

	E. mosenii	*E. prasina*	*M. splendens*	*M. strigipes*	*E. brasiliensis*
EC_{50} ($\mu g \cdot mL^{-1}$)	8.14 ± 0.6	2.57 ± 0.5	8.15 ± 0.7	6.75 ± 0.4	3.03 ± 0.3

Considering that the extracts were toxic to Vero E6/ACE2 cells only at concentrations above 500 $\mu g \cdot mL^{-1}$, we aimed to assess the viability of Calu-3, non-infected and treated with the intermediate concentration of 200 $\mu g \cdot mL^{-1}$ for 72 h, using the colorimetric assay that detects lactate dehydrogenase (LDH) enzyme. Overall, all five plant species showed only low or moderate cytotoxicity. The results demonstrated that the best cell viability indices were observed in treatments with extracts from *E. prasina* (92%), *E. brasiliensis* (82%), and *E. mosenii* (74%), while *M. strigipes* was responsible for causing the greatest cytotoxic effect in a pulmonary cell model (40%) (Figure 9). The concentration used in cytotoxicity assays was up to 24 times higher than the maximum EC_{50} obtained in antiviral assays. The viability data were obtained in comparison with control cells treated with vehicle (DMSO) in the same proportion.

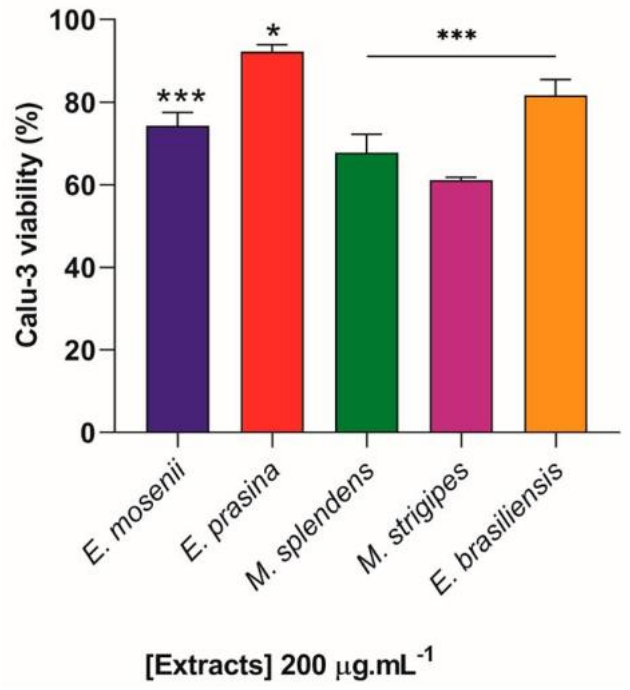

Figure 9. Cytotoxicity of plant extracts in Calu-3 cells. Uninfected cells were exposed to 200 $\mu g \cdot mL^{-1}$ for 72 h at 37 °C, 5% CO_2. Cell viability was determined using the LDH assay. * $p \leq 0.05$ and *** $p \leq 0.001$ in relation to DMSO-exposed cells (control) (n = 4).

Plant extracts and plant-derived secondary metabolites have broad-spectrum antimicrobial activity and can exhibit properties against SARS-CoV-2 replication [5,39–41]. Here, chemometric analyses suggest that myrtucommulones, more prevalent in the multitarget species *E. mosenii* and *E. prasina*, may be the main contributor to the strong inhibitory virus effect exhibited by these extracts. Furthermore, our antiviral assays with Calu-3 cells revealed that other species within this family also demonstrated potent effects against the coronavirus, raising the hypothesis that the action of these biocompounds may occur on other proteases that are also targets of the infection or even that antiviral efficacy may vary in different cell lineages.

Interestingly, studies have revealed that extracts from the species *Scutellaria barbata* D. Don (SBD), belonging to the Lamiaceae family, inhibited the action of the viral proteases

CLpro and TMPRSS2, indicating that SBD blocked the entry of SARS-CoV-2 pseudoparticles into the Calu-3 cells by affecting TMPRSS2 activity [42]. Molecular docking analyses revealed that the bioactive compound gingerol, extracted from *Zingiber officinale* (*Zingiberaceae* family), prevents the entry and fusion of coronavirus by blocking the TMPRSS2 receptor [43,44]. Flavonoids such as kaempferol, luteolin, sulforaphane, quercetin, and cryptotanshinone, found in different plant families, also exhibit inhibitory properties on the same serine protease, in addition to acting as anti-inflammatory agents in the treatment of this respiratory disease [45]. In summary, these findings elucidate the several active compounds found in medicinal plants and open ways for future research that encompasses the mechanisms of action of acylphloroglucinol compounds and their immunomodulatory effects in COVID-19, as well as the role of the Myrtaceae family on other therapeutic targets, such as the transmembrane serine protease 2, required for SARS-CoV-2 invasion into pneumocytes cells.

In view of the promising results obtained from the *in vitro* assays and the prediction studies, we decided to perform molecular docking analyses for compounds **1** to **5** to characterize their behavior at the binding sites (3CL^{pro}, PL^{pro}, and Spike) and to elucidate the existing molecular interactions.

2.6. Docking Analysis and Ligand Interactions of Compounds **1**–**5** *with Spike Protein and ACE2*

2.6.1. Molecular Docking of ACE2 and Spike Protein

The comprehensive molecular docking analysis with the SARS-CoV-2 Spike protein and ACE2 has provided us with a deeper understanding of the potential binding affinities of various ligands. The fitness score, a reflection of binding strength, was used as the primary metric for evaluation.

For interactions with the SARS-CoV-2 Spike protein, the ligand compound **3** (*m*/*z* 473 [M − H]$^-$) had a score of 19.18, while compound **4** (*m*/*z* 633 [M − H]$^-$) achieved 18.24. The ligand compound **5** (*m*/*z* 841 [M − H]$^-$) stood out with a score of 20.20, outperforming the other candidates, which prompted us to focus on its interaction analyses. Meanwhile, *nor*-semimyrtucommulone (**2**) and semimyrtucommulone (**1**) had scores of 14.15 and 19.17, respectively (Table 5).

Table 5. Fitness of top-ranked individuals from GOLD docking.

Ligand Name	ACE2 (Fitness Score)	Spike (Fitness Score)
compound **3** (*m*/*z* 473 [M − H]$^-$)	45.41	19.18
compound **4** (*m*/*z* 633 [M − H]$^-$)	56.37	18.24
compound **5** (*m*/*z* 841 [M − H]$^-$)	67.74	20.2
nor-semimyrtucommulone **2**	42.18	14.15
semimyrtucommulone **1**	44.65	19.17

Turning our attention to ACE2, the ligand compound **3** achieved 45.41, and compound **4** displayed a score of 56.37. Remarkably, compound **5** reached a significant score of 67.74, further emphasizing its potential importance in the interaction landscape. The ligands *nor*-semimyrtucommulone (**2**) and semimyrtucommulone (**1**) showed scores of 42.18 and 44.65, respectively.

Collectively, these scores underline the potential interactions and affinities of the ligands with both the Spike protein and ACE2 (Table 5). Our decision to prioritize the interaction analyses for ligand compound **5** was driven by its superior docking scores, suggesting a promising interaction profile.

2.6.2. Interactions of the Ligand Compound **5** with ACE2

Our investigation into the molecular interactions of ACE2 has unveiled additional specific interactions, emphasizing the complexity of ACE2's molecular associations.

Starting with hydrophobic interactions, the residue 321 PRO displayed an interaction at 3.98 Å. The residue 376 HIS showed an interaction at 3.91 Å. The residue 479 PHE presented a hydrophobic interaction with 3.86 Å. Remarkably, the residue 485 TYR displayed two distinct interactions at distances of 3.39 Å and 3.67 Å, respectively.

In the realm of hydrogen bonds, the residue 322 THR formed a bond with 1.64 Å, an angle of 2.43°, and a dihedral angle of 138.95°, involving atoms 4855 [O3] and 2621 [O3]. The residue 485 TYR demonstrated a bond with 2.67 Å, an angle of 3.28°, and a dihedral angle of 123.42°, connecting atoms 3948 [O3] and 4859 [O3]. Another interesting observation was with residue 489 ARG, which showed two hydrogen bonds: the first with a distance of 3.03 Å, an angle of 3.73°, and a dihedral angle of 129.78° involving atoms 3983 [Ng+] and 4861 [O2]; the second with a distance of 2.00 Å, an angle of 2.96°, and a dihedral angle of 164.71° connecting atoms 3984 [Ng+] and 4861 [O2]. Lastly, the residue 490 TYR established two hydrogen bonds: the first at a distance of 3.19 Å, an angle of 3.77°, and a dihedral angle of 121.26° involving atoms 4862 [O3] and 3996 [O3] and the second with a distance of 2.56 Å, an angle of 3.40°, and a dihedral angle of 150.14° connecting atoms 3996 [O3] and 4853 [O2].

Lastly, our data also highlighted π-cation interactions. Specifically, the residue 489 ARG showcased a π-cation interaction with 4.36 Å and a deviation of 1.98 Å.

2.6.3. Interactions of the Ligand Compound **5** with the Spike Protein

In our in-depth analysis of molecular interactions between the ligand and the SARS- CoV-2 Spike protein, specific interactions have been identified, highlighting the possible intricate association between them.

Amongst the hydrophobic interactions, the Spike protein residue 340 GLU showed an interaction at 3.32 Å. The residue 341 VAL exhibited an interaction at 3.93 Å. The residue 344 ALA displayed a hydrophobic interaction with 3.66 Å. Furthermore, the residue 346A ARG formed an interaction at 3.35 Å. The residue 347 PHE also demonstrated a hydrophobic interaction with 3.48 Å. The residue 354 ASN presented an interaction with 3.57 Å. Impressively, the residue 358 ILE showcased two distinct interactions: the first with 3.86 Å and the second at a shorter distance of 3.04 Å.

Regarding hydrogen bonds, the Spike protein residue 340 GLU formed a bond with 1.57 Å, an angle of 2.53°, and a dihedral angle of 167.25°, involving atoms 58 [O3] and 290 [O.CO2]. The residue 354 ASN established a bond at 2.27 Å, an angle of 3.16°, and a dihedral angle of 149.37°, connecting atoms 407 [Nam] and 49 [O2]. Another significant interaction was observed with the residue 356A LYS displaying a bond distance of 2.29 Å, an angle of 2.73°, and a dihedral angle of 104.76°, involving atoms 428 [N3+] and 48 [O2]. While our comprehensive investigation has elucidated a multitude of interactions between the ligand and both the SARS-CoV-2 Spike protein and ACE2, it is noteworthy to mention that the interactions identified are not among those described in known hotspots. Given the significance of hotspot interactions in biological function and therapeutic targeting, this observation suggests that these proteins may not be the most promising candidates for further molecular dynamic studies. Future work will prioritize ligands and protein targets that exhibit interactions within or near known functional hotspots.

2.7. PL^{pro} and 3CL^{pro} Interaction Analysis and Molecular Dynamics

The docking results for PL^{pro} showed that compound **5** (m/z 841 $[M - H]^-$) had the highest score (69.08), followed by compound **3** (m/z 473 $[M - H]^-$) (61.07), *nor*-semimyrtucommulone (**2**) (49.57), semimyrtucommulone (**1**) (48.71), and compound **4** (m/z 633 $[M - H]^-$) (37.19) respectively.

Chemical interaction predictions between PL^{pro} and the molecules were made. Compound **3** made H-bonds with ASP 164 (1.21 Å) and ARG 166 (1.41 Å). Semimyrtucommulone (1) h-bonds were predicted with ARG 166 (1.60 Å and 2.68 Å) and TYR 264 (1.70 Å). Compound **4** was predicted to do h-bonds with GLU 167 (1.55 Å). Both compound **5** (Figure 10) and nor-semimyrtucommulone (**2**) had no h-bond predicted.

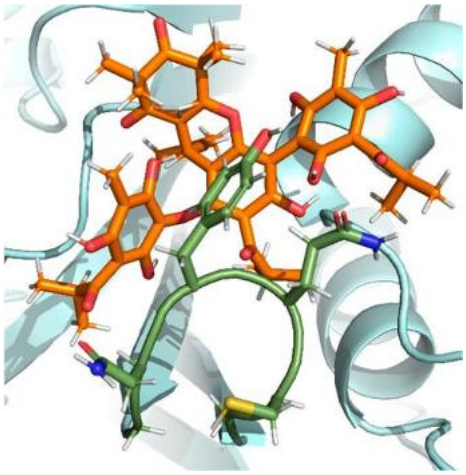

Figure 10. Interaction of the PL^{pro}–compound **5** complex in the BL2loop. The protein is colored in pale cyan, the residues of BL2loop are colored in green (residues G266, N267, Y268, Q269, C270, and G271), and the ligand compound **5** is colored in orange (PDBid: 7JRN).

As seen with PL^{pro}, the docking analyses showed that compound **5** also obtained the highest score with $3CL^{pro}$, equal to 65.01, among the substances analyzed. Compound **4** had the second-best score (59.99), followed by compound 3 (58.43), *nor*-semimyrtucommulone (2) (55.55), and semimyrtucommulone (**1**) (50.14), in that order. The evaluation of the receptor–ligand interaction for compound **5** revealed an H-bond between O7 (Supplementary Figure S11) and CYS145 (2.32 Å), representative of the HIS41-CYS145 catalytic dyad [10]. OH29 from the same position forms an H-bond with ARG188 (2.39 Å), and OH23 forms a bond at 2.52 Å with GLN189, located in the S2 region of the active groove [46].

Considering that $3CL^{pro}$ has a described allosteric binding region between the homodimer chains [10], the possible inhibition of the enzyme at this site was also tested. Again, compound **5** stood out from the other compounds, with a score of 63.61. Figure 11 shows the interaction of compound **5** in the region between the protease chains. A chemical interaction was predicted with OH29 of the ligand (Supplementary Figure S11), which formed a 1.71 Å H-bond with Leu287 of the A chain. The ranking of the other compounds continues with compound **4** leading with a 63.37 score, then semimyrtucommulone (**1**) (56.61), then compound **3** (54.02), and lastly the *nor*-semimyrtucommulone (**2**) (53.41).

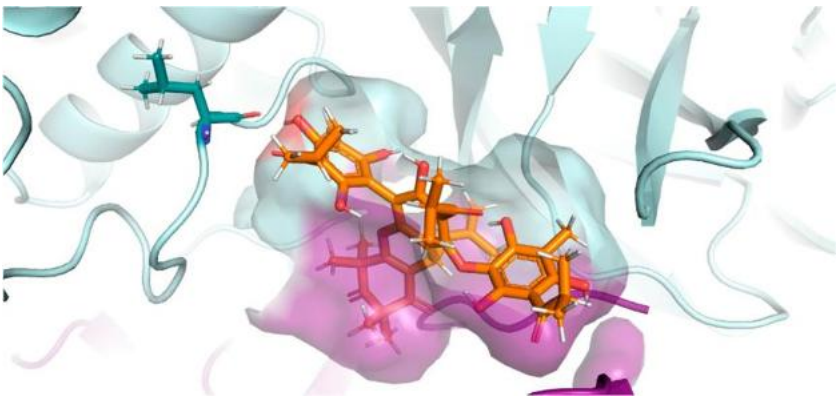

Figure 11. Interaction of the $3CL^{pro}$–compound **5** complex in the allosteric site. The A-chain of the homodimer is colored in grayish green, and the B-chain residues that interacted in the cavity are colored in magenta. A-Leu287 is represented by dark green sticks. Compound **5** is shown in orange within the alternative interaction groove (PDBid: 6XQT).

To further investigate the results obtained, MD were performed, and the results can be viewed in the Supplementary Data (Movies S1–S3). These simulations were used to evaluate the dynamics of the interaction between the PL^{pro}–compound **5** (Movie S1) and $3CL^{pro}$ active site–compound **5** (Movie S2) and $3CL^{pro}$ allosteric groove–compound **5** (Movie S3) complexes. Our results for PL^{pro} showed that in the first 50 nanoseconds of our simulation, we observed that the average number of hydrogen bonds formed between PL^{pro} and compound **5** was typically around 3. However, during certain moments within these nanoseconds, this number increased, reaching up to 7 hydrogen bonds (Figure 12A). After 50 ns, the average became 2 h-bonds formed until the last 10 ns. In this mark, no h-bonds were predicted (Figure 12A). Ligand RMSD has a 3 staged profile, with an average of 1.8 Å during the first 50 ns, 2.5 Å from 50 ns to approximately 175 ns, and in the last of the 25 ns reaching an RMSD higher than 10 Å (Figure 12B). This high RMSD and the lack of predicted h-bonds at the end of the simulation allude to the exit of the ligand from the binding site. This is demonstrated in the RMSD of the BL2loop, which maintains an average of 1.8 Å until approximately 175 ns when the average climbs to approximately 4.5 Å, showing that this region has moved (Figure 12C). The RMSF graph (Figure 12D) shows how the BL2loop residues (residues 266, 267, 268, 269, 270, 271) highly fluctuated during the simulation (approximately 5 Å, with some residues reaching 6 Å).

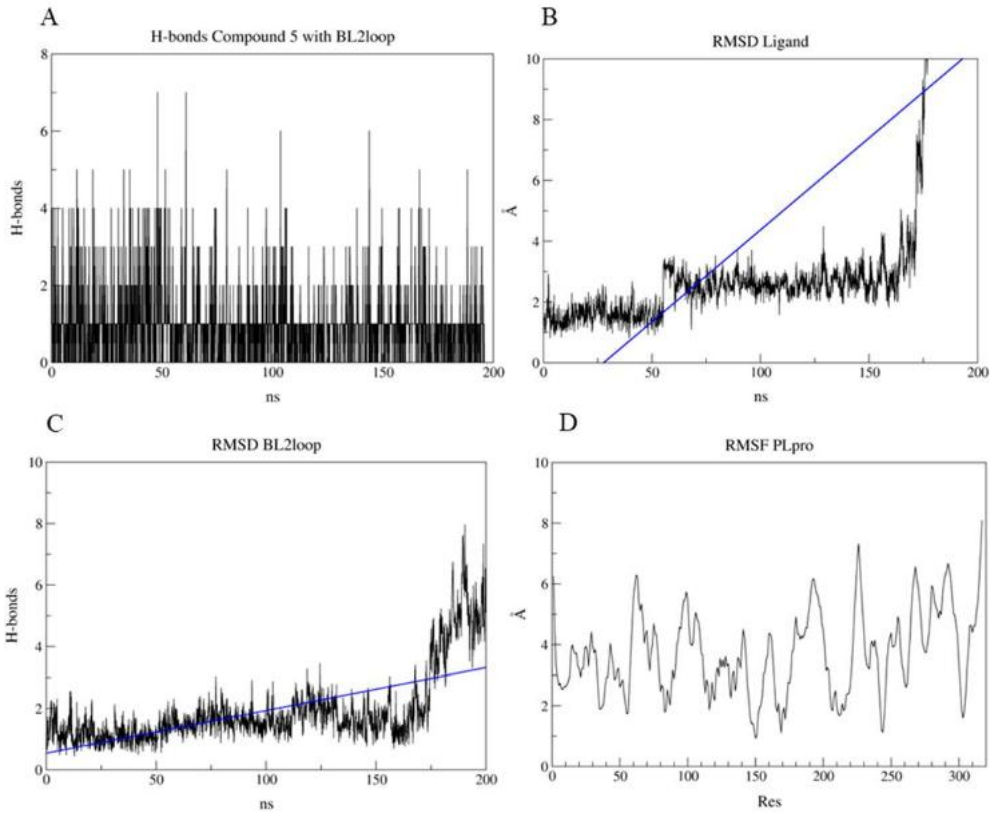

Figure 12. Results of the molecular dynamics of the PL^{pro}–compound **5** complex in 200 ns. (**A**) Predicted h-bonds between the BL2loop residues and compound **5**. (**B**) Calculated RMSD of the ligand compound **5** for the duration of the simulation. (**C**) Calculated RMSD of the BL2loop for the duration of the simulation. (**D**) Calculated RMSF for the residues of the PL^{pro}.

Furthermore, the MD results for complex $3CL^{pro}$–compound **5** targeted to the active site of the protease did not show any hydrogen bonds with residues of interest (HIS41 and CYS145). However, an average of 2 h-bond was reported during the 200 ns of simulation, with greater frequency up to 100 ns (Figure 13A). In this period, the residues with the highest occupancy were GLN189 and ARG188, confirming the result obtained with Maestro. Moreover, the ligand RMSD (Figure 13B) showed instability with a plateau starting at 110 ns,

maintaining an average of 7 Å. This can be justified due to the larger size of the ligand and the fact that the active site of the protease is shallow [47], so when it reaches this plateau there is a smaller area of the ligand that can remain stable in the interaction with the target. In contrast to the instability of the ligand, the catalytic cavity remained relatively stable during the 200 ns (Figure 13C), maintaining a mean RMSD of 1.5 Å. Our results indicate that although the ligand remained partially in the groove, it did not generate stability in the protein, given the increase in ligand RMSD (Figure 13B) and the increase in variability assessed by RMSF. Figure 13D shows high movement in the region formed by the residues of interest (HIS41, CYS145, GLU166, GLN189, and ARG188).

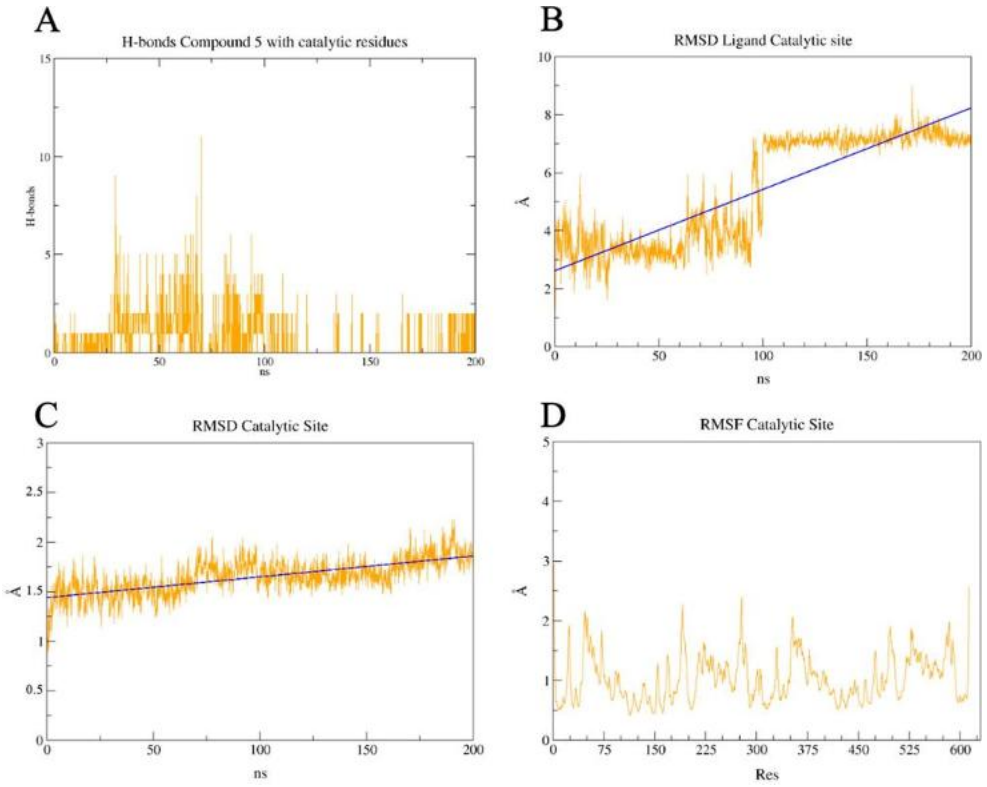

Figure 13. Results of the molecular dynamics of the $3CL^{pro}$-compound 5 complex in 200 ns. (**A**) Predicted h-bonds between compound **5** and the residues CYS145, HIS41, GLU166, ARG188, and GLN189. (**B**) Calculated RMSD of the ligand compound **5** for the duration of the simulation. (**C**) Calculated RMSD of the catalytic site for the duration of the simulation. (**D**) Calculated RMSF for the residues of the $3CL^{pro}$.

The results of the simulation in aqueous solution showed greater stability of the ligand in the allosteric site than when compared to the active site. The compound **5** ligand did not show any h-bond with LEU287. However, GLY170 stood out. A 95% occupancy and an average of 4 h-bonds with GLY170 and compound **5** were predicted over the entire simulated time (Figure 14A). In contrast to the ligand RMSD targeted to the active site, the ligand RMSD in the predicted allosteric pocket showed greater stability (Figure 14B), with an average RMSD of less than 1 Å over the 200 ns. While the cavity was more unstable, the RMSD varied between 0.5 Å and 2.5 Å over 200 ns (Figure 14C). One hypothesis is that this is due to greater perturbation of the residues for the ligand to fit into the cavity. This can also be assessed by the flexibility of the residues in the RMSF plot of the protein (Figure 14D).

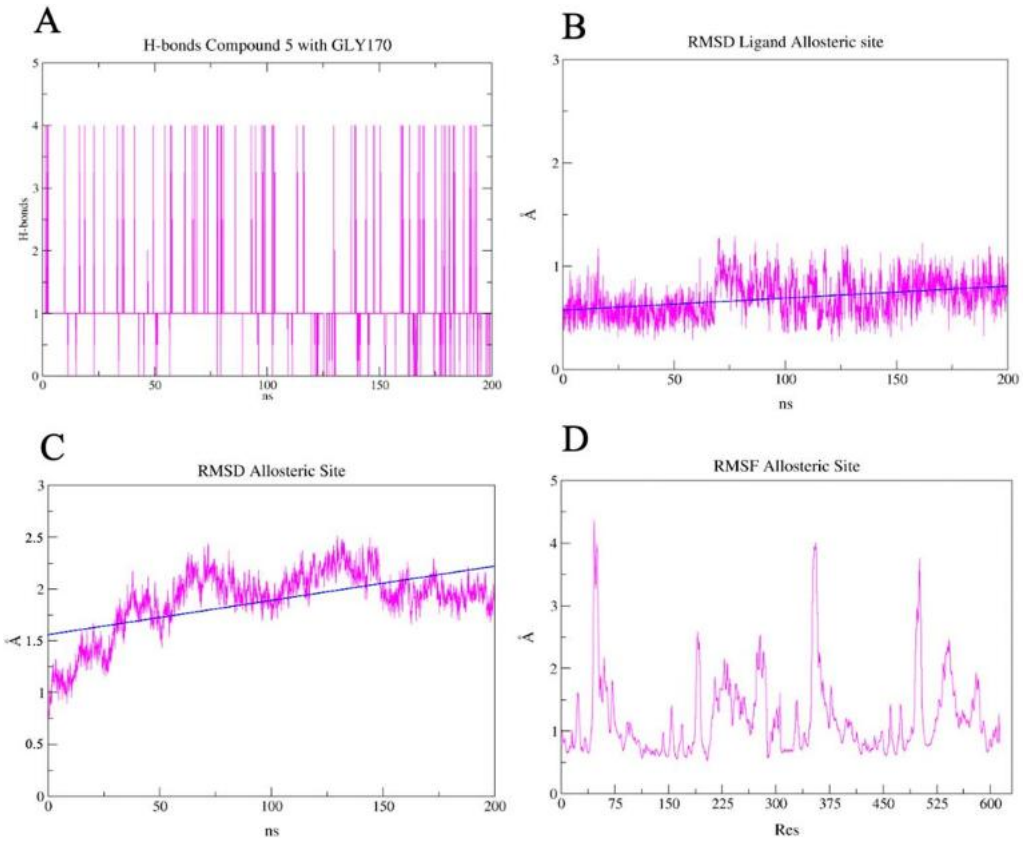

Figure 14. Results of the molecular dynamics of the $3CL^{pro}$-compound **5** complex in 200 ns. (**A** Predicted h-bonds between compound **5** and the residues GLY170. (**B**) Calculated RMSD of the ligand compound **5** for the duration of the simulation. (**C**) Calculated RMSD of the allosteric site for the duration of the simulation. (**D**) Calculated RMSF for the residues of the $3CL^{pro}$.

Moving forward to the analysis of the pharmacokinetic properties, the Lipinski rule of 5 criteria predicts that compound **3**, semimyrtucommulone (**1**), and *nor*-semimyrtucommulone (**2**) are promising drugs. Furthermore, Table 6 shows that their lipophilicity satisfies membrane permeability according to the LogP value. The Caco-2 assessment of the same three compounds indicates satisfactory absorption criteria, which are presented in Supplementary Table S1. While compounds **4** and **5** are metabolized through their properties as inhibitors of cytochromes CYP1A2, CYP2C19, CYP2D6, and CYP3A4.

Table 6. *In silico* prediction of physicochemical properties of compounds **1**–**5**.

Compounds	MW (Da)	nHA	nHD	TPSA (Å)	nRot	LogP
compound **3** (m/z 473 $[M-H]^-$)	474.26	7	3	128.97	7	4.706
compound **4** (m/z 633 $[M-H]^-$)	634.28	10	5	178.66	6	7.036
compound **5** (m/z 841 $[M-H]^-$)	842.35	14	7	245.42	10	8.359
nor-semimyrtucommulone **2**	432.21	7	3	128.97	5	3.845
semimyrtucommulone **1**	446.23	7	3	128.97	5	4.04

MW: Molecular Weight; nHA: number of hydrogen bond acceptors; nHD: number of hydrogen bond donors; TPSA: topological polar surface area; nRot: number of rotatable bonds; LogP: logarithm of the n-octanol/water distribution coefficient.

The high content of Plasma Protein Binding (PPB) restricts the bioavailability of all five compounds. Moreover, all compounds must be capable of crossing the Blood–Brain

Barrier (BBB) (Supplementary Table S1). The tested molecules are expected to cause hepatotoxicity in humans (H-HT) and drug-induced liver injury (DILI). Nevertheless, they do not demonstrate genotoxicity, as concluded by the Ames test. The compounds do not have carcinogenic or respiratory toxicity properties (see Table 7), except for semimyrtucommulone **1**, which shows potential for both. In addition, since the *in silico* prediction indicated the presence of a PAINS warning, it is possible that this higher promiscuity in compounds **4** and **5** can interfere with the *in vitro* testing and, therefore, generate false-positive results.

Table 7. Toxicity prediction. Interpret the colors so that green means the substance is not toxic, yellow means it may be toxic, and red means toxic.

Compounds	H-HT	DILI	AMES	Carc.	R.T.	PAINS
compound **3**						
compound **4**						
compound **5**						
nor-semimyrtucommulone **2**						
semimyrtucommulone **1**						

H-HT: human hepatotoxicity; DILI: drug-induced liver injury; Ames: Ames toxicity; Carc.: carcinogenicity; R.T.: respiratory toxicity; PAINS: pan-assay interference. The green color is the probability of the compound meeting that prediction (values from 0 to 0.3); yellow represents medium probability (values >0.3 to 0.6) and values greater than 0.6 to 1 are represented in red.

In brief, compound **5** shows greater promise in interacting with ACE2-Spike, PL^{pro}, and $3CL^{pro}$ targets of SARS-CoV-2 based on *in silico* analysis. Nonetheless, its physicochemical features suggest that structural modifications to the molecule may be required. Such changes may also enhance the receptor-ligand complex interaction, rendering compound **5** an encouraging multitarget drug candidate.

3. Materials and Methods

3.1. Chemicals, Materials and Plant Extracts

E. brasiliensis (RB00658589/AL1707) and *M. strigipes* (RB01071480/TROVO526) were collected in the Floresta da Tijuca (State of Rio de Janeiro), *E. mosenii* (RB00776077/AL1901) and *M. splendens* (RB00662950/AL1721) were collected in the Parque Nacional de Itatiaia (State of Rio de Janeiro), and *E. prasina* (RB00831331/PARDOC2233) was collected in Parque Nacional da Serra dos Órgãos (PARNASO—State of Rio de Janeiro). The first code in parentheses refers to the voucher specimen number deposited at Jardim Botanico do Rio de Janeiro herbarium, and the second represents the original reference code in the extract bank. The leaves were dried in a ventilated oven and grounded in a hammer mill. Extracts of the leaves were obtained by maceration with ethanol: water (9:1), filtrated, and the solvent removed by rotary evaporation under reduced pressure. These extracts belong to the Federal University of Rio de Janeiro plant extract bank (LABEXTRACT, Centro de Ciências da Saúde, Universidade Federal do Rio de Janeiro). This work was authorized by the Directing Council of Genetic Heritage (Conselho de Gestão do Patrimônio Genético, CGEN) with bioprospecting purposes by the authorization ACADBDD.

3.2. Human Lung Cells Culture

The human lung submucosal gland cells (Calu-3), kindly donated by the Farmanguin- hos RPT11M platform, were cultured and maintained in high-glucose medium—Dulbecco's modified Eagle medium (DMEM, GibcoTM, Waltham, MA, USA) supplemented with 10% fetal bovine serum (FBS, GibcoTM, Waltham, MA, USA), 1% penicillin/streptomycin (GibcoTM, Waltham, MA, USA) and Hepes (GibcoTM, Waltham, MA, USA), and maintained at 37 °C with 5% CO_2 atmosphere. Calu-3 cells were seeded into 96-well plates (1.5×10^4 cells/well; Jet Biofil, Guangzhou, China) and incubated for 120 h in an incubator and then used for cytotoxicity or antiviral assays.

3.3. SARS-CoV-2 Virus

The SARS-CoV-2 B.1 lineage (GenBank#MT710714, SisGen AC58AE2) was maintained in growth in culture flasks (150 cm^2, Jet Biofil, Guangzhou, China) containing semi-confluent Vero E6 cells for 72 h at 37 °C and 5% CO_2. The virus supernatant was collected and stored at −80 °C. In all procedures, the SARS-CoV-2 culture was handled at a biosafety level 3 (BSL3) in the multiuser environment according to World Health Organization (WHO) guidelines [48].

3.4. SARS-CoV-2 RBD:ACE2 Interaction

The commercial kit Lumit™ SARS-CoV-2 Spike RBD:ACE2 immunoassay (Promega, Madison, WI, USA) was used to measure the inhibition of the RBD and ACE2 interaction following the instructions of the manufacturer and as previously described [5]. For this, 1 mg of each sample was separately solubilized in DMSO (dimethyl sulfoxide—Sigma- Aldrich, St. Louis, MO, USA) to a final concentration of 10 $mg{\cdot}mL^{-1}$. The solutions were centrifuged (5804 R—Eppendorf) for 5 min at 2500 RPM, and the supernatants were collected. After the reaction, the resulting bioluminescence was recorded in a SpectraMax M5 (Molecular Devices, San Jose, CA, USA) microplate reader at 500 ms of exposure.

3.5. SARS-CoV-2 Spike-Pseudotyped VSV Neutralization Assay

SARS-CoV-2 Spike pseudotyped virus was constructed using a human vesicular stomatitis virus (VSV) packaging system. The pseudoviruses were produced in HEK293-T cells, carrying the luciferase gene as a reporter. Briefly, cells were transfected with VSV-G plasmid using Lipofectamine 3000 (Invitrogen, Waltham, MA, USA) reagent following the instructions provided by the manufacturer to produce VSV-Luciferase viruses, which were then used to perform the infection in the cells transfected with original SARS-CoV-2 Spike protein expression plasmid.

The neutralization assay using the SARS-CoV-2 Spike-pseudotyped VSV was performed using Vero E6 cells overexpressing ACE2, seeded in flat bottom 96-well plates in a concentration of 5×10^4 per well (ThermoFisher Scientific, Waltham, MA, USA). The viruses were pre-treated with the extracts in different concentrations (25, 50, 125 and 250 $\mu g{\cdot}mL^{-1}$) for 1 h and then added to cells, and the plates were incubated for 24 h at 37 °C and 5% CO_2. After incubation, luciferase substrate was added to cells (ONE-Glo™ Luciferase Assay System, Promega, Madison, WI, USA) following manufacturer instructions, and after 30 min, luminescence was recorded in a SpectraMax M5 (Molecular Devices, San Jose, CA, USA) microplate reader in 1000 ms of exposure.

All the extracts were resuspended in 100% dimethyl sulfoxide (DMSO) for the *in vitro* tests in a proportion not exceeding 1% (*v*/*v*) for the final concentration and not affecting cell growth.

3.6. In Vitro Inhibition of SARS-CoV-2 $3CL^{pro}$ and PL^{pro}

Recombinant SARS-CoV-2 $3CL^{pro}$ and PL^{pro} expressed in *E. coli* BL21(DE3)pLysS and BL21(DE3) cells, respectively, were used in a fluorescent resonance energy transfer (FRET) assay using the peptides DABCYL-AVLQ↓SGFRKE-EDANS as substrate for $3CL^{pro}$ and DABCYL-ALKG↓GKIVE-Glu(EDANS) for PL^{pro}. The $3CL^{pro}$ concentration was fixed at 1.5 μM and the substrate at 50 μM, and the extracts were tested at 100 μM using a high concentration in order to assess the maximum inhibitory effect promoted by each extract. The mixture was incubated in 5 mM NaCl, 20 mM Tris.HCl pH 8.0, and 5 mM DTT for 15 min at 37 °C prior to starting with the substrate. For PL^{pro}, a similar protocol was used, with the exception that the enzyme concentration was fixed at 1 μM and the reaction buffer was 150 mM NaCl and 20 mM Tris.HCl pH 8.0, and 5 mM DTT. The emission fluorescence of EDANS was monitored in the following parameters: λexc = 330 nm and λem = 490 nm at 37 °C for 45 min. Fluorescence data (RFU) were converted into substrate cleavage- specific activity using fluorescent conversion factor (FEC) previously calculated based on the EDANS-DABCYL fluorophore pair. Maximum enzyme activity was considered in the

situation with vehicle (DMSO), and the values were used to calculate the enzyme inhibition by the compounds.

3.7. Cytotoxicity Assays

i. MTT assay: Vero E6 cells (overexpressing ACE2 receptor, ATCC, USA) were culti- vated in DMEM High Glucose (Sigma-Aldrich, St. Louis, MO, USA) supplemented with 10% fetal bovine serum and 1% of the antibiotics penicillin and streptomycin (ThermoFisher Scientific, Waltham, MA, USA). Cells were seeded in 96-well plates (1.5×10^4 cell/well) and incubated with the extracts in different concentrations (6.25 to 500 $\mu g \cdot mL^{-1}$) for 1 h. Then, the viability was measured by adding a 5 mg·mL−1 MTT (3-(4,5-dimethylthiazol-2-yl)-2,5-diphenyltetrazolium bromide) solution (Sigma-Aldrich, St. Louis, MO, USA) in 1× PBS to the cell monolayers for 4 h at 37 °C and 5% CO_2. Then, 100% dimethyl sulfox- ide (DMSO, Sigma-Aldrich, St. Louis, MO, USA) was added, and plates were read in a spectrophotometer at 540 nm.

ii. LDH assay: Calu-3 (1.5×10^4 cells/well) was maintained in a 96-well plate (Jet Biofil, Guangzhou, China) with *E. mosenii*, *E. prasina*, *M. splendens*, *M. strigipes* and *E. brasiliensis*, at a concentration of 200 $\mu g \cdot mL^{-1}$ for 72 h at 37 °C, 5% CO_2. The supernatants were collected to evaluate cell viability using the CytoTox 96® Non-Radioactive colorimetric kit (Promega, Madison, USA) according to the manufacturer's instructions. Lysis solution 1× (Promega, Madison, USA) was used to lyse Calu-3 cells, and purified lactate dehydrogenase (LDH) was used as a positive control. The reaction product was analyzed at 490 nm using a 96-well plate reader (Loccus, São Paulo, Brazil). All the extracts were resuspended in 100% DMSO for the *in vitro* tests. The DMSO final concentrations do not exceed 1% (v/v) in the experiments, thereby not affecting cell growth.

3.8. LC-MS/MS Analysis

Ultra-high-performance liquid chromatography coupled with tandem mass spectrom- etry (UHPLC-MS/MS) analysis was performed using a UHPLC DionexTM UltiMateTM 3000 system, coupled with an LCQ Fleet (ThermoFisher Scientific, Waltham, MA, USA) consisting of an oven, a solvent degasser, an ultra-high-pressure pump, an autosampler, a diode array detector, and a column temperature manager. An ACQUITY UPLC® BEH C18 reversed-phase column (2.1 × 100 mm, 1.7 µm, Waters, Milford, MA, USA) was used at a flow rate of 0.45 $mL \cdot min^{-1}$. The column temperature was kept at 40 °C, and the mobile phases were 0.1% formic acid in water for A and acetonitrile for B. The gradient elution mode was as follows: 5% B in 0–5 min, 5–100% in 5–25 min, 100% in 25–30 min, 100–5% in 30–31 min, and 5% B in 31–36 min.

The mass spectrometer (MS), equipped with an electrospray ionization (ESI) and atmo- spheric pressure chemical ionization (APCI) sources and an ion trap analyzer (with 1.000 of resolution), was operated in positive- and negative-ion modes. High-purity nitrogen (N2) was used as the sheath gas (20 arbitrary units) and auxiliary gas (10 arbitrary units). High-purity helium (He) was used as the collision gas. Full scan data acquisition (mass range: m/z 100–1000) and data-dependent acquisition (topN = 3) were performed. The normalized collision energy of the collision-induced dissociation (CID) cell was set at 35 eV. All analyses were carried out for three different preparation samples of each of the five species of the Myrtaceae family.

3.9. Data Processing, Statistical Analysis and Molecular Networking

Graphs of biological data were generated using the GraphPad Prism 8.0 software. The results RBD:ACE2 interaction and $r3CL^{pro}$ and rPL^{pro} inhibition were determined using linear regression. For SARS-CoV-2 Spike-pseudotyped VSV neutralization assay, the EC_{50} values were determined with the nonlinear regression of log (inhibitor) vs. normalized response. Values correspond to the best curve generated based on R^2 values ≥ 0.9. All experiments were realized with three technical replicates.

The data obtained from LC-MS analyses were converted to the mzML format using the parameters: subset, msLevel 1-2 and polarity positive or negative, as well as Peak Picking, vendor algorithm (msLevel 1-2) in the Proteowizard—MSconvert version 3.02 tool. Then, the data were processed in MZmine v.2.53. The mass detection varied according to the intensity and quality of the signals obtained in each analysis method (ESI or APCI [+/−]). The mass chromatogram construction and wavelet deconvolution were carried out using the ADAP Chromatogram Builder algorithm. Isotopes were eliminated through the Isotopic Peaks Grouper, with the most intense isotope selected as the representative, and alignment was performed using the join aligner. The table list was saved to an ASCII text file.

Process chemical data and biological data were then exported to UnscramblerX software version 10.4. The study aimed to predict potential active compounds inhibiting Spike:ACE2 interaction and proteolytic activities of r3CLpro and rPLpro. Fifteen ethanol extracts from Myrtaceae family species underwent LC-MS/MS analysis in positive and negative modes. Chemometric analyses were performed, and a Partial Least Squares Regression model correlated LC-MS data with inhibitory activities. The PLS regression identified sample patterns, classifying them into two groups based on average activity values: active (≥50% inhibition) and non-active (<50% inhibition) samples.

The MZmine results were uploaded to the open-source Global Natural Products Social (GNPS) online platform, along with the open-source converted files (.mzML) and metadata table. These files were used to build the molecular networks and to dereplicate the present compounds. Along with GNPS annotation, a custom database was also used. The parameters used were those recommended in the GNPS documentation for unity resolution data. The GNPS-generated data were downloaded and processed in Cytoscape 3.9.1 to obtain the results of the molecular networking analysis.

3.10. Anti-SARS-CoV-2 Assay in Calu-3 Cells

Monolayers of Calu-3 cells were infected with SARS-CoV-2 at a multiplicity of infection (MOI) of 0.01 for 1 h at 37 °C and 5% CO_2. The supernatants were removed, and the cells were treated with a concentration curve (0.781, 1.563, 3.125, 6.25, 12.5, 25, 50 and 100 $\mu g \cdot mL^{-1}$) of Myrtaceae extracts for 24 h. Then, the supernatant was collected and used for the virus titration assay. The concentration of the extract required to obtain 50% of maximum effective virus inhibition (EC_{50}) was assessed compared with control cells (infected and untreated cells) [49,50].

3.11. Virus Titration

A semiconfluent culture of Vero E6 cells (1×10^4 cells/well) in 96-well plates (Jet Biofil, Guangzhou, China) was infected with serial dilutions (1:200–1:25,600) of supernatants containing SARS-CoV-2 for 1 h at 37 °C and 5% CO_2. After that, fresh semisolid medium containing 2.4% carboxymethylcellulose (CMC [DMEM-High glucose 10×, 2.4% carboxymethylcellulose, 2% FBS, 1% penicillin and streptomycin, and 4.4% sodium bicarbonate]) was added, and the culture was maintained in an incubator for 72 h. Then, cells were fixed with 4% formalin for 3 h at room temperature and stained with 0.04% crystal violet for 1 h [50]. For the titration control, uninfected cells followed the same steps described above. The virus titers were determined by plaque-forming unit assay (PFU/mL).

3.12. Statistical Analysis

Cytotoxicity and antiviral assays on Calu-3 cells were performed with four technical replicates per assay. The generated data were analyzed using GraphPad Prism 10.0 software (GraphPad Software, La Jolla, CA, USA). Differences between the compounds were analyzed using one-way ANOVA with post-testing of Dunnett, and the EC_{50} values were determined using nonlinear regression of Log(inhibitor) vs. normalized response. The equations used to fit the best curve were generated based on R^2 values 0.81 to 0.92.

3.13. Assessment of Pharmacokinetic Characteristics

ADMETlab 2.0 [51] was used to predict the following: pharmacokinetic properties of the molecules of molecular weight (MW), number of hydrogen bond acceptors (nHA), number of hydrogen bond donors (nHD), number of rotatable bonds (nRot), topological polar surface area (TPSA), logarithm of the n-octanol/water distribution coefficient (LogP), pan assay interference compounds (PAINS), prediction of intestinal cellular absorption (Caco-2 permeability), substrate capability prediction (Pgp-sub) or inhibitor (Pgp-inh) of P-glycoprotein, human intestinal absorption (HIA), penetration of blood–brain barrier (BBB), fraction unbound in plasms (Fu), prediction if the molecules were substrate or inhibitors of isozymes CYP, human hepatotoxicity (H-HT), drug-induced liver injury (DILI), Ames test for mutagenicity, carcinogenicity, and respiratory toxicity.

3.14. Molecular Docking Analysis

Docking between SARS-CoV-2's viral proteins—PL^{pro} (Pdbid: 7JRN), $3CL^{pro}$ homodimer (Pdbid: 6XQT), Spike's Receptor Binding Domain (RBD) [52] portion and Angiotensin-converting enzyme 2 (ACE2) (PDBid: 7A97)—and the substances semimyrtucommulone, *nor*-semimyrtucommulone, compound **3** (m/z 473 $[M - H]^-$), compound **4** (m/z 633 $[M - H]^-$) and compound **5** (m/z 841 $[M - H]^-$) was performed using GOLD suite with GoldScore score function.

For PL^{pro}, the binding site was defined with a centre in the coordinates of the original ligand GRL0617 present in the crystal with radius of 10 Å. The radius simulation for $3CL^{pro}$ was established with 10 Å from HIS 41 in target docking and 35 Å for blind docking, which in the last case, includes the union of the two chains. For the RBD, a blind docking was realized, with the simulation radius of 70 Å with centre in LEU 455. Finally, docking with ACE2 followed the same methodology described for Spike. However, in the latter case, the radius of 80 A was determined from GLN598 establishing the simulation region.

The interaction analysis between amino acid residues and substances was performed using Maestro (Schrödinger Release 2023-3: Maestro, Schrödinger, LLC, New York, NY, USA, 2023) and Protein-Ligand Interaction Profiler.

3.15. Molecular Dynamics

Molecular Dynamics (MD) was performed using the AMBER 2022 and AmberTools-2022 [53] software packages. For both PL^{pro} (Pdbid: 7JRN) and $3CL^{pro}$ (Pdbid: 6XQT), the protein file was protonated to pH 8.0 using an H++ web server (http://newbiophysics.cs.vt.edu/H++/, accessed on 13 October 2023) [54–56]. Ligand preparation was performed using the Antechamber tool.

The PL^{pro} complex preparation was performed using the MCPB.py tool [57] and GAMESS-US [58] to properly simulate the zinc atom present in the protein and its effects on protein motility.

Force fields used were ff19SB, gaff2, and OPC for waters. Solvation was made in a truncated Octahedron box with a 12.0 Å distance from the box edge. Salt molarity was calculated using the method described by Machado [59] to neutralize the system and be at 0.15 M.

Relaxation was made with 1000 cycles of Steepest descent. Temperature was set to 310 K. Final simulations were for 200 ns with MonteCarlo Barostat. SHAKE was used for restraining hydrogen bonds. Time step was defined to 0.001.

4. Conclusions

The study's findings indicate that among the five Myrtaceae species examined, two (*E. prasina* and *E. mosenii*) demonstrated noteworthy potential as multitarget agents against SARS-CoV-2 targets (Spike:ACE2, PLpro, and 3CLpro). Moreover, all five species of the Myrtaceae family exhibited high inhibitory capacity against SARS-CoV-2 B.1 lineage replication in the human lung epithelial cells model. Notably, ions identified as myrtucommulones were correlated with the observed activity. In addition, the established workflow employs

molecular network databases and predictive chemometric models through tandem mass spectrometry to accelerate the dereplication of molecules before subsequent compound isolation. This abbreviates the lengthy process of bioprospecting using bio-guided fractionation. The comprehensive investigation seamlessly integrates biological and chemical analyses, significantly advancing our understanding of the antiviral properties of Myrtaceae. This study represents the first documentation of such activity for these compound types, encouraging further isolation efforts and testing on the models employed.

Supplementary Materials: The following supporting information can be downloaded at https://www.mdpi.com/article/10.3390/ph17040436/s1, Figure S1: Scores (A), X-loadings weight (B) for the PLS model based on the LC-MS data obtained in the electrospray ionization in negative mode of the 15 samples of five species of Myrtaceae family, and the inhibition values of the extracts on the RBD:ACE2 interaction of SARS-CoV-2. The dashed line indicates the cutoff for contributions exceeding 0.1 (loadings weights); Figure S2: Scores (A), X-loadings weight (B) for the PLS model based on the LC-MS data obtained in the electrospray ionization in negative mode of the 15 samples of five species of Myrtaceae family, and the inhibition values of the extracts on the activity of the $r3CL^{pro}$ enzyme of SARS-CoV-2. The dashed line indicates the cutoff for contributions exceeding 0.1 (loadings weights); Figure S3: Scores (A), X-loadings weight (B) for the PLS model based on the LC-MS data obtained in the electrospray ionization in negative mode of the 15 samples of five species of Myrtaceae family, and the inhibition values of the extracts on the activity of the rPL^{pro} enzyme of SARS-CoV-2. The dashed line indicates the cutoff for contributions exceeding 0.1 (loadings weights); Figure S4: Feature Based Molecular Network (FBMN) of Myrtaceae extracts; Figure S5: MS/MS spectrum of compound **1** at m/z 445.1 $[M-H]^-$ (semimyrtucommulone); Figure S6: MS/MS spectrum of compound **2** at m/z 431.1 $[M-H]^-$ (*nor*-semimyrtucommulone); Figure S7. MS/MS spectrum of proposed compound **3** at m/z 473.2 $[M-H]^-$; Figure S8. MS/MS spectrum of proposed compound **4** at m/z 633.3 $[M-H]^-$; Figure S9. MS/MS spectrum of proposed compound **5** at m/z 841.3 $[M-H]^-$; Figure S10. Molecular network of chalcone and chalcone- derivative compounds and MS/MS spectrum of m/z 271.1 $[M-H]^-$ (2′6′-dihydroxy-4′-methoxy dihydrochalcone); Figure S11. 2D structure of compound **5** (m/z 841 $[M-H]^-$) with atomic positions; Table S1—Description of the pharmacokinetic properties of the compounds **3**, **4**, **5**, nor-semimyrtucommulone (**2**), and semimyrtucommulone (**1**); Movie S1—Molecular dynamics results of the complex PL^{pro} with compound **5**. The protein structure is shown in gray, the BL2loop is shown in yellow, and compound 5 is shown in blue. The file is available in https://doi.org/10.5281/zenodo.10257486 (accessed on 4 December 2023); Movie S2—Molecular dynamics results of the complex 3CLpro active site with compound 5. The protein structure is shown in gray, and compound 5 is shown in orange. The file is available at https://doi.org/10.5281/zenodo.10257448 (accessed on 4 December 2023); Movie S3—Molecular dynamics results of the complex 3CLpro allosteric groove with compound 5. The protein structure is shown in gray, and the compound 5 is shown in magenta. The file is available at https://doi.org/10.5281/zenodo.10257460 (accessed on 4 December 2023).

Author Contributions: Conceptualization, S.C.M. and B.A.G.; methodology, S.C.M., B.A.G., A.R.T., T.K.F.d.O., A.d.S.R., V.N.d.S.F., J.N.H.L. and M.D.M.; software, S.C.M., B.A.G., M.E.A.E., B.V.A., M.T.S. and C.F.d.A.R.C.; validation, L.J.d.C., M.L.d.S., M.T.S., D.A., G.G.L. and S.G.L.; formal analysis, S.C.M., B.A.G., M.F.C., T.S.d.F., M.E.A.E., B.V.A., C.F.d.A.R.C., L.E.C.C., S.d.S.C. and P.T.C.; investigation, S.C.M., B.A.G., M.F.C., T.S.d.F., M.E.A.E., B.V.A., C.F.d.A.R.C., L.E.C.C., S.d.S.C., P.T.C., A.R.T., T.K.F.d.O., A.d.S.R., V.N.d.S.F. and J.N.H.L.; resources, M.D.M., D.A., G.G.L. and S.G.L.; data curation, S.C.M., B.A.G., M.F.C., P.T.C., T.S.d.F., A.R.T., T.K.F.d.O., A.d.S.R., V.N.d.S.F. and J.N.H.L.; writing—original draft preparation, S.C.M., B.A.G., M.F.C., T.S.d.F., M.E.A.E., B.V.A., C.F.d.A.R.C., L.E.C.C., S.d.S.C., P.T.C., A.R.T., T.K.F.d.O., A.d.S.R., V.N.d.S.F. and J.N.H.L.; writing—review and editing, L.J.d.C., M.L.d.S., M.T.S., M.D.M., D.A., G.G.L. and S.G.L.; visualization, M.F.C., T.S.d.F., M.E.A.E., B.V.A., C.F.d.A.R.C. and L.E.C.C.; supervision, L.J.d.C., M.L.d.S., M.T.S., M.E.A.E., M.D.M., D.A., G.G.L. and S.G.L.; project administration, D.A., G.G.L. and S.G.L.; funding acquisition, M.D.M., D.A., L.J.d.C., G.G.L. and S.G.L. All authors have read and agreed to the published version of the manuscript.

Funding: This work was supported by the Coordenação de Aperfeiçoamento de Pessoal de Nível Superior (CAPES, fellowships), Conselho Nacional de Desenvolvimento Científico e Tecnológico (CNPq—desenvolvimento tecnológico e extensão inovadora 312027/2022-2), Fundação de Am-

paro à Pesquisa do Estado do Rio de Janeiro (FAPERJ—E-26/211.285/2021, E-26/210.683/2021, E-26/201.426/2022, E-26/201.063/22, E-26/203.183/2023), Instituto Oswaldo Cruz (IOC), Fiocruz, FIOTEC (IOC-023-FIO-18-2-58); Programa INOVA Fiocruz (VPPIS-004-FIO-22-2-21).

Institutional Review Board Statement: Not applicable.

Data Availability Statement: Data are contained within the article.

Acknowledgments: The authors are grateful to FAPERJ and CNPq for financial support and CAPES for the PhD scholarships. We would like to thank the Instituto de Biofísica Carlos Chagas Filho and the Central Analítica, Faculdade de Farmácia of the Universidade Federal do Rio de Janeiro for allowing the use of their multiuser facilities. The authors also thank LABEXTRACT for the access to the extract bank. Thanks are due to the Biosafety Level 3 (BSL3) laboratory facility in Pavilhão Leonidas Deane, Instituto Oswaldo Cruz, Fiocruz, RJ; and Andre Sampaio from Farmanguinhos, platform RPT11M, for kindly donating the Calu-3 cells.

Conflicts of Interest: The authors declare no conflicts of interest.

References

1. Wagner, M.D.A.; Bogoni, J.A.; Fiaschi, P. Myrtaceae Richness and Distribution across the Atlantic Forest Domain Are Constrained by Geoclimatic Variables. *Plant Ecol.* **2022**, *223*, 1079–1092. [CrossRef]
2. Celaj, O.; Durán, A.G.; Cennamo, P.; Scognamiglio, M.; Fiorentino, A.; Esposito, A.; D'Abrosca, B. Phloroglucinols from Myrtaceae: Attractive Targets for Structural Characterization, Biological Properties and Synthetic Procedures. *Phytochem. Rev.* **2021**, *20*, 259–299. [CrossRef]
3. Leal, C.M.; Leitão, S.G.; Sausset, R.; Mendonça, S.C.; Nascimento, P.H.A.; De Araujo, R.; Cheohen, C.F.; Esteves, M.E.A.; Leal Da Silva, M.; Gondim, T.S.; et al. Flavonoids from *Siparuna cristata* as Potential Inhibitors of SARS-CoV-2 Replication. *Rev. Bras. Farmacogn.* **2021**, *31*, 658–666. [CrossRef]
4. Cheohen, C.F.D.A.R.; Esteves, M.E.A.; Da Fonseca, T.S.; Leal, C.M.; Assis, F.D.L.F.; Campos, M.F.; Rebelo, R.S.; Allonso, D.; Leitão, G.G.; Da Silva, M.L.; et al. In Silico Screening of Phenylethanoid Glycosides, a Class of Pharmacologically Active Compounds as Natural Inhibitors of SARS-CoV-2 Proteases. *Comput. Struct. Biotechnol. J.* **2023**, *21*, 1461–1472. [CrossRef]
5. Campos, M.F.; Mendonça, S.C.; Peñaloza, E.M.C.; De Oliveira, B.A.C.; Rosa, A.S.; Leitão, G.G.; Tucci, A.R.; Ferreira, V.N.S.; Oliveira, T.K.F.; Miranda, M.D.; et al. Anti-SARS-CoV-2 Activity of *Ampelozizyphus amazonicus* (Saracura-Mirá): Focus on the Modulation of the Spike-ACE2 Interaction by Chemically Characterized Bark Extracts by LC-DAD-APCI-MS/MS. *Molecules* **2023**, *28*, 3159. [CrossRef]
6. Kaul, R.; Paul, P.; Kumar, S.; Büsselberg, D.; Dwivedi, V.D.; Chaari, A. Promising Antiviral Activities of Natural Flavonoids against SARS-CoV-2 Targets: Systematic Review. *Int. J. Mol. Sci.* **2021**, *22*, 11069. [CrossRef]
7. Jackson, C.B.; Farzan, M.; Chen, B.; Choe, H. Mechanisms of SARS-CoV-2 Entry into Cells. *Nat. Rev. Mol. Cell Biol.* **2022**, *23*, 3–20. [CrossRef] [PubMed]
8. Scialo, F.; Daniele, A.; Amato, F.; Pastore, L.; Matera, M.G.; Cazzola, M.; Castaldo, G.; Bianco, A. ACE2: The Major Cell Entry Receptor for SARS-CoV-2. *Lung* **2020**, *198*, 867–877. [CrossRef]
9. Salian, V.S.; Wright, J.A.; Vedell, P.T.; Nair, S.; Li, C.; Kandimalla, M.; Tang, X.; Carmona Porquera, E.M.; Kalari, K.R.; Kandimalla, K.K. COVID-19 Transmission, Current Treatment, and Future Therapeutic Strategies. *Mol. Pharm.* **2021**, *18*, 754–771. [CrossRef]
10. Zhang, L.; Lin, D.; Sun, X.; Curth, U.; Drosten, C.; Sauerhering, L.; Becker, S.; Rox, K.; Hilgenfeld, R. Crystal Structure of SARS-CoV-2 Main Protease Provides a Basis for Design of Improved α-Ketoamide Inhibitors. *Science* **2020**, *368*, 409–412. [CrossRef]
11. Khan, R.J.; Jha, R.K.; Amera, G.M.; Jain, M.; Singh, E.; Pathak, A.; Singh, R.P.; Muthukumaran, J.; Singh, A.K. Targeting SARS-CoV-2: A Systematic Drug Repurposing Approach to Identify Promising Inhibitors against 3C-like Proteinase and 2′-O-Ribose Methyltransferase. *J. Biomol. Struct. Dyn.* **2021**, *39*, 2679–2692. [CrossRef] [PubMed]
12. Bosken, Y.K.; Cholko, T.; Lou, Y.-C.; Wu, K.-P.; Chang, C.A. Insights Into Dynamics of Inhibitor and Ubiquitin-Like Protein Binding in SARS-CoV-2 Papain-Like Protease. *Front. Mol. Biosci.* **2020**, *7*, 174. [CrossRef] [PubMed]
13. Gao, X.; Qin, B.; Chen, P.; Zhu, K.; Hou, P.; Wojdyla, J.A.; Wang, M.; Cui, S. Crystal Structure of SARS-CoV-2 Papain-like Protease. *Acta Pharm. Sin. B* **2021**, *11*, 237–245. [CrossRef] [PubMed]
14. Osipiuk, J.; Azizi, S.-A.; Dvorkin, S.; Endres, M.; Jedrzejczak, R.; Jones, K.A.; Kang, S.; Kathayat, R.S.; Kim, Y.; Lisnyak, V.G.; et al. Structure of Papain-like Protease from SARS-CoV-2 and Its Complexes with Non-Covalent Inhibitors. *Nat. Commun.* **2021**, *12*, 743. [CrossRef] [PubMed]
15. Santos, L.S.; Alves Filho, E.G.; Ribeiro, P.R.V.; Zocolo, G.J.; Silva, S.M.; De Lucena, E.M.P.; Alves, R.E.; De Brito, E.S. Chemotaxonomic Evaluation of Different Species from the Myrtaceae Family by UPLC-qToF/MS-MS Coupled to Supervised Classification Based on Genus. *Biochem. Syst. Ecol.* **2020**, *90*, 104028. [CrossRef]
16. Alipour, G.; Dashti, S.; Hosseinzadeh, H. Review of Pharmacological Effects of *Myrtus communis* L. and Its Active Constituents: *Myrtus communis* L. and Its Active Constituents. *Phytother. Res.* **2014**, *28*, 1125–1136. [CrossRef] [PubMed]

17. Nicoletti, R.; Salvatore, M.; Ferranti, P.; Andolfi, A. Structures and Bioactive Properties of Myrtucommulones and Related Acylphloroglucinols from Myrtaceae. *Molecules* **2018**, *23*, 3370. [CrossRef] [PubMed]
18. Knauthe, A.; Mittag, S.; Bloch, L.; Albring, K.F.; Schmidt, M.; Werz, O.; Huber, O. Hyperforin and Myrtucommulone Derivatives Act as Natural Modulators of Wnt/β-Catenin Signaling in HCT116 Colon Cancer Cells. *Int. J. Mol. Sci.* **2022**, *23*, 2984. [CrossRef]
19. Moradi, M.T.; Karimi, A.; Rafieian, M.; Kheiri, S.; Saedi, M. The Inhibitory Effects of Myrtle (*Myrtus communis*) Extract on Herpes Simplex Virus-1 Replication in Baby Hamster Kidney Cells. *J. Shahrekord Univ. Med. Sci.* **2011**, *12*, 54–61.
20. Chen, M.; Chen, L.-F.; Li, M.-M.; Li, N.-P.; Cao, J.-Q.; Wang, Y.; Li, Y.-L.; Wang, L.; Ye, W.-C. Myrtucomvalones A–C, Three Unusual Triketone–Sesquiterpene Adducts from the Leaves of *Myrtus communis* 'Variegata'. *RSC Adv.* **2017**, *7*, 22735–22740. [CrossRef]
21. Liu, J.; Song, J.-G.; Su, J.-C.; Huang, X.-J.; Ye, W.-C.; Wang, Y. Tomentodione E, a New *Sec*-Pentyl Syncarpic Acid-Based Meroterpenoid from the Leaves of *Rhodomyrtus tomentosa*. *J. Asian Nat. Prod. Res.* **2018**, *20*, 67–74. [CrossRef]
22. Peron, G.; López, A.M.; Cabada-Aquirre, P.; Garay Buenrosto, K.D.; Ostos Mendoza, K.C.; Mahady, G.B.; Seidel, V.; Sytar, O.; Koirala, N.; Gurung, R.; et al. Antiviral and Antibacterial Properties of Phloroglucinols: A Review on Naturally Occurring and (Semi)Synthetic Derivatives with Potential Therapeutic Interest. *Crit. Rev. Biotechnol.* **2023**, *44*, 319–336. [CrossRef]
23. Alves, J.; Engel, L.; De Vasconcelos Cabral, R.; Rodrigues, E.L.; De Jesus Ribeiro, L.; Higa, L.M.; Da Costa Ferreira Júnior, O.; Castiñeiras, T.M.P.P.; De Carvalho Leitão, I.; Tanuri, A.; et al. A Bioluminescent and Homogeneous SARS-CoV-2 Spike RBD and hACE2 Interaction Assay for Antiviral Screening and Monitoring Patient Neutralizing Antibody Levels. *Sci. Rep.* **2021**, *11*, 18428. [CrossRef]
24. Hariono, M.; Rollando, R.; Yoga, I.; Harjono, A.; Suryodanindro, A.; Yanuar, M.; Gonzaga, T.; Parabang, Z.; Hariyono, P.; Febriansah, R.; et al. Bioguided Fractionation of Local Plants against Matrix Metalloproteinase9 and Its Cytotoxicity against Breast Cancer Cell Models: *In Silico* and *In Vitro* Study (Part II). *Molecules* **2021**, *26*, 1464. [CrossRef]
25. Wang, M.; Carver, J.J.; Phelan, V.V.; Sanchez, L.M.; Garg, N.; Peng, Y.; Nguyen, D.D.; Watrous, J.; Kapono, C.A.; Luzzatto-Knaan, T.; et al. Sharing and Community Curation of Mass Spectrometry Data with Global Natural Products Social Molecular Networking. *Nat. Biotechnol.* **2016**, *34*, 828–837. [CrossRef]
26. Afoullouss, S.; Balsam, A.; Allcock, A.L.; Thomas, O.P. Optimization of LC-MS2 Data Acquisition Parameters for Molecular Networking Applied to Marine Natural Products. *Metabolites* **2022**, *12*, 245. [CrossRef]
27. Goodger, J.Q.D.; Seneratne, S.L.; Nicolle, D.; Woodrow, I.E. Foliar Essential Oil Glands of *Eucalyptus* Subgenus *Eucalyptus* (Myrtaceae) Are a Rich Source of Flavonoids and Related Non-Volatile Constituents. *PLoS ONE* **2016**, *11*, e0151432. [CrossRef]
28. Appendino, G.; Bianchi, F.; Minassi, A.; Sterner, O.; Ballero, M.; Gibbons, S. Oligomeric Acylphloroglucinols from Myrtle (*Myrtus communis*). *J. Nat. Prod.* **2002**, *65*, 334–338. [CrossRef]
29. Hans, M.; Charpentier, M.; Huch, V.; Jauch, J.; Bruhn, T.; Bringmann, G.; Quandt, D. Stereoisomeric Composition of Natural Myrtucommulone A. *J. Nat. Prod.* **2015**, *78*, 2381–2389. [CrossRef] [PubMed]
30. Zaki, M.A.; Nanayakkara, N.P.D.; Hetta, M.H.; Jacob, M.R.; Khan, S.I.; Mohammed, R.; Ibrahim, M.A.; Samoylenko, V.; Coleman, C.; Fronczek, F.R.; et al. Bioactive Formylated Flavonoids from *Eugenia rigida*: Isolation, Synthesis, and X-Ray Crystallography. *J. Nat. Prod.* **2016**, *79*, 2341–2349. [CrossRef] [PubMed]
31. de Oliveira, F.M.G.; Romão, W.; Kuster, R.M. Identification of Phenolic Compounds in *Eugenia uniflora* Leaves by FTICR MS in Association with Different Ionization Sources. *Anal. Methods* **2018**, *10*, 1647–1655. [CrossRef]
32. Yoshida, T.; Amakura, Y.; Yoshimura, M. Structural Features and Biological Properties of Ellagitannins in Some Plant Families of the Order Myrtales. *Int. J. Mol. Sci.* **2010**, *11*, 79–106. [CrossRef] [PubMed]
33. Ogando, N.S.; Dalebout, T.J.; Zevenhoven-Dobbe, J.C.; Limpens, R.W.A.L.; Van Der Meer, Y.; Caly, L.; Druce, J.; De Vries, J.J.C.; Kikkert, M.; Bárcena, M.; et al. SARS-Coronavirus-2 Replication in Vero E6 Cells: Replication Kinetics, Rapid Adaptation and Cytopathology. *J. Gen. Virol.* **2020**, *101*, 925–940. [CrossRef]
34. Mellott, D.M.; Tseng, C.-T.; Drelich, A.; Fajtová, P.; Chenna, B.C.; Kostomiris, D.H.; Hsu, J.; Zhu, J.; Taylor, Z.W.; Kocurek, K.I.; et al. A Clinical-Stage Cysteine Protease Inhibitor Blocks SARS-CoV-2 Infection of Human and Monkey Cells. *ACS Chem. Biol.* **2021**, *16*, 642–650. [CrossRef]
35. Mautner, L.; Hoyos, M.; Dangel, A.; Berger, C.; Ehrhardt, A.; Baiker, A. Replication Kinetics and Infectivity of SARS-CoV-2 Variants of Concern in Common Cell Culture Models. *Virol. J.* **2022**, *19*, 76. [CrossRef]
36. White, J.M.; Schiffer, J.T.; Bender Ignacio, R.A.; Xu, S.; Kainov, D.; Ianevski, A.; Aittokallio, T.; Frieman, M.; Olinger, G.G.; Polyak, S.J. Drug Combinations as a First Line of Defense against Coronaviruses and Other Emerging Viruses. *mBio* **2021**, *12*, e03347-21. [CrossRef]
37. Kumar, S.; Sarma, P.; Kaur, H.; Prajapat, M.; Bhattacharyya, A.; Avti, P.; Sehkhar, N.; Kaur, H.; Bansal, S.; Mahendiratta, S.; et al. Clinically Relevant Cell Culture Models and Their Significance in Isolation, Pathogenesis, Vaccine Development, Repurposing and Screening of New Drugs for SARS-CoV-2: A Systematic Review. *Tissue Cell* **2021**, *70*, 101497. [CrossRef] [PubMed]
38. Mahoney, M.; Damalanka, V.C.; Tartell, M.A.; Chung, D.H.; Lourenco, A.L.; Pwee, D.; Mayer Bridwell, A.E.; Hoffmann, M.; Voss, J.; Karmakar, P.; et al. A Novel Class of TMPRSS2 Inhibitors Potently Block SARS-CoV-2 and MERS-CoV Viral Entry and Protect Human Epithelial Lung Cells. *Proc. Natl. Acad. Sci. USA* **2021**. [CrossRef] [PubMed]
39. Mukherjee, P.K.; Efferth, T.; Das, B.; Kar, A.; Ghosh, S.; Singha, S.; Debnath, P.; Sharma, N.; Bhardwaj, P.K.; Haldar, P.K. Role of Medicinal Plants in Inhibiting SARS-CoV-2 and in the Management of Post-COVID-19 Complications. *Phytomedicine* **2022**, *98*, 153930. [CrossRef]

40. Jamal, Q.M.S. Antiviral Potential of Plants against COVID-19 during Outbreaks—An Update. *Int. J. Mol. Sci.* **2022**, *23*, 13564. [CrossRef]
41. Gupta, S.; Singh, V.; Varadwaj, P.K.; Chakravartty, N.; Katta, A.V.S.K.M.; Lekkala, S.P.; Thomas, G.; Narasimhan, S.; Reddy, A.R.; Reddy Lachagari, V.B. Secondary Metabolites from Spice and Herbs as Potential Multitarget Inhibitors of SARS-CoV-2 Proteins. *J. Biomol. Struct. Dyn.* **2022**, *40*, 2264–2283. [CrossRef] [PubMed]
42. Huang, S.-T.; Chen, Y.; Chang, W.-C.; Chen, H.-F.; Lai, H.-C.; Lin, Y.-C.; Wang, W.-J.; Wang, Y.-C.; Yang, C.-S.; Wang, S.-C.; et al. *Scutellaria barbata* D. Don Inhibits the Main Proteases (M^{pro} and TMPRSS2) of Severe Acute Respiratory Syndrome Coronavirus 2 (SARS-CoV-2) Infection. *Viruses* **2021**, *13*, 826. [CrossRef]
43. Tallei, T.E.; Tumilaar, S.G.; Niode, N.J.; Fatimawali; Kepel, B.J.; Idroes, R.; Effendi, Y.; Sakib, S.A.; Emran, T.B. Potential of Plant Bioactive Compounds as SARS-CoV-2 Main Protease (Mpro) and Spike (S) Glycoprotein Inhibitors: A Molecular Docking Study. *Scientifica* **2020**, *2020*, 6307457. [CrossRef]
44. Llivisaca-Contreras, S.A.; Naranjo-Morán, J.; Pino-Acosta, A.; Pieters, L.; Vanden Berghe, W.; Manzano, P.; Vargas-Pérez, J.; León-Tamariz, F.; Cevallos-Cevallos, J.M. Plants and Natural Products with Activity against Various Types of Coronaviruses: A Review with Focus on SARS-CoV-2. *Molecules* **2021**, *26*, 4099. [CrossRef]
45. Fornari Laurindo, L.; Taynara Marton, L.; Minniti, G.; Dogani Rodrigues, V.; Buzinaro Suzuki, R.; Maria Cavallari Strozze Catharin, V.; Joshi, R.K.; Barbalho, S.M. Exploring the Impact of Herbal Therapies on COVID-19 and Influenza: Investigating Novel Delivery Mechanisms for Emerging Interventions. *Biologics* **2023**, *3*, 158–186. [CrossRef]
46. Kumar, Y.; Singh, H.; Patel, C.N. *In Silico* Prediction of Potential Inhibitors for the Main Protease of SARS-CoV-2 Using Molecular Docking and Dynamics Simulation Based Drug-Repurposing. *J. Infect. Public Health* **2020**, *13*, 1210–1223. [CrossRef]
47. Ullrich, S.; Nitsche, C. The SARS-CoV-2 Main Protease as Drug Target. *Bioorg. Med. Chem. Lett.* **2020**, *30*, 127377. [CrossRef]
48. WHO—World Health Organization Coronavirus Dashboard. Available online: https://covid19.who.int (accessed on 5 March 2024).
49. Tucci, A.R.; Da Rosa, R.M.; Rosa, A.S.; Augusto Chaves, O.; Ferreira, V.N.S.; Oliveira, T.K.F.; Coutinho Souza, D.D.; Borba, N.R.R.; Dornelles, L.; Rocha, N.S.; et al. Antiviral Effect of 5′-Arylchalcogeno-3-Aminothymidine Derivatives in SARS-CoV-2 Infection. *Molecules* **2023**, *28*, 6696. [CrossRef]
50. Caleffi, G.S.; Rosa, A.S.; De Souza, L.G.; Avelar, J.L.S.; Nascimento, S.M.R.; De Almeida, V.M.; Tucci, A.R.; Ferreira, V.N.; Da Silva, A.J.M.; Santos-Filho, O.A.; et al. Aurones: A Promising Scaffold to Inhibit SARS-CoV-2 Replication. *J. Nat. Prod.* **2023**, *86*, 1536–1549. [CrossRef] [PubMed]
51. Xiong, G.; Wu, Z.; Yi, J.; Fu, L.; Yang, Z.; Hsieh, C.; Yin, M.; Zeng, X.; Wu, C.; Lu, A.; et al. ADMETlab 2.0: An Integrated Online Platform for Accurate and Comprehensive Predictions of ADMET Properties. *Nucleic Acids Res.* **2021**, *49*, W5–W14. [CrossRef] [PubMed]
52. da-Costa-Rodrigues, B.; Cheohen, C.; Sciammarella, F.; Pierre-Bonetti-Pozzobon, A.; Ribeiro, L.; Nepomuceno-Silva, J.L.; Medeiros, M.; Mury, F.; Monteiro-de-Barros, C.; Lazoski, C.; et al. SARS-CoV-2 Spatiotemporal Genomic and Molecular Analysis of the First Wave of the COVID-19 Pandemic in Macaé, the Brazilian Capital of Oil. *Int. J. Mol. Sci.* **2022**, *23*, 11497. [CrossRef]
53. Case, D.A.; Aktulga, H.M.; Belfon, K.; Cerutti, D.S.; Cisneros, G.A.; Cruzeiro, V.W.D.; Forouzesh, N.; Giese, T.J.; Götz, A.W.; Gohlke, H.; et al. AmberTools. *J. Chem. Inf. Model.* **2023**, *63*, 6183–6191. [CrossRef]
54. Anandakrishnan, R.; Aguilar, B.; Onufriev, A.V. H++ 3.0: Automating pK Prediction and the Preparation of Biomolecular Structures for Atomistic Molecular Modeling and Simulations. *Nucleic Acids Res.* **2012**, *40*, W537–W541. [CrossRef]
55. Gordon, J.C.; Myers, J.B.; Folta, T.; Shoja, V.; Heath, L.S.; Onufriev, A. H++: A Server for Estimating pKas and Adding Missing Hydrogens to Macromolecules. *Nucleic Acids Res.* **2005**, *33*, W368–W371. [CrossRef]
56. Myers, J.; Grothaus, G.; Narayanan, S.; Onufriev, A. A Simple Clustering Algorithm Can Be Accurate Enough for Use in Calculations of p*Ks* in Macromolecules. *Proteins Struct. Funct. Bioinform.* **2006**, *63*, 928–938. [CrossRef]
57. Li, P.; Merz, K.M. MCPB.Py: A Python Based Metal Center Parameter Builder. *J. Chem. Inf. Model.* **2016**, *56*, 599–604. [CrossRef]
58. Barca, G.M.J.; Bertoni, C.; Carrington, L.; Datta, D.; De Silva, N.; Deustua, J.E.; Fedorov, D.G.; Gour, J.R.; Gunina, A.O.; Guidez, E.; et al. Recent Developments in the General Atomic and Molecular Electronic Structure System. *J. Chem. Phys.* **2020**, *152*, 154102. [CrossRef]
59. Machado, M.R.; Pantano, S. Split the Charge Difference in Two! A Rule of Thumb for Adding Proper Amounts of Ions in MD Simulations. *J. Chem. Theory Comput.* **2020**, *16*, 1367–1372. [CrossRef]

Disclaimer/Publisher's Note: The statements, opinions and data contained in all publications are solely those of the individual author(s) and contributor(s) and not of MDPI and/or the editor(s). MDPI and/or the editor(s) disclaim responsibility for any injury to people or property resulting from any ideas, methods, instructions or products referred to in the content.

6.2. Artigo 2: *Predicting the Anti-SARS-CoV-2 Potential of Isoquinoline Alkaloids from Brazilian Siparunaceae Species Using Chemometric Tools*

O artigo *"Predicting the Anti-SARS-CoV-2 Potential of Isoquinoline Alkaloids from Brazilian Siparunaceae Species Using Chemometric Tools"* foi publicado na revista *International Journal of Molecular Sciences*, em janeiro de 2025 (Volume 26, artigo 633). A *International Journal of Molecular Sciences* (IJMS) é classificada como Qualis A2 e possui um fator de impacto de 4.9.

O estudo investiga o potencial antiviral de alcaloides isoquinolínicos de espécies brasileiras da família Siparunaceae contra o SARS-CoV-2. Utilizando uma abordagem combinada *in vitro* e *in silico*, a pesquisa avaliou a potencial atividade dessas espécies na inibição de proteínas essenciais para o ciclo viral, como a SP, a $3CL^{pro}$ e a PL^{pro}. A aplicação de técnicas avançadas, incluindo UHPLC-MS/MS e ferramentas quimiométricas, permitiu a determinação de metabólitos potencialmente bioativos. Além disso, estudos de *docking* e dinâmica molecular, e predições ADMET reforçaram a viabilidade das substâncias como potenciais candidatos a fármacos antivirais.

Neste estudo, o aluno desempenhou papel fundamental, sendo responsável pela implementação do fluxo experimental, incluindo colaboração na triagem dos extratos vegetais contra as proteases virais $3CL^{pro}$ e PL^{pro}, bem como pela condução das análises químicas e quimiométricas. Além disso, esteve à frente do processamento de dados dos espectros de massa e da construção dos modelos preditivos, colaborando ativamente na anotação dos compostos bioativos e na interpretação dos resultados. O aluno também contribuiu significativamente para a redação do manuscrito e a revisão crítica dos dados apresentados.

International Journal of Molecular Sciences

MDPI

Article

Predicting the Anti-SARS-CoV-2 Potential of Isoquinoline Alkaloids from Brazilian Siparunaceae Species Using Chemometric Tools

Brendo Araujo Gomes [1,2,†], Diégina Araújo Fernandes [3,†], Simony Carvalho Mendonça [2,4], Mariana Freire Campos [1,2], Thamirys Silva da Fonseca [2,4], Larissa Esteves Carvalho Constant [5], Natalia Ferreira de Sousa [6], Renata Priscila Barros de Menezes [6], Beatriz Albuquerque Custódio de Oliveira [7], Stephany da Silva Costa [7], Giovanna Barbosa Frensel [7], Alice Santos Rosa [8,9], Thamara Kelcya Fonseca Oliveira [8,9], Amanda Resende Tucci [8,9], Júlia Nilo Henrique Lima [8], Vivian Neuza Santos Ferreira [8], Milene Dias Miranda [8,9], Diego Allonso [5,7,10], Marcus Tullius Scotti [6,10], Suzana Guimarães Leitão [1,2,4,*] and Gilda Guimarães Leitão [3,4,*]

1 Programa de Pós-Graduação em Biotecnologia Vegetal e Bioprocessos, Centro de Ciências da Saúde, Universidade Federal do Rio de Janeiro, Rio de Janeiro 21941-902, RJ, Brazil; brendoo.bc@ufrj.br (B.A.G.); ccamposmariana@ufrj.br (M.F.C.)
2 Departamento de Produtos Naturais e Alimentos, Faculdade de Farmácia, Universidade Federal do Rio de Janeiro, Rio de Janeiro 21941-902, RJ, Brazil; sy2802@ufrj.br (S.C.M.); thamirysfonseca@ufrj.br (T.S.d.F.)
3 Instituto de Pesquisas de Produtos Naturais, Universidade Federal do Rio de Janeiro, Rio de Janeiro 21941-902, RJ, Brazil; diegina@ufrj.br
4 Programa de Pós-Graduação em Ciências Farmacêuticas, Faculdade de Farmácia, Universidade Federal do Rio de Janeiro, Rio de Janeiro 21941-902, RJ, Brazil
5 Programa de Pós-Graduação em Ciências Biológicas, Instituto de Biofísica Carlos Chagas Filho, Universidade Federal do Rio de Janeiro, Rio de Janeiro 21941-590, RJ, Brazil; larissaestevescarvalho@gmail.com (L.E.C.C.); diegoallonso@pharma.ufrj.br (D.A.)
6 Programa de Pós-Graduação em Produtos Naturais e Sintéticos Bioativos, Universidade Federal da Paraíba, João Pessoa 58015-970, PB, Brazil; nataliafsousa@ltf.ufpb.br (N.F.d.S.); renatabarros@ltf.ufpb.br (R.P.B.d.M.); mtscotti@ccae.ufpb.br (M.T.S.)
7 Laboratório de Biotecnologia e Bioengenharia Estrutural, Centro de Ciências da Saúde, Universidade Federal do Rio de Janeiro, Bloco G, Rio de Janeiro 21941-902, RJ, Brazil; beatrizalbuquerquecp2@gmail.com (B.A.C.d.O.); stephanycosta@biof.ufrj.br (S.d.S.C.); gfrensel@peq.coppe.ufrj.br (G.B.F.)
8 Laboratório de Morfologia e Morfogênese Viral, Oswaldo Cruz Institute, Oswaldo Cruz Foundation, Rio de Janeiro 21041-250, RJ, Brazil; alicerosa@aluno.fiocruz.br (A.S.R.); thamarafonseca@ufmg.br (T.K.F.O.); artucci.bio@gmail.com (A.R.T.); julianilo@ufrj.br (J.N.H.L.); vivian.ferreira@ioc.fiocruz.br (V.N.S.F.); mmiranda@ioc.fiocruz.br (M.D.M.)
9 Programa de Pós-Graduação em Biologia Celular e Molecular, Instituto Oswaldo Cruz, Fundação Oswaldo Cruz, Rio de Janeiro 21041-250, RJ, Brazil
10 Departamento de Biotecnologia Farmacêutica, Faculdade de Farmácia, Universidade Federal do Rio de Janeiro, Rio de Janeiro 21941-902, RJ, Brazil
* Correspondence: sgleitao@pharma.ufrj.br (S.G.L.); ggleitao@ippn.ufrj.br (G.G.L.)
† These authors contributed equally to this work.

check for updates

Academic Editor: Ana Paula Coelho Duarte

Received: 1 December 2024
Revised: 23 December 2024
Accepted: 3 January 2025
Published: 13 January 2025

Citation: Gomes, B.A.; Fernandes, D.A.; Mendonça, S.C.; Campos, M.F.; da Fonseca, T.S.; Constant, L.E.C.; de Sousa, N.F.; Priscila Barros de Menezes, R.; de Oliveira, B.A.C.; da Silva Costa, S.; et al. Predicting the Anti-SARS-CoV-2 Potential of Isoquinoline Alkaloids from Brazilian Siparunaceae Species Using Chemometric Tools. *Int. J. Mol. Sci.* **2025**, *26*, 633. https://doi.org/10.3390/ijms26020633

Correction Statement: This article has been republished with a minor change. The change does not affect the scientific content of the article and further details are available within the backmatter of the website version of this article.

Copyright: © 2025 by the authors. Licensee MDPI, Basel, Switzerland. This article is an open access article distributed under the terms and conditions of the Creative Commons Attribution (CC BY) license (https://creativecommons.org/licenses/by/4.0/).

Abstract: The COVID-19 pandemic has caused over 7 million deaths globally in the past four years. *Siparuna* spp. (Siparunaceae), which is used in Brazilian folk medicine, is considered a genus with potential antiviral alternatives. This study explored the correlation between phytochemicals in *Siparuna* leaf extracts (*S. ficoides*, *S. decipiens*, *S. glycycarpa*, *S. reginae*, and *S. cymosa*) and their potential against various SARS-CoV-2 targets. In vitro assays examined interactions between the spike protein and the ACE2 receptor, protease activity, and viral replication inhibition in Calu-3 cell models. UHPLC-MS/MS analysis, processed with MZmine and evaluated chemometrically, revealed isoquinoline alkaloids with bulbocapnine, showing promising therapeutic potential. Predictions regarding absorption, distribution, metabolism, excretion, and toxicity were conducted, along with molecular docking and dynamics simulations, to evaluate protein−ligand interaction

stability. The results confirmed the antiviral activity of the *Siparuna* genus against SARS-CoV-2 targets, with 92% of the extracts maintaining over 70% cellular viability at 200 μg·mL^{-1} and 80% achieving more than 50% viral activity suppression at 50 μg·mL^{-1}. These findings highlight the potential of isoquinoline alkaloids as novel anti-coronavirus agents and support the need for further exploration, isolation, and testing of *Siparuna* compounds in the fight against COVID-19.

Keywords: Brazilian folk medicine; *Siparuna* spp.; SARS-CoV-2; UHPLC-MS/MS; chemometric analyses; molecular docking; dynamics simulations; ADMET predictions; bulbocapnine

1. Introduction

Members of the Coronaviridae family include seasonal and highly pathogenic viruses [1]. The severe acute respiratory syndrome coronavirus 2 (SARS-CoV-2) caused a significant global impact, with over 775 million cases and 7 million deaths resulting from coronavirus disease 2019 (COVID-19) until 2024 [2,3]. The COVID-19 pandemic significantly impacted Brazil, marked by the co-circulation of multiple variants resulting from multiple independent introduction events over time. According to the WHO, Brazil reported more than 37 million confirmed cases and more than 702 thousand deaths by April 2024, making it one of the countries most affected by this disease [4,5].

SARS-CoV-2 is a positive-sense single-stranded RNA virus with a genome size of approximately 30 kb. Its genome contains several key regions that encode both structural and non-structural proteins that are essential for viral particle assembly, replication, and successful infection [6,7]. Since 2020, significant progress has been made in the research of anti-SARS-CoV-2 compounds, with different viral proteins emerging as critical targets for combating COVID-19 [1,8–14], such as the Spike protein, focusing on its interaction with angiotensin-converting enzyme 2 (ACE2) receptors in host cells and chymotrypsin- like cysteine protease(3CL^{pro}) and papain-like protease (PL^{pro}), which are primarily responsible for proteolytic cleavage of polyproteins pp1a and pp1ab during the replication process [7,15,16]. Understanding the roles of these proteins during SARS-CoV-2 infection provides valuable insights for identifying and developing effective therapeutic strategies for the management of COVID-19.

Vaccination has significantly reduced the number of severe cases and fatalities associated with COVID-19. More than 10 billion vaccine doses have been administered globally since the beginning of the pandemic, shifting the severity of the disease from a potentially fatal to a mild/moderate hazard level [3,17,18]. Despite continued vaccination efforts, including guidelines recommending vaccine boosters, SARS-CoV-2 is still circulating, and the likelihood of new strain emergence highlights the need to develop new and effective therapeutic alternatives with broad activity against different variants of SARS-CoV-2 [19,20].

Recent studies showed that plant extracts, fractions, and isolated compounds can be used to target SARS-CoV-2, either by blocking CoVs binding to host-specific receptors, such as ACE2, or preventing RNA processing by inhibiting virus-encoded proteases, such as PL^{pro} and 3CL^{pro}, known as the main protease (M^{pro}) [8,14,19,21,22], as well as inhibition of virus replication in cellular models (Human Lung Adenocarcinoma Cell Line Calu-3) assays [23,24].

Brazil has the greatest biodiversity in the world and a long tradition of using medicinal plants to treat major public health emergencies, making it a powerful place for discovering new antivirals [25–27]. Plants of the genus *Siparuna*, Siparunaceae family, are used in Brazil-

ian folk medicine, especially in the Amazon region, for treating colds, fever, headaches, rheumatic pain, and gastrointestinal disorders, and have been studied for over 20 years by our research group [28–31].

The species *Siparuna apiosyce* (Mart.) A. DC ("limão bravo") is mentioned in the first Brazilian Pharmacopeia due to its importance as an ingredient in syrup and cough drops [29]. Dichloromethane extracts from *Siparuna ficoides* Renner and Hausner (orig- inally identified as *S. cristata* Poepp. and Endl. A.DC.) [32] contains the *O*-methylated flavonoids retusin and kumatakenin, which are able to inhibit the in vitro replication of SARS-CoV-2 with EC_{50} as low as 0.6 and 0.3 μM, in Calu-3 cells, respectively. Furthermore, in silico studies utilizing the Pymol, UCSF Chimera, and AutoDock Vina software v.1.1.2. programs showed a potential interaction between these flavonoids and the viral proteases $3CL^{pro}$ and PL^{pro}, suggesting a possible mechanism of action [31,33]. Another in silico study, employing molecular docking and AutoDock Vina software v.1.1.2., analyzed the interaction of terpenes from the essential oil of *Siparuna guianensis* Aublet with SARS-CoV-2 proteins and ACE2, revealing considerable binding affinity of sesquiterpenes with the tested macromolecules, showing a promising herbal therapeutic adjuvant against SARS-CoV-2 infections [9].

Computational tools for drug design have emerged as a paramount approach for identifying bioactive compounds originating from natural products. The integration of various in vitro and in silico techniques has become a promising and advantageous strategy. These methods facilitate the precise and efficient analysis of drugs and bioactive compounds against specific protein targets [34,35]. In this manner, one can predict which metabolites are probable contributors to a specific biological activity, even prior to isolating the target compounds. This aids in the rational design of new therapeutic agents [36,37].

In this study, we combined biological and chemical screenings of *Siparuna* plant extracts with computational methods aiming to predict compounds with potential anti-SARS-CoV-2 activity from the species *Siparuna ficoides* Renner and Hausner; *Siparuna decipiens* (Tul.) A.DC., *Siparuna glycycarpa* (Ducke) Renner and Hausner, *Siparuna reginae* (Tul.) A.DC. and *Siparuna cymosa* Tolm (originally identified as *S. sarmentosa* Perkins) [32], thereby contributing to the discovery of natural product-based therapeutic options for COVID-19.

2. Results and Discussion

2.1. Siparuna spp. Extracts Against SARS-CoV-2 Targets

Five Siparunas species, *S. ficoides* (SF), *S. decipiens* (SD), *S. glycycarpa* (SG), *S. reginae* (SR), and *Siparuna cymosa* (SC), were selected based on previous literature regarding their usefulness as sources of antiviral compounds [31,33]. Thus, in this work, we tested the ability of crude ethanol extracts (CEE) from their leaves, as well as the extracts obtained after liquid-liquid extraction (hexane-HEX, dichloromethane-DCM, ethyl acetate-EtOAc, and butanol-BuOH). All the samples were subjected to different approaches in order to identify any potential inhibitory activity against SARS-CoV-2: proteases ($3CL^{pro}$ and PL^{pro}) and spike protein-ACE2 interaction.

2.1.1. Siparuna Extracts Inhibit Spike Protein-ACE2 Interaction

The capacity of inhibiting RDB:ACE2 complex formation was evaluated using the immunoassay Lumit™ (Promega, Madison, WI, USA), which is a bioluminescence-based, no-wash, add-and-read kit designed for testing the potential of inhibitory samples [23]. Of the 25 assayed extracts, 16 were able to inhibit more than 50% of the Receptor Binding Domain (RBD) and ACE2 interaction (Figure 1). Notably, the addition of SG (DCM, EtOAc, and BuOH), SR (CEE and EtOAc), and SC (CEE, EtOAc, and BuOH) extracts resulted

in over 90% inhibition of RBD:ACE2 complex formation. Overall, the extracts obtained from the SG, SR, and SC species proved to be the most effective in blocking the entry of SARS-CoV-2 into cells. Only SD (CEE) did not interfere with the RBD:ACE2 interaction.

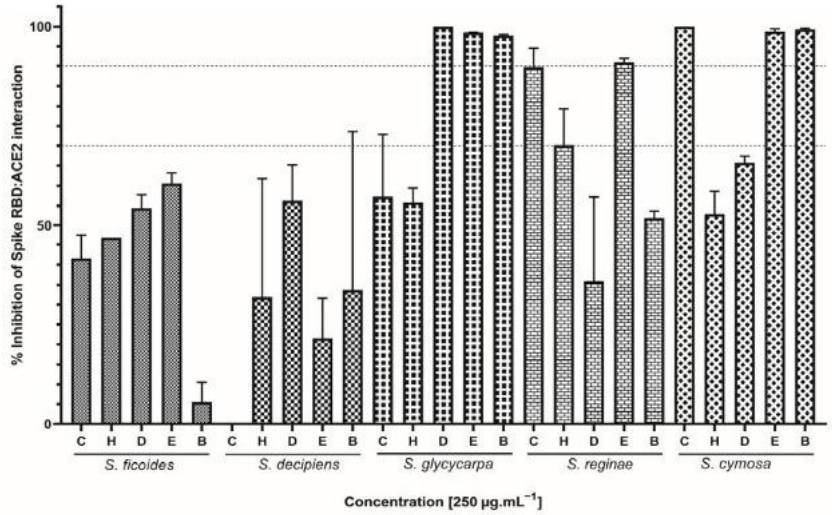

Figure 1. Effect of *Siparuna* extracts on spike protein-ACE2 interaction. C: crude ethanolic extract; H: hexane; D: dichloromethane; E: ethyl acetate; B: butanol. Data are expressed as means of three individual experiments (n = 3). Dotted lines indicate 70% and 90% inhibition.

2.1.2. Siparuna Extracts Inhibit 3CL^{pro} Activity

SARS-CoV-2 3CL^{pro} and PL^{pro} proteolytic activities were assessed using the fluorescence resonance energy transfer (FRET) approach. This assay has already been applied to investigate potential enzyme activity inhibitors from natural sources [24]. Thirteen extracts successfully inhibited over 50% of 3CL^{pro} activity (Figure 2). Particularly, the inclusion of SD (EtOAc) extract led to over 90% inhibition of this protease in the conducted assay. Overall, SF, SG, and SC were the most promising, as all the tested extracts showed some potential for inhibiting protease activity. Only SD (CEE, HEX, and DCM) and SR (DCM and BuOH) did not interfere with 3CL^{pro} activity.

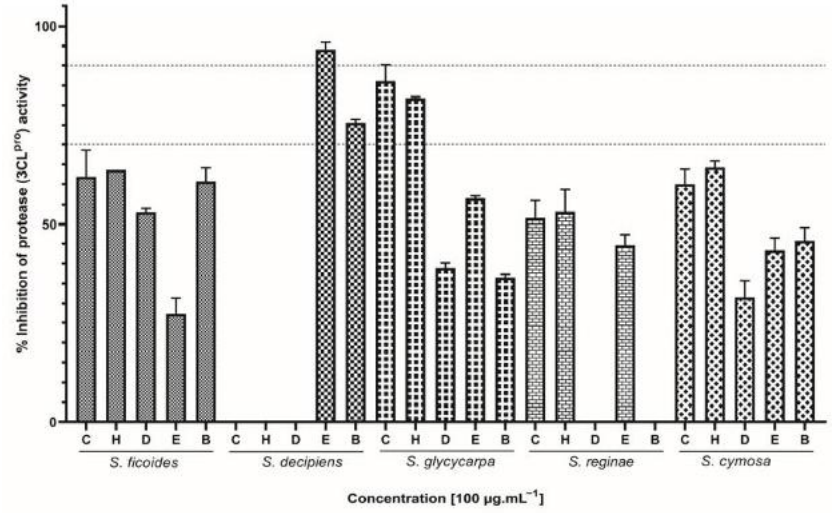

Figure 2. Effect of *Siparuna* extracts on 3CL^{pro} activity. C: crude ethanolic extract; H: hexane; D: dichloromethane; E: ethyl acetate; B: butanol. Data are expressed as means of three individual experiments (n = 3). Dotted lines indicate 70% and 90% inhibition.

2.1.3. Siparuna Extracts Inhibit PL^{pro} Activity

Sixteen extracts successfully inhibited over 50% of PL^{pro} viral activity (Figure 3). Specifically, the inclusion of SG (CEE and HEX), SR (BuOH), and SC (CEE, DCM, EtOAc, and BuOH) extracts resulted in over 90% inhibition of this protease in the conducted assay. Consistent with what was observed previously for RBD:ACE2 inhibition, extracts from SG, SR, and SC demonstrated the highest inhibitory effect against PL^{pro}. Only SF (HEX), SD (BuOH), SG (EtOAc and BuOH), and SR (EtOAc) did not interfere with PL^{pro} activity.

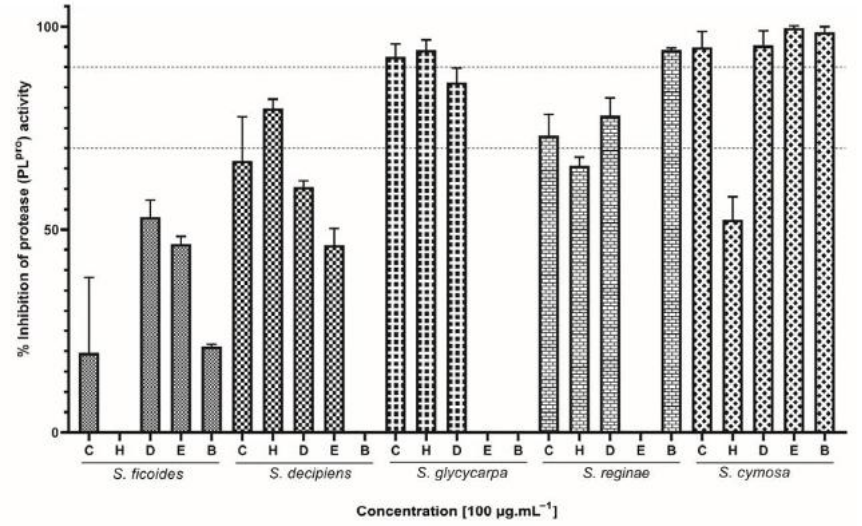

Figure 3. Effect of *Siparuna* extracts on PL^{pro} activity. C: crude ethanolic extract; H: hexane; D: dichloromethane; E: ethyl acetate; B: butanol. Data are expressed as means of three individual experiments (n = 3). Dotted lines indicate 70% and 90% inhibition.

To establish a successful infection process, SARS-CoV-2 should bind to ACE2 and promote the fusion of the viral and cell membranes or induce particle endocytosis. This step is known as the virus entry process and occurs very early during infection. Natural compounds that inhibit the interaction between the S protein and ACE2 will directly aid in the management of COVID-19 by restricting the entry of SARS-CoV-2 into the host cell [38]. Similarly, inhibition of other targets, such as 3CL^{pro} and PL^{pro,} may suppress SARS-CoV-2 infection [39].

Based on our results, the species *S. cymosa* showed to be the most promising among the three evaluated activities, because all assayed extracts were able to block virus entry into the cell by inhibiting the RBD:ACE2 interaction. Additionally, they demonstrated the ability to interact with 3CL^{pro} and PL^{pro} proteases in varying proportions. The species *S. glycycarpa* also stood out for presenting one of the highest percentages of interaction against SARS-CoV-2 targets for the majority of the evaluated extracts, followed by *S. reginae*, *S. decipiens*, and *S. ficoides*, with emphasis on the extracts that showed the highest inhibition potential, namely EtOAc, BuOH, CEE, DCM, and HEX, respectively.

A previous study conducted by our research group showed that BuOH extracts from SG and SC were the most active, inhibiting 96.0 ± 1.3% and 89.5 ± 0.8% of influenza virus replication 24 h post-infection [31]. A bioassay-guided fractionation of the n-butanol extract of SG by centrifugal partition chromatography (CPC) reported annotated compounds in the CPC fractions belonging to the isoquinoline alkaloid class, flavonoid glycosides, and dihydrochalcones. Benzylisoquinoline and aporphine alkaloids were annotated in the most active fractions, whereas tetrahydroprotoberberines were the least active ones [40].

Recent studies on extracts from various plants have demonstrated their potential antiviral activities, suggesting their potential use as adjuvants in the treatment of SARS-CoV-2 infections. The ethanol extract of pomegranate peels (*Punica granatum* L.) used at different

concentrations inhibited the interaction between Spike and ACE2 by up to 74%, and this effect was dose-dependent. This extract inhibited the activity of the viral $3CL^{pro}$ up to 80% when used at 0.2 $mg \cdot mL^{-1}$ [10]. Methanol extracts from turmeric (*Curcuma longa* L.) rhizomes, mustard (*Brassica nigra* L.) seeds, and wall rocket (*Diplotaxis erucoides* (L.) DC. subsp. *erucoides*) at 500 $\mu g \cdot mL^{-1}$ displayed significant inhibition of the $3CL^{pro}$ activity, resulting in inhibition protease activities of 100.0%, 90.6%, and 85.1%, respectively [11].

In vitro experiments for viral inhibition of SARS-CoV-2 revealed that whole-plant extracts (aqueous and alcoholic) of *Cissampelos pareira* L. could inhibit the virus by at least 60% SARS-CoV-2 replication in infected Vero cell cultures. The hydroalcoholic whole-plant extract showed an inhibition of 98%. The single-molecule constituents of *C. pareira* could also inhibit viral particles, with pareirarine (an isoquinoline alkaloid) showing the highest inhibition of 80%. Interestingly, the highest inhibition was shown by the whole-plant hydroalcoholic extract, which comprises various constituents. This suggests a synergistic effect of the constituents on viral inhibition [41].

The promising in vitro results obtained with plant extracts encourage the continuation of studies through their chemical analysis in the search for bioactive compounds that can be used as active principles in product formulations or as prototypes for the development of semi-synthetic derivatives, which may potentially act in the fight against emerging viral diseases, such as COVID-19 [42].

2.2. Chemometric Analyses Using PLS Regression Model

The analysis sought to predict the active compounds inhibiting the Spike:ACE2 interaction and the proteolytic activities of $r3CL^{pro}$ and rPL^{pro}. Twenty-five extracts from the Siparunaceae family species were subjected to LC-MS/MS (ESI and APCI) analysis in positive and negative ionization modes. The chemical data were processed and concatenated using low-level data fusion. Chemometric analyses based on binary activity values in the three target models were performed. A Partial Least Squares (PLS) analysis model was constructed to correlate LC-MS data fusion with extract inhibitory activity.

The PLS regression employed the LC-MS dataset (m/z ions and Retention Time—RT) of 75 samples as independent variables (X). The dependent variable (Y) reflected the inhibition activities against the three target models. This algorithm combines principal component analysis (PCA) and linear regression with the goal of identifying latent variables that optimize the correlation between predictors and biological activity.

To build the dataset of independent variables (X), a low-level data fusion strategy was employed. In this approach, spectral data from mass spectrometry analysis using ESI and APCI sources in positive and negative ionization modes were processed separately (normalization), concatenated, and formed an independent data matrix. The new dataset (low-level data matrix) was autoscaled. The low-level data matrix consisted of 75 rows (samples) and 460 columns (m/z ions and Retention Time), including ESI [+], 196 ions; ESI [−], 40 ions; APCI [+], 138 ions; and APCI [−], 86 ions. For the dataset of dependent variables (Y), three columns were constructed, one for each target model (Spike:ACE2; $r3CL^{pro}$; rPL^{pro}). Inhibition values were transformed into binary variables, with active samples (≥50% inhibition; 1) and non-active samples (<50% inhibition; −1).

In this study, three models, with one target focused on individual targets (Spike:ACE2, $r3CL^{pro}$, and rPL^{pro}), were created. The X-loading weight plot highlights the ions that have the most positive impact in elucidating the desired activity, specifically those exclusively present and/or more abundant in the extracts exhibiting higher activity. For these analyses, the top 10 ions that contributed the most to explaining the investigated activity were arbitrarily selected.

Upon evaluating the top 10 ions with the highest likelihood of correlation with the activity in each target, it was noticeable that among these, seven ions reappeared as those with the greatest contribution to explaining the inhibition of the Spike:ACE2 interaction, the activity of r3CL^{pro}, and rPL^{pro}. The presence of these seven similar ions in the three single-target models provides insights into their potential roles in the conducted experimental assays and suggests the possible multitarget activity of these compounds.

In Figures 4–6, the green bars in the scores plot (A) represent active samples (≥50% inhibition), and red bars indicate inactive samples (<50% inhibition). The height of the bars indicates the sample's magnitude relative to the principal component, and the direction (upward or downward) indicates the position relative to the mean. In the loadings plot (B), bar height reflects each variable's contribution to the principal component, with higher values indicating a stronger influence on the model. Seven highlighted ions were consistently among the top 10 most relevant across the three PLS models for the Spike (RBD):ACE2, 3CL^{pro}, and PL^{pro} targets, indicating their multitarget potential.

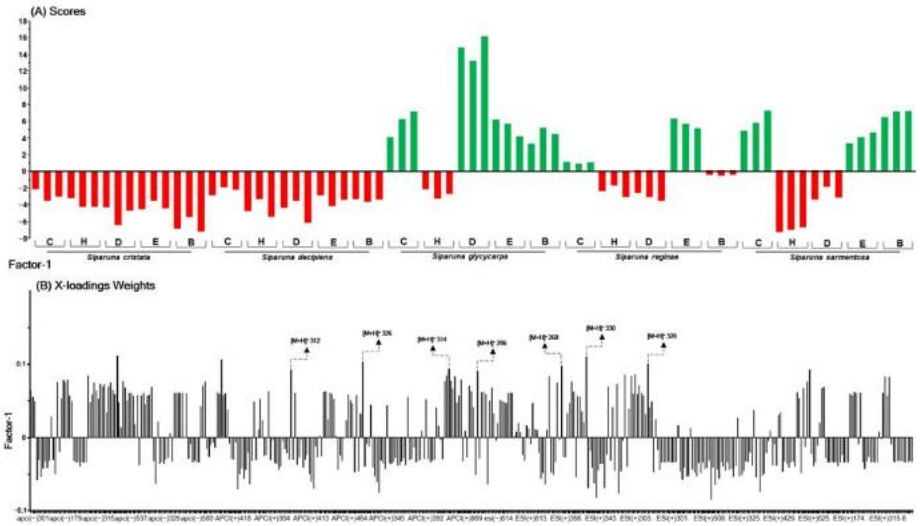

Figure 4. Scores (**A**), X-loadings weight (**B**) for the PLS model based on the LC-MS data obtained in the low-level data matrix (concatenated ESI and APCI [+/−]) of the 75 samples of five species of the the Siparunaceae family, and the inhibition values of the extracts on the RBD:ACE2 interaction. C: crude ethanolic extract; H: hexane; D: dichloromethane; E: ethyl acetate; B: butanol.

In the investigation model of Spike:ACE2 interaction inhibitors (Figure 4A,B), the explained variance was 99% (six factors), with R^2, 0.99, and Q^2, 0.87. The values of the Root Mean Square Error of Calibration (RMSEC) were 0.09, and those of the Root Mean Square Error of Cross-Validation (RMSECV) were 0.36. In this analysis, the ten ions with the greatest contribution to explaining the inhibition of the Spike:ACE2 interaction by the active extracts were $[M + H]^+$ m/z 268, 271, 286, 312, 314, 315, 317, 326, 328, and 330.

For the model r3CL^{pro} activity inhibitors (Figure 5A,B), 99% of the variance was explained by five factors, yielding an R^2 of 0.99 and Q^2 of 0.92. The RMSEC value was 0.06, and the RMSECV value was 0.21. In this analysis, of the 10 ions predicted as likely significantly related to explaining the inhibition of r3CL^{pro} activity, seven ($[M + H]^+$ m/z 268, 286, 312, 314, 326, 328, and 330) had already been marked for the Spike:ACE2 model. Only the ions $[M + H]^+$ m/z 297, 609, and 625 are exclusive to this model.

Finally, in the model of rPL^{pro} activity inhibitors (Figure 6A,B), six factors explained 99% of the variance, resulting in an R^2 of 0.99 and a Q^2 of 0.88. The RMSEC value was 0.10, and the RMSECV value was 0.35. During this analysis, seven similar ions were previously

predicted for the Spike:ACE2 and r3CL^{pro} models were observed again. Meanwhile, the ions exclusive to the rPL^{pro} model were $[M + H]^+$ m/z 359, 397, and 603.

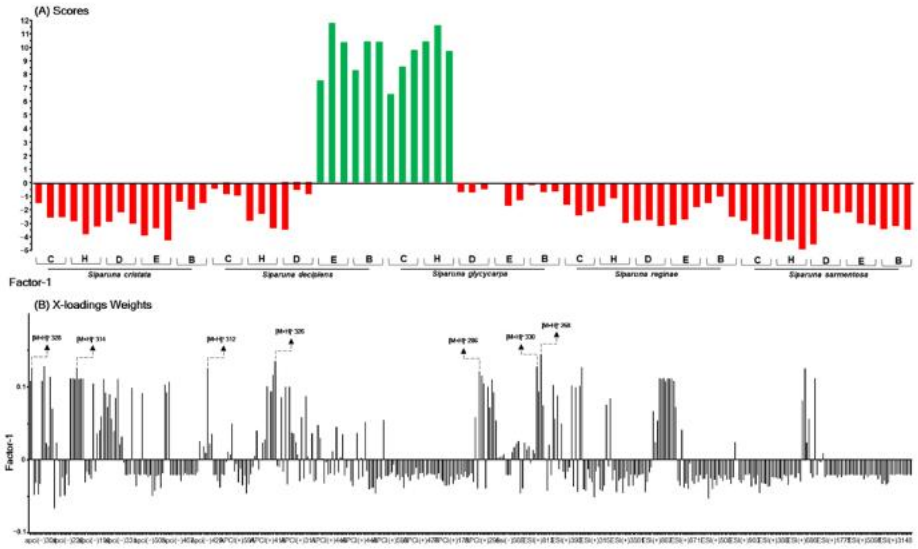

Figure 5. Scores (**A**), X-loadings weight (**B**) for the PLS model based on the LC-MS data obtained in the low-level data matrix (concatenated ESI and APCI [+/−]) of the 75 samples of five species of Siparunaceae family, and the inhibition values of the extracts on the r3CL^{pro} activity. C: crude ethanolic extract; H: hexane; D: dichloromethane; E: ethyl acetate; B: butanol.

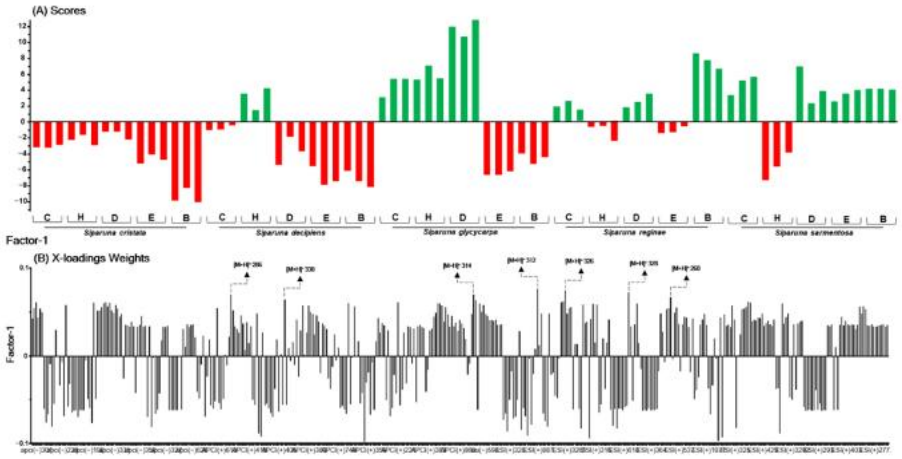

Figure 6. Scores (**A**), X-loadings weight (**B**) for the PLS model based on the LC-MS data obtained in the low-level data matrix (concatenated ESI and APCI [+/−]) of the 75 samples of five species of Siparunaceae family, and the inhibition values of the extracts on the rPL^{pro} activity. C: crude ethanolic extract; H: hexane; D: dichloromethane; E: ethyl acetate; B: butanol.

The values of explained variance, $R^{2,}$ and Q^2, as well as the lowest Root Mean Square Error (RMSE) for all obtained models, indicate a reliable fit, with the representativeness of the calibration data and the absence of overfitting. In all models, separation between the two distinct groups is evident (active and non-active samples). By selecting the 10 ions with the highest contribution, it is possible to ensure the investigation of ions with the highest likelihood of correlation with the potential activity in the three evaluated targets (multitarget), as well as streamline other computational assays, such as molecular network annotation, and studies of docking and molecular dynamics.

When evaluating the three models, it was possible to observe that the seven predicted ions (multitarget) had very close masses, within the range of $[M + H]^+$ m/z 268–330. They also exhibited similar retention times (Rt: 9.0–11.6 min) and better ionization in positive

mode, indicating possible nitrogenous and polar compounds. Therefore, it is conceivable that these ions belong to the same chemical class. Thus, these seven ions are of greater interest to be annotated and subjected to additional in silico assays, as they demonstrate the highest multitarget potential. Other ions predicted in the one-target models, such as *m*/*z* $[M + H]^+$ 271, 315, and 317 (for Spike), 297, 609, and 625 (for $3CL^{pro}$), and 397, 329, and 603 (for PL^{pro}), were not considered as they were not significant in the multitarget model. Additionally, the fragmentation profiles appeared to be different from those of the predicted compounds in the multitarget model, suggesting the presence of molecules of the phenolic class.

2.3. Annotated Compounds Using Custom Library

After data processing, a few multitarget predicted ions emerged, which had already been reported in other works by our group as anti-influenza agents [31,40]. Therefore, their APCI/ESI-MS/MS fragmentation patterns were checked (Supplementary Materials Figures S1–S7) and annotated (Table 1).

Table 1. LC-MS/MS data of predicted ions and annotation of the proposed compounds.

ID	Rt (min)	Molecular Formula	$[M + H]^+$ *m*/*z*	Source	MS/MS (MS^2)	Proposed Compound	Ref.
1	9.0	$C_{17}H_{19}NO_3$	286	ESI	269 (-NH_3), 237 (-NH_3-CH_3OH), 209 (-NH_3-CH_3OH-CO), 191 (-NH_3-CH_3OH-CO-H_2O)	coclaurine	[31,40]
2	10.1	$C_{19}H_{23}NO_4$	330	APCI	299 (-CH_3NH_2), 281 (-CH_3NH_2-H_2O), 267 (-CH_3NH_2-CH_3OH), 235 (-CH_3NH_2-2xCH_3OH), 207 (-CH_3NH_2-2xCH_3OH-CO)	reticuline	[31,40]
3	10.3	$C_{19}H_{21}NO_4$	328	ESI/APCI	297 (-CH_3NH_2), 282 (-CH_3NH_2-CH_3), 265 (-CH_3NH_2-CH_3OH), 237 (-CH_3NH_2-CH_3OH-CO)	boldine	[40]
4	10.6	$C_{18}H_{19}NO_4$	314	APCI	297 (-NH_3), 282 (-CH_3OH), 265 (-NH_3-CH_3OH)	laurolitsine	[31]
5	10.8	$C_{17}H_{17}NO_2$	268	ESI	251 (-NH_3), 219 (-NH_3-CH_3OH), 191 (-NH_3-CH_3OH-CO)	asimilobine	[43]
6	11.2	$C_{18}H_{17}NO_4$	312	ESI	295 (-NH_3), 280 (-CH_3OH), 263 (-NH_3-CH_3OH), 254 (-CH_2O-CO)	actinodaphnine	[31,44]
7	11.6	$C_{19}H_{19}NO_4$	326	ESI	295 (-CH_3NH_2), 280 (-CH_3NH_2-CH_3), 263 (-CH_3NH_2-CH_3OH), 235 (-CH_3NH_2-CH_3OH-CO)	bulbocapnine	[31]

These compounds present the same fragmentation profile with a first loss of CH_3NH_2 (−31 Da) for compounds **2**, **3**, and **7**, or NH_3 (−17 Da) for compounds **1**, **4**, **5**, and **6**. In addition, the losses of CH_3OH (−32 Da) followed by CO (−28 Da) were observed when an OH and an OCH_3 group were vicinal in the aromatic ring (compounds **1**–**7**) and CH_2O (−30 Da) followed by CO when there was a methylenedioxy group (compounds **6** and **7**) [45], characteristic of the isoquinoline alkaloids class (Figure 7).

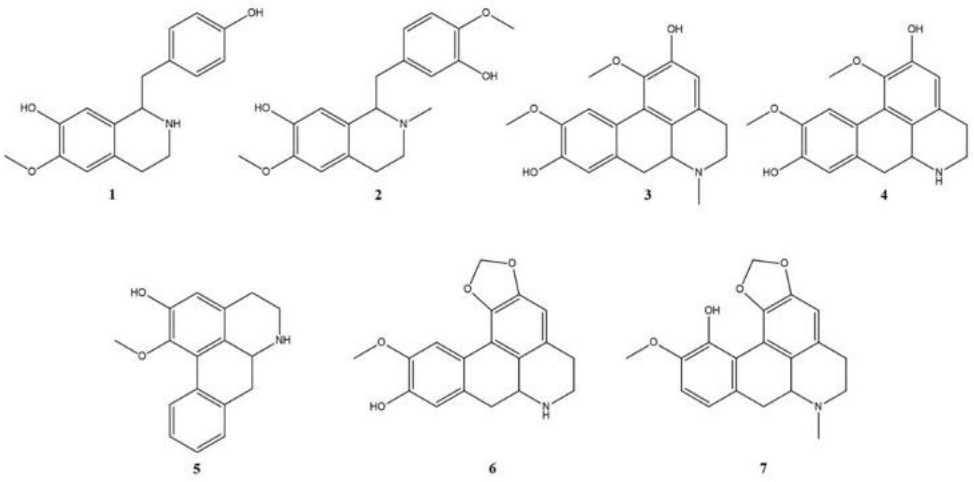

Figure 7. Structure of the chemical compounds identified in *Siparuna* spp. Coclaurine (**1**), reticuline (**2**), boldine (**3**), laurolitsine (**4**), asimilobine (**5**), actinodaphnine (**6**), and bulbocapnine (**7**).

In this way, it was possible to annotate seven isoquinoline alkaloids in the extracts that were most active against the different targets of SARS-CoV-2. Among them, five are aporphine alkaloids: actinodaphnine (**6**), boldine (**3**), laurolitsine (**4**), asimilobine (**5**), and bulbocapnine (**7**), and two are benzylisoquinolines alkaloids: coclaurine (**1**) and reticuline (**2**).

Compound **6** has been previously identified in the CEE of the *Siparuna* species investigated in the present study [31]. Compound **3** was isolated from an alkaloidal extract of *S. decipiens* [44]. Compounds **1**, **3**, **4**, and **7**, in turn, have already been identified in the BuOH extracts of *S. cymosa*, while compounds **1** and **2** have been identified in the same extract of *S. glycycarpa* [31]. Compound **5** has been isolated from *Siparuna tonduziana* Perk [43].

Natural products serve as rich sources of active compounds with diverse chemical and biochemical structures. The evaluation of antiviral activities of certain medicinal herbal extracts against CoV suggests that the phytochemicals contributing to the inhibitory effects may include flavonoids, terpenoids, and other phenolic compounds, along with alkaloids, which are prominent components in the extracts that demonstrated inhibition of viral replication and enzymatic activity [1,19,21].

Several studies have reported that flavonoids and alkaloids are the major compounds in *Siparuna* species [28,31,46]. A review of phytochemical studies of 18 species of this genus reported the isolation of 74 substances. Of these, 28 are alkaloids, 16 of which are derived from the aporphine nucleus, and liriodenine is the most cited as an isolated alkaloid among the species [30].

Alkaloids have stood out for showing significant antiviral activity and/or have been used as prototypes in the development of synthetic antiviral drugs, with sev- eral investigations of their actions against different types of coronaviruses, including SARS-CoV-2 [47–49]. The isoquinoline alkaloids are the second-largest class of alkaloids after indole alkaloids and may be divided into 13 classes: bis-benzylisoquinolines, apor- phines, benzyltetrahydro-isoquinoline, benzylisoquinolines, benzophenanthridine, cular- ines, morphinans, naphythylisoquinoline, pavines, phthalideisoquinoline, promorphinans, protoberberine, and ipecac alkaloids [39].

In view of their great structural diversity, isoquinoline alkaloid derivatives obtained from different plant sources have been reported to show antiviral effects on various targets. Studies have shown that compound **6** isolated from *Actinodaphne hookeri* Meissn, could inhibit viral replication of the Herpes Simplex virus [50]; compound **3** collected from *Peumus boldus* Molina, has been investigated for the anti-influenza A virus [51]; and

compound **4** isolated from the family Lauraceae, showed a significant inhibitory effect on HIV-1 integrase [52].

Kumar et al. [53] used various computational tools to identify the most eligible drug candidate with the capabilities to halt the replication of the SARS-CoV-2 virus by inhibiting M^{pro} ($3CL^{pro}$). From a library of 100 molecules, it was observed that among the top 10 molecules, eight were alkaloid derivatives, with two aporphine alkaloids (boldine **3** and laurolitsine **4**) and laurolitsine having the highest binding affinities. This signifies that the structure of the alkaloid derivatives has the desired pharmacophoric features to perfectly bind and halt the activity of the enzyme.

The compound **7** was active against the RNA virus *Parainfluenza* (PI-3) and was employed for antiviral assessment of the compounds using Mad-ine-Darby bovine kidney and Vero cell lines [54]. An in silico study showed that compounds **1** and **2** inhibited colorectal cancer pathogenic gene products better than their native ligands, with the best binding energy [55].

Compound **1** obtained from *Cocculus hirsutus* (L.) W. Theob. was found to be promising with significant binding affinity to SARS-CoV-2 $3CL^{pro}$ in comparison to the control and showed stable interactions with the amino acid residues present on the active site of the protease, being considered a promising anti-COVID-19 candidate [56].

Alkaloids have also been reported to have good binding affinities with important enzymes of SARS-CoV-2 in bioinformatics studies [47,57,58]. Norboldine, an aporphine alkaloid that can be extracted from the roots of *Lindera aggregate* (Sims) Kosterm., has binding potential with three target proteins: ACE2, M^{pro} ($3CL^{pro}$), and PL^{pro} [59]. Magnoflorine is another important aporphine-type alkaloid obtained from *Tinospora cordifolia* (Willd.) Hook. f. and Thomson, and displayed a good binding energy to $3CL^{pro}$ and S protein of SARS-CoV-2 and ACE2 [14]. Moreover, Ellinger et al. [59] demonstrated the potential of emetine and papaverine to reduce the cytotoxic effects of SARS-CoV-2 in certain tissues.

Brown et al. [12], using a protein-based FRET-biosensor to identify inhibitors of $3CL^{pro}$ from SARS-CoV-2, identified 19 compounds that have EC_{50} values below 1 μM, five (N-allylnorapomorphine, R(−)-propylnorapomorphine, R(−)-2-hydroxyapomorphine, and R(−)-2,10,11-trihydroxy-N-propylnoraporphine) of which were aporphine alkaloids not previously identified as $3CL^{pro}$ inhibitors, suggesting a promising starting point for structure-activity-relationship studies to develop new antiviral compounds.

In exploring the potential structure-activity relationships of isoquinoline alkaloids, Sharma et al. [39] underscored the significance of a nitrogen atom, particularly quaternary, and the presence of methyl groups within the structure of bioactive molecules. Compounds with such attributes, such as berberine, offer indirect support in combating diseases, enhancing immune responses (immunomodulation), or modulating pro-inflammatory reactions [60]. Moreover, other methoxylated alkaloids, including tetrandrine, neferine, berbamine, cephranthine, and hernandezine, have demonstrated substantial potential for combating SARS-CoV-2 infection by impeding viral entry into host cells. These compounds disrupt various pathways involved in the entry stage, including the inhibition of clathrin-mediated fusion induced by Ca^{2+} influx, as well as the blockade of two-pore channel 2 and TRPMLs [61–64]. Furthermore, these compounds may target other crucial phases of viral infection, such as replication. Ghareeb et al. [65] and Varghese et al. [66] demonstrated that berberine inhibits $3CL^{pro}$ and PL^{pro} activity while also suppressing the expression of both the E-gene and RNA-dependent RNA polymerase (RdRp). These findings collectively highlight the multifaceted potential of isoquinoline alkaloids in combating viral infections and underscore their importance in therapeutic development.

2.4. *Siparunaceae* Extracts Inhibit SARS-CoV-2 Replication in Human Infected Lung Cell Model

After confirming that the extracts exhibited inhibitory activity against viral proteases and the interaction between the viral spike protein and cellular ACE2, we assessed their ability to inhibit viral replication in a complex cellular system. For this purpose, experimental assays were performed using the human pneumocyte line Calu-3, acknowledged as an optimal model for in vitro infection and the screening of anti-coronavirus agents due to its elevated susceptibility to SARS-CoV-2 via a transmembrane serine protease 2 (TMPRSS2)-dependent entry mechanism [53,67–69]. Initially, Calu-3 cells were subjected to infection at a multiplicity of infection (MOI) of 0.01. The extracts were then tested for their antiviral efficacy at a concentration of 50 $\mu g \cdot mL^{-1}$ over a 24-h treatment period to identify the plant species demonstrating the most effective antiviral properties (Figure 8). The extracts' impact on viral replication in Calu-3 cells revealed that 20 (80%) extracts resulted in a reduction of viral activity by over 50%, and 10 (40%) of them inhibited more than 80% of viral replication under the same previously described conditions.

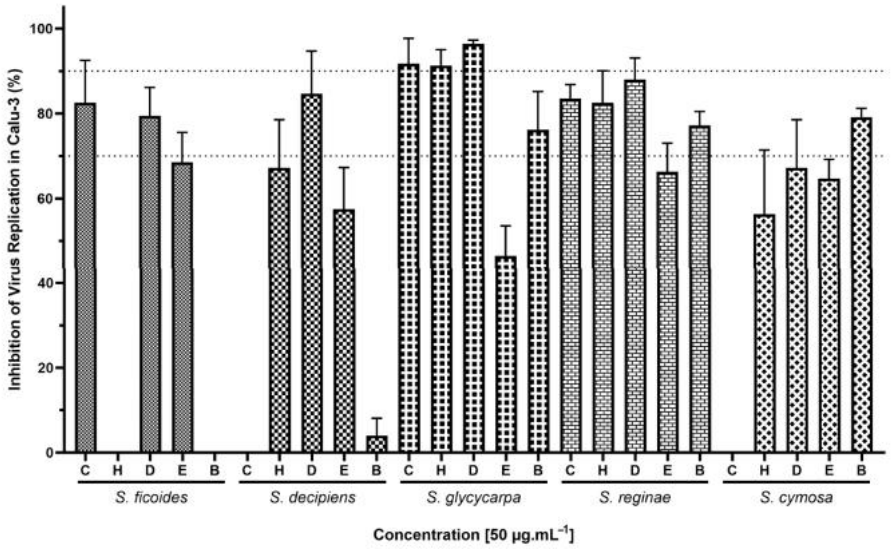

Figure 8. Calu-3 cells infected with SARS-CoV-2 at an MOI of 0.01, were treated with 25 extracts from *Siparuna* species at 50 $\mu g \cdot mL^{-1}$ for 24 h at 37 °C, 5% CO_2. C: crude ethanolic extract; H: hexane; D: dichloromethane; E: ethyl acetate; B: butanol. Viral titers were assessed by plaque assay in PFU/mL and compared to infected and untreated controls ($n = 4$). Dotted lines indicate 70% and 90% inhibition.

To evaluate the toxicity of compounds in the Calu-3 cell model, we exposed the cells to the maximum possible concentration of the extract, ensuring that the dimethyl sulfoxide (DMSO) content did not exceed 1% in the culture medium to prevent interference with cellular viability from DMSO (Figure 9). It was observed that the components of the extracts were non-toxic to this cellular model, as 23 (92%) extracts facilitated at least 70% cellular viability, with 18 (72%) achieving viability above 80%.

These results indicate that the concentration required for the extracts to cause any cellular damage is at least four times higher than the concentration needed to inhibit at least 50% of viral replication. This significant difference between the therapeutic efficacy and cytotoxicity underscores the potential safety and effectiveness of Siparunaceae extracts as anti-SARS-CoV-2 agents. The ability to achieve substantial antiviral effects at low concentrations, where cellular damage is minimal, highlights their promise in the bioprospecting of new anti-SARS-CoV-2 compounds. These results not only reinforce previous observations regarding the potent antiviral capabilities of Siparunaceae extracts, as discussed by our research group and others [31,33,70], but also highlight the specific impact of these botanical compounds on a relevant model of respiratory viral infection. The high efficacy of certain

extracts in blocking SARS-CoV-2 replication suggests that bioactive compounds within these plants, possibly alkaloids and flavonoids, interact with viral particles or cellular mechanisms in a manner that markedly disrupts the viral life cycle.

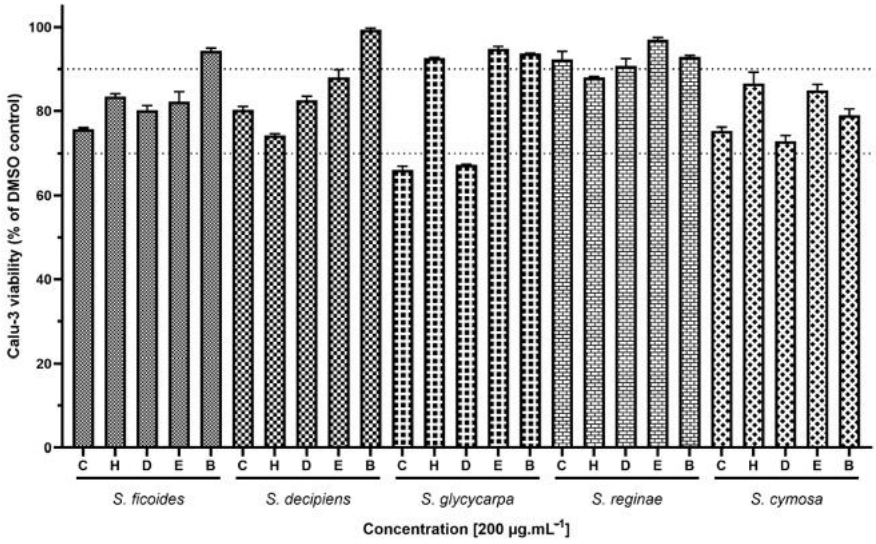

Figure 9. Calu-3 cells were treated with the 25 extracts of *Siparuna* species at 200 µg·mL^{-1} for 72 h at 37 °C and 5% CO_2. C: crude ethanolic extract; H: hexane; D: dichloromethane; E: ethyl acetate; B: butanol. Cell viability was assessed by analyzing the activity of the enzyme lactate dehydrogenase (LDH) and comparing it with that of the untreated controls. (n = 3). Dotted lines indicate 70% and 90% of inhibition.

This potent antiviral effect, particularly in a respiratory cell model, supports the potential therapeutic application of Siparunaceae extracts in treating infections caused by SARS-CoV-2. Further pharmacological exploration is required to identify the active constituents and to understand their mechanisms of action. Such research could pave the way for the development of novel antiviral agents derived from Siparunaceae, offering a natural and effective option for managing pandemics similar to COVID-19.

2.5. Results from ADMET Predictions

Initially, absorption, distribution, metabolism, excretion, and toxicity (ADMET) predictions were conducted using the Swiss ADME and Osiris DataWarrior platforms (Supplementary Materials Table S1). The aim of this analysis was to identify compounds with favorable pharmacokinetic, pharmacodynamic, and pharmacological profiles, indicating their potential for further development. All analyzed compounds have a high probability of being absorbed through the gastrointestinal tract and crossing the blood-brain barrier (BBB). Additionally, none of them showed a significant probability of toxicity to the reproductive system, nor were they likely to be skin irritants, mutagenic, or tumorigenic. The only exception was compound **1**, which showed a high probability of tumorigenic activity.

The potential interactions of the seven identified compounds with the five major isoforms of cytochrome P450 (CYP1A2, CYP2C19, CYP2C9, CYP2D6, and CYP3A4) were investigated (Table 2). Interestingly, only the compound bulbocapnine was predicted to have the potential to inhibit all CYP isoforms, especially the CYP2C19 and CYP2C9 isoforms, for which no other compound was predicted as an inhibitor.

The gastrointestinal absorption and brain penetration of the seven identified compounds were illustrated using the Boiled Egg diagram, as depicted in Figure 10, using the Swiss ADME web tool. In the figure, the white region represents the area with the highest likelihood of absorption by the human gastrointestinal system, while the yellow

portion (the yolk) indicates the region with the highest likelihood of brain penetration. The diagram revealed that all examined compounds fell within the yellow region, suggesting a high probability of absorption by the human gastrointestinal tract and brain permeation.

Table 2. Predicted interactions with cytochrome P450 (CYP) for the seven compounds.

ID	CYP1A2	CYP2C19	CYP CYP2C9	CYP2D6	CYP3A4
1	No	No	No	Yes	No
2	No	No	No	Yes	No
3	Yes	No	No	Yes	Yes
4	Yes	No	No	Yes	Yes
5	Yes	No	No	Yes	Yes
6	Yes	No	No	Yes	Yes
7	Yes	Yes	Yes	Yes	Yes

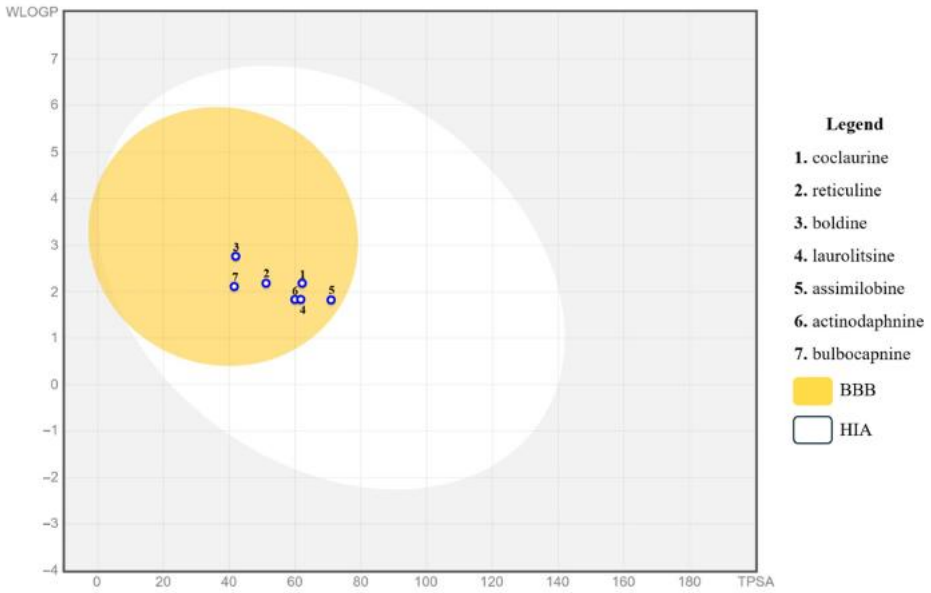

Figure 10. Boiled egg diagram of the seven compounds under study. Points located in the yellow area indicate molecules predicted to passively permeate the blood−brain barrier (BBB). The white area represents the molecules passively absorbed by the human gastrointestinal tract (HIA). Blue points indicate molecules predicted to be effluxed from the central nervous system by P-glycoprotein.

2.6. Docking Analysis

The seven compounds under study were subjected to molecular docking simulations to analyze the probability of interaction with the proteases of SARS-CoV-2, with the results demonstrated in three different scoring functions corresponding to the MolDock Score, Rerank Score, and PLANTS Score (the binding energy values of the compounds under study for the proteins related to the inhibition of the SARS-CoV-2 virus can be viewed in Supplementary Materials Tables S2–S7).

Prior to conducting the docking, redocking was performed to validate the methodology under study, given that redocking corresponds to the Root Mean Square Deviation (RMSD) value of the ligand. It is considered ideal for the RMSD value in docking to be equal to or less than 2.0 Å. Thus, an RMSD less than 2.0 Å is widely accepted as a discriminant in reproducing a known binding mode, indicating the success of the method [71]. The ligands were selected based on their similarity to the compounds under study according to the criteria of heavy atoms, chemical groups, and molecular mass. The co-crystallized ligands available in the crystallography made available in the PDB are representative and

biologically relevant: since they were experimentally validated, it has been demonstrated in reference articles [72–77] that they represent a relevant biological interaction with the target studied. In this way, it is possible to show that the docking protocol is capable of predicting a pose similar to the experimental one. According to the obtained RMSD value, it can be observed that it was below 2.0 Å (Table 3). These data indicated that the generated pose correctly positioned the ligand in the active site, suggesting that the program provided values that were considered satisfactory for docking validation.

Table 3. Information about the target proteins of SARS-CoV-2, their respective ligands, and the RMSD values obtained from the redocking procedure.

Protein ID	Ligand	Redocking, RMSD Value (Å)	Reference
$3CL^{pro}$ (6M2N)	5,6,7-trihydroxy-2-phenyl-4H-chromen-4one	0.1019	[74]
$3CL^{pro}$ (7B3E)	3,5,7-trihydroxy-2-(3,4,5-trihydroxyphenyl)-4H-chr- romen-4-one	0.1583	[75]
PL^{pro} (7LBR)	5-[(azetidine-3-yl)amino]-N-[(1R)-1-{3-[5-({[(1S,3R)-3-hydroxycyclopentyl]amino}methyl)thiophe-n-2-yl]phenyl}ethyl]-2-methylbenzamide	1.1780	[76]
PL^{pro} (7TZJ)	–[(3-fluorophenyl)methyl]-1-[(1R)-1-naphtalen-1-ylethyl]piperidine-4-carboxamide	1.2253	[77]

Regarding the 3D structures (PDB 3SCI and 6M0J) of the Spike protein [72,73], it was observed that they do not have co-crystallized ligands. The active site of these proteins was identified through the reference article of the PDB and the use of molecular pocket predictions such as the Bite Net Platform—Skoltech I Molecule, 2022 [78]. The coordinates used for the identification of the active site of the Spike protein were X: 12.70 and −32.26, Y: −6.44 and 21.10, and Z: 60.95 and −8.16 for PDBs 3SCI and 6M0J, respectively. For the Spike protein, remdesivir was used as a positive control [79].

The docking results regarding the total probability values for the enzymes under study can be viewed in the main text and in the Supplementary Materials (Supplementary Materials Tables S2–S7). From this perspective, it can be observed that the compounds under study exhibited negative binding energy values in all enzymes studied, indicating interactions with the targets under study. The following sections discuss the results related to the compounds' affinity to the targets under study.

Docking in Different Targets of SARS-CoV-2

The results of the probability of activity for the target Spike protein, $3CL^{pro}$, and PL^{pro} are shown in Table 4. All test compounds displayed *p* enzyme values above 0.6. In the Spike protein, the PDB ligand (positive control) exhibited the highest affinity (*p* enzyme 0.98). Notably, bulbocapnine (**7**) had the second-highest activity probability for the Spike protein in PDB 3SCI ($p = 0.77$), while reticuline (**2**) ranked second for PDB 6M0J ($p = 0.78$). These compounds maintained high affinity for the *p* enzyme, with compound **7** at $p = 0.73$ and compound **2** at $p = 0.77$. For $3CL^{pro}$, compound **2** had the highest *p* enzyme value ($p = 0.90$), followed by boldine (**3**) ($p = 0.89$). The *p* enzyme value of the PDB was lower ($p = 0.72$) than that of these compounds. Compound **7** also had the highest total probability value for the 3D structure with code 6M2N ($p = 0.94$), and for PDB 7B3E, compound **3** had the highest activity probability value ($p = 0.89$). In turn, for PL^{pro}, the PDB ligand showed the highest affinity, with the *p* enzyme equal to 0.99. Actinodaphine (**6**) stood out with a probability value of $p = 0.62$ for PDB 7LBR, while for PDB 7TZJ, the highest value ($p = 0.84$) was from compound **7**. Considering both targets, compounds **6** (*p* Enzyme 0.69) and **7** (*p* Enzyme 0.66) had the highest probability values after the ligand.

In the analysis of the Spike protein (PDB 6M0J), compound **2** demonstrated polar interactions (hydrogen bonding), including hydroxyl groups (OH) and oxygen atoms of methoxyl groups (OCH_3) with the residues Ala 348, Arg 393, Asp 350, Asp 382, Glu 37, Gly 352, His 378, His 401, Phe 40, and Phe 390. Moreover, hydrophobic interactions were observed, including Pi-alkyl, alkyl, Pi-pi stacked, and Pi-pi T interactions, through residues Arg 393, Asp 382, His 401, and Phe 390. In PDB 3SCI, compound **7** showed hydrogen interactions with residues Ala 348, Asn 394, Asn 397, His 401, Gly 395, Glu 398, and Glu 402, accompanied by hydrophobic interactions with Ala 348, His 378, and His 401. The similar residues between the compounds and the positive control (PC) are in bold. The molecular interactions of compounds **2** and **7**, along with the positive control (PDB ligand), with the Spike protein (PDBs 3SCI and 6M0J) are illustrated in Figure 11.

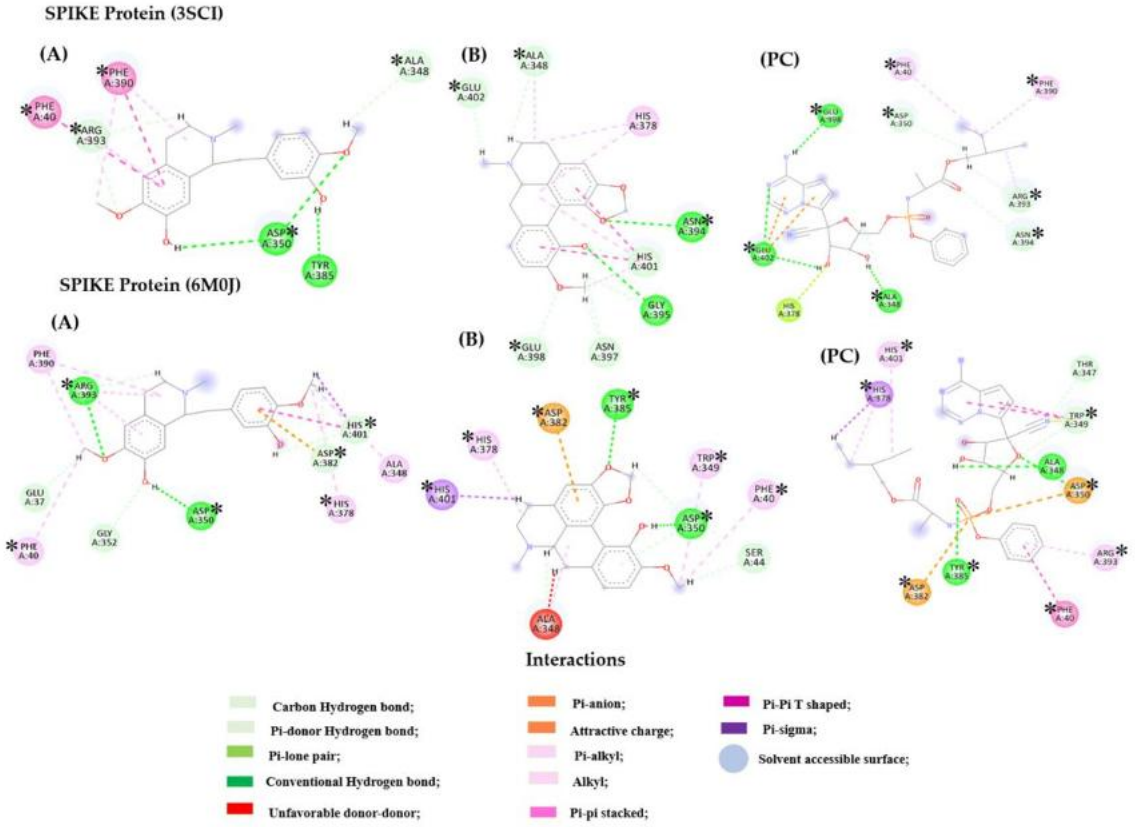

Figure 11. 2D and 3D interactions among compound reticuline (**2**) (**A**), bulbocapnine (**7**) (**B**), positive control (**PC**), and targets of SARS-CoV-2 (PDBs 3SCI and 6M0J—Spike). Residues: Ala (Alanine), Arg (Arginine), Asn (Asparagine), Asp (Aspartic acid), Glu (Glutamic acid), Gly (Glycine), His (Histidine), Phe (Phenylalanine), and Tyr (Tyrosine). * Indicates the occurrence of similar residues in the interactions between compounds and PC.

Table 4. Score values and probability of activity of the test compounds on the targets of SARS-CoV-2.

ID	Spike Protein			$3CL^{pro}$			PL^{pro}		
	***p* Total (3SCI)**	***p* Total (6M0J)**	**(*p*) Enzyme**	***p* Total (6M2N)**	***p* Total (7B3E)**	**(*p*) Enzyme**	***p* Total (7LBR)**	***p* Total (7TZJ)**	**(*p*) enzyme**
1	0.68	0.76	0.72	0.87	0.72	0.80	**0.62 ***	0.76	**0.69 ***
2	0.73	0.66	0.69	0.89	**0.89 ***	**0.89 ***	0.54	0.66	0.60
3	0.72	0.69	0.71	0.89	0.79	0.84	0.57	0.64	0.61
4	0.64	0.63	0.64	0.71	0.45	0.58	0.54	0.65	0.60
5	**0.77 ***	0.69	**0.73 ***	0.85	0.88	0.87	0.61	0.72	**0.66 ***

Table 4. *Cont.*

ID	Spike Protein			3CL^{pro}			PL^{pro}		
	***p* Total (3SCI)**	***p* Total (6M0J)**	**(*p*) Enzyme**	***p* Total (6M2N)**	***p* Total (7B3E)**	**(*p*) Enzyme**	***p* Total (7LBR)**	***p* Total (7TZJ)**	**(*p*) enzyme**
6	0.74	0.69	0.72	0.89	0.72	0.81	0.56	0.76	0.65
7	0.75	**0.78 ***	**0.77 ***	**0.94 ***	0.87	**0.90 ***	0.45	**0.84 ***	0.65
PDB/PC	1.0	0.97	0.98	0.85	0.60	0.72	1.0	0.99	0.99

PDB: Ligand PDB; PC: Positive Control; * In bold is the lowest score.

For the Spike protein, the highest affinity was observed for the positive control remdesivir, corresponding to *p* Enzyme equal 0.98. This compound is still used worldwide as a medication for the treatment of COVID-19. It prevents the entry and replication of the virus in the body, thereby reducing the infection process [80–82]. Thus, it emerges as an excellent alternative as a positive control for this target. It was also noted that remdesivir exhibited the highest probability values for the PDB structures 3SCI (p = 1) and 6M0J (p = 0.97). Interactions with the Spike protein, like those demonstrated by remdesivir, were observed for compounds **5** and **7**, corresponding to all residues for polar and non-polar interactions, except His 378, in the structure PDB 3SCI. Meanwhile, for the PDB 6M0J structure, there were similar interactions with the positive control in all residues except for Ala 348 and Thr 347 (polar interactions) and Asp 350 (non-polar interactions). Due to the similarity of interactions between the standard medication against COVID-19, remdesivir, and compounds **2** and **7**, one could speculate a possible similar inhibitory action on the specified target, the Spike protein.

In the 3CL^{pro} enzyme (PDB 6M2N), compound **2** involved polar interactions through the -OH and -OCH_3 groups with residues Asp 48, Asp 187, Asn 142, Cys 44, Cys 145, Gly 143, His 41, Leu 27, Met 49, Pro 52, and Tyr 54. Pi-sulfur interactions were observed with aromatic rings, along with alkyl and Pi-alkyl interactions involving residues Cys 44, Cys 145, His 41, Met 49, and Met 165. For PDB 7B3E, compound **3** hydrogen bonding interactions were observed with residues Glu 166 and Met 165, accompanied by prominent hydrophobic interactions with Cys 145, His 41, and Met 165. Similar residues between the compounds and PC are in bold. These interactions demonstrated that the studied compounds exhibited important interactions with both the 3D structures under investigation (Figure 12).

The tested compounds (**2** and **3**) formed important interactions with residues constituting the enzyme's active site, including Cys 145 and His 41, which are part of the enzyme's catalytic dyad. The hydrogen bond interaction established by residue Glu 166 is crucial in the enzyme's main chain. Hydrophobic interactions formed by residues Cys 44, His 41, and Met 49 are important in the S2 subsite. The hydrophobic interaction established by residue Met 165 is crucial for maintaining the enzyme's intermediate chain.

In the PL^{pro} enzyme structure (PDB 7LBR), compound **6** formed hydrogen bonds with residues Asp 164, Gln 269, Tyr 264, and Tyr 268 and hydrophobic interactions with Asp 164, Tyr 268, and Glu 167, interacting with these residues in the flexible β-hairpin loop BL2 of the enzyme. In this region of greater importance (β-hairpin loop BL2), the most relevant residues present in the PDB 7TZJ structure formed polar (Arg 166, Asp 302, and Thr 301) and non-polar (Arg 166, Met 208, Pro 247/248, and Tyr 264/268/273) strongly interacted with compound **7**. Overall, the studied compounds **1** and **5** exhibited significant interactions with the active sites of the enzymes, demonstrating potential therapeutic relevance. In bold are the similar residues between the compounds and PC. Figure 13 shows the interactions of compounds **6**, **7**, and the PDB ligand (PC) with PL^{pro} (PDBs 7LBR and 7TZJ).

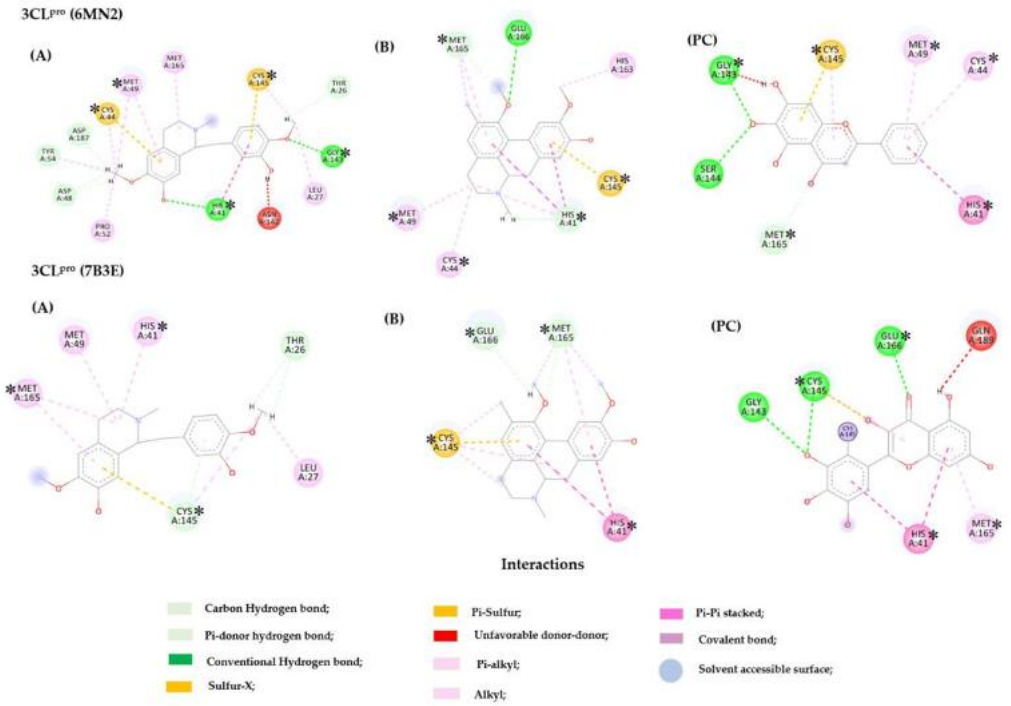

Figure 12. 2D and 3D interactions among compound reticuline (**2**) (**A**), boldine (**3**) (**B**), positive control (**PC**), and targets of SARS-CoV-2 (PDBs 6MN2 and 7B3E—3CL^{pro}). Residues: Ala (Alanine), Arg (Arginine), Asn (Asparagine), Asp (Aspartic acid), Glu (Glutamic acid), Gly (Glycine), His (Histidine), Phe (Phenylalanine), and Tyr (Tyrosine). * Indicates the occurrence of similar residues in the interactions with the compounds and PC.

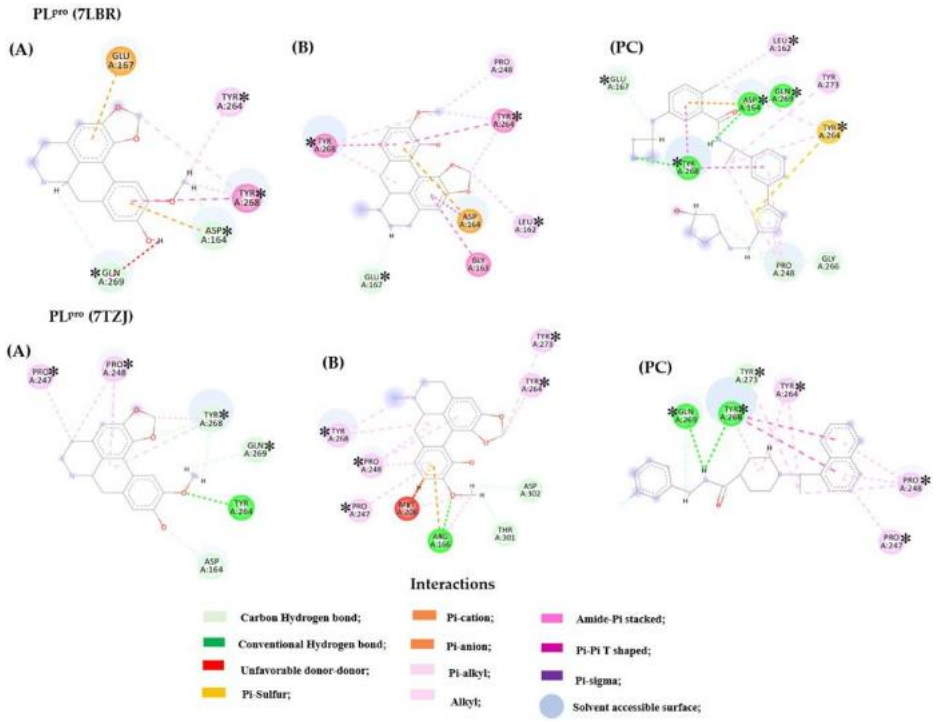

Figure 13. 2D and 3D interactions between compound actinodaphnine (**6**) (**A**), bulbocapnine (**7**) (**B**), positive control (**PC**), and targets of SARS-CoV-2 (PDBs 7LBR and 7TZJ). Residues: Ala (Alanine), Arg (Arginine), Asn (Asparagine), Asp (Aspartic acid), Glu (Glutamic acid), Gly (Glycine), His (Histidine), Phe (Phenylalanine), and Tyr (Tyrosine). * Indicates the occurrence of similar residues in the interactions with the compounds and PC.

When evaluating all compounds across the three targets, it can be observed that actinodaphnine (**6**), boldine (**3**), bulbocapnine (**7**), and reticuline (**2**) formed interactions of greater relevance with the Spike protein, as well as with the active sites of the $3CL^{pro}$ and PL^{pro} enzymes. However, it is worth noting that compounds **2** and **7** exhibited interaction probabilities in the active site of more proteins, with significant *p* enzyme values. Thus, aiming for expediency in the search for compounds with potential activity, further in silico assays (Molecular Dynamic Analysis) were conducted, focusing solely on these two compounds.

2.7. Molecular Dynamics Analysis

The investigation of potential drugs and their interactions with target proteins is a crucial step in the development of effective therapies, especially in vital areas such as pharmacology. The molecules bulbocapnine (**7**) and reticuline (**2**) have emerged as the most promising molecules in molecular docking analysis, standing out for their ability to interact with all the proteins analyzed. This characteristic makes them particularly intriguing for further investigations, such as molecular dynamics studies.

Molecular dynamics play a fundamental role in evaluating the stability of interactions between molecules and protein active sites. For this investigation, only one specific PDB file was selected for each protein of interest. For example, PDB file 6M2N was chosen for the $3CL^{pro}$ protein, while 7TZJ was selected for the PL^{pro} protein, and file 6M0J for the Spike protein.

Initially, root mean square deviation (RMSD) analyses were conducted to assess the structural stability of the receptor structure over time. These analyses provided valuable insights into the stability of the interactions of the studied molecules. Notably, it was observed that compound **7** demonstrated greater interaction stability with target proteins compared to compound **2**. Furthermore, compound **7** also exhibited greater interaction stability than the standard inhibitor ligands for each protein. This finding is crucial, indicating that the molecular interactions between compound **7** and the enzymes are relatively more stable and long-lasting, which are key factors in the development of effective drugs. These findings are shown in Figure 14.

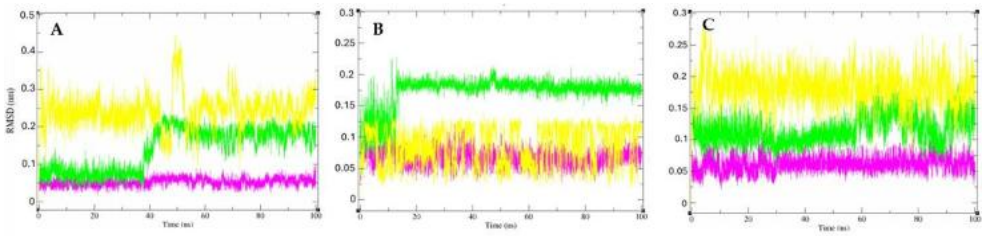

Figure 14. Root mean square deviation (RMSD). (**A**) Spike (6M0J), (**B**) 3CLpro (6M2N), and (**C**) PL^{pro} (7TZJ). bulbocapnine (**7**) (Pink), reticuline (**2**) (green), and inhibitor protein (yellow).

Subsequently, residue flexibility was analyzed using root mean square fluctuation (RMSF) values, revealing similar patterns between the isolated protein and the protein−ligand complex throughout the simulation. This consistency indicates the stability of the molecule-protein interaction, with no significant variations in the protein that could hinder the interaction (Figure 15).

Additionally, we also analyzed the evolution of protein packing levels alone and in complex with Bulbocapnine, Reticuline, and the standard inhibitor ligand of each protein through radius of gyration (Rg) values. In summary, Rg provides an idea of how compact or extended a molecule is during a molecular dynamics simulation, providing information about the conformation, stability, interactions, and flexibility of the molecules under analysis. It was observed that the molecules, when coupled with proteins, did not

exhibit significant variations compared to the protein alone (Figure 16). This indicates that the complexes are stable with low fluctuations in the tertiary structure of the enzymes.

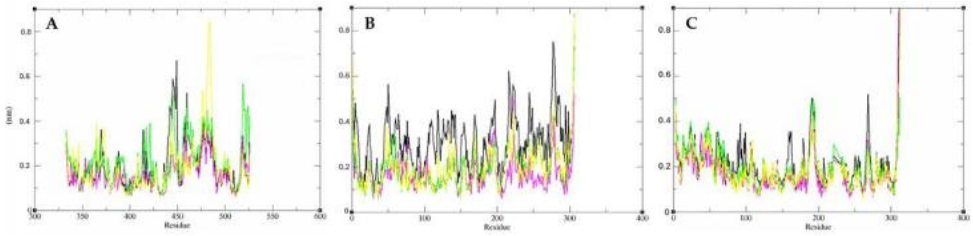

Figure 15. Root mean square fluctuation (RMSF). (**A**) Spike (6M0J), (**B**) $3CL^{pro}$ (6M2N), and (**C**) PL^{pro} (7TZJ). Complex protein bulbocapnine (**7**) (pink), complex protein reticuline (**2**) (green), complex protein inhibitor protein (yellow), and protein alone (black).

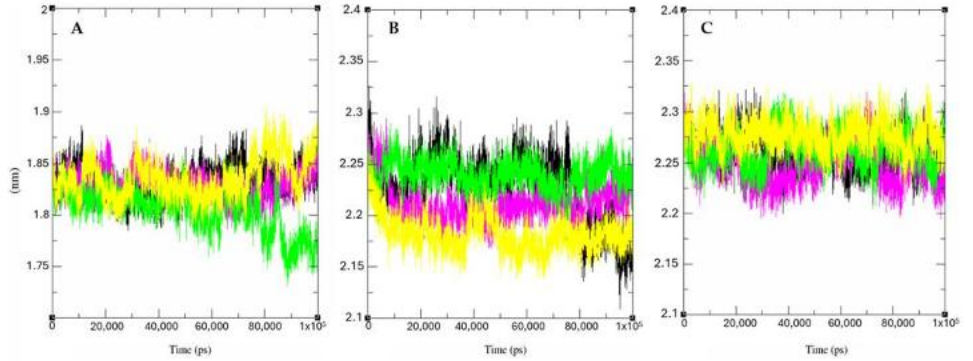

Figure 16. The radius of gyration (Rg). (**A**) Spike (6M0J); (**B**) $3CL^{pro}$ (6M2N); and (**C**) PL^{pro} (7TZJ). Complex protein bulbocapnine (**7**) (pink), complex protein reticuline (**2**) (green), complex protein inhibitor protein (yellow), and protein alone (black).

The search for therapeutic alternatives to COVID-19 using natural products presents a complex challenge that requires innovative and integrated strategies. The main obstacles include the need for high-level biosafety laboratories to handle SARS-CoV-2, high costs associated with consumables and equipment, and rapid mutagenicity of the virus, which favors the spread of new variants. Although in vitro assays targeting viral structural proteins and key enzymes have advanced significantly, these approaches remain financially demanding and limited in their ability to replicate the complexity of in vivo environments. In parallel, computational approaches, such as molecular docking, provide valuable insights but face restrictions when applied to complex matrices, such as crude extracts, due to the high demand for computational resources and specialized infrastructure. In this context, the present study stands out for applying a robust multidisciplinary workflow that combines advanced experimental and computational techniques, such as chemometric analyses, molecular docking, and molecular dynamics, integrated with in vitro assays. This approach enables the efficient identification of bioactive compounds with antiviral potential by optimizing resources and reducing costs in the discovery of new molecules. The integrated use of experimental and computational data generates accurate predictive models, which can help direct efforts toward compounds with greater potential for viral inhibition. However, it is essential to acknowledge the study's limitations. The absence of in vivo models to validate the therapeutic effects observed in in vitro assays constitutes a significant restriction, as it limits the extrapolation of results to more complex physiological conditions. Moreover, despite the rigor of applying computational tools, their predictive nature requires additional experimental validation, particularly regarding the bioavailability, metabolism, and toxicity of the identified compounds. Overcoming these limitations will require future studies involving in vivo assays, expansion of chemical libraries, and

refinement of existing computational approaches. In light of these considerations, the present study offers significant methodological advancement by proposing an integrated and efficient workflow for discovering antiviral compounds from natural products. The combination of predictive chemometric models with targeted experimental validation expands the possibilities of identifying bioactive compounds with antiviral properties, optimizing resource use, and accelerating the discovery process. The results obtained contribute to advancing research in the field of natural antivirals and establishing a solid foundation for developing innovative and potentially patentable methods that will support future investigations in combating COVID-19 and other emerging viral pathogens.

3. Materials and Methods

3.1. Plant Material

Leaves of *S. ficoides*, *S. decipiens*, *S. glycycarpa*, *S. reginae*, and *S. cymosa* were collected from Reserva Adolpho Ducke/Manaus/Brazil (59°52′40″ and 59°52′00″ W, 03°00′00″ and 03°08′00″ S) [83], in August 2015. Voucher specimens are deposited at the Instituto Nacional de Pesquisas da Amazônia (INPA) herbarium (Manaus, Brazil) under the registration numbers INPA: 269731, 269734, 269732, 269735, and 269733, respectively. This work was authorized by the Directing Council of Genetic Heritage (Conselho de Gestão do Patrimônio Genético, CGEN) under authorization A3C04CB.

Dried and ground leaves were extracted by percolation with ethanol 96° GL. Part of the CEE was partitioned between water−methanol 7:3 (*v*/*v*) and HEX, DCM, EtOAc, and BuOH, affording their respective extracts. This method was performed as described by Leal et al. [31].

3.2. Functional Biological Assays

3.2.1. Lumit™ RBD:ACE2 Interaction ASSAYS

SARS-CoV-2 Spike protein and human ACE2 complex formation were assessed using Lumit™ SARS-CoV-2 Spike RBD:ACE2 immunoassay (Promega, Madison, WI, USA). For this, 1 mg of each sample (*Siparuna* extracts) was separately solubilized in DMSO (dimethyl sulfoxide—Sigma-Aldrich, St. Louis, MO, USA) to a final concentration of 10 mg·mL^{-1}. The solutions were centrifuged (5804 R—Eppendorf, Hamburg, Germany) for 5 min at 2500 RPM, and the supernatants were collected.

Briefly, the samples were added to a white 96-well plate to a final concentration of 250 µg·mL^{-1}, followed by the addition of RBD (7.5 nM) and brief incubation (30 min). After adding ACE2 (7.5 nM), detection was carried out using secondary antibodies coupled to light particles after a 60 min incubation. The generated luminous signal was recorded in a SpectraMax M5 (Molecular Devices, San Jose, CA, USA) microplate reader at 500 ms of exposure as Relative Light Units (RLU). Percent inhibition was determined considering the total RLU resulting from successful RBD:ACE2 interaction (positive control), according to the following formula:

Complex formation (%) = [(treatment RLU − negative control 2)/total RLU in the positive control] × 100

The maximum interaction between RBD and ACE2 in the presence of the vehicle (DMSO) was used as the positive control for this assay. The negative controls comprised extracts with the detection reagents (negative control 1) and the detection reagents alone as a blank (negative control 2). The results are expressed as the means of three independent experiments.

3.2.2. FRET Protease Assays with SARS-CoV-2 r3CL^{pro} and rPL^{pro}

Recombinant SARS-CoV-2 3CL^{pro} and PL^{pro} enzymes expressed in *E. coli* BL21(DE3)pLysS and BL21(DE3) cells, respectively, were employed in a fluorescence resonance energy transfer

(FRET) assay. The extracts were tested in triplicate at 100 µg/mL to evaluate the maximal inhibitory effect of each extract. For $3CL^{pro}$, the enzyme concentration was maintained at 1.5 µM, and the mixture was incubated with 5 mM NaCl, 20 mM Tris-HCl (pH 8.0), and 5 mM DTT (Merck, Darmstadt, Germany—97%, CAS 3483-12-3) for 15 min at 37 °C. For PL^{pro}, a similar protocol was followed, but with the enzyme concentration set at 1 µM and reaction buffer containing 150 mM NaCl, 20 mM Tris-HCl (pH 8.0), and 5 mM DTT.

The reaction was initiated by adding the substrate (50 µM dissolved in DMSO). The customized fluorogenic substrates used were DABCYL-Ala-Val-Leu-Gln↓Ser-Gly-Phe-Arg-Lys-EDANS for $3CL^{pro}$ and DABCYL-Ala-Leu-Lys-Gly↓Gly-Lys-Iso-Val-EDANS for PL^{pro} (GenScript, Piscataway, NJ, USA, >95%). Fluorescence was measured using a SpectraMax M5 multi-mode microplate reader (Molecular Devices, San Jose, CA, USA). EDANS fluorescence emission was monitored at λexc = 330 nm and λem = 490 nm at 37 °C for 45 min. Fluorescence data (RFU) were converted to substrate cleavage-specific activity based on a previously calculated fluorescence conversion factor (FEC) for the EDANS-DABCYL fluorophore pair. The maximum enzyme activity was measured using the vehicle (DMSO), and these values were used to calculate the inhibition percentages of the test extracts. Additionally, the fluorescence profiles of the test extracts were assessed under the same assay conditions (dissolved in DMSO, buffer, and substrate). This step was essential to confirm the reliability of the inhibition results. Enzyme activity was also evaluated using the commercial inhibitors CG-376 for $3CL^{pro}$ and GRL-0617 for PL^{pro} (Supplementary Materials Figures S8 and S9).

3.3. UHPLC-MS/MS Analysis

The extracts (2 mg·mL^{-1}) were analyzed in UHPLC Dionex Ultimate 3000 (ThermoFischer Scientific, Waltham, MA, USA) coupled to LCQfleet (ThermoFischer Scientific, Waltham, MA, USA). The analyses were performed using an Acquity BEH C18 column (Waters Corporation, Milford, MA, USA—1.7 µm, 2.1 × 100 mm, 100 Å) with a flow rate of 0.45 mL·min^{-1} according to the elution gradient: (0 min, 5%B), (5 min, 5%B), (25 min, 100%B), (30 min, 100%B), (31 min, 5%B), (36 min, 5%B).

The mass spectrometer, equipped with atmospheric pressure chemical ionization (APCI) and electrospray ionization (ESI), was operated in positive and negative ionization modes. MS spectra were acquired in the range of m/z 100–1000, and the normalized collision energy of the collision-induced dissociation (CID) cell was set at 35 eV. LC-MS/MS analysis was conducted on 25 extracts (five extracts of each *Siparuna* spp.) in three replicates (totaling 300 analyses).

3.4. Computational Analysis and Annotation of Molecules

The data acquired from LC-MS/MS analyses were converted to the mzML format using specific parameters, including subset, msLevel 1–2, and positive or negative polarity. Additionally, Peak Picking with the vendor algorithm (msLevel 1–2) in the Proteowizard—MSconvert version 3.02 tool (ProteoWizard Software Foundation, Palo Alto, CA, USA) was applied. Subsequently, MZmine v.2.53 (University of Helsinki, Helsinki, Finland) was employed for data processing, with mass detection adjusted based on signal intensity and quality obtained from different analysis methods (ESI or APCI [+/−]). The ADAP Chromatogram Builder algorithm facilitated mass chromatogram construction and wavelet deconvolution. Isotopes were removed using the Isotopic Peaks Grouper, with the most intense isotope chosen as the representative, and alignment was performed using the join aligner.

Following this, both processed chemical data (m/z ions and retention time) and biological data (% inhibition) were exported to UnscramblerX software version 10.4

(CAMO Software, Oslo, Norway). The aim of this study was to predict potential active compounds inhibiting the Spike:ACE2 interaction and the proteolytic activities of r3CL^{pro} and rPL^{pro}. Chemometric analyses were performed with low-level data fusion (concatenated ESI and APCI [+/−] data) and a Partial Least Squares Regression model correlated LC-MS (data fusion) with inhibitory activities. For PLS regression, the samples were classified into two groups (binary values) based on average activity values: active samples (≥50% inhibition—[1]) and non-active samples (<50% inhibition—[−1]). The NIPALS algorithm was used to build the PLS model, and the cross-validation method used was Leave-One-Out. The ions indicated in the PLS prediction models were obtained from a custom data library.

3.5. In Vitro Studies in Calu-3 Cells

3.5.1. Cytotoxicity ASSAY

The Calu-3 cell line, originating from human bronchial adenocarcinoma and supplied by the Farmanguinhos platform RPT11M, was propagated in 96-well plates (1.5 × 10^4 cells/well). These cells were exposed to 25 different extracts at a concentration of 200 µg·mL^{-1} for a duration of 72 h to evaluate cytotoxicity using the CytoTox 96® Non-Radioactive Colorimetric Assay Kit (Promega, Madison, WI, USA). This assay quan- tifies the activity of the enzyme Lactate Dehydrogenase (LDH) as per the guidelines provided by the manufacturer, replicating previously conducted procedures [24]. Briefly, cells in the control group (non-treated) were lysed using the Lysis Solution included in the kit. Subsequently, the plate was centrifuged at 400× *g* for three minutes, after which 50 µL of the supernatant was carefully transferred to another plate. CytoTox 96® reagent was then added to this supernatant, and the mixture was incubated for 30 min at room temperature, shielded from light. Following incubation, the Stop Solution was administered, and absorbance was recorded at 490 nm using a spectrophotometer (Loccus, São Paulo, Brazil). The results were expressed as a percentage of viable cells based on the following calculation:

$$Cell\ Viability\ = 100 - ([(DMSO\ -\ treatment) \times 100])/(Lysis\ Control)$$

For this investigation, the extracts were first dissolved in 100% dimethyl sulfoxide (DMSO) and then further diluted in Dulbecco's Modified Eagle Medium (DMEM—Gibco, Waltham, MA, USA). The concentrations of DMSO were carefully maintained below 1% (*v*/*v*) to minimize any impact on cellular proliferation and viability [84]. The graph was constructed and analyzed using GraphPad Prism software, version 10.2.1 (GraphPad Software, San Diego, CA, USA), and represents the mean of the data performed with at least 3 technical replicates.

3.5.2. Anti-SARS-CoV-2 Assay

To assess the antiviral properties of the 25-extracts, Calu-3 cells were prepared as previously described and infected with SARS-CoV-2 virus, B1 lineage (GenBank MT710714, SisGen AC58AE2), at a multiplicity of infection (MOI) of 0.01. The infection process involved incubating the cells at 37 °C and 5% CO_2 for one hour to enable viral adsorption and entry. Post-viral entry, the extracts were administered at 50 µg·mL^{-1} over 24 h. After the treatment period, supernatants were collected to measure viral titers using the plaque assay technique. This involved inoculating Vero E6 (African green monkey kidney cells, ATCC CRL-1586) cells at 1.0 × 10^4 cells/well, exposing them to serial dilutions (from 1:200 to 1:25,600) of the supernatants for one hour, and overlaying with 50 µL of a 2.4% Carboxymethylcellulose medium, which includes DMEM-High Glucose 10×, 2.4% Carboxymethylcellulose, 2% Fetal Bovine Serum, and 1% Penicillin/Streptomycin.

After a 72-h incubation under consistent conditions, cells were fixed with 100 µL of 4% formalin for three hours and stained with 0.04% crystal violet for one hour. Plaque-forming units (PFU) were counted, and viral titers were expressed as PFU/mL. The viral titers in the supernatants of the infected and treated cells were compared with those of the untreated control cells and expressed as a percentage of viral replication inhibition. Notably, all experimental procedures and viral handling were conducted in a biosafety level-3 laboratory (BSL-3) in strict accordance with the WHO guidelines [85]. The graph was constructed and analyzed using GraphPad Prism software, version 10.2.1, and represents the mean of the data, performed with at least3 technical replicates.

3.6. In Silico Studies

3.6.1. ADMET Predictions

Prediction of absorption, distribution, metabolism, and excretion (ADME) parameters was calculated using the Swiss ADME open-access web tool (Swiss Institute of Bioinformatics, Lausanne, Switzerland) [86,87]. The toxicity prediction was performed in DataWarrior v. 4.7.2 software called OpenMolecules (Actelion Pharmaceuticals Ltd., Allschwil, Switzerland) [88,89].

3.6.2. Molecular Docking

Six proteins associated with SARS-CoV-2 were sourced from the Protein Data Bank (PDB) library [90,91]. Specifically, these proteins included those corresponding to the Spike protein (PDB 3SCI and 6M0J) [72,73], $3CL^{pro}$ (PDB 6M2N and 7B3E) [74,75], and PL^{pro} (PDB 7LBR and 7TZJ) [76,77]. The active site regions were defined based on the information available in the PDB library reference articles [92] cited above. In cases where enzymes did not have co-crystallized ligands, the active sites were defined based on ligand-protein coordinates.

All compounds were prepared, drawn using Marvin Sketch v19.18 (ChemAxon, Budapest, Hungary—https://chemaxon.com/marvin, accessed on 1 July 2024), and saved as .sdf files. Standardization was carried out using Standardizer v21.2.0 (Standardizer v21.2.0—https://chemaxon.com/standardizer, accessed on 1 July 2024), involving the addition of hydrogen atoms, aromatic ring standardization, salt removal, and structure conversion to 3D. Molecular docking was then performed, involving the removal of water molecules and the creation of a "template" between the macromolecule and co-crystallized ligand to delineate the active site, followed by the insertion of test molecules.

For enzymes lacking co-crystallized ligands, like the Spike protein (PDB 3SCI and 6M0J), the active site was identified using Molecular Pocket Predictors, such as the Bite Net Platform—Skoltech iMolecule, 2022 (Skoltech, Skolkovo Institute of Science and Technology, Moscow, Russia) [78,93–95]. Control compounds, including remdesivir [79], were used for validation.

The Molegro Virtual Docker v.6.0.1 (MVD) software (CLC bio, QIAGEN, Aarhus, Denmark) was employed with its default parameters. The active site was defined using the complexed ligand. Subsequently, the compounds were imported for analysis of system stability based on interactions identified with the enzyme active site, referencing the energetic value of the MolDock Score algorithm [96–98].

The MolDock SE and PLANTS (Simplex Evolution) algorithms were utilized with the following parameters: a total of 30 runs, a maximum of 3000 interactions, a population of 50 individuals, 2000 minimization steps for each flexible residue, and 2000 global minimization steps per run. The MolDock Score, PLANTS Score, and Rerank Score scoring functions were applied to calculate the docking energy values. A GRID was established at 0.3 Å, and the search sphere had a radius of 15 Å. The evaluation of ligand energy encompassed the analysis of internal electrostatic interactions, internal

hydrogen bonds, and sp2-sp2 torsions. Discovery Studio Visualizer v20.1. Software (BIOVIA, Dassault Systèmes, San Diego, CA, USA) [99] was employed to visualize the interactions and generate molecular docking figures.

3.6.3. Docking Consensus

A consensus analysis was performed using three scoring functions—MolDock Score, Rerank Score, and PLANTS Score to reduce false positives [100,101]. The affinity results from each function were included in the consensus calculations. For each scoring function, the relative score (p) was calculated by dividing each compound's score by the score of the compound with the lowest energy, as shown in Equation (1).

$$Prob = ((E\ Lig))/((EMin\ Lig)) \quad (1)$$

Probability ($Prob$) represents the probability of activity, while $E\ Lig$ is the calculated energy for each ligand in the docking simulation. $EMin\ Lig$ corresponds to the lowest energy obtained among the analyzed ligands. In the consensus analysis, the overall average is calculated for all biomarkers under study. Thus, the probability for each compound is obtained as an overall average of the probabilities for each biomarker. After calculating these probabilities in each scoring function analyzed, the total probability (P) is determined by summing the probabilities and dividing by the total number of observations (n)—that is, the number of scoring functions considered—as per Equation (2).

$$Ptotal = ((P\ MolDock\ Score + P\ Rerank\ Score + P\ Plants\ Score))/(n) \quad (2)$$

After calculating the total probability for each of the PDB structures used, the probability for the target under study (P Enzyme—Equation (3)) was obtained by summing the total probabilities and dividing by the number of 3D structures considered.

$$P\ enzyme = ((Ptotal\ 01 + Ptotal\ 02))/n \quad (3)$$

This analysis was conducted to offer a more thorough understanding of the compounds' affinity for the target, as the total probability value incorporated multiple crystallographic structures.

3.6.4. Molecular Dynamics

The Gromacs 5.0 software (Royal Institute of Technology, Stockholm, Sweden) [102,103] was used to perform molecular dynamics simulations to evaluate the stability of interactions between proteins and ligands. The topology of the binder was prepared through the topology generator PRODRG [104], applying the same force field as Gromacs for the protein, GROMOS43a1. For the molecular dynamics simulation, the SPC model of the extended point load was used in a dodecahedron box [105].

For electrical neutralization of the system, chloride and sodium ions were added, and the minimization of the system was also balanced at a temperature of 300 K by the V-resizing algorithm at 100 ps NVT set (constant number of particles, volume, and temperature), followed by equilibrium at 1 atm of pressure with the Parrinello–Rahman algorithm as set NPT (constant number of particles, pressure, and temperature) to 100 ps. DM simulations were performed for 50,000,000 cycles at 50 ns.

To determine the stability of the structure and if the complex was stable near the experimental framework, the mean square root displacement (RMSD) of all heavy atoms was calculated relative to the starting structures. Residual fluctuations (RMSF) were also analyzed to understand the role of residues near the receptor-binding site. To verify the interaction energy

of the protein–ligand complex, we calculated the short-range Coulombic interaction energy and the Lennard-Jones short-range energy for 50 ns. The Root Mean Square Deviation (RMSD) and Root Mean Square Fluctuation (RMSF) plots were generated in the Grace [106] software, and the protein and ligands were visualized with UCSF Chimera (Resource for Biocomputing, Visualization, and Informatics, University of California, San Francisco, CA, USA) [107].

4. Conclusions

In the present study, the established workflow combining biological and chemical screening of crude plant extracts, along with computational methods, enabled the accelerated prediction of compounds with potential anti-SARS-CoV-2 activity from the Siparunaceae family. Biological assays conducted with extracts from the leaves of *Siparuna cymosa*, *S. decipiens*, *S. ficoides*, *S. glycycarpa*, and *S. reginae* on different SARS-CoV-2 targets corroborate previous studies reporting the antiviral potential of this genus. The results identified extracts with significant multitarget activity, particularly in inhibiting the RBD:ACE2 interaction and the activities of $3CL^{pro}$ and PL^{pro} proteases.

The integration of chemometric simulations and custom library searches revealed the presence of seven isoquinoline alkaloids previously isolated and/or identified in *Siparuna* species, with an emphasis on *S. decipiens*, *S. glycycarpa*, and *S. cymosa*. Among these, two compounds stood out: bulbocapnine (an aporphine alkaloid) and reticu- line (a benzylisoquinoline alkaloid), which demonstrated superior binding potential to SARS-CoV-2 target proteins in molecular docking studies. Notably, the ADME re- sults indicated that none of the molecules violated Lipinski's rules, although coclaurine exhibited potential tumorigenicity.

Molecular dynamics simulations highlighted bulbocapnine for its exceptional stability in protein−ligand interactions, making it a promising multitarget inhibitor of coronaviruses. This compound emerged with the highest activity potential across all constructed chemometric models, along with favorable ADMET profiles when compared to the respective positive controls (protein inhibitors). Importantly, this study is the first to report bulbocapnine as a potential anti-SARS-CoV-2 agent.

Additionally, bulbocapnine was observed to be relatively more abundant in the dichloromethane extracts of *S. glycycarpa*, positioning this extract as a viable option for the purification of this compound. These findings support further exploration, isolation, and in-depth testing of bulbocapnine and related alkaloids, contributing to the ongoing search for new drug candidates derived from natural products as alternative treatments for COVID-19. In conclusion, bulbocapnine's stable and enduring interactions with multiple SARS-CoV-2 target proteins underscore its significant therapeutic potential.

Supplementary Materials: The following supporting information can be downloaded at https://www.mdpi.com/article/10.3390/ijms26020633/s1.

Author Contributions: B.A.G. and D.A.F. contributed equally as first authors and, together with S.G.L. and G.G.L., provided the design of this work (conceptualization). M.D.M., M.T.S., D.A., S.G.L. and G.G.L. contributed equally as senior authors (supervision and funding acquisition). D.A.F., B.A.G., S.C.M., N.F.d.S., R.P.B.d.M., M.F.C., L.E.C.C., T.S.d.F., B.A.C.d.O., S.d.S.C., G.B.F., A.S.R., T.K.F.O., A.R.T., J.N.H.L. and V.N.S.F. conducted the experiments (methodology). B.A.G., D.A.F., S.C.M., N.F.d.S., R.P.B.d.M., M.F.C., L.E.C.C., T.S.d.F., A.S.R., T.K.F.O. and A.R.T. analyzed the data (formal analysis and investigation). B.A.G., D.A.F., S.C.M., N.F.d.S., R.P.B.d.M., M.F.C., L.E.C.C., T.S.d.F., M.D.M., M.T.S., S.G.L., D.A. and G.G.L. interpreted the results (data curation). B.A.G., D.A.F., S.C.M., N.F.d.S., R.P.B.d.M., M.F.C., L.E.C.C., M.D.M. and T.S.d.F. drafted the manuscript (writing—original draft preparation). M.D.M., M.T.S., S.G.L., D.A. and G.G.L. revised the manuscript (writing—review and editing). S.G.L. and G.G.L. (project administration). All authors have read and agreed to the published version of the manuscript.

Funding: This work was supported by the Coordenação de Aperfeiçoamento de Pessoal de Nível Superior (CAPES—88887.694990/2022-00), Conselho Nacional de Desenvolvimento Científico e Tecnológico (CNPq—desenvolvimento tecnológico e extensão inovadora 312027/2022-2), Fundação de Amparo à Pesquisa do Estado do Rio de Janeiro (FAPERJ—E-26/211.285/2021, E-26/210.683/2021, E-26/201.426/2022, E-26/201.063/22, E-26/203.183/2023 and E-26/203.628/2024), Instituto Oswaldo Cruz (IOC), Fiocruz, FIOTEC (IOC-023-FIO-18-2-58); Programa INOVA Fiocruz (VPPIS-004-FIO-22-2-21).

Institutional Review Board Statement: Not applicable.

Informed Consent Statement: Not applicable.

Data Availability Statement: The data presented in this study are available on request from the corresponding authors.

Acknowledgments: We are grateful to the Central Analítica, Faculdade de Farmácia, Universidade Federal do Rio de Janeiro, for allowing us to use rtheir multi-user facilities. Thanks are due to the Biosafety Level 3 (BSL3) laboratory facility in Pavilhão Leonidas Deane, Instituto Oswaldo Cruz. Fiocruz, RJ; and Andre Sampaio from Farmanguinhos, platform RPT11M, for kindly donating the Calu-3 cells.

Conflicts of Interest: The authors declare no conflicts of interest.

References

1. Chaves, O.A.; Lima, C.R.; Fintelman-Rodrigues, N.; Sacramento, C.Q.; De Freitas, C.S.; Vazquez, L.; Temerozo, J.R.; Rocha, M.E.N.; Dias, S.S.G.; Carels, N.; et al. Agathisflavone, a Natural Biflavonoid That Inhibits SARS-CoV-2 Replication by Targeting Its Proteases. *Int. J. Biol. Macromol.* **2022**, *222*, 1015–1026. [CrossRef] [PubMed]
2. Bayani, F.; Hashkavaei, N.S.; Arjmand, S.; Rezaei, S.; Uskokovic´, V.; Alijanianzadeh, M.; Uversky, V.N.; Ranaei Siadat, S.O.; Mozaffari-Jovin, S.; Sefidbakht, Y. An Overview of the Vaccine Platforms to Combat COVID-19 with a Focus on the Subunit Vaccines. *Prog. Biophys. Mol. Biol.* **2023**, *178*, 32–49. [CrossRef] [PubMed]
3. World Health Organization Coronavirus (COVID-19) Dashboard. Available online: http://covid19.who.int (accessed on 2 May 2024).
4. Alcantara, L.C.J.; Nogueira, E.; Shuab, G.; Tosta, S.; Fristch, H.; Pimentel, V.; Souza-Neto, J.A.; Coutinho, L.L.; Fukumasu, H.; Sampaio, S.C.; et al. SARS-CoV-2 Epidemic in Brazil: How the Displacement of Variants Has Driven Distinct Epidemic Waves. *Virus Res.* **2022**, *315*, 198785. [CrossRef] [PubMed]
5. World Health Organization Coronavirus (COVID-19) Dashboard: Brazil. Available online: https://covid19.who.int/region/amro/country/br (accessed on 2 May 2024).
6. Kabir, M.T.; Uddin, M.S.; Hossain, M.F.; Abdulhakim, J.A.; Alam, M.A.; Ashraf, G.M.; Bungau, S.G.; Bin-Jumah, M.N.; Abdel-Daim, M.M.; Aleya, L. nCOVID-19 Pandemic: From Molecular Pathogenesis to Potential Investigational Therapeutics. *Front. Cell Dev. Biol.* **2020**, *8*, 616. [CrossRef] [PubMed]
7. Huang, Y.; Yang, C.; Xu, X.; Xu, W.; Liu, S. Structural and Functional Properties of SARS-CoV-2 Spike Protein: Potential Antivirus Drug Development for COVID-19. *Acta Pharmacol. Sin.* **2020**, *41*, 1141–1149. [CrossRef]
8. Jantan, I.; Arshad, L.; Septama, A.W.; Haque, M.A.; Mohamed-Hussein, Z.; Govender, N.T. Antiviral Effects of Phytochemicals against Severe Acute Respiratory Syndrome Coronavirus 2 and Their Mechanisms of Action: A Review. *Phytother. Res.* **2023**, *37*, 1036–1056. [CrossRef]
9. Costa, R.; Martins, R.; De Lima, G.; Stamford, T.; Tadei, W.; Maciel, M.A.; Do Rêgo, A.; Xavier-Júnior, F. Molecular Docking in Silico. Analysis of Brazilian Essential Oils Against Host Targets and SARS-CoV-2 Proteins. *J. Braz. Chem. Soc.* **2022**, *33*, 1219–1235. [CrossRef]
10. Tito, A.; Colantuono, A.; Pirone, L.; Pedone, E.; Intartaglia, D.; Giamundo, G.; Conte, I.; Vitaglione, P.; Apone, F. Pomegranate Peel Extract as an Inhibitor of SARS-CoV-2 Spike Binding to Human ACE2 Receptor (In Vitro): A Promising Source of Novel Antiviral Drugs. *Front. Chem.* **2021**, *9*, 638187. [CrossRef]
11. Guijarro-Real, C.; Plazas, M.; Rodríguez-Burruezo, A.; Prohens, J.; Fita, A. Potential In Vitro Inhibition of Selected Plant Extracts against SARS-CoV-2 Chymotripsin-Like Protease (3CLPro) Activity. *Foods* **2021**, *10*, 1503. [CrossRef]
12. Brown, A.S.; Ackerley, D.F.; Calcott, M.J. High-Throughput Screening for Inhibitors of the SARS-CoV-2 Protease Using a FRET-Biosensor. *Molecules* **2020**, *25*, 4666. [CrossRef]

13. Cheohen, C.F.D.A.R.; Esteves, M.E.A.; Da Fonseca, T.S.; Leal, C.M.; Assis, F.D.L.F.; Campos, M.F.; Rebelo, R.S.; Allonso, D.; Leitão, G.G.; Da Silva, M.L.; et al. In Silico Screening of Phenylethanoid Glycosides, a Class of Pharmacologically Active Compounds as Natural Inhibitors of SARS-CoV-2 Proteases. *Comput. Struct. Biotechnol. J.* **2023**, *21*, 1461–1472. [CrossRef] [PubMed]
14. He, Z.; Yuan, J.; Zhang, Y.; Li, R.; Mo, M.; Wang, Y.; Ti, H. Recent Advances towards Natural Plants as Potential Inhibitors of SARS-Cov-2 Targets. *Pharm. Biol.* **2023**, *61*, 1186–1210. [CrossRef]
15. Klemm, T.; Ebert, G.; Calleja, D.J.; Allison, C.C.; Richardson, L.W.; Bernardini, J.P.; Lu, B.G.; Kuchel, N.W.; Grohmann, C.; Shibata, Y.; et al. Mechanism and Inhibition of the Papain-like Protease, PLpro, of SARS-CoV-2. *EMBO J.* **2020**, *39*, e106275. [CrossRef]
16. Jin, Z.; Du, X.; Xu, Y.; Deng, Y.; Liu, M.; Zhao, Y.; Zhang, B.; Li, X.; Zhang, L.; Peng, C.; et al. Structure of Mpro from SARS-CoV-2 and Discovery of Its Inhibitors. *Nature* **2020**, *582*, 289–293. [CrossRef]
17. Iacopetta, D.; Ceramella, J.; Catalano, A.; Saturnino, C.; Pellegrino, M.; Mariconda, A.; Longo, P.; Sinicropi, M.S.; Aquaro, S. COVID-19 at a Glance: An Up-to-Date Overview on Variants, Drug Design and Therapies. *Viruses* **2022**, *14*, 573. [CrossRef]
18. Pérez-Vargas, J.; Shapira, T.; Olmstead, A.D.; Villanueva, I.; Thompson, C.A.H.; Ennis, S.; Gao, G.; De Guzman, J.; Williams, D.E.; Wang, M.; et al. Discovery of Lead Natural Products for Developing Pan-SARS-CoV-2 Therapeutics. *Antivir. Res.* **2023**, *209*, 105484. [CrossRef]
19. Mukherjee, P.K.; Efferth, T.; Das, B.; Kar, A.; Ghosh, S.; Singha, S.; Debnath, P.; Sharma, N.; Bhardwaj, P.K.; Haldar, P.K. Role of Medicinal Plants in Inhibiting SARS-CoV-2 and in the Management of Post-COVID-19 Complications. *Phytomedicine* **2022**, *98*, 153930. [CrossRef]
20. Aleem, A.; Samad, A.B.A.; Vaqar, S. Emerging Variants of SARS-CoV-2 and Novel Therapeutics Against Coronavirus (COVID-19). Available online: https://www.ncbi.nlm.nih.gov/books/NBK570580/ (accessed on 8 May 2024).
21. De Loera, D. The Role of Traditional Medicine in the Fight against SARS-CoV-2. In *Biomedical Innovations to Combat COVID-19*; Elsevier: Amsterdam, The Netherlands, 2022; pp. 339–385, ISBN 978-0-323-90248-9.
22. Abou Baker, D.H.; Hassan, E.M.; El Gengaihi, S. An Overview on Medicinal Plants Used for Combating Coronavirus: Current Potentials and Challenges. *J. Agric. Food Res.* **2023**, *13*, 100632. [CrossRef]
23. Campos, M.F.; Mendonça, S.C.; Peñaloza, E.M.C.; De Oliveira, B.A.C.; Rosa, A.S.; Leitão, G.G.; Tucci, A.R.; Ferreira, V.N.S.; Oliveira, T.K.F.; Miranda, M.D.; et al. Anti-SARS-CoV-2 Activity of *Ampelozizyphus amazonicus* (Saracura-Mirá): Focus on the Modulation of the Spike-ACE2 Interaction by Chemically Characterized Bark Extracts by LC-DAD-APCI-MS/MS. *Molecules* **2023**, *28*, 3159. [CrossRef]
24. Mendonça, S.C.; Gomes, B.A.; Campos, M.F.; da Fonseca, T.S.; Esteves, M.E.A.; Andriolo, B.V.; Cheohen, C.F.d.A.R.; Constant, L.E.C.; da Silva Costa, S.; Calil, P.T.; et al. Myrtucommulones and Related Acylphloroglucinols from Myrtaceae as a Promising Source of Multitarget SARS-CoV-2 Cycle Inhibitors. *Pharmaceuticals* **2024**, *17*, 436. [CrossRef]
25. Filardi, F.L.R.; de Barros, F.; Baumgratz, J.F.A.; Bicudo, C.E.; Cavalcanti, T.B.; Coelho, M.A.N.; Costa, A.F.; Costa, D.P.; Goldenberg, R.; Labiak, P.H.; et al. The Brazil Flora Group Brazilian Flora 2020: Innovation and Collaboration to Meet Target 1 of the Global Strategy for Plant Conservation (GSPC). *Rodriguésia* **2018**, *69*, 1513–1527. [CrossRef]
26. Melo, C.M.L.D.; Silva, G.A.S.; Melo, A.R.S.; Freitas, A.C.D. COVID-19 Pandemic Outbreak: The Brazilian Reality from the First Case to the Collapse of Health Services. *An. Acad. Bras. Ciênc.* **2020**, *92*, e20200709. [CrossRef] [PubMed]
27. Silva, E.D.D.; Matias, S.M.S.; Barros, B.G.A.; Oliveira, F.J.V.D. A Importância Do Uso Das Plantas Medicinais, Frente Ao Cenário Atual Da Pandemia Causada Pelo SARS-CoV-2. *Res. Soc. Dev.* **2021**, *10*, e399101119834. [CrossRef]
28. Leitão, G.G.; Simas, N.K.; Soares, S.S.V.; De Brito, A.P.P.; Claros, B.M.G.; Brito, T.B.M.; Delle Monache, F. Chemistry and Pharmacology of Monimiaceae: A Special Focus on *Siparuna* and *Mollinedia*. *J. Ethnopharmacol.* **1999**, *65*, 87–102. [CrossRef]
29. Leitão, G.G.; Soares, S.S.V.; Brito, M.; Delle Monache, F.; De Barros, T. Kaempferol Glycosides from *Siparuna apiosyce*. *Phytochemistry* **2000**, *55*, 679–682. [CrossRef]
30. Silva, I.; Oliveira, F.; Oliveira, R. *Siparuna* Aublet Genus (Siparunaceae): From Folk Medicine to Chemical Composition and Biological Activity. *Trends Phytochem. Res.* **2021**, *5*, 168–189. [CrossRef]
31. Leal, C.M.; Simas, R.C.; Miranda, M.; Campos, M.F.; Gomes, B.A.; Siqueira, M.M.; Vale, G.D.; Gomes De Almeida, C.V.; Leitão, S.G.; Leitão, G.G. Amazonian *Siparuna* Extracts as Potential Anti-Influenza Agents: Metabolic Fingerprinting. *J. Ethnopharmacol.* **2021**, *270*, 113788. [CrossRef]
32. Instituto Nacional de Pesquisas da Amazônia Herbário INPA. Available online: https://specieslink.net/search/ (accessed on 10 April 2024).
33. Leal, C.M.; Leitão, S.G.; Sausset, R.; Mendonça, S.C.; Nascimento, P.H.A.; Cheohen, C.F.; Esteves, M.E.A.; Leal Da Silva, M.; Gondim, T.S.; Monteiro, M.E.S.; et al. Flavonoids from *Siparuna cristata* as Potential Inhibitors of SARS-CoV-2 Replication. *Rev. Bras. Farmacogn.* **2021**, *31*, 658–666. [CrossRef]
34. Ouassaf, M.; Belaidi, S.; Chtita, S.; Lanez, T.; Abul Qais, F.; Md Amiruddin, H. Combined Molecular Docking and Dynamics Simulations Studies of Natural Compounds as Potent Inhibitors against SARS-CoV-2 Main Protease. *J. Biomol. Struct. Dyn.* **2022**, *40*, 11264–11273. [CrossRef]

35. Elattar, M.M.; Hammoda, H.M.; Ghareeb, D.A.; El-Hosseny, M.F.; Seadawy, M.G.; Celik, I.; Darwish, R.S.; Dawood, H.M. An Integrated Strategy Combining UPLC-MS/MS, Chemometrics, Molecular Docking, and Molecular Dynamics Simulation for Metabolic Profiling of Onion (*Allium cepa* L.) Cultivars and Unravelling Potential Anti-COVID-19 Metabolites. *S. Afr. J. Bot.* **2023**, *162*, 885–900. [CrossRef]
36. Darwish, R.S.; El-Banna, A.A.; Ghareeb, D.A.; El-Hosseny, M.F.; Seadawy, M.G.; Dawood, H.M. Chemical Profiling and Unraveling of Anti-COVID-19 Biomarkers of Red Sage (*Lantana camara* L.) Cultivars Using UPLC-MS/MS Coupled to Chemometric Analysis, In Vitro Study and Molecular Docking. *J. Ethnopharmacol.* **2022**, *291*, 115038. [CrossRef] [PubMed]
37. Sweilam, S.H.; Alqarni, M.H.; Youssef, F.S. Antimicrobial Alkaloids from Marine-Derived Fungi as Drug Leads versus COVID-19 Infection: A Computational Approach to Explore Their Anti-COVID-19 Activity and ADMET Properties. *Evid. Based Complement. Alternat. Med.* **2022**, *2022*, 5403757. [CrossRef] [PubMed]
38. Junior, A.G.; Tolouei, S.E.L.; Dos Reis Lívero, F.A.; Gasparotto, F.; Boeing, T.; De Souza, P. Natural Agents Modulating ACE-2: A Review of Compounds with Potential against SARS-CoV-2 Infections. *Curr. Pharm. Des.* **2021**, *27*, 1588–1596. [CrossRef] [PubMed]
39. Sharma, D.; Sharma, N.; Manchanda, N.; Prasad, S.K.; Sharma, P.C.; Thakur, V.K.; Rahman, M.M.; Dhobi, M. Bioactivity and In Silico Studies of Isoquinoline and Related Alkaloids as Promising Antiviral Agents: An Insight. *Biomolecules* **2023**, *13*, 17. [CrossRef]
40. Leal, C.M.; Leitão, S.G.; De Mello, L.L.O.; Rangel, I.D.C.; Da Silva, C.V.A.; Miranda, M.D.; Tucci, A.R.; De Assis, C.B.; Sacramento, C.D.Q.; Fintelman-Rodrigues, N.; et al. Bioassay-Guided Fractionation of *Siparuna glycycarpa* n-Butanol Extract with Inhibitory Activity against Influenza A(H1N1)Pdm09 Virus by Centrifugal Partition Chromatography (CPC). *Molecules* **2022**, *27*, 399. [CrossRef]
41. Haider, M.; Anand, V.; Enayathullah, M.G.; Parekh, Y.; Ram, S.; Kumari, S.; Anmol; Panda, G.; Shukla, M.; Dholakia, D.; et al. Anti-SARS-CoV-2 Potential of *Cissampelos Pareira* L. Identified by Connectivity Map-Based Analysis and In Vitro Studies. *BMC Complement. Med. Ther.* **2022**, *22*, 114. [CrossRef]
42. Abdallah, H.M.; El-Halawany, A.M.; Darwish, K.M.; Algandaby, M.M.; Mohamed, G.A.; Ibrahim, S.R.M.; Koshak, A.E.; Elhady, S.S.; Fadil, S.A.; Alqarni, A.A.; et al. Bio-Guided Isolation of SARS-CoV-2 Main Protease Inhibitors from Medicinal Plants: In Vitro Assay and Molecular Dynamics. *Plants* **2022**, *11*, 1914. [CrossRef]
43. Lopez, J.; Laurito, J.; Lin, F.-T.; Duah, F.; Sharaf, M.; Aly, Y.; Wong, L.; Schiff, P. Alkaloids of *Siparuna tonduziana*. *Planta Med.* **1990**, *56*, 492. [CrossRef]
44. Marti, G.; Eparvier, V.; Morleo, B.; Ven, J.; Apel, C.; Bodo, B.; Amand, S.; Dumontet, V.; Lozach, O.; Meijer, L.; et al. Natural Aristolactams and Aporphine Alkaloids as Inhibitors of CDK1/Cyclin B and DYRK1A. *Molecules* **2013**, *18*, 3018–3027. [CrossRef]
45. Stévigny, C.; Jiwan, J.H.; Rozenberg, R.; De Hoffmann, E.; Quetin-Leclercq, J. Key Fragmentation Patterns of Aporphine Alkaloids by Electrospray Ionization with Multistage Mass Spectrometry. *Rapid Commun. Mass Spectrom.* **2004**, *18*, 523–528. [CrossRef]
46. Torres Castañeda, H.G.; Colmenares Dulcey, A.J.; Isaza Martínez, J.H. Flavonoid Glycosides from *Siparuna gigantotepala* Leaves and Their Antioxidant Activity. *Chem. Pharm. Bull.* **2016**, *64*, 502–506. [CrossRef] [PubMed]
47. Fielding, B.C.; Da Silva Maia Bezerra Filho, C.; Ismail, N.S.M.; Sousa, D.P.D. Alkaloids: Therapeutic Potential against Human Coronaviruses. *Molecules* **2020**, *25*, 5496. [CrossRef] [PubMed]
48. Lima, N.; Andrade, T.; Acquah, K.; Oliveira, M.; Gois, K.; Medeiros, L. Phytochemicals as Potential Antiviral Agents in SARS-COV-2 Therapy: An Update. *Quím. Nova* **2021**, *44*, 667–672. [CrossRef]
49. Abookleesh, F.L.; Al-Anzi, B.S.; Ullah, A. Potential Antiviral Action of Alkaloids. *Molecules* **2022**, *27*, 903. [CrossRef] [PubMed]
50. Mohanty, S.S.; Sahoo, C.R.; Paidesetty, S.K.; Padhy, R.N. Role of Phytocompounds as the Potential Anti-Viral Agent: An Overview. *Naunyn. Schmiedebergs Arch. Pharmacol.* **2023**, *396*, 2311–2329. [CrossRef]
51. Sadeghi, M.; Miroliaei, M. Inhibitory Effects of Selected Isoquinoline Alkaloids against Main Protease (Mpro) of SARS-CoV-2, in Silico Study. *Silico Pharmacol.* **2022**, *10*, 5. [CrossRef]
52. Ti, H.; Zhuang, Z.; Yu, Q.; Wang, S. Progress of Plant Medicine Derived Extracts and Alkaloids on Modulating Viral Infections and Inflammation. *Drug Des. Dev. Ther.* **2021**, *15*, 1385–1408. [CrossRef]
53. Kumar, N.; Singh, A.; Gulati, H.K.; Bhagat, K.; Kaur, K.; Kaur, J.; Dudhal, S.; Duggal, A.; Gulati, P.; Singh, H.; et al. Phytoconstituents from Ten Natural Herbs as Potent Inhibitors of Main Protease Enzyme of SARS-COV-2: In Silico Study. *Phytomedicine Plus* **2021**, *1*, 100083. [CrossRef]
54. Özçelik, B.; Kartal, M.; Orhan, I. Cytotoxicity, Antiviral and Antimicrobial Activities of Alkaloids, Flavonoids, and Phenolic Acids. *Pharm. Biol.* **2011**, *49*, 396–402. [CrossRef]
55. Al-Zahrani, M.H.; Alghamdi, R.A. In Silico Molecular Docking Analysis of the Potential Role of Reticuline and Coclaurine as Anti-Colorectal Cancer Alkaloids. *J. Pharm. Res. Int.* **2022**, *34*, 33–42. [CrossRef]
56. Rajan, M.; Prabhakaran, S.; Prusty, J.S.; Chauhan, N.; Gupta, P.; Kumar, A. Phytochemicals of *Cocculus hirsutus* Deciphered SARS-CoV-2 Inhibition by Targeting Main Proteases in Molecular Docking, Simulation, and Pharmacological Analyses. *J. Biomol. Struct. Dyn.* **2023**, *41*, 7406–7420. [CrossRef] [PubMed]

57. Dinda, B.; Dinda, M.; Dinda, S.; Chakraborty, M. Some Natural Compounds and Their Analogues Having Potent Anti-SARS-CoV-2 and Anti-Proteases Activities as Lead Molecules in Drug Discovery for COVID-19. *Eur. J. Med. Chem. Rep.* **2022**, *6*, 100079. [CrossRef] [PubMed]
58. Faisal, S.; Badshah, S.L.; Kubra, B.; Emwas, A.-H.; Jaremko, M. Alkaloids as Potential Antivirals. A Comprehensive Review. *Nat. Prod. Bioprospecting* **2023**, *13*, 4. [CrossRef] [PubMed]
59. Ellinger, B.; Bojkova, D.; Zaliani, A.; Cinatl, J.; Claussen, C.; Westhaus, S.; Keminer, O.; Reinshagen, J.; Kuzikov, M.; Wolf, M.; et al. A SARS-CoV-2 Cytopathicity Dataset Generated by High-Content Screening of a Large Drug Repurposing Collection. *Sci. Data* **2021**, *8*, 70. [CrossRef] [PubMed]
60. Wang, Z.; Li, K.; Maskey, A.R.; Huang, W.; Toutov, A.A.; Yang, N.; Srivastava, K.; Geliebter, J.; Tiwari, R.; Miao, M.; et al. A Small Molecule Compound Berberine as an Orally Active Therapeutic Candidate against COVID-19 and SARS: A Computational and Mechanistic Study. *FASEB J.* **2021**, *35*, e21360. [CrossRef]
61. Heister, P.M.; Poston, R.N. Pharmacological Hypothesis: TPC2 Antagonist Tetrandrine as a Potential Therapeutic Agent for COVID-19. *Pharmacol. Res. Perspect.* **2020**, *8*, e00653. [CrossRef]
62. Huang, S.-T.; Chen, Y.; Chang, W.-C.; Chen, H.-F.; Lai, H.-C.; Lin, Y.-C.; Wang, W.-J.; Wang, Y.-C.; Yang, C.-S.; Wang, S.-C.; et al. *Scutellaria barbata* D. Don Inhibits the Main Proteases (Mpro and TMPRSS2) of Severe Acute Respiratory Syndrome Coronavirus 2 (SARS-CoV-2) Infection. *Viruses* **2021**, *13*, 826. [CrossRef]
63. Xia, B.; Shen, X.; He, Y.; Pan, X.; Liu, F.-L.; Wang, Y.; Yang, F.; Fang, S.; Wu, Y.; Duan, Z.; et al. SARS-CoV-2 Envelope Protein Causes Acute Respiratory Distress Syndrome (ARDS)-like Pathological Damages and Constitutes an Antiviral Target. *Cell Res.* **2021**, *31*, 847–860. [CrossRef]
64. He, C.-L.; Huang, L.-Y.; Wang, K.; Gu, C.-J.; Hu, J.; Zhang, G.-J.; Xu, W.; Xie, Y.-H.; Tang, N.; Huang, A.-L. Identification of Bis-Benzylisoquinoline Alkaloids as SARS-CoV-2 Entry Inhibitors from a Library of Natural Products. *Signal Transduct. Target. Ther.* **2021**, *6*, 131. [CrossRef]
65. Ghareeb, D.A.; Saleh, S.R.; Seadawy, M.G.; Nofal, M.S.; Abdulmalek, S.A.; Hassan, S.F.; Khedr, S.M.; AbdElwahab, M.G.; Sobhy, A.A.; Abdel-Hamid, A.S.A.; et al. Nanoparticles of ZnO/Berberine Complex Contract COVID-19 and Respiratory Co-Bacterial Infection in Addition to Elimination of Hydroxychloroquine Toxicity. *J. Pharm. Investig.* **2021**, *51*, 735–757. [CrossRef]
66. Varghese, F.; Van Woudenbergh, E.; Overheul, G.; Eleveld, M.; Kurver, L.; Van Heerbeek, N.; Van Laarhoven, A.; Miesen, P.; Den Hartog, G.; De Jonge, M.; et al. Berberine and Obatoclax Inhibit SARS-Cov-2 Replication in Primary Human Nasal Epithelial Cells In Vitro. *Viruses* **2021**, *13*, 282. [CrossRef] [PubMed]
67. Kanimozhi, G.; Pradhapsingh, B.; Singh Pawar, C.; Khan, H.A.; Alrokayan, S.H.; Prasad, N.R. SARS-CoV-2: Pathogenesis, Molecular Targets and Experimental Models. *Front. Pharmacol.* **2021**, *12*, 638334. [CrossRef] [PubMed]
68. Mahoney, M.; Damalanka, V.C.; Tartell, M.A.; Chung, D.H.; Lourenço, A.L.; Pwee, D.; Mayer Bridwell, A.E.; Hoffmann, M.; Voss, J.; Karmakar, P.; et al. A Novel Class of TMPRSS2 Inhibitors Potently Block SARS-CoV-2 and MERS-CoV Viral Entry and Protect Human Epithelial Lung Cells. *Proc. Natl. Acad. Sci. USA* **2021**, *118*, e2108728118. [CrossRef]
69. White, J.M.; Schiffer, J.T.; Bender Ignacio, R.A.; Xu, S.; Kainov, D.; Ianevski, A.; Aittokallio, T.; Frieman, M.; Olinger, G.G.; Polyak, S.J. Drug Combinations as a First Line of Defense against Coronaviruses and Other Emerging Viruses. *mBio* **2021**, *12*, e03347-21. [CrossRef]
70. Andrade, M.A.; Cardoso, M.G.; Gomes, M.S.; Brown, L. Biological Activity of *Siparuna guianensis* Essential Oils: A Potential Source in the Antiviral Therapy. *Braz. J. Microbiol.* **2015**, *56*, 457–464.
71. Hung, L.-H.; Guerquin, M.; Samudrala, R. GPU-Q-J, a Fast Method for Calculating Root Mean Square Deviation (RMSD) after Optimal Superposition. *BMC Res. Notes* **2011**, *4*, 97. [CrossRef]
72. Wu, K.; Peng, G.; Wilken, M.; Geraghty, R.J.; Li, F. Mechanisms of Host Receptor Adaptation by Severe Acute Respiratory Syndrome Coronavirus. *J. Biol. Chem.* **2012**, *287*, 8904–8911. [CrossRef]
73. Lan, J.; Ge, J.; Yu, J.; Shan, S.; Zhou, H.; Fan, S.; Zhang, Q.; Shi, X.; Wang, Q.; Zhang, L.; et al. Structure of the SARS-CoV-2 Spike Receptor-Binding Domain Bound to the ACE2 Receptor. *Nature* **2020**, *581*, 215–220. [CrossRef]
74. Su, H.; Yao, S.; Zhao, W.; Li, M.; Liu, J.; Shang, W.; Xie, H.; Ke, C.; Hu, H.; Gao, M.; et al. Anti-SARS-CoV-2 Activities In Vitro of Shuanghuanglian Preparations and Bioactive Ingredients. *Acta Pharmacol. Sin.* **2020**, *41*, 1167–1177. [CrossRef]
75. Kuzikov, M.; Costanzi, E.; Reinshagen, J.; Esposito, F.; Vangeel, L.; Wolf, M.; Ellinger, B.; Claussen, C.; Geisslinger, G.; Corona, A.; et al. Identification of Inhibitors of SARS-CoV-2 3CL-Pro Enzymatic Activity Using a Small Molecule In Vitro Repurposing Screen. *ACS Pharmacol. Transl. Sci.* **2021**, *4*, 1096–1110. [CrossRef]
76. Shen, Z.; Ratia, K.; Cooper, L.; Kong, D.; Lee, H.; Kwon, Y.; Li, Y.; Alqarni, S.; Huang, F.; Dubrovskyi, O.; et al. Design of SARS-CoV-2 PLpro Inhibitors for COVID-19 Antiviral Therapy Leveraging Binding Cooperativity. *J. Med. Chem.* **2022**, *65*, 2940–2955. [CrossRef] [PubMed]
77. Calleja, D.J.; Kuchel, N.; Lu, B.G.C.; Birkinshaw, R.W.; Klemm, T.; Doerflinger, M.; Cooney, J.P.; Mackiewicz, L.; Au, A.E.; Yap, Y.Q.; et al. Insights Into Drug Repurposing, as Well as Specificity and Compound Properties of Piperidine-Based SARS-CoV-2 PLpro Inhibitors. *Front. Chem.* **2022**, *10*, 861209. [CrossRef]

78. Skoltech iMolecule. Available online: https://sites.skoltech.ru/imolecule/tools/bitenet (accessed on 4 April 2024).
79. Eweas, A.F.; Alhossary, A.A.; Abdel-Moneim, A.S. Molecular Docking Reveals Ivermectin and Remdesivir as Potential Repurposed Drugs Against SARS-CoV-2. *Front. Microbiol.* **2021**, *11*, 592908. [CrossRef] [PubMed]
80. Ministério da Saúde. Medicamentos para COVID-19. Available online: https://www.gov.br/anvisa/pt-br/assuntos/paf/coronavirus/medicamentos (accessed on 3 July 2023).
81. European Medicines Agency. COVID-19 Medicines. Available online: https://www.ema.europa.eu/en/human-regulatory/overview/public-health-threats/coronavirus-disease-covid-19/covid-19-medicines#authorised-covid-19-treatments-section (accessed on 3 July 2023).
82. Food & Drug Administration. Coronavirus Drugs. Available online: https://www.fda.gov/drugs/emergency-preparedness-drugs/coronavirus-covid-19-drugs (accessed on 3 July 2023).
83. Pinto, A.M.; Ribeiro, R.J.; Alencar, J.D.C.; Barbosa, A.P. Fenologia de Simarouba Amara Aubl. Na Reserva Florestal Adolpho Ducke, Manaus, AM. *Acta Amaz.* **2005**, *35*, 347–352. [CrossRef]
84. Dludla, P.V.; Jack, B.; Viraragavan, A.; Pheiffer, C.; Johnson, R.; Louw, J.; Muller, C.J.F. A Dose-Dependent Effect of Dimethyl Sulfoxide on Lipid Content, Cell Viability and Oxidative Stress in 3T3-L1 Adipocytes. *Toxicol. Rep.* **2018**, *5*, 1014–1020. [CrossRef]
85. World Health Organization. Laboratory Biosafety Guidance Related to SARS-CoV-2 (COVID-19): Interim Guidance (Update). Available online: https://policycommons.net/artifacts/11487640/laboratory-biosafety-guidance-related-to-sars-cov-2-covid-19/12378871/ (accessed on 2 May 2024).
86. Daina, A.; Michielin, O.; Zoete, V. SwissADME: A Free Web Tool to Evaluate Pharmacokinetics, Drug-Likeness and Medicinal Chemistry Friendliness of Small Molecules. *Sci. Rep.* **2017**, *7*, 42717. [CrossRef]
87. Molecular Modeling Group of the Swiss Institute of Bioinformatics. SwissADME: SwissDrugDesign. Available online: http://www.swissadme.ch (accessed on 4 April 2024).
88. Sander, T.; Freyss, J.; Von Korff, M.; Rufener, C. DataWarrior: An Open-Source Program For Chemistry Aware Data Visualization And Analysis. *J. Chem. Inf. Model.* **2015**, *55*, 460–473. [CrossRef]
89. Sander, T. Openmolecules.Org. Available online: https://openmolecules.org/about.html (accessed on 1 January 2024).
90. Berman, H.M.; Bhat, T.N.; Bourne, P.E.; Feng, Z.; Gilliland, G.; Weissig, H.; Westbrook, J. The Protein Data Bank and the Challenge of Structural Genomics. *Nat. Struct. Mol. Biol.* **2000**, *7*, 957–959. [CrossRef]
91. RCSB Protein Data Bank (RCSB PDB). Available online: https://www.rcsb.org/ (accessed on 3 April 2024).
92. wwPDB consortium; Burley, S.K.; Berman, H.M.; Bhikadiya, C.; Bi, C.; Chen, L.; Costanzo, L.D.; Christie, C.; Duarte, J.M.; Dutta, S.; et al. Protein Data Bank: The Single Global Archive for 3D Macromolecular Structure Data. *Nucleic Acids Res.* **2019**, *47*, D520–D528. [CrossRef]
93. Kozlovskii, I.; Popov, P. Spatiotemporal Identification of Druggable Binding Sites Using Deep Learning. *Commun. Biol.* **2020**, *3*, 618. [CrossRef]
94. Kozlovskii, I.; Popov, P. Protein–Peptide Binding Site Detection Using 3D Convolutional Neural Networks. *J. Chem. Inf. Model.* **2021**, *61*, 3814–3823. [CrossRef] [PubMed]
95. Kozlovskii, I.; Popov, P. Structure-Based Deep Learning for Binding Site Detection in Nucleic Acid Macromolecules. *NAR Genom. Bioinform.* **2021**, *3*, lqab111. [CrossRef] [PubMed]
96. De Azevedo, W., Jr. MolDock Applied to Structure-Based Virtual Screening. *Curr. Drug Targets* **2010**, *11*, 327–334. [CrossRef]
97. Thomsen, R.; Christensen, M.H. MolDock: A New Technique for High-Accuracy Molecular Docking. *J. Med. Chem.* **2006**, *49*, 3315–3321. [CrossRef]
98. Damayanti; Prakoeswa, C.R.S.; Purwanto, D.A.; Endaryanto, A.; Siswandono. Molecullar Docking of Epigallocatechin-3-Gallate (EGCG) on Keap1-Nrf2 Complex Protein in Photoaging Prevention. *Medico-Leg. Update* **2020**, *20*, 305–311. [CrossRef]
99. Dassault Systemes Biovia. *Discovery Studio visualizer v20.1*; Dassault Systemes BIOVIA: San Diego, CA, USA, 2019; Available online: https://discover.3ds.com/discovery-studio-visualizer-download (accessed on 1 January 2025).
100. Palacio-Rodríguez, K.; Lans, I.; Cavasotto, C.N.; Cossio, P. Exponential Consensus Ranking Improves the Outcome in Docking and Receptor Ensemble Docking. *Sci. Rep.* **2019**, *9*, 5142. [CrossRef]
101. Blanes-Mira, C.; Fernández-Aguado, P.; De Andrés-López, J.; Fernández-Carvajal, A.; Ferrer-Montiel, A.; Fernández-Ballester, G. Comprehensive Survey of Consensus Docking for High-Throughput Virtual Screening. *Molecules* **2022**, *28*, 175. [CrossRef]
102. Rishton, G.M. Nonleadlikeness and Leadlikeness in Biochemical Screening. *Drug Discov. Today* **2003**, *8*, 86–96. [CrossRef]
103. Veber, D.F.; Johnson, S.R.; Cheng, H.-Y.; Smith, B.R.; Ward, K.W.; Kopple, K.D. Molecular Properties That Influence the Oral Bioavailability of Drug Candidates. *J. Med. Chem.* **2002**, *45*, 2615–2623. [CrossRef]
104. Wahyuni, T.S.; Utsubo, C.A.; Hotta, H. Promising Anti-Hepatitis C Virus Compounds from Natural Resources. *Nat. Prod. Commun.* **2016**, *11*, 1193–1200. [CrossRef]
105. Koutsoudakis, G.; Romero-Brey, I.; Berger, C.; Pérez-Vilaró, G.; Monteiro Perin, P.; Vondran, F.W.R.; Kalesse, M.; Harmrolfs, K.; Müller, R.; Martinez, J.P.; et al. Soraphen A: A Broad-Spectrum Antiviral Natural Product with Potent Anti-Hepatitis C Virus Activity. *J. Hepatol.* **2015**, *63*, 813–821. [CrossRef]

106. GRACE. Available online: https://plasma-gate.weizmann.ac.il/Grace/ (accessed on 2 May 2024).
107. Elsebai, M.F.; Koutsoudakis, G.; Saludes, V.; Pérez-Vilaró, G.; Turpeinen, A.; Mattila, S.; Pirttilä, A.M.; Fontaine-Vive, F.; Mehiri, M.; Meyerhans, A.; et al. Pan-Genotypic Hepatitis C Virus Inhibition by Natural Products Derived from the Wild Egyptian Artichoke.
J. Virol. **2016**, *90*, 1918–1930. [CrossRef]

Disclaimer/Publisher's Note: The statements, opinions and data contained in all publications are solely those of the individual author(s) and contributor(s) and not of MDPI and/or the editor(s). MDPI and/or the editor(s) disclaim responsibility for any injury to people or property resulting from any ideas, methods, instructions or products referred to in the content.

7. CONCLUSÃO

O *workflow* empregado neste estudo representa uma abordagem inovadora e integrada para a descoberta de substâncias bioativas com potencial antiviral. A combinação de triagem química e biológica permite a identificação preliminar de extratos promissores, enquanto o processamento avançado de dados químicos, aliado a técnicas de *data mining*, possibilita a extração de padrões relevantes associados à bioatividade. A aplicação de modelos preditivos baseados em métodos quimiométricos aprimora a seleção das substâncias mais promissoras, reduzindo o número de ensaios experimentais necessários. Além disso, o uso de redes moleculares auxilia na anotação das substâncias e visualização qualitativa da atividade *onetarget e/ou multitarget*, proporcionando uma interpretação mais robusta dos resultados. Para validar a viabilidade das substâncias preditas, são empregados ensaios *in silico*, incluindo *docking* e dinâmica molecular e ADMET, permitindo a análise da afinidade de ligação, estabilidade conformacional e perfil farmacocinético e de toxidez. Por fim, a eficácia dos extratos das espécies selecionadas é confirmada experimentalmente por meio de ensaios em pseudovírus e no vírus SARS-CoV-2, corroborando os resultados obtidos nos testes direcionados às proteínas essenciais do ciclo viral. Esse fluxo de trabalho não apenas acelera a descoberta de novas moléculas antivirais, mas também otimiza recursos, tornando o processo mais eficiente e racional na busca por terapias eficazes.

Neste cenário, as famílias Siparunaceae e Myrtaceae destacam-se por fornecer substâncias com potencial de inibição de alvos virais essenciais à infecção e replicação do vírus. A triagem biológica revelou que extratos de *Siparuna* spp. e *Eugenia* spp. apresentam significativa ação inibitória na interação *Spike*:ACE2 e nas proteases $3CL^{pro}$ e PL^{pro}. A caracterização química por LC-MS/MS permitiu anotar substâncias *multitarget* bioativas, com destaque para alcaloides como bulbocapnina e reticulina, além de myrtucommulonas e derivados de acilfloroglucinóis, reforçando sua relevância na busca por antivirais. A aplicação de ferramentas computacionais otimizou a seleção dos bioativos. Essa abordagem possibilitou a identificação de padrões associados à atividade antiviral, fornecendo evidências robustas sobre os extratos analisados e facilitando a anotação estrutural das substâncias ativas.

Além de validar achados experimentais, os resultados destes estudos reforçam a importância da biodiversidade brasileira na descoberta de antivirais. A combinação das técnicas propostas vem tonando o processo mais eficiente e reduzindo a necessidade de ensaios prolongados e onerosos. Logo, esse estudo contribui significativamente para a triagem e modelagem preditiva de substâncias naturais, otimizando recursos científicos e financeiros

na busca por novos tratamentos anti-SARS-CoV-2.

Diante da ameaça constante de novas variantes e pandemias emergentes, manter esforços na busca por alternativas terapêuticas eficazes e acessíveis é essencial. Além de ampliar o conhecimento sobre os potenciais de espécies brasileiras e suas substâncias, o estudo propõe novas metodologias para a triagem e priorização de bioativos, impulsionando avanços em farmacognosia e bioprospecção. O emprego de modelos preditivos na farmacognosia e na química de produtos naturais abre novas possibilidades para a identificação otimizada de antivirais, direcionando ensaios mais eficazes *in vitro* e *in vivo*.

Os impactos desse estudo vão além da COVID-19 ou de doenças antivirais, pois as estratégias desenvolvidas podem ser aplicadas na descoberta de fármacos para diversas outras doenças, destacando a importância de abordagens interdisciplinares na ciência para beneficiar a saúde pública global.

8. PERSPECTIVAS

Este projeto conta com dados adicionais que não integram este documento, mas que já estão submetidos. O trabalho intitulado "*Plants metabolites as in vitro inhibitors of SARS-CoV-2 targets: a systematic review and computational analysis*", foi encabeçado pelo aluno e fruto de colaboração com todo corpo discente do laboratório FitoFar e diversos colaboradores. Atualmente, o artigo encontra-se submetido e em fase de revisão.

A pesquisa envolveu uma revisão sistemática, conduzida de acordo com as diretrizes PRISMA, com buscas realizadas em seis bases de dados eletrônicas (*Scielo*, *ScienceDirect*, *Scopus*, *Springer*, *Web of Science* e *PubMed*) entre janeiro de 2020 e fevereiro de 2024. No total, foram encontradas 330 substâncias derivadas de plantas com potencial inibitório *in vitro* contra os alvos do SARS-CoV-2, incluindo $3CL^{pro}$, PL^{pro}, SP e RdRp. Foram empregadas análises computacionais utilizando SwissADME, pkCSM, ADMETlab, ProTox3, Toxtree e DataWarrior para prever os perfis de absorção, distribuição, metabolismo, excreção e toxicidade (ADMET), além de outros parâmetros relevantes da química medicinal. Os resultados indicam que diversos metabólitos vegetais demonstram inibição significativa *in vitro* contra os alvos virais, embora poucos apresentem viabilidade para desenvolvimento farmacêutico sem modificações adicionais. Entre os compostos analisados, ácidos fenólicos se destacaram como potenciais candidatos ao desenvolvimento de terapias anti-SARS-CoV-2.

Todas as atividades propostas no projeto (triagens químicas e biológicas) foram concluídas com êxito, garantindo a obtenção de resultados robustos e essenciais para a elaboração de modelos preditivos das atividades *onetarget* e *multitarget* para cada família botânica investigada. Até o momento, dois artigos foram finalizados com foco no desenvolvimento de modelos quimiométricos de predição para os extratos das famílias Siparunaceae e Myrtaceae. Os modelos dos extratos da família Rhamnaceae já foram construídos, os íons preditos estão sendo anotados, e o manuscrito em fase final de preparação para submissão ainda no primeiro semestre de 2025.

Mesmo com a conclusão do doutorado, ainda há um vasto conjunto de dados a ser explorado, impulsionando novas publicações para o grupo. Pretende-se manter a colaboração com a equipe para a construção de modelos preditivos das quatro famílias botânicas restantes (Verbenaceae, Lamiaceae, Loranthaceae e Annonaceae), além do desenvolvimento de um modelo unificado para espécies da biodiversidade brasileira e de um modelo preditivo para os descritores moleculares mais promissores, utilizando *machine learning* e outras abordagens em quimioinformática. A viabilidade desses estudos foi e continuará a ser garantida pelo esforço

conjunto de uma equipe interdisciplinar, composta por alunos de pós-graduação, iniciação científica, pós-doutorado e professores colaboradores dos laboratórios FitoFar e FitoCCC.

9. REFERÊNCIAS BIBLIOGRÁFICAS

AFOULLOUSS, Sam; BALSAM, Agata; ALLCOCK, A. Louise; THOMAS, Olivier P.. Optimization of LC-MS2 Data Acquisition Parameters for Molecular Networking Applied to Marine Natural Products. **Metabolites**, [S.L.], v. 12, n. 3, p. 245, 14 mar. 2022. MDPI AG. http://dx.doi.org/10.3390/metabo12030245.

AKAY, Metin; SUBRAMANIAM, Shankar; BRENNAN, Colin; BONATO, Paolo; WAITS, Charlotte Mae K.; WHEELER, Bruce C.; FOTIADIS, Dimitrios I.. Healthcare Innovations to Address the Challenges of the COVID-19 Pandemic. **Ieee Journal Of Biomedical And Health Informatics**, [S.L.], v. 26, n. 7, p. 3294-3302, jul. 2022. Institute of Electrical and Electronics Engineers (IEEE). http://dx.doi.org/10.1109/jbhi.2022.3144941.

AL-HARRASI, Ahmed; BEHL, Tapan; UPADHYAY, Tanuj; CHIGURUPATI, Sridevi; BHATT, Shvetank; SEHGAL, Aayush; BHATIA, Saurabh; SINGH, Sukhbir; SHARMA, Neelam; VIJAYABALAN, Shantini. Targeting natural products against SARS-CoV-2. **Environmental Science and Pollution Research**, [S.L.], v. 29, n. 28, p. 42404-42432, 1 abr. 2022. Springer Science and Business Media LLC. http://dx.doi.org/10.1007/s11356-022-19770-2.

ALI, Kashif; IQBAL, Muzamal; KORTHOUT, Henrie A. A. J.; MALTESE, Federica; FORTES, Ana Margarida; PAIS, Maria Salomé; VERPOORTE, Robert; CHOI, Young Hae. NMR spectroscopy and chemometrics as a tool for anti-TNFα activity screening in crude extracts of grapes and other berries. **Metabolomics**, [S.L.], v. 8, n. 6, p. 1148-1161, 17 fev. 2012. Springer Science and Business Media LLC. http://dx.doi.org/10.1007/s11306-012-0406-8.

ALZAABI, Moza Mohamed; HAMDY, Rania; ASHMAWY, Naglaa S.; HAMODA, Alshaimaa M.; ALKHAYAT, Fatemah; KHADEMI, Neda Naser; JOUD, Sara Mahmoud Abo Al; EL-KEBLAWY, Ali A.; SOLIMAN, Sameh S. M.. Flavonoids are promising safe therapy against COVID-19. **Phytochemistry Reviews**, [S.L.], v. 21, n. 1, p. 291-312, 22 maio 2021. Springer Science and Business Media LLC. http://dx.doi.org/10.1007/s11101-021-09759-z.

AMPARO, Tatiane Roquete; SEIBERT, Janaína Brandão; SILVEIRA, Benila Maria; COSTA, Fernanda Senna Ferreira; ALMEIDA, Tamires Cunha; BRAGA, Saulo Fehelberg Pinto;

SILVA, Glenda Nicioli da; SANTOS, Orlando David Henrique dos; SOUZA, Gustavo Henrique Bianco de. Brazilian essential oils as source for the discovery of new anti-COVID-19 drug: a review guided by in silico study. **Phytochemistry Reviews**, [S.L.], v. 20, n. 5, p. 1013-1032, 13 abr. 2021. Springer Science and Business Media LLC. http://dx.doi.org/10.1007/s11101-021-09754-4.

ANDERSEN, Kristian G.; RAMBAUT, Andrew; LIPKIN, W. Ian; HOLMES, Edward C.; GARRY, Robert F.. The proximal origin of SARS-CoV-2. **Nature Medicine**, [S.L.], v. 26, n. 4, p. 450-452, 17 mar. 2020. Springer Science and Business Media LLC. http://dx.doi.org/10.1038/s41591-020-0820-9.

ANTONIO, Ananda da Silva; WIEDEMANN, Larissa Silveira Moreira; VEIGA-JUNIOR, Valdir Florêncio. Natural products' role against COVID-19. **Rsc Advances**, [S.L.], v. 10, n. 39, p. 23379-23393, 2020. Royal Society of Chemistry (RSC). http://dx.doi.org/10.1039/d0ra03774e.

ANVISA - Agência Nacional de Vigilância Sanitária. Coronavírus. **Informações sobre vacinas**. Ministério da Saúde - Governo Federal, Brasil. 2025. Disponível em: https://www.gov.br/anvisa/pt-br/assuntos/paf/coronavirus/vacinas. Acesso em: 02 fev. 2025a.

ANVISA - Agência Nacional de Vigilância Sanitária. Coronavírus. **Medicamentos para Covid-19**. Ministério da Saúde - Governo Federal, Brasil. 2025. Disponível em: https://www.gov.br/anvisa/pt-br/assuntos/paf/coronavirus/medicamentos. Acesso em: 02 fev. 2025b.

BARROS NETO, Benício de; SCARMINIO, Ieda S.; BRUNS, Roy E.. 25 anos de quimiometria no Brasil. **Química Nova**, [S.L.], v. 29, n. 6, p. 1401-1406, dez. 2006. FapUNIFESP (SciELO). http://dx.doi.org/10.1590/s0100-40422006000600042.

BAR-ON, Yinon M.; GOLDBERG, Yair; MANDEL, Micha; BODENHEIMER, Omri; FREEDMAN, Laurence; ALROY-PREIS, Sharon; ASH, Nachman; HUPPERT, Amit; MILO, Ron. Protection against Covid-19 by BNT162b2 Booster across Age Groups. **New England Journal Of Medicine**, [S.L.], v. 385, n. 26, p. 2421-2430, 23 dez. 2021. Massachusetts Medical Society. http://dx.doi.org/10.1056/nejmoa2115926.

BERNAL, Jamie Lopez; ANDREWS, Nick; GOWER, Charlotte; GALLAGHER, Eileen; SIMMONS, Ruth; THELWALL, Simon; STOWE, Julia; TESSIER, Elise; GROVES, Natalie; DABRERA, Gavin. Effectiveness of Covid-19 Vaccines against the B.1.617.2 (Delta) Variant. **New England Journal Of Medicine**, [S.L.], v. 385, n. 7, p. 585-594, 12 ago. 2021. Massachusetts Medical Society. http://dx.doi.org/10.1056/nejmoa2108891.

BHUIYAN, Farhana Rumzum; HOWLADER, Sabbir; RAIHAN, Topu; HASAN, Mahmudul. Plants Metabolites: possibility of natural therapeutics against the covid-19 pandemic. **Frontiers In Medicine**, [S.L.], v. 7, p. 1-27, 7 ago. 2020. Frontiers Media SA. http://dx.doi.org/10.3389/fmed.2020.00444.

BIOMOL website. **FRET Substrates for COVID-19.** 2025. Disponível em: https://www.biomol.com/resources/biomol-blog/fret-substrates-for-covid-19-vaccine-development. Acesso em: 20 de fev. de 2025.

BOLCATO, Giovanni; BISSARO, Maicol; PAVAN, Matteo; STURLESE, Mattia; MORO, Stefano. Targeting the coronavirus SARS-CoV-2: computational insights into the mechanism of action of the protease inhibitors lopinavir, ritonavir and nelfinavir. **Scientific Reports**, [S.L.], v. 10, n. 1, p. 20927, 1 dez. 2020. Springer Science and Business Media LLC. http://dx.doi.org/10.1038/s41598-020-77700-z.

BOOZARI, Motahareh; HOSSEINZADEH, Hossein. Natural products for COVID -19 prevention and treatment regarding to previous coronavirus infections and novel studies. **Phytotherapy Research**, [S.L.], p. 1-13, 27 set. 2020. Wiley. http://dx.doi.org/10.1002/ptr.6873.

BORGES, Ricardo; RESENDE, João; MORAES, Aldebaran; PEREIRA, Alana; GARRETT, Rafael; BAUERMEISTER, Anelize; SILVA, Antonio. GUIA PARA PROCESSAMENTO DE DADOS DE CROMATOGRAFIA ACOPLADA A ESPECTROMETRIA DE MASSAS. **Química Nova**, [S.L.], p. 608-620, 2021. Sociedade Brasileira de Quimica (SBQ). http://dx.doi.org/10.21577/0100-4042.20170838.

BRITTIN, Nathaniel J.; ANDERSON, Josephine M.; BRAUN, Doug R.; RAJSKI, Scott R.; CURRIE, Cameron R.; BUGNI, Tim S. Machine learning-based bioactivity classification of natural products using LC-MS/MS metabolomics. **Journal of Natural Products**, [S.L.], v. 88,

p. 361–372, 2025. American Chemical Society and American Society of Pharmacognosy. https://doi.org/10.1021/acs.jnatprod.4c01123.

CAMPOS, Mariana Freire; MENDONÇA, Simony Carvalho; PEÑALOZA, Evelyn Maribel Condori; OLIVEIRA, Beatriz A. C. de; ROSA, Alice S.; LEITÃO, Gilda Guimarães; TUCCI, Amanda R.; FERREIRA, Vivian Neuza S.; OLIVEIRA, Thamara Kelcya F.; MIRANDA, Milene Dias. Anti-SARS-CoV-2 Activity of Ampelozizyphus amazonicus (Saracura-Mirá): focus on the modulation of the spike-ace2 interaction by chemically characterized bark extracts by lc-dad-apci-ms/ms. **Molecules**, [S.L.], v. 28, n. 7, p. 3159, 1 abr. 2023. MDPI AG. http://dx.doi.org/10.3390/molecules28073159.

CHAPMAN, Robert L.; ANDURKAR, Shridhar V. A review of natural products, their effects on SARS-CoV-2 and their utility as lead compounds in the discovery of drugs for the treatment of COVID-19. **Medicinal Chemistry Research**, [S.L.], v. 31, n. 1, p. 40-51, 2 dez. 2021. Springer Science and Business Media LLC. http://dx.doi.org/10.1007/s00044-021-02826-2.

CHALECKIS, Romanas; MEISTER, Isabel; ZHANG, Pei; WHEELOCK, Craig e. Challenges, progress and promises of metabolite annotation for LC–MS-based metabolomics. **Current Opinion In Biotechnology**, [S.L.], v. 55, p. 44-50, fev. 2019. Elsevier BV. http://dx.doi.org/10.1016/j.copbio.2018.07.010.

CHEOHEN, Caio Felipe de Araujo Ribas; ESTEVES, Maria Eduarda Alves; FONSECA, Thamirys Silva da; LEAL, Carla Monteiro; ASSIS, Fernanda de Lemos Fernandes; CAMPOS, Mariana Freire; REBELO, Raianne Soares; ALLONSO, Diego; LEITÃO, Gilda Guimarães; SILVA, Manuela Leal da. In silico screening of phenylethanoid glycosides, a class of pharmacologically active compounds as natural inhibitors of SARS-CoV-2 proteases. **Computational And Structural Biotechnology Journal**, [S.L.], v. 21, p. 1461-1472, 2023. Elsevier BV. http://dx.doi.org/10.1016/j.csbj.2023.02.020.

CONSTANT, Larissa Esteves Carvalho. “Expressão e purificação das proteases $3CL^{pro}$ e PL^{pro} de SARS-CoV-2 e identificação de compostos provenientes da biodiversidade brasileira como potenciais inibidores virais” - 02/09/2022 99 f. Mestrado em Ciências biológicas (Biofísica) Instituição de ensino: Universidade Federal do Rio de Janeiro, Rio de Janeiro, biblioteca depositária: biblioteca central do CCS.

CORREIA, Paulo R. M.; FERREIRA, Márcia M. C. Reconhecimento de padrões por métodos não supervisionados: explorando procedimentos quimiométricos para tratamento de dados analíticos. **Química Nova**, [S.L.], v. 30, n. 2, p. 481-487, abr. 2007. FapUNIFESP (SciELO). http://dx.doi.org/10.1590/s0100-40422007000200042.

DHAR, Mahesh S.; MARWAL, Robin; VS, Radhakrishnan; PONNUSAMY, Kalaiarasan; JOLLY, Bani; BHOYAR, Rahul C.; SARDANA, Viren; NAUSHIN, Salwa; ROPHINA, Mercy; MELLAN, Thomas A.. Genomic characterization and epidemiology of an emerging SARS-CoV-2 variant in Delhi, India. **Science**, [S.L.], v. 374, n. 6570, p. 995-999, 19 nov. 2021. American Association for the Advancement of Science (AAAS). http://dx.doi.org/10.1126/science.abj9932.

DÖMLING, Alexander; GAO, Li. Chemistry and Biology of SARS-CoV-2. **Chem**, [S.L.], v. 6, n. 6, p. 1283-1295, jun. 2020. Elsevier BV. http://dx.doi.org/10.1016/j.chempr.2020.04.023.

EKIERT, Halina Maria; SZOPA, Agnieszka. Biological Activities of Natural Products. **Molecules**, [S.L.], v. 25, n. 23, p. 5769, 7 dez. 2020. MDPI AG. http://dx.doi.org/10.3390/molecules25235769.

EMA – European Medicines Agency. Estratégia e políticas: Resposta ao coronavírus. **Vacinas seguras contra a COVID-19 para os europeus.** 2025. Disponível em: https://commission.europa.eu/strategy-and-policy/coronavirus-response/safe-covid-19-vaccines-europeans_pt#garantir-vacinas-seguras-e-eficazes. Acesso em: 02 fev. 2025a.

EMA – European Medicines Agency. Estratégia e políticas: Human regulatory. **COVID-19 medicines.** 2025. Disponível em: https://www.ema.europa.eu/en/human-regulatory/overview/public-health-threats/coronavirus-disease-covid-19/covid-19-medicines#authorised-covid-19-treatments-section. Acesso em: 02 fev. 2025b.

FDA – Food & Drug Administration. Vaccines, Blood & Biologics. **Vaccines**. Vaccines Licensed for use in the United States. 2025. Disponível em: https://www.fda.gov/vaccines-blood-biologics/vaccines/vaccines-licensed-use-united-states. Acesso em: 02 fev. 2025a.

FDA – Food & Drug Administration. Drugs: Emergency Preparedness. **Coronavirus Drugs**. 2025. Disponível em: https://www.fda.gov/drugs/emergency-preparedness-drugs/coronavirus-covid-19-drugs. Acesso em: 02 fev. 2025b.

FERREIRA, Marcia Miguel Castro. **Quimiometria: conceitos, métodos e aplicações**. Campinas, SP: Editora Unicamp, 2015. 493 p.

GAO, Xiaopan; QIN, Bo; CHEN, Pu; ZHU, Kaixiang; HOU, Pengjiao; WOJDYLA, Justyna Aleksandra; WANG, Meitian; CUI, Sheng. Crystal structure of SARS-CoV-2 papain-like protease. **Acta Pharmaceutica Sinica B**, [S.L.], v. 11, n. 1, p. 237-245, jan. 2021. Elsevier BV. http://dx.doi.org/10.1016/j.apsb.2020.08.014.

GBIF – Global Biodiversity Information Facility. GBIF Secretariat: Plantae. GBIF Backbone Taxonomy. **Checklist dataset Plantae.** 2023. Disponível em: https://doi.org/10.15468/39omei. Acesso em: 03 jul. 2023.

GNPS – Global Natural Products Society Molecular Networking. **Documentations**. Disponível em: https://ccms-ucsd.github.io/GNPSDocumentation/featurebasedmolecularnetworking-with-mzmine2. Acesso em: 03 jul. 2023.

GODINHO, Patrícia I. C.; SOENGAS, Raquel G.; SILVA, Vera L. M.. Therapeutic Potential of Glycosyl Flavonoids as Anti-Coronaviral Agents. **Pharmaceuticals**, [S.L.], v. 14, n. 6, p. 546, 7 jun. 2021. MDPI AG. http://dx.doi.org/10.3390/ph14060546.

GUPTA, Divya; AWADHIYA, Onkar; SAIGAL, Saurabh; KUMAR, Ashok. Structure, genomic analysis, and pathogenesis of SARS-CoV-2. **Advanced Biosensors For Virus Detection**, [S.L.], p. 37-60, 2022. Elsevier. http://dx.doi.org/10.1016/b978-0-12-824494-4.00003-5.

GYEBI, Gideon A.; ADEGUNLOYE, Adegbenro P.; IBRAHIM, Ibrahim M.; OGUNYEMI, Oludare M.; AFOLABI, Saheed O.; OGUNRO, Olalekan B.. Prevention of SARS-CoV-2 cell entry: insight from in silico interaction of drug-like alkaloids with spike glycoprotein, human ace2, and tmprss2. **Journal Of Biomolecular Structure And Dynamics**, [S.L.], v. 40, n. 5, p. 2121-2145, 22 out. 2020. Informa UK Limited. http://dx.doi.org/10.1080/07391102.2020.1835726.

HU, Ben; GUO, Hua; ZHOU, Peng; SHI, Zheng-Li. Characteristics of SARS-CoV-2 and COVID-19. **Nature Reviews Microbiology**, [S.L.], v. 19, n. 3, p. 141-154, 6 out. 2020. Springer Science and Business Media LLC. http://dx.doi.org/10.1038/s41579-020-00459-7.

HUANG, Yuan; YANG, Chan; XU, Xin-Feng; XU, Wei; LIU, Shu-Wen. Structural and functional properties of SARS-CoV-2 spike protein: potential antivirus drug development for covid-19. **Acta Pharmacologica Sinica**, [S.L.], v. 41, n. 9, p. 1141-1149, 3 ago. 2020. Springer Science and Business Media LLC. http://dx.doi.org/10.1038/s41401-020-0485-4.

IQHRAMMULLAH, Muhammad; RIZKI, Diva Rayyan; PURNAMA, Agnia; DUTA, Teuku Fais; HARAPAN, Harapan; IDROES, Rinaldi; GINTING, Binawati. Antiviral Molecular Targets of Essential Oils against SARS-CoV-2: a systematic review. **Scientia Pharmaceutica**, [S.L.], v. 91, n. 1, p. 15, 6 mar. 2023. MDPI AG. http://dx.doi.org/10.3390/scipharm91010015.

JEONG, Gi Uk; SONG, Hanra; YOON, Gun Young; KIM, Doyoun; KWON, Young-Chan. Therapeutic Strategies Against COVID-19 and Structural Characterization of SARS-CoV-2: a review. **Frontiers In Microbiology**, [S.L.], v. 11, p. 1-11, 14 jul. 2020. Frontiers Media SA. http://dx.doi.org/10.3389/fmicb.2020.01723.

KUMAR, Sanjay; PAUL, Pradipta; YADAV, Pardeep; KAUL, Ridhima; MAITRA, S.s.; JHA, Saurabh Kumar; CHAARI, Ali. A multi-targeted approach to identify potential flavonoids against three targets in the SARS-CoV-2 life cycle. **Computers In Biology And Medicine**, [S.L.], v. 142, p. 105231, mar. 2022. Elsevier BV. http://dx.doi.org/10.1016/j.compbiomed.2022.105231.

LAN, Jun; GE, Jiwan; YU, Jinfang; SHAN, Sisi; ZHOU, Huan; FAN, Shilong; ZHANG, Qi; SHI, Xuanling; WANG, Qisheng; ZHANG, Linqi. Structure of the SARS-CoV-2 spike receptor-binding domain bound to the ACE2 receptor. **Nature**, [S.L.], v. 581, n. 7807, p. 215-220, 30 mar. 2020. Springer Science and Business Media LLC. http://dx.doi.org/10.1038/s41586-020-2180-5.

LANÇAS, Fernando M. **Espectrometria de Massas:** Fundamentos, Instrumentação e Aplicações. Campinas, SP: Editora Átomo, 2019. 356 pp.

LEAL, Carla Monteiro; LEITÃO, Suzana Guimarães; SAUSSET, Romain; MENDONÇA, Simony C.; NASCIMENTO, Pedro H. A.; CHEOHEN, Caio Felipe de Araujo R.; ESTEVES, Maria Eduarda A.; SILVA, Manuela Leal da; GONDIM, Tayssa Santos; MONTEIRO, Maria Eduarda S.. Flavonoids from *Siparuna cristata* as Potential Inhibitors of SARS-CoV-2 Replication. **Revista Brasileira de Farmacognosia**, [S.L.], v. 31, n. 5, p. 658-666, 20 jul.

2021a. Springer Science and Business Media LLC. http://dx.doi.org/10.1007/s43450-021-00162-5.

LEAL, Carla Monteiro; SIMAS, Rosineide Costa; MIRANDA, Milene; CAMPOS, Mariana Freire; GOMES, Brendo Araujo; SIQUEIRA, Marilda M.; VALE, Gabrielle do; ALMEIDA, Carlos Vitor Gomes de; LEITÃO, Suzana Guimarães; LEITÃO, Gilda Guimarães. Amazonian *Siparuna* extracts as potential anti-influenza agents: metabolic fingerprinting. **Journal Of Ethnopharmacology**, [S.L.], v. 270, p. 113788, abr. 2021b. Elsevier BV. http://dx.doi.org/10.1016/j.jep.2021.113788.

LI, Zhucui; LU, Yan; GUO, Yufeng; CAO, Haijie; WANG, Qinhong; SHUI, Wenqing. Comprehensive evaluation of untargeted metabolomics data processing software in feature detection, quantification and discriminating marker selection. **Analytica Chimica Acta**, [S.L.], v. 1029, p. 50-57, out. 2018. Elsevier BV. http://dx.doi.org/10.1016/j.aca.2018.05.001.

LU, Roujian; ZHAO, Xiang; LI, Juan; NIU, Peihua; YANG, Bo; WU, Honglong; WANG, Wenling; SONG, Hao; HUANG, Baoying; ZHU, Na. Genomic characterisation and epidemiology of 2019 novel coronavirus: implications for virus origins and receptor binding. **The Lancet**, [S.L.], v. 395, n. 10224, p. 565-574, fev. 2020. Elsevier BV. http://dx.doi.org/10.1016/s0140-6736(20)30251-8.

MAGALHÃES, Washington Luiz Esteves; THÁ, Emanoela Lundgren; LEME, Daniela Morais. **Comunicado técnico n° 427: Método de determinação de concentrações não citotóxicas para avaliação da capacidade protetora da lignina contra danos ao DNA.** Colombo, PR: Embrapa. 2018. 12 p.

MAJNOONI, Mohammad Bagher; FAKHRI, Sajad; BAHRAMI, Gholamreza; NASERI, Maryam; FARZAEI, Mohammad Hosein; ECHEVERRÍA, Javier. Alkaloids as Potential Phytochemicals against SARS-CoV-2: approaches to the associated pivotal mechanisms. **Evidence-Based Complementary And Alternative Medicine**, [S.L.], v. 2021, p. 1-21, 13 maio 2021. Hindawi Limited. http://dx.doi.org/10.1155/2021/6632623.

MALIK, Y. A. Properties of coronavirus and SARS-CoV-2. **Malaysian Journal of Pathology**, v. 42, n. 1, p. 3–11, abr. 2020.

MARASCHIN, Marcelo; ZEGGIO, Amélia R. Somensi; TOMAZZOLI, Maíra M.; OLIVEIRA, Simone K.; RAMLOV, Fernanda; VELEIRINHO, Maria Beatriz; ROCHA,

Miguel. METABOLÔMICA 1 E QUIMIOMETRIA COMO FERRAMENTAS PARA ANÁLISES QUIMIO(BIO) DIVERSAS. In: RESENDE, Rodrigo Ribeiro. **Biotecnologia Aplicada à Agro&Indústria**: fundamentos & aplicações. São Paulo, SP: Blucher, 2017. p. 1-1072.

MARTINEZ, J. P.; SASSE, F.; BRÖNSTRUP, M.; DIEZ, J.; MEYERHANS, A.. Antiviral drug discovery: broad-spectrum drugs from nature. **Natural Product Reports**, [S.L.], v. 32, n. 1, p. 29-48, 2015. Royal Society of Chemistry (RSC). http://dx.doi.org/10.1039/c4np00085d.

MENGIST, Hylemariam Mihiretie; DILNESSA, Tebelay; JIN, Tengchuan. Structural Basis of Potential Inhibitors Targeting SARS-CoV-2 Main Protease. **Frontiers In Chemistry**, [S.L.], v. 9, p. 622898, 12 mar. 2021. Frontiers Media SA. http://dx.doi.org/10.3389/fchem.2021.622898.

MOCÁK, Ján. Chemometrics in Medicine and Pharmacy. **Nova Biotechnologica Et Chimica**, [S.L.], v. 11, n. 1, p. 11-26, 1 jun. 2012. University of Saints Cyril and Methodius. http://dx.doi.org/10.2478/v10296-012-0002-3.

MOURA, Mariana de Souza; BELLETE, Barbara Sayuri; VIEIRA, Lucas Campos Curcino; SAMPAIO, Olívia Moreira. Use of Molecular Networking for Compound Annotation in Metabolomics. **Revista Virtual de Química**, [S.L.], v. 14, n. 2, p. 214-223, 2022. Sociedade Brasileira de Quimica (SBQ). http://dx.doi.org/10.21577/1984-6835.20210116.

NEWMAN, David J.; CRAGG, Gordon M.. Natural Products as Sources of New Drugs over the Nearly Four Decades from 01/1981 to 09/2019. **Journal Of Natural Products**, [S.L.], v. 83, n. 3, p. 770-803, 12 mar. 2020. American Chemical Society (ACS). http://dx.doi.org/10.1021/acs.jnatprod.9b01285.

OMS - Organização Mundial da Saúde. WHO Coronavirus (COVID-19) **Dashboard**. Disponível em: <https://covid19.who.int/>. Acesso em 03 de Ju. de 2025.

OMS - Organização Mundial da Saúde. WHO Coronavirus (COVID-19): **Tracking SARS-CoV-2 variants**. Disponível em: < https://www.who.int/activities/tracking-SARS-CoV-2-variants>. Acesso em 03 de Julho de 2023.

OSIPIUK, Jerzy; AZIZI, Saara-Anne; DVORKIN, Steve; ENDRES, Michael; JEDRZEJCZAK, Robert; JONES, Krysten A.; KANG, Soowon; KATHAYAT, Rahul S.; KIM, Youngchang; LISNYAK, Vladislav G.. Structure of papain-like protease from SARS-CoV-2

and its complexes with non-covalent inhibitors. **Nature Communications**, [S.L.], v. 12, n. 1, p. 743, 2 fev. 2021. Springer Science and Business Media LLC. http://dx.doi.org/10.1038/s41467-021-21060-3.

Our World In Data. **COVID-19 Data Explorer**: people vaccinated. People Vaccinated. 2025. Disponível em: https://ourworldindata.org/explorers/coronavirus-data-explorer. Acesso em: 20 fev. 2025.

PARK, Yun; BAEK, Seung-A; CHOI, Yongsoo; KIM, Jae; PARK, Sang. Metabolic Profiling of Nine Mentha Species and Prediction of Their Antioxidant Properties Using Chemometrics. **Molecules**, [S.L.], v. 24, n. 2, p. 258, 11 jan. 2019. MDPI AG. http://dx.doi.org/10.3390/molecules24020258.

PILON, Alan; SELEGATO, Denise; FERNANDES, Richard; BUENO, Paula; PINHO, Danielle; CARNEVALE NETO, Fausto; FREIRE, Rafael; CASTRO-GAMBOA, Ian; BOLZANI, Vanderlan; LOPES, Norberto. METABOLÔMICA DE PLANTAS: métodos e desafios. **Química Nova**, [S.L.], p. 329-354, 2020. Sociedade Brasileira de Quimica (SBQ). http://dx.doi.org/10.21577/0100-4042.20170499.

PILON, Alan; VIEIRA, Natália; AMARAL, Juliano; MONTEIRO, Afif; SILVA, Ricardo; SPÍNDOLA, Laila; CASTRO-GAMBOA, Ian; LOPES, Norberto. REDES MOLECULARES: uma análise sobre anotações e descoberta de novos ativos. **Química Nova**, [S.L.], p. 1168-1179, 2021. Sociedade Brasileira de Quimica (SBQ). http://dx.doi.org/10.21577/0100-4042.20170777.

PROMEGA website. **Lumit™ Immunoassay.** 2025. Disponível em: https://www.promega.com.br/products/immunoassay-elisa/lumit-immunoassays/lumit-immunoassay-labeling-kit-and-detection-reagents/?catNum=VB2500. Acesso em: 20 de fev. de 2025.

RATHAHAO-PARIS, Estelle; ALVES, Sandra; JUNOT, Christophe; TABET, Jean-Claude. High resolution mass spectrometry for structural identification of metabolites in metabolomics. **Metabolomics**, [S.L.], v. 12, n. 1, p. 08828, 14 nov. 2015. Springer Science and Business Media LLC. http://dx.doi.org/10.1007/s11306-015-0882-8.

SHAJAHAN, Asif; PEPI, Lauren E.; ROUHANI, Daniel S.; HEISS, Christian; AZADI, Parastoo. Glycosylation of SARS-CoV-2: structural and functional insights. **Analytical And Bioanalytical Chemistry**, [S.L.], v. 413, n. 29, p. 7179-7193, 7 jul. 2021. Springer Science and Business Media LLC. http://dx.doi.org/10.1007/s00216-021-03499-x.

SHARMA, Venu; SHARMA, Ankita; BHARATE, Sandip B.. Natural Products in Mitigation of SARS CoV Infections. **Current Medicinal Chemistry**, [S.L.], v. 28, n. 22, p. 4454-4483, 2 ago. 2021. Bentham Science Publishers Ltd. http://dx.doi.org/10.2174/0929867327666201027153940.

SIBBR – Sistema de Informação sobre a Biodiversidade Brasileira. **Biodiversidade Brasileira.** 2023. Disponível em: https://www.sibbr.gov.br/page/infografico.html. Acesso em: 03 jul. 2023.

SILVA, Joanda Paolla Raimundo e; ACEVEDO, Chonny Alexander Herrera; SOUZA, Thalisson Amorim de; MENEZES, Renata Priscila Barros de; SESSIONS, Zoe L.; ABREU, Lucas Silva; CIBULSKI, Samuel Paulo; SCOTTI, Luciana; SILVA, Marcelo Sobral da; MURATOV, Eugene N.. Natural Products as Potential Agents against SARS-CoV and SARSCoV- 2. **Current Medicinal Chemistry**, [S.L.], v. 28, n. 27, p. 5498-5526, 8 set. 2021. Bentham Science Publishers Ltd.. http://dx.doi.org/10.2174/0929867328666210125113938.

SPITERI, Gianfranco; FIELDING, James; DIERCKE, Michaela; CAMPESE, Christine; ENOUF, Vincent; GAYMARD, Alexandre; BELLA, Antonino; SOGNAMIGLIO, Paola; MOROS, Maria José Sierra; RIUTORT, Antonio Nicolau. First cases of coronavirus disease 2019 (COVID-19) in the WHO European Region, 24 January to 21 February 2020. **Eurosurveillance**, [S.L.], v. 25, n. 9, p. 1-6, 5 mar. 2020. European Centre for Disease Control and Prevention (ECDC). http://dx.doi.org/10.2807/1560-7917.es.2020.25.9.2000178.

THE BRAZILIAN FLORA GROUP. Brazilian Flora 2020: innovation and collaboration to meet target 1 of the global strategy for plant conservation (gspc). **Rodriguésia**, [S.L.], v. 69, n. 4, p. 1513-1527, dez. 2018. FapUNIFESP (SciELO). http://dx.doi.org/10.1590/2175-7860201869402.

TORTORICI, M. Alejandra; VEESLER, David. Structural insights into coronavirus entry. **Advances In Virus Research**, [S.L.], p. 93-116, 2019. Elsevier. http://dx.doi.org/10.1016/bs.aivir.2019.08.002.

VERMA, Surjeet; TWILLEY, Danielle; ESMEAR, Tenille; OOSTHUIZEN, Carel B.; REID, Anna-Mari; NEL, Marizé; LALL, Namrita. Anti-SARS-CoV Natural Products With the Potential to Inhibit SARS-CoV-2 (COVID-19). **Frontiers In Pharmacology**, [S.L.], v. 11, p. 1-20, 25 set. 2020. Frontiers Media SA. http://dx.doi.org/10.3389/fphar.2020.561334.

V'KOVSKII, Philip; KRATZEL, Annika; STEINER, Silvio; STALDER, Hanspeter; THIEL, Volker. Coronavirus biology and replication: implications for sars-cov-2. Nature Reviews Microbiology, [S.L.], v. 19, n. 3, p. 155-170, 28 out. 2020. **Springer Science and Business Media LLC**. http://dx.doi.org/10.1038/s41579-020-00468-6.

XIAN, Yanfang; ZHANG, Juan; BIAN, Zhaoxiang; ZHOU, Hua; ZHANG, Zhenbiao; LIN, Zhixiu; XU, Hongxi. Bioactive natural compounds against human coronaviruses: a review and perspective. **Acta Pharmaceutica Sinica B**, [S.L.], v. 10, n. 7, p. 1163-1174, jul. 2020. Elsevier BV. http://dx.doi.org/10.1016/j.apsb.2020.06.002.

XUE, Hai Tao; STANLEY-BAKER, Michael; KONG, Adams Wai Kin; LI, Hoi Leung; GOH, Wilson Wen Bin. Data considerations for predictive modeling applied to the discovery of bioactive natural products. **Drug Discovery Today**, [S.L.], v. 27, n. 8, p. 2235-2243, ago. 2022. Elsevier BV. http://dx.doi.org/10.1016/j.drudis.2022.05.009.

WEI, Juntong; XIANG, Li; CAI, Zongwei. Emerging environmental pollutants hydroxylated polybrominated diphenyl ethers: from analytical methods to toxicology research. **Mass Spectrometry Reviews**, [S.L.], v. 40, n. 3, p. 255-279, jul. 2020. Wiley. http://dx.doi.org/10.1002/mas.21640.

YADAV, Rohitash; CHAUDHARY, Jitendra Kumar; JAIN, Neeraj; CHAUDHARY, Pankaj Kumar; KHANRA, Supriya; DHAMIJA, Puneet; SHARMA, Ambika; KUMAR, Ashish; HANDU, Shailendra. Role of Structural and Non-Structural Proteins and Therapeutic Targets of SARS-CoV-2 for COVID-19. **Cells**, [S.L.], v. 10, n. 4, p. 821, 6 abr. 2021. MDPI AG. http://dx.doi.org/10.3390/cells10040821.

YANG, Jun-Yu; MA, Yi-Xuan; LIU, Yan; PENG, Xiang-Jun; CHEN, Xiang-Zhao. A Comprehensive Review of Natural Flavonoids with Anti-SARS-CoV-2 Activity. **Molecules**, [S.L.], v. 28, n. 6, p. 2735, 17 mar. 2023. MDPI AG. http://dx.doi.org/10.3390/molecules28062735.

ZHANG, Qianqian; XIANG, Rong; HUO, Shanshan; ZHOU, Yunjiao; JIANG, Shibo; WANG, Qiao; YU, Fei. Molecular mechanism of interaction between SARS-CoV-2 and host cells and interventional therapy. **Signal Transduction And Targeted Therapy**, [S.L.], v. 6, n. 1, p. 233, 11 jun. 2021. Springer Science and Business Media LLC. http://dx.doi.org/10.1038/s41392-021-00653-w.

ZHOU, Peng; YANG, Xing-Lou; WANG, Xian-Guang; HU, Ben; ZHANG, Lei; ZHANG, Wei; SI, Hao-Rui; ZHU, Yan; LI, Bei; HUANG, Chao-Lin. A pneumonia outbreak associated with a new coronavirus of probable bat origin. **Nature**, [S.L.], v. 579, n. 7798, p. 270-273, 3 fev. 2020a. Springer Science and Business Media LLC. http://dx.doi.org/10.1038/s41586-020-2012-7.

ZHOU, Tongqing; TSYBOVSKY, Yaroslav; GORMAN, Jason; RAPP, Micah; CERUTTI, Gabriele; CHUANG, Gwo-Yu; KATSAMBA, Phinikoula S.; SAMPSON, Jared M.; SCHÖN, Arne; BIMELA, Jude. Cryo-EM Structures of SARS-CoV-2 Spike without and with ACE2 Reveal a pH-Dependent Switch to Mediate Endosomal Positioning of Receptor-Binding Domains. **Cell Host & Microbe**, [S.L.], v. 28, n. 6, p. 867-879, dez. 2020b. Elsevier BV. http://dx.doi.org/10.1016/j.chom.2020.11.004.

ANEXO 1: Quadro das amostras do Banco de Extratos (Fito-Extractoteca) pertencente ao Laboratório de Fitoquímica e Farmacognosia (FitoFar) e ao Laboratório de Fitoquímica e Cromatografia Contracorrente (FitoCCC) que foram submetidos as etapas de triagem química por UHPLC-(ESI+/-)-MS/MS, e triagem biológica na inibição da interação *Spike*:ACE2 e da atividade das proteases $3CL^{pro}$ e PL^{pro}.

EXTRATOS	**Origem**
Rhamnaceae	
Ampelozizyphus amazonicus Ducke (Lenho - Hidroalcóolico)	Oriximiná, PA
Ampelozizyphus amazonicus Ducke (Cascas - Hidroalcóolico)	Oriximiná, PA
Ampelozizyphus amazonicus Ducke (Cascas - Aquoso)	Oriximiná, PA
Ampelozizyphus amazonicus Ducke (Lenho - Aquoso)	Oriximiná, PA
Sarcomphalus joazeiro (Mart.) Hauenschild (Cascas - Hidroalcóolico)	Agricolândia, PI
Sarcomphalus joazeiro (Mart.) Hauenschild (Folhas - Hidroalcóolico)	Campina Grande, PB
Verbenaceae	
Lantana fucata Lindl. (Partes Aéreas - Hexano)	Juiz de Fora, MG
Lantana fucata Lindl. (Partes Aéreas - Diclorometano)	Juiz de Fora, MG
Lantana fucata Lindl. (Partes Aéreas Butanol)	Juiz de Fora, MG
Lantana trifolia L. (Folhas - Hexano)	Mendes, RJ
Lantana trifolia L. (Folhas - Diclorometano)	Mendes, RJ
Lantana trifolia L. (Galhos - Hexano)	Mendes, RJ

Lantana trifolia L. (Caule - Hexano)	Mendes, RJ
Lantana trifolia L. (Galhos - Diclorometano)	Mendes, RJ
Lantana trifolia L. (Galhos - Hidroalcóolico)	Mendes, RJ
Lantana trifolia L. (Galhos - Butanol)	Mendes, RJ
Lantana trifolia L. (Caule - Butanol)	Mendes, RJ
Lippia lacunosa Mart. & Schauer (Folhas - Hidroalcóolico)	Juiz de Fora, MG
Lippia lacunosa Mart. & Schauer (Folhas - Hexano)	Juiz de Fora, MG
Lippia lacunosa Mart. & Schauer (Folhas - Acetato de Etila)	Juiz de Fora, MG
Lippia lacunosa Mart. & Schauer (Folhas - Butanol)	Juiz de Fora, MG
Lippia rotundifolia Cham. (Folhas - Hidroalcóolico)	Juiz de Fora, MG
Lippia rotundifolia Cham. (Folhas - Hexano)	Juiz de Fora, MG
Lippia rotundifolia Cham. (Folhas - Diclorometano)	Juiz de Fora, MG
Lippia rotundifolia Cham. (Folhas - Acetato de Etila)	Juiz de Fora, MG
Lippia rotundifolia Cham. (Folhas - Butanol)	Juiz de Fora, MG
Lippia origanoides Kunth [LOVV] (Partes Aéreas - Hidroalcóolico)	Petrópolis, RJ
Lippia origanoides Kunth [LOM] (Partes Aéreas - Hidroalcóolico)	Manaus, AM
Lippia aristata Schauer (Partes Aéreas - Hidroalcóolico)	Juiz de Fora, MG
Lippia aristata Schauer (Partes Aéreas - Hexano)	Juiz de Fora, MG

Lippia aristata Schauer (Partes Aéreas - Diclorometano)	Juiz de Fora, MG
Lippia aristata Schauer (Partes Aéreas - Acetato de Etila)	Juiz de Fora, MG
Lippia aristata Schauer (Partes Aéreas - Butanol)	Juiz de Fora, MG
Lippia aristata Schauer (Partes Aéreas - Aquoso)	Juiz de Fora, MG
Lippia brasiliensis T.R.S. Silva (Partes Aéreas - Hidroalcóolico)	Juiz de Fora, MG
Lippia brasiliensis T.R.S. Silva (Partes Aéreas - Hexano)	Juiz de Fora, MG
Lippia brasiliensis T.R.S. Silva (Partes Aéreas - Diclorometano)	Juiz de Fora, MG
Lippia brasiliensis T.R.S. Silva (Partes Aéreas - Acetato de Etila)	Juiz de Fora, MG
Lippia brasiliensis T.R.S. Silva (Partes Aéreas - Butanol)	Juiz de Fora, MG
Lippia brasiliensis T.R.S. Silva (Partes Aéreas - Aquoso)	Juiz de Fora, MG
Lippia rubella T.R.S. Silva & Salimena (Partes Aéreas - Hidroalcóolico)	Juiz de Fora, MG
Lippia rubella T.R.S. Silva & Salimena (Partes Aéreas - Hexano)	Juiz de Fora, MG
Lippia rubella T.R.S. Silva & Salimena (Partes Aéreas - Diclorometano)	Juiz de Fora, MG
Lippia rubella T.R.S. Silva & Salimena (Partes Aéreas - Acetato de Etila)	Juiz de Fora, MG
Lippia rubella T.R.S. Silva & Salimena (Partes Aéreas - Butanol)	Juiz de Fora, MG
Siparunaceae	
Siparuna cristata (Poepp. & Endl.) A.DC. (Partes Aéreas - Hidroalcóolico)	Manaus, AM
Siparuna cristata (Poepp. & Endl.) A.DC. (Partes Aéreas - Hexano)	Manaus, AM

Siparuna cristata (Poepp. & Endl.) A.DC. (Partes Aéreas - Diclorometano)	Manaus, AM
Siparuna cristata (Poepp. & Endl.) A.DC. (Partes Aéreas - Acetato de Etila)	Manaus, AM
Siparuna cristata (Poepp. & Endl.) A.DC. (Partes Aéreas - Butanol)	Manaus, AM
Siparuna sarmentosa Perkins (Partes Aéreas - Hidroalcóolico)	Manaus, AM
Siparuna sarmentosa Perkins (Partes Aéreas - Hexano)	Manaus, AM
Siparuna sarmentosa Perkins (Partes Aéreas - Diclorometano)	Manaus, AM
Siparuna sarmentosa Perkins (Partes Aéreas - Acetato de Etila)	Manaus, AM
Siparuna sarmentosa Perkins (Partes Aéreas - Butanol)	Manaus, AM
Siparuna glycycarpa (Ducke) Renner & Hausner (Partes Aéreas - Hidroalcóolico)	Manaus, AM
Siparuna glycycarpa (Ducke) Renner & Hausner (Partes Aéreas - Hexano)	Manaus, AM
Siparuna glycycarpa (Ducke) Renner & Hausner (Partes Aéreas - Diclorometano)	Manaus, AM
Siparuna glycycarpa (Ducke) Renner & Hausner (Partes Aéreas - Acetato de Etila)	Manaus, AM
Siparuna glycycarpa (Ducke) Renner & Hausner (Partes Aéreas - Butanol)	Manaus, AM
Siparuna decipiens (Tul.) A.DC. (Partes Aéreas - Hidroalcóolico)	Manaus, AM
Siparuna decipiens (Tul.) A.DC. (Partes Aéreas - Hexano)	Manaus, AM

Siparuna decipiens (Tul.) A.DC. (Partes Aéreas - Diclorometano)	Manaus, AM
Siparuna decipiens (Tul.) A.DC. (Partes Aéreas - Acetato de Etila)	Manaus, AM
Siparuna decipiens (Tul.) A.DC. (Partes Aéreas - Butanol)	Manaus, AM
Sipanura reginae (Tul.) A.DC. (Partes Aéreas - Hidroalcóolico)	Manaus, AM
Sipanura reginae (Tul.) A.DC. (Partes Aéreas - Hexano)	Manaus, AM
Sipanura reginae (Tul.) A.DC. (Partes Aéreas - Diclorometano)	Manaus, AM
Sipanura reginae (Tul.) A.DC. (Partes Aéreas Acetato de Etila)	Manaus, AM
Sipanura reginae (Tul.) A.DC. (Partes Aéreas - Butanol)	Manaus, AM
Lamiaceae	
Amasonia lasiocaulos Mart. ex Benth. (Partes Aéreas - Mhidroalcóolico)	Oriximiná, PA
Amasonia lasiocaulos Mart. ex Benth. (Partes Aéreas - Hexano)	Oriximiná, PA
Hyptis monticola Mart. ex Benth. (Folhas - Hidroalcóolico)	Petrópolis, RJ
Hyptis monticola Mart. ex Benth. (Folhas - Hexano)	Petrópolis, RJ
Hyptis monticola Mart. ex Benth. (Folhas - Diclorometano)	Petrópolis, RJ
Hyptis monticola Mart. ex Benth. (Folhas - Aquoso)	Petrópolis, RJ
Hyptis monticola Mart. ex Benth. (Flores - Hidroalcóolico)	Petrópolis, RJ
Hyptis monticola Mart. ex Benth. (Flores - Diclorometano)	Petrópolis, RJ
Hyptis monticola Mart. ex Benth. (Flores - Butanol)	Petrópolis, RJ

Hyptis monticola Mart. ex Benth. (Flores - Aquoso)	Petrópolis, RJ
Hyptis monticola Mart. ex Benth. (Galhos - Hidroalcóolico)	Petrópolis, RJ
Hyptis monticola Mart. ex Benth. (Galhos - Hexano)	Petrópolis, RJ
Hyptis monticola Mart. ex Benth. (Galhos - Diclorometano)	Petrópolis, RJ
Hyptis monticola Mart. ex Benth. (Galhos - Acetato de Etila)	Petrópolis, RJ
Hyptis monticola Mart. ex Benth. (Galhos - Butanol)	Petrópolis, RJ
Hyptis monticola Mart. ex Benth. (Galhos - Aquoso)	Petrópolis, RJ
Vitex cooperi Standl. (Cascas - Mhidroalcóolico)	Campo Grande, MS
Vitex cooperi Standl. (Folhas - Hexano)	Campo Grande, MS
Vitex cymosa Bertero ex Spreng. (Partes Aéreas - Butanol)	Campo Grande, MS
Vitex polygama Cham. (Folhas - Hidroalcóolico)	Maricá, RJ
Vitex polygama Cham. (Folhas - Hexano)	Maricá, RJ
Vitex polygama Cham. (Folhas - Diclorometano)	Maricá, RJ
Vitex polygama Cham. (Folhas - Acetato de Etila)	Maricá, RJ
Hesperozygis myrtoides (A.St.-Hil. ex Benth.) Epling (Partes Aéreas - Hidroalcóolico*)*	Petrópolis, RJ
Myrtaceae	
Eugenia brasiliensis Lam. [AL1707M] (Partes Aéreas - Hidroalcóolico)	Rio de Janeiro, RJ (Biblioteca de extratos CCS – UFRJ)

Myrcia splendens (Sw.) DC. [AL1721M] (Partes Aéreas - Hidroalcóolico)	Rio de Janeiro, RJ (Biblioteca de extratos CCS – UFRJ)
Eugenia sp. [AL1912M] (Partes Aéreas - Hidroalcóolico)	Rio de Janeiro, RJ (Biblioteca de extratos CCS – UFRJ)
Eugenia chlorophylla O. Berg. [AL1901M] (Partes Aéreas - Hidroalcóolico)	Rio de Janeiro, RJ (Biblioteca de extratos CCS – UFRJ)
Myrcia neoglabra E.Lucas & C. E. Wilson [TROVO526M] (Partes Aéreas - Hidroalcóolico)	Rio de Janeiro, RJ (Biblioteca de extratos CCS – UFRJ)
Eugenia prasina O. Berg. [PARDO2233M] (Partes Aéreas - Hidroalcóolico)	Rio de Janeiro, RJ (Biblioteca de extratos CCS – UFRJ)
Annonaceae	
Annona sylvatica A.St.-Hil. (Partes Aéreas - Hidroalcóolico)	Rio de Janeiro, RJ
Annona sylvatica A.St.-Hil. (Partes Aéreas - Hexano)	Rio de Janeiro, RJ
Annona sylvatica A.St.-Hil. (Partes Aéreas - Diclorometano)	Rio de Janeiro, RJ
Annona sylvatica A.St.-Hil. (Partes Aéreas – Acetato de Etila)	Rio de Janeiro, RJ
Annona sylvatica A.St.-Hil. (Partes Aéreas - Butanol)	Rio de Janeiro, RJ
Annona glabra L. (Partes Aéreas - Hidroalcóolico)	Rio de Janeiro, RJ
Annona glabra L. (Partes Aéreas - Hexano)	Rio de Janeiro, RJ
Annona glabra L. (Partes Aéreas - Diclorometano)	Rio de Janeiro, RJ
Annona glabra L. (Partes Aéreas – Acetato de Etila)	Rio de Janeiro, RJ
Annona glabra L. (Partes Aéreas - Butanol)	Rio de Janeiro, RJ

Annona dolabripetala Raddi (Partes Aéreas - Hidroalcóolico)	Rio de Janeiro, RJ
Annona dolabripetala Raddi (Partes Aéreas - Hexano)	Rio de Janeiro, RJ
Annona dolabripetala Raddi (Partes Aéreas - Diclorometano)	Rio de Janeiro, RJ
Annona dolabripetala Raddi (Partes Aéreas – Acetato de Etila)	Rio de Janeiro, RJ
Annona dolabripetala Raddi (Partes Aéreas – Butanol)	Rio de Janeiro, RJ
Annona mucosa Jacq. (Partes Aéreas - Hidroalcóolico)	Rio de Janeiro, RJ
Annona mucosa Jacq. (Partes Aéreas - Hexano)	Rio de Janeiro, RJ
Annona mucosa Jacq. (Partes Aéreas - Diclorometano)	Rio de Janeiro, RJ
Annona mucosa Jacq. (Partes Aéreas – Acetato de Etila)	Rio de Janeiro, RJ
Annona mucosa Jacq. (Partes Aéreas - Butanol)	Rio de Janeiro, RJ
Anaxagorea dolichocarpa Sprague & Sandwith (Partes Aéreas – Hidroalcóolico)	Rio de Janeiro, RJ
Anaxagorea dolichocarpa Sprague & Sandwith (Partes Aéreas – Hexano)	Rio de Janeiro, RJ
Anaxagorea dolichocarpa Sprague & Sandwith (Partes Aéreas – Diclorometano)	Rio de Janeiro, RJ
Anaxagorea dolichocarpa Sprague & Sandwith (Partes Aéreas – Acetato de Etila)	Rio de Janeiro, RJ
Anaxagorea dolichocarpa Sprague & Sandwith (Partes Aéreas – Butanol)	Rio de Janeiro, RJ

Annona dolabripetala Raddi [Marcos] (Partes Aéreas – Hidroalcóolico)	Rio de Janeiro, RJ
Annona dolabripetala Raddi [Marcos] (Partes Aéreas – Hexano)	Rio de Janeiro, RJ
Annona dolabripetala Raddi [Marcos] (Partes Aéreas – Diclorometano)	Rio de Janeiro, RJ
Annona dolabripetala Raddi [Marcos] (Partes Aéreas – Acetato de Etila)	Rio de Janeiro, RJ
Annona dolabripetala Raddi [Marcos] (Partes Aéreas – Butanol)	Rio de Janeiro, RJ
Annona parviflora (A.St.-Hil.) H.Rainer (Partes Aéreas – Hidroalcóolico)	Rio de Janeiro, RJ
Annona parviflora (A.St.-Hil.) H.Rainer (Partes Aéreas – Hexano)	Rio de Janeiro, RJ
Annona parviflora (A.St.-Hil.) H.Rainer (Partes Aéreas – Diclorometano)	Rio de Janeiro, RJ
Annona parviflora (A.St.-Hil.) H.Rainer (Partes Aéreas – Acetato de Etila)	Rio de Janeiro, RJ
Annona parviflora (A.St.-Hil.) H.Rainer (Partes Aéreas – Butanol)	Rio de Janeiro, RJ
Guatteria australis A.St.-Hil. (Partes Aéreas – Hidroalcóolico)	Rio de Janeiro, RJ
Guatteria australis A.St.-Hil. (Partes Aéreas – Hexano)	Rio de Janeiro, RJ
Guatteria australis A.St.-Hil. (Partes Aéreas – Diclorometano)	Rio de Janeiro, RJ
Guatteria australis A.St.-Hil. (Partes Aéreas – Acetato de Etila)	Rio de Janeiro, RJ
Guatteria australis A.St.-Hil. (Partes Aéreas – Butanol)	Rio de Janeiro, RJ
Xylopia langsdorffiana A.St.-Hil. (Partes Aéreas – Hidroalcóolico)	Rio de Janeiro, RJ
Xylopia langsdorffiana A.St.-Hil. (Partes Aéreas – Hexano)	Rio de Janeiro, RJ
Xylopia langsdorffiana A.St.-Hil. (Partes Aéreas – Diclorometano)	Rio de Janeiro, RJ

Xylopia langsdorffiana A.St.-Hil. (Partes Aéreas – Acetato de Etila)	Rio de Janeiro, RJ
Xylopia langsdorffiana A.St.-Hil. (Partes Aéreas – Butanol)	Rio de Janeiro, RJ
Loranthaceae	
Struthanthus acuminatus (Ruiz & Pav.) Kuijt (Partes Aéreas – Hidroalcóolico)	Nova Friburgo, RJ
Struthanthus acuminatus (Ruiz & Pav.) Kuijt (Partes Aéreas – Hexano)	Nova Friburgo, RJ
Struthanthus acuminatus (Ruiz & Pav.) Kuijt (Partes Aéreas – Diclorometano)	Nova Friburgo, RJ
Struthanthus acuminatus (Ruiz & Pav.) Kuijt (Partes Aéreas – Acetato de Etila)	Nova Friburgo, RJ
Struthanthus acuminatus (Ruiz & Pav.) Kuijt (Partes Aéreas – Butanol)	Nova Friburgo, RJ
Struthanthus acuminatus (Ruiz & Pav.) Kuijt (Partes Aéreas – Aquoso)	Nova Friburgo, RJ
Struthanthus marginatus (Desr.) G.D. (Partes Aéreas – Hidroalcóolico)	Petrópolis, RJ
Struthanthus marginatus (Desr.) G.D. (Partes Aéreas – Hexano)	Petrópolis, RJ
Struthanthus marginatus (Desr.) G.D. (Partes Aéreas – Diclorometano)	Petrópolis, RJ
Struthanthus marginatus (Desr.) G.D. (Partes Aéreas – Acetato de Etila)	Petrópolis, RJ
Struthanthus marginatus (Desr.) G.D. (Partes Aéreas – Butanol)	Petrópolis, RJ
Struthanthus marginatus (Desr.) G.D. (Partes Aéreas – Aquoso)	Petrópolis, RJ

ANEXO 2: Material suplementar do artigo "*Myrtucommulones and Related Acylphloroglucinols from Myrtaceae as a Promising Source of Multitarget SARS-CoV-2 Cycle Inhibitors*" publicado na revista *Pharmaceuticals* (Qualis A1; FI 4.3) em março de 2024 (Volume 17, artigo 436).

Supplementary material

Myrtucommulones and Related Acylphloroglucinols from Myrtaceae as a Promising Source of Multitarget SARS-CoV-2 Cycle Inhibitors

Simony Carvalho Mendonça [1,†], Brendo Araujo Gomes [1,2,†], Mariana Freire Campos [1,2], Thamirys Silva da Fonseca [3], Maria Eduarda Alves Esteves [4], Bruce Veiga Andriolo [5], Caio Felipe de Araujo Ribas Cheohen [6], Larissa Esteves Carvalho Constant [7], Stephany da Silva Costa [7], Pedro Telles Calil [8], Amanda Resende Tucci [9,10], Thamara Kelcya Fonseca de Oliveira [9,10], Alice dos Santos Rosa [9,10], Vivian Neuza dos Santos Ferreira [9], Julia Nilo Henrique Lima [9], Milene Dias Miranda [9,10], Luciana Jesus da Costa [8], Manuela Leal da Silva [4,5,6], Marcus Tullius Scotti [11], Diego Allonso [7,12], Gilda Guimarães Leitão [13,*] and Suzana Guimarães Leitão [1,2,3,*]

[1] Departamento de Produtos Naturais e Alimentos, Faculdade de Farmácia, Universidade Federal do Rio de Janeiro, Rio de Janeiro 21941-902, RJ, Brazil; sy2802@ufrj.br (S.C.M.); brendoo.bc@ufrj.br (B.A.G.); camposmariana@biof.ufrj.br (M.F.C.)

[2] Programa de Pós-Graduação em Biotecnologia Vegetal e Bioprocessos, Centro de Ciências da Saúde, Universidade Federal do Rio de Janeiro, Rio de Janeiro 21941-902, RJ, Brazil

[3] Programa de Pós-Graduação em Ciências Farmacêuticas, Faculdade de Farmácia, Universidade Federal do Rio de Janeiro, Rio de Janeiro 21941-902, RJ, Brazil; thamirysfonseca@ufrj.br

[4] Programa de Pós-Graduação em Biologia Computacional e Sistemas, Instituto Oswaldo Cruz, Rio de Janeiro 21040-900, RJ, Brazil; mariaesteves@aluno.fiocruz.br (M.E.A.E.); manuela@macae.ufrj.br (M.L.d.S.)

[5] Programa de Pós-Graduação em Biotecnologia, Instituto Nacional de Metrologia, Qualidade e Tecnologia, Duque de Caxias 25250-020, RJ, Brazil; bruceandriolo@ufrj.br

[6] Programa de Pós-Graduação Multicêntrico em Ciências Fisiológicas, Centro de Ciências da Saúde, Instituto de Biodiversidade e Sustentabilidade NUPEM, Universidade Federal do Rio de Janeiro, Macaé 27965-045, RJ, Brazil; caiocheohen@ufrj.br

[7] Programa de Pós-Graduação em Ciências Biológicas, Instituto de Biofísica Carlos Chagas Filho, Universidade Federal do Rio de Janeiro, Rio de Janeiro 21941-590, RJ, Brazil; larissaconstant@biof.ufrj.br (L.E.C.C.); stephanycosta@biof.ufrj.br (S.d.S.C.); diegoallonso@pharma.ufrj.br (D.A.)

[8] Departamento de Virologia, Instituto de Microbiologia Paulo de Góes, Universidade Federal do Rio de Janeiro, Rio de Janeiro 21941-590, RJ, Brazil; ptcalil@micro.ufrj.br (P.T.C.); ljcosta@micro.ufrj.br (L.J.d.C.)

[9] Laboratory of Morphology and Viral Morphogenesis, Oswaldo Cruz Institute, Oswaldo Cruz Foundation, Rio de Janeiro 21041-250, RJ, Brazil; amanda.tucci@ioc.fiocruz.br (A.R.T.); thamara.oliveira@ioc.fiocruz.br (T.K.F.d.O.); alicerosa@aluno.fiocruz.br (A.d.S.R.); vivian.ferreira@ioc.fiocruz.br (V.N.d.S.F.); julianilo@ufrj.br (J.N.H.L.); mmiranda@ioc.fiocruz.br (M.D.M.)

[10] Programa de Pós-Graduação em Biologia Celular e Molecular, Instituto Oswaldo Cruz, Fundação Oswaldo Cruz, Rio de Janeiro 21041-250, RJ, Brazil

[11] Departamento de Química, Universidade Federal da Paraíba, João Pessoa 58033-455, PB, Brazil; mtscotti@ccae.ufpb.br

[12] Departamento de Biotecnologia Farmacêutica, Faculdade de Farmácia, Universidade Federal do Rio de Janeiro, Rio de Janeiro 21941-902, RJ, Brazil

[13] Instituto de Pesquisas de Produtos Naturais, Universidade Federal do Rio de Janeiro, Rio de Janeiro 21941-902, RJ, Brazil

* Correspondence: ggleitao@ippn.ufrj.br (G.G.L.); sgleitao@pharma.ufrj.br (S.G.L.); Tel.: +55-21-3938-6513 (G.G.L.); +55-21-3938-6414 (S.G.L.)

† These authors contributed equally to this work.

Figure S1. Scores (A), X-loadings weight (B) for the PLS model based on the LC-MS data obtained in the electrospray ionization in negative mode of the 15 samples of five species of Myrtaceae family, and the inhibition values of the extracts on the RBD:ACE2 interaction of SARS-CoV-2. The dashed line indicates the cutoff for contributions exceeding 0.1 (loadings weights).

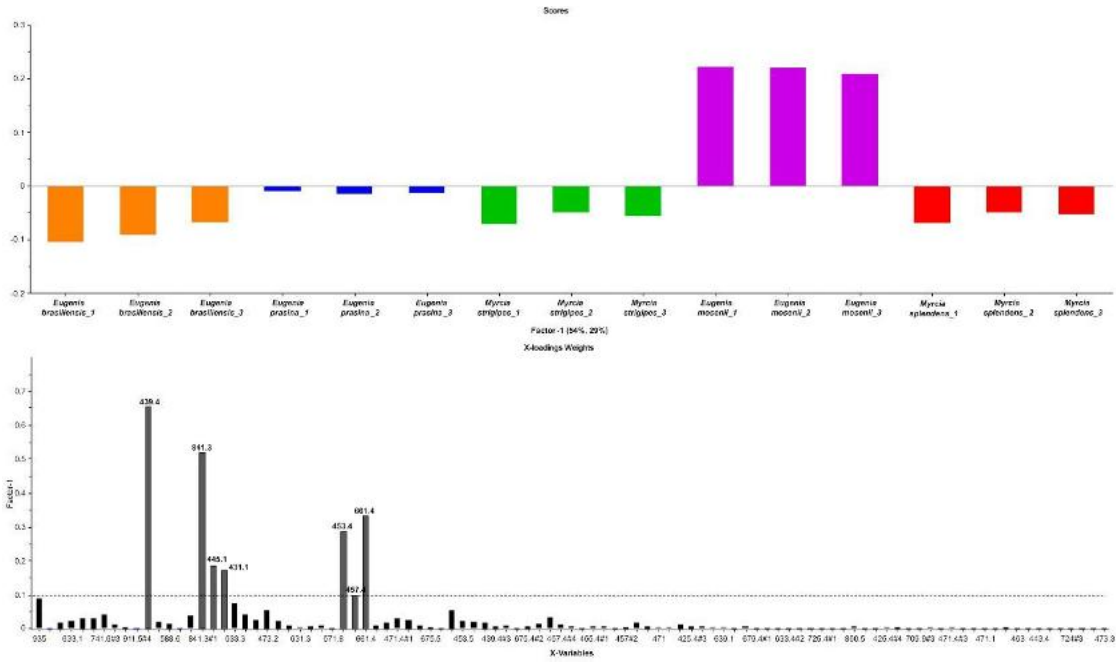

Figure S2. Scores (A), X-loadings weight (B) for the PLS model based on the LC-MS data obtained in the electrospray ionization in negative mode of the 15 samples of five species of Myrtaceae family, and the inhibition values of the extracts on the activity of the r3CLpro enzyme of SARS-CoV-2. The dashed line indicates the cutoff for contributions exceeding 0.1 (loadings

weights).

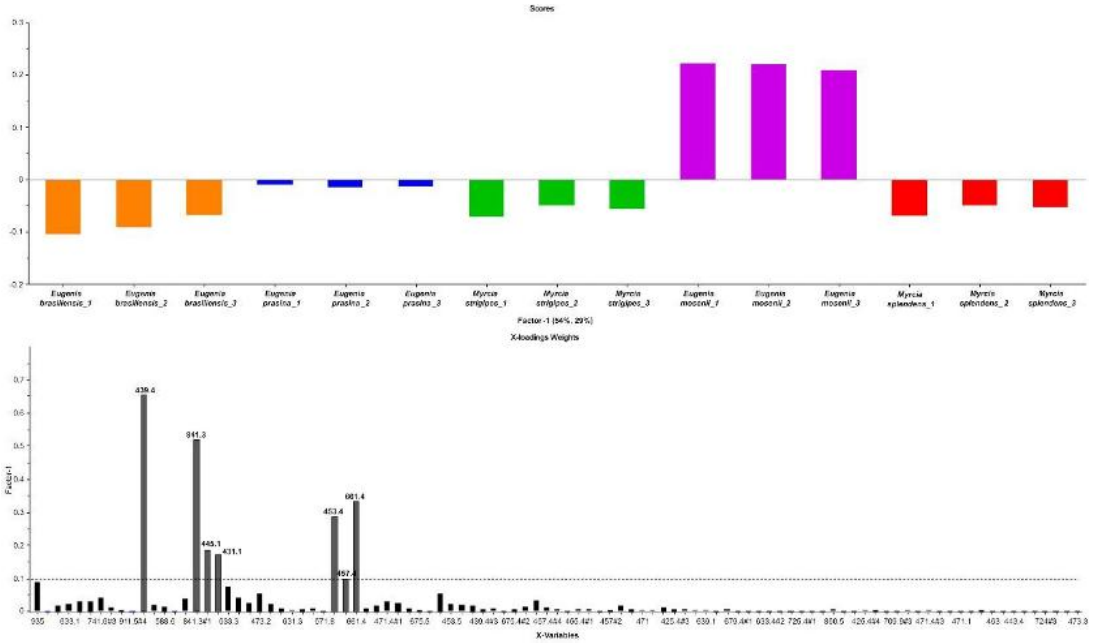

Figure S3. Scores (A), X-loadings weight (B) for the PLS model based on the LC-MS data obtained in the electrospray ionization in negative mode of the 15 samples of five species of Myrtaceae family, and the inhibition values of the extracts on the activity of the rPLpro enzyme of SARS-CoV-2. The dashed line indicates the cutoff for contributions exceeding 0.1 (loadings weights).

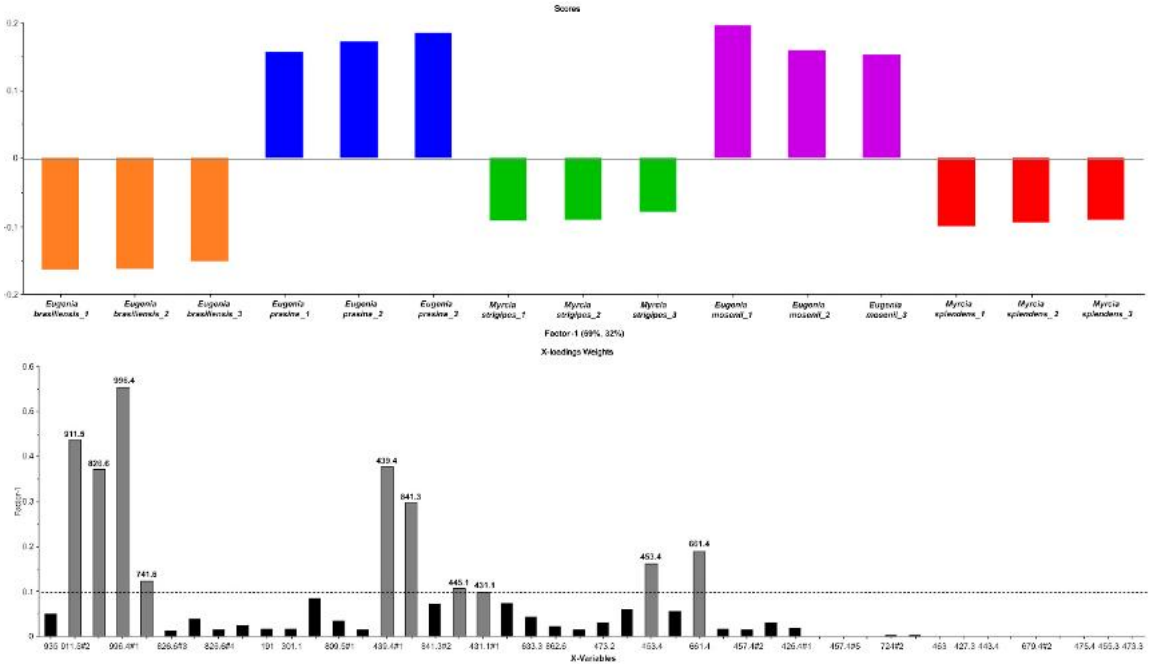

Figure S4. Feature Based Molecular Network (FBMN) of Myrtaceae extracts

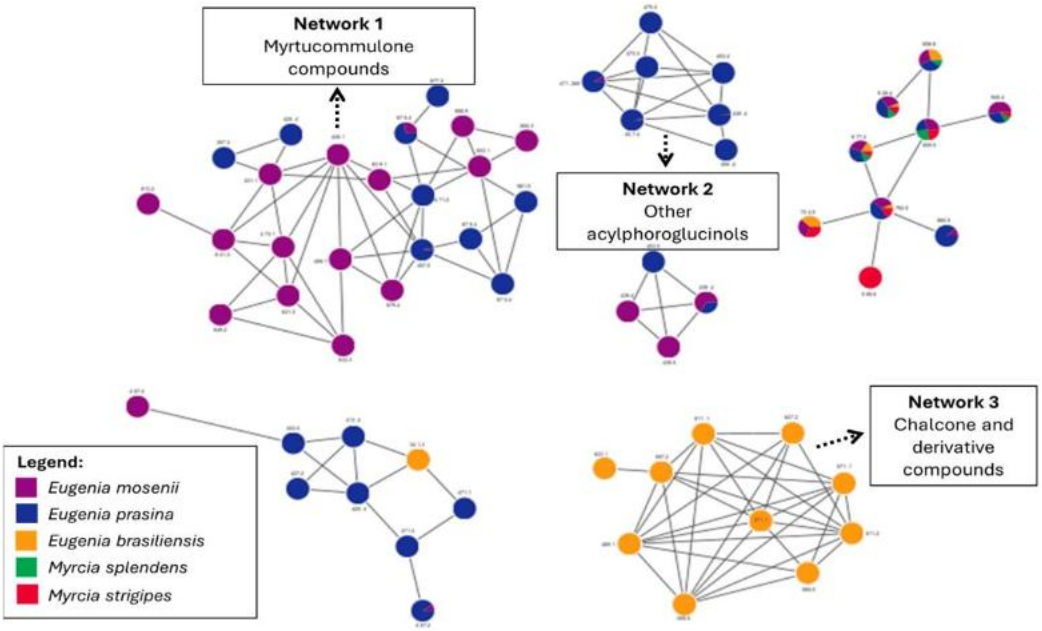

Figure S5. MS/MS spectrum of compound **1** at *m/z* 445.1 $[M-H]^-$ (semimyrtucommulone)

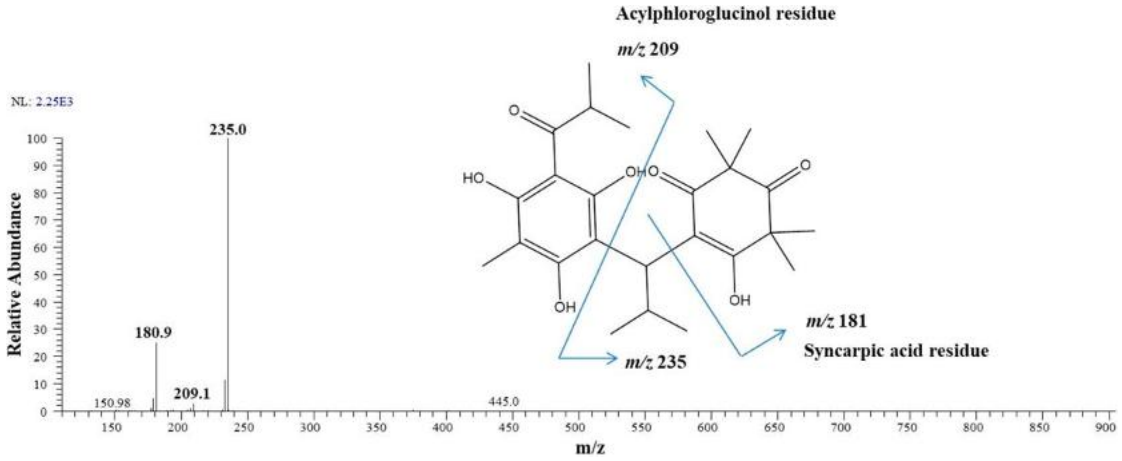

Figure S6. MS/MS spectrum of compound **2** at *m/z* 431.1 $[M-H]^-$ (*nor*-semimyrtucommulone)

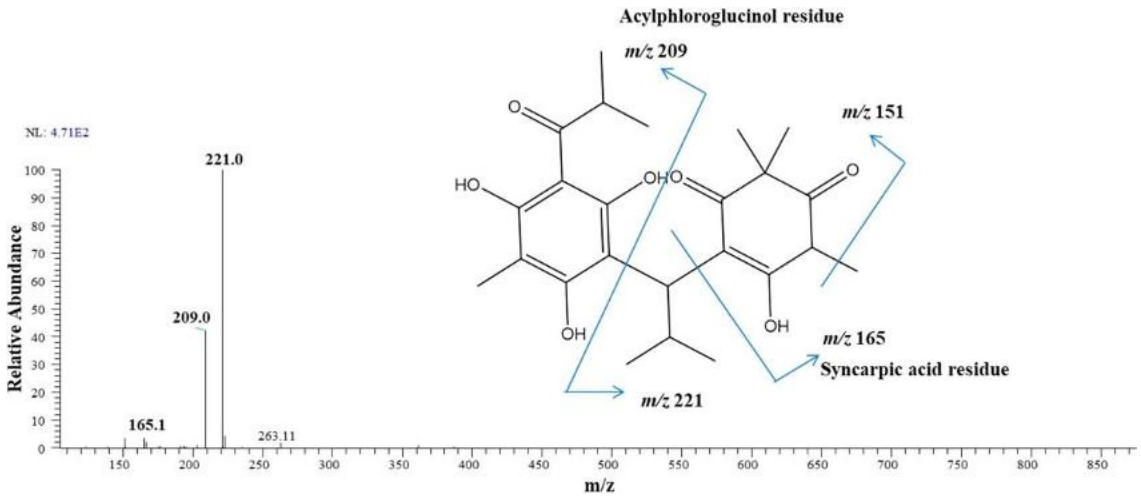

Figure S7. MS/MS spectrum of proposed compound **3** at *m/z* 473.2 $[M-H]^-$

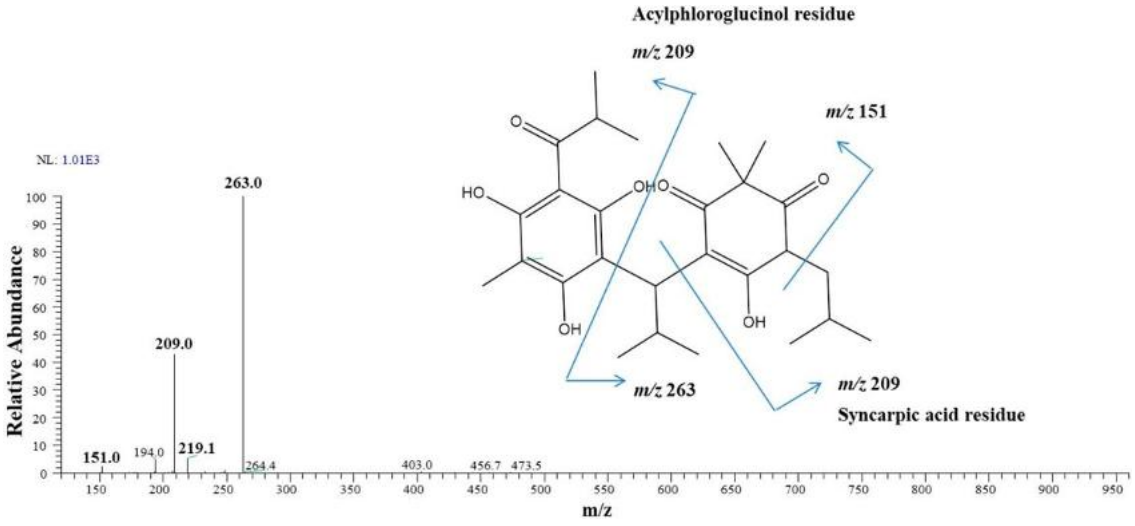

Figure S8. MS/MS spectrum of proposed compound **4** at *m/z* 633.3 $[M-H]^-$

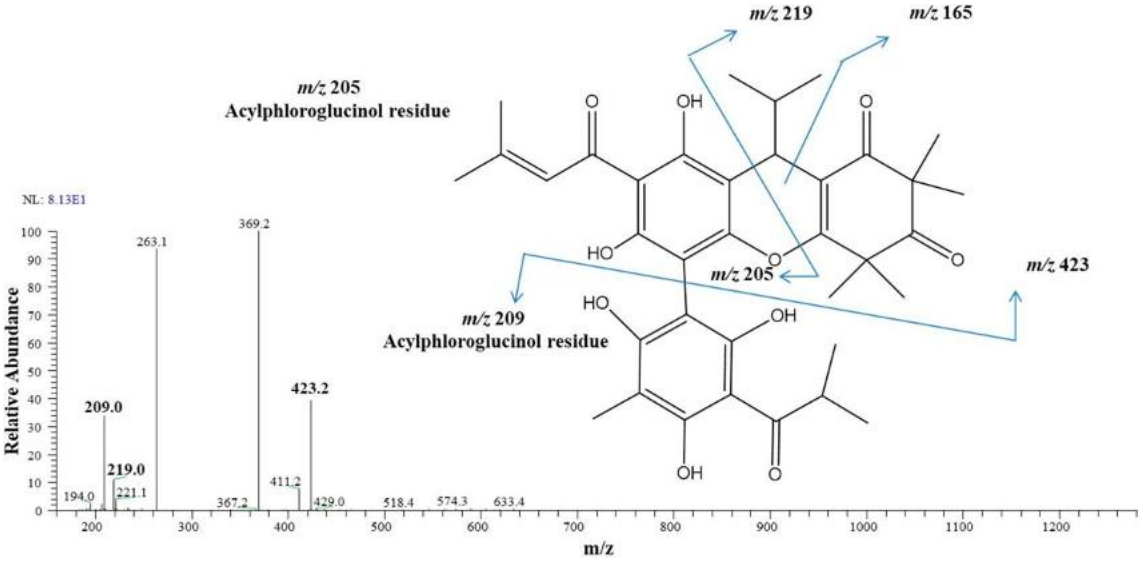

Figure S9. MS/MS spectrum of proposed compound **5** at *m/z* 841.3 $[M-H]^-$

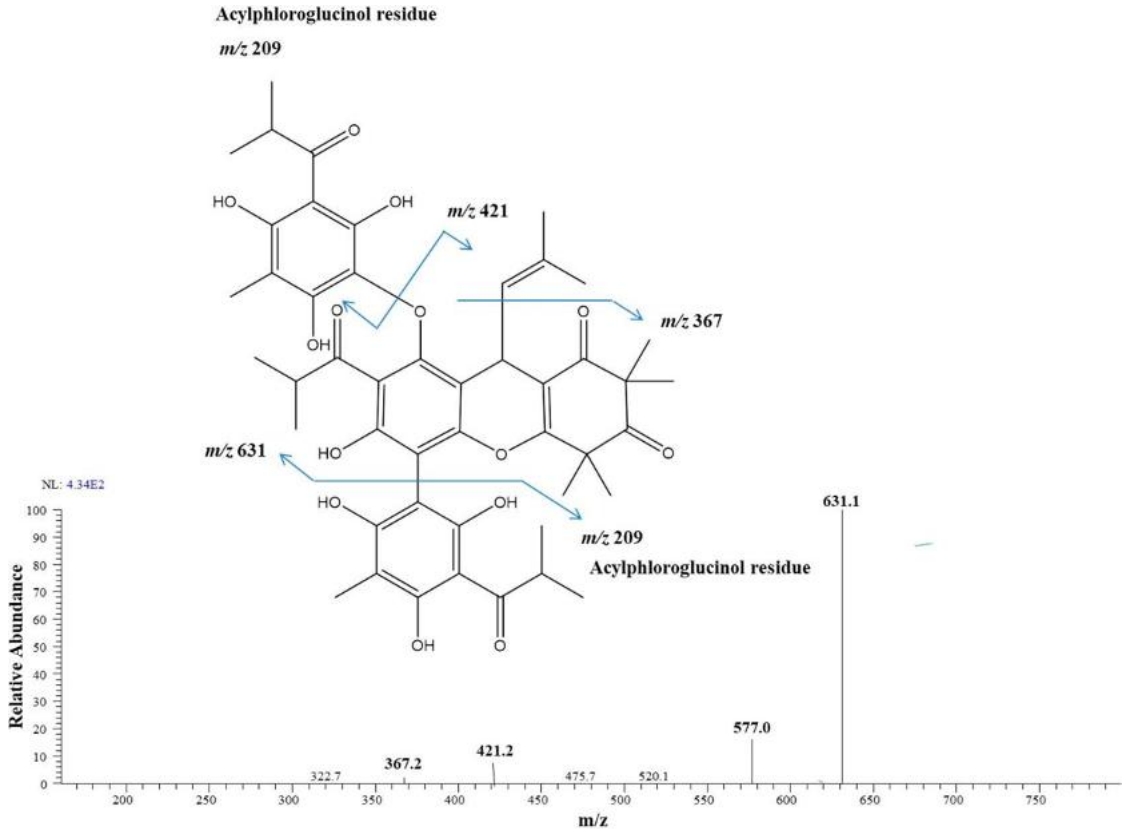

Figure S10. Molecular network of chalcone and chalcone-derivative compounds and MS/MS spectrum of *m/z* 271.1 $[M-H]^-$ (2',6'-dihydroxy-4'-methoxydihydrochalcone)

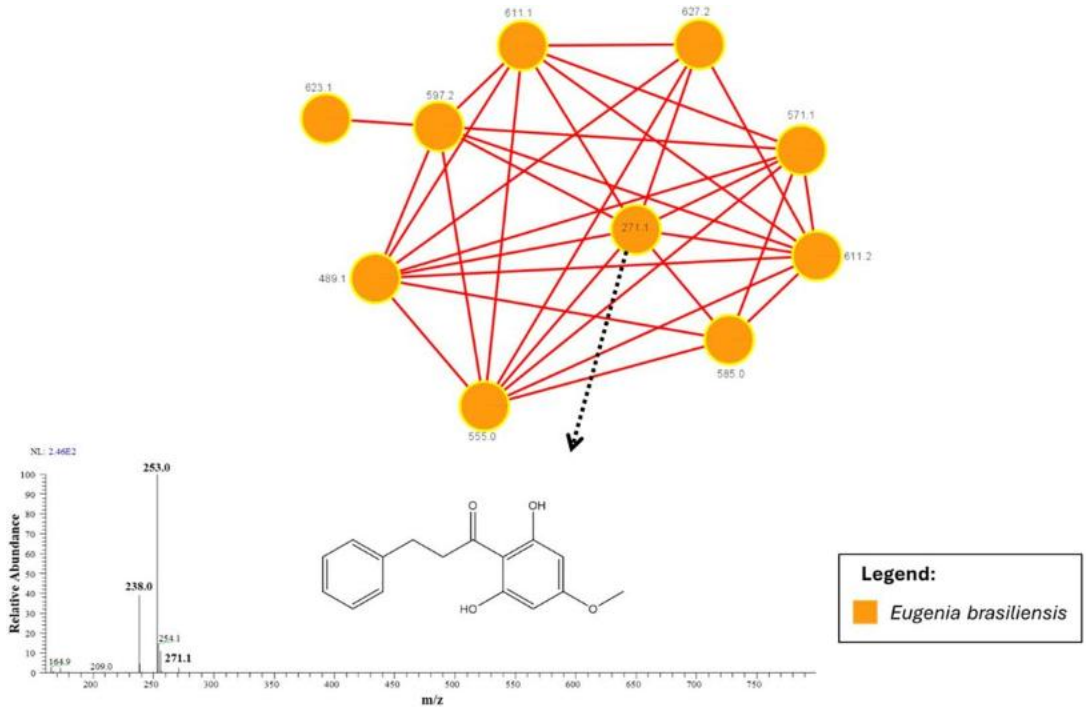

Figure S11. 2D structure of compound **5** (*m/z* 841 [M-H]$^-$) with atomic positions.

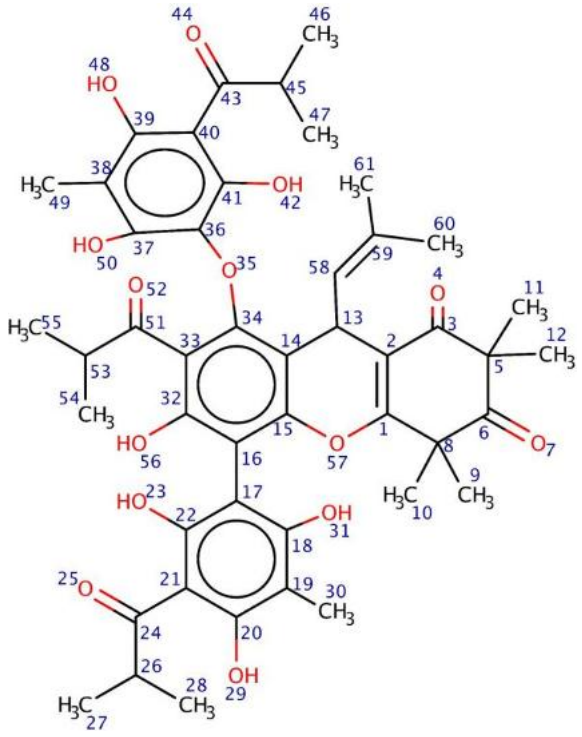

Movie S1 - Molecular dynamics results of the complex PLpro with compound 5. The protein structure is shown in gray, the BL2loop is shown in yellow and the compound 5 is shown in blue. The file is available in 10.5281/zenodo.10257486.

Movie S2 - Molecular dynamics results of the complex 3CL^{pro} active site with compound **5**. The protein structure is shown in gray and the compound **5** is shown in orange. The file is available in https://doi.org/10.5281/zenodo.10257448.

Movie S3 - Molecular dynamics results of the complex 3CL^{pro} allosteric groove with compound **5**. The protein structure is shown in gray and the compound **5** is shown in magenta. The file is available in https://doi.org/10.5281/zenodo.10257460.

Table S1 - Description of the pharmacokinetic properties of the compounds **3**, **4**, **5**, *nor*-semimyrtucommulone (**2**), and semimyrtucommulone (**1**).

	COMPOUND 3 (*m/z* 473 [M-H]-)	compound 4 (*m/z* 633 $[M-H]^-$)	compound 5 (*m/z* 841 $[M-H]^-$)	*nor*-semimyrtucommulone (2)	semimyrtucommulone (1)
CYP1A2-INH	Yes	Yes	Yes	Yes	Yes
CYP1A2-SUB	No	No	No	No	No
CYP2C19-INH	Yes	Yes	Yes	Yes	Yes
CYP2C19-SUB	No	Yes	Yes	No	No
CYP2C9-INH	Yes	No	Yes	Yes	Yes
CYP2C9-SUB	No	No	No	No	No
CYP2D6-INH	Yes	Yes	Yes	Yes	Yes
CYP2D6-SUB	Yes	Yes	Yes	Yes	Yes
CYP3A4-INH	Yes	Yes	Yes	Yes	Yes
CYP3A4-SUB	No	No	No	No	No
CACO-2	Yes	No	No	Yes	Yes
BBB	Yes	Yes	Yes	Yes	Yes
PPB	High	High	High	High	High
FU (%)	High	High	High	High	Less

CYP: Cytochrome P; Caco-2: *Cancer coli* –2; BBB: Blood–Brain Barrier; PPB: Plasma protein binding; Fu: Fraction unbound.

ANEXO 3: Material suplementar do artigo *"Predicting the Anti-SARS-CoV-2 Potential of Isoquinoline Alkaloids from Brazilian Siparunaceae Species Using Chemometric Tools"* foi publicado na revista *International Journal of Molecular Sciences* (Qualis A2; FI 4.9) em janeiro de 2025 (Volume 26, artigo 633).

Supplementary material

Predicting the Anti-SARS-CoV-2 Potential of Isoquinoline Alkaloids from Brazilian Siparunaceae Species Using Chemometric Tools

Brendo Araujo Gomes [1,2,†], Diégina Araújo Fernandes [3,†], Simony Carvalho Mendonça [2,4], Mariana Freire Campos [1,2], Thamirys Silva da Fonseca [2,4], Larissa Esteves Carvalho Constant [5], Natalia Ferreira de Sousa [6], Renata Priscila Barros de Menezes [6], Beatriz Albuquerque Custódio de Oliveira [7], Stephany da Silva Costa [7], Giovanna Barbosa Frensel [7], Alice Santos Rosa [8,9], Thamara Kelcya Fonseca Oliveira [8,9], Amanda Resende Tucci [8,9], Júlia Nilo Henrique Lima [8], Vivian Neuza Santos Ferreira [8], Milene Dias Miranda [8,9], Diego Allonso [5,7,10], Marcus Tullius Scotti [6,10], Suzana Guimarães Leitão [1,2,4,*] and Gilda Guimarães Leitão [3,4,*]

[1] Programa de Pós-Graduação em Biotecnologia Vegetal e Bioprocessos, Centro de Ciências da Saúde, Universidade Federal do Rio de Janeiro, Rio de Janeiro 21941-902, RJ, Brazil; brendoo.bc@ufrj.br (B.A.G.); ccamposmariana@ufrj.br (M.F.C.)
[2] Departamento de Produtos Naturais e Alimentos, Faculdade de Farmácia, Universidade Federal do Rio de Janeiro, Rio de Janeiro 21941-902, RJ, Brazil; sy2802@ufrj.br (S.C.M.); thamirysfonseca@ufrj.br (T.S.d.F.)
[3] Instituto de Pesquisas de Produtos Naturais, Universidade Federal do Rio de Janeiro, Rio de Janeiro 21941-902, RJ, Brazil; diegina@ufrj.br (D.A.F.); ggleitao@ippn.ufrj.br (G.G.L.)
[4] Programa de Pós-Graduação em Ciências Farmacêuticas, Faculdade de Farmácia, Universidade Federal do Rio de Janeiro, Rio de Janeiro 21941-902, RJ, Brazil
[5] Programa de Pós-Graduação em Ciências Biológicas, Instituto de Biofísica Carlos Chagas Filho, Universidade Federal do Rio de Janeiro, Rio de Janeiro 21941-590, RJ, Brazil; larissaestevescarvalho@gmail.com (L.E.C.C.); diegoallonso@pharma.ufrj.br (D.A.)
[6] Programa de Pós-Graduação em Produtos Naturais e Sintéticos Bioativos, Universidade Federal da Paraíba, João Pessoa 58015-970, PB, Brazil; nataliafsousa@ltf.ufpb.br (N.F.d.S.); renatabarros@ltf.ufpb.br (R.P.B.d.M.); mtscotti@ccae.ufpb.br (M.T.S.)
[7] Laboratório de Biotecnologia e Bioengenharia Estrutural, Universidade Federal do Rio de Janeiro, Centro de Ciências da Saúde, Bloco G, Rio de Janeiro 21941-902, RJ, Brazil; beatrizalbuquerquecp2@gmail.com (B.A.C.d.O.); stephanycosta@biof.ufrj.br (S.d.S.C.); gfrensel@peq.coppe.ufrj.br(G.B.F.)
[8] Laboratório de Morfologia e Morfogênese Viral, Oswaldo Cruz Institute, Oswaldo Cruz Foundation, Rio de Janeiro 21041-250, RJ, Brazil; alicerosa@aluno.fiocruz.br (A.S.R.); thamarafonseca@ufmg.br (T.K.F.O.); artucci.bio@gmail.com(A.R.T.); julianilo@ufrj.br (J.N.H.L.); vivian.ferreira@ioc.fiocruz.br (V.N.S.F.); mmiranda@ioc.fiocruz.br (M.D.M.)
[9] Programa de Pós-Graduação em Biologia Celular e Molecular, Instituto Oswaldo Cruz, Fundação Oswaldo Cruz, Rio de Janeiro 21041-250, RJ, Brazil
[10] Departamento de Biotecnologia Farmacêutica, Faculdade de Farmácia, Universidade Federal do Rio de Janeiro, Rio de Janeiro 21941-902, RJ, Brazil
* Correspondence: sgleitao@pharma.ufrj.br (S.G.L.), ggleitao@ippn.ufrj.br (G.G.L.)
† These authors contributed equally to this work.

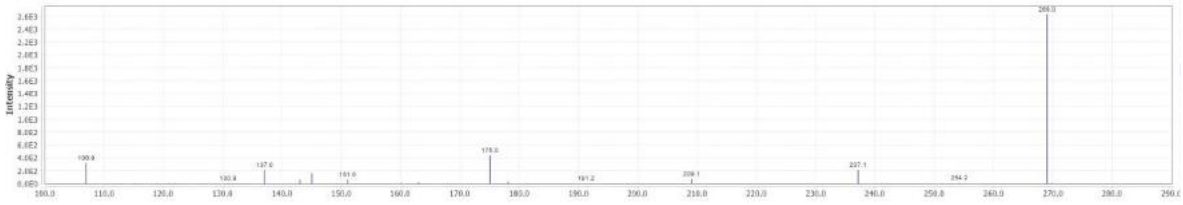

Figure S1. ESI-MS/MS spectrum of compound **1** at *m*/*z* 286 $[M+H]^+$ (coclaurine)

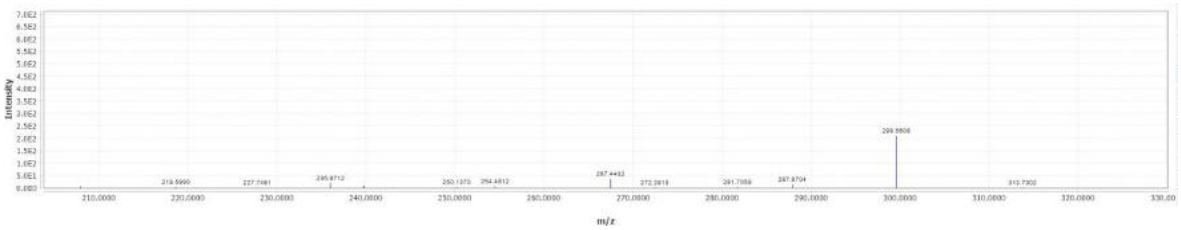

Figure S2. APCI-MS/MS spectrum of compound **2** at *m*/*z* 330 $[M+H]^+$ (reticuline)

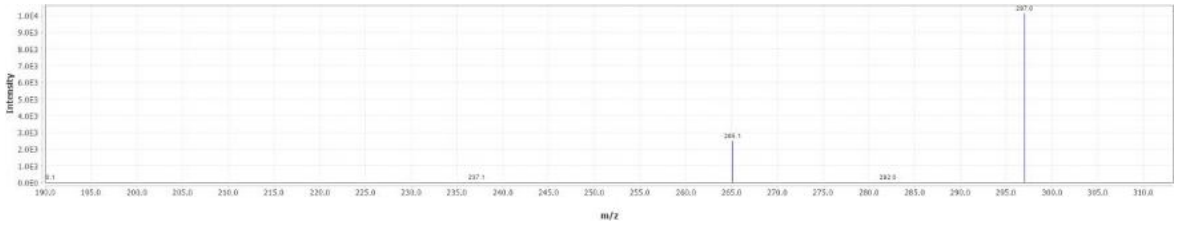

Figure S3. ESI-MS/MS spectrum of compound **3** at *m*/*z* 328 $[M+H]^+$ (boldine)

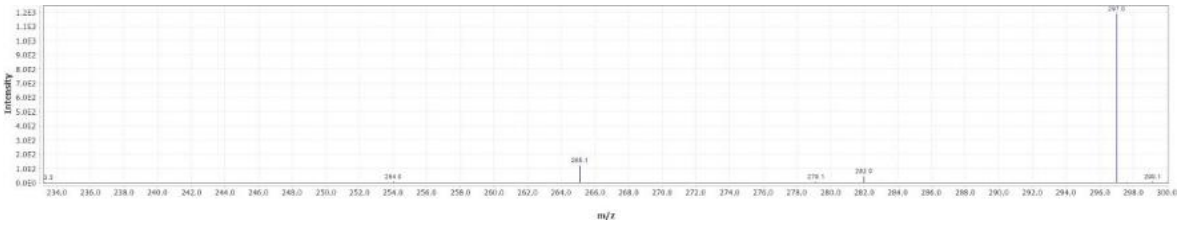

Figure S4. APCI-MS/MS spectrum of compound **4** at *m*/*z* 314 $[M+H]^+$ (laurolitsine)

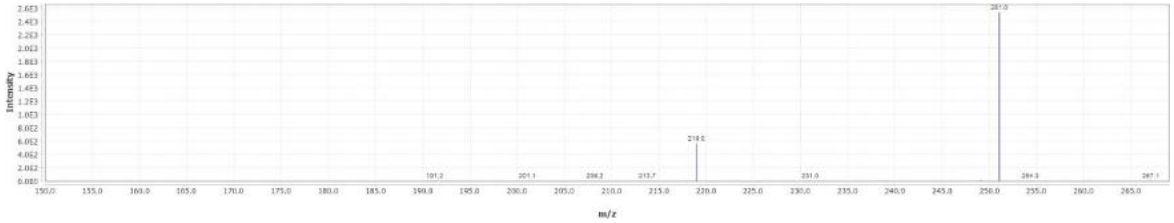

Figure S5. ESI-MS/MS spectrum of compound **5** at *m*/*z* 268 $[M+H]^+$ (assimilobine)

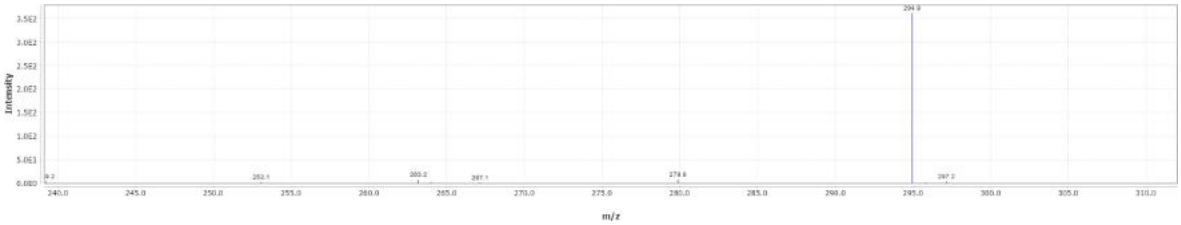

Figure S6. ESI-MS/MS spectrum of compound **6** at *m/z* 312 $[M+H]^+$ (actinodaphnine)

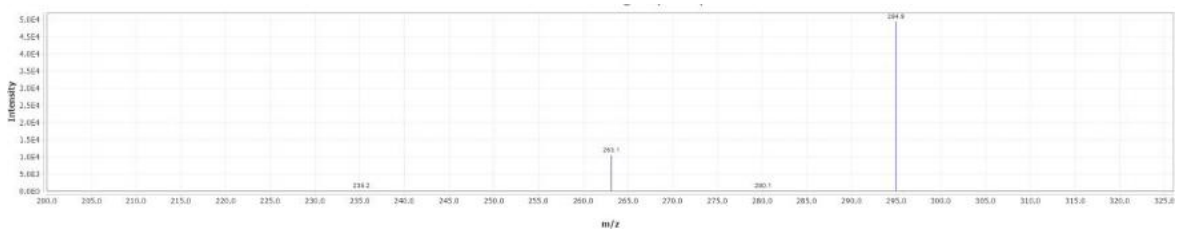

Figure S7. ESI-MS/MS spectrum of compound **7** at *m/z* 326 $[M+H]^+$ (bulbocapnine)

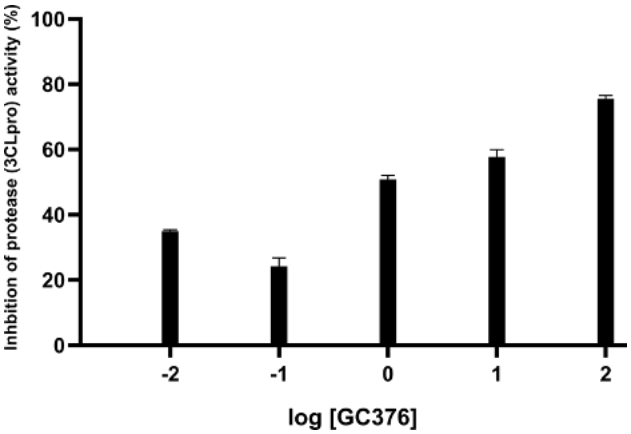

Figure S8. Evaluation of the inhibitory activity of GC-376 against $3CL^{pro}$ at concentrations of 100, 10, 1, 0.1, and 0.01 μM.

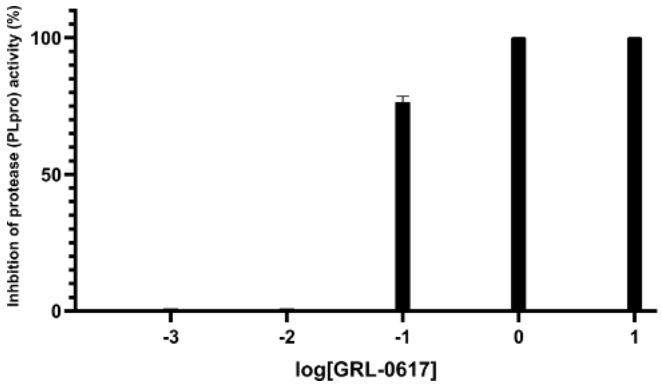

Figure S9. Evaluation of the inhibitory activity of GRL-0617 against $3CL^{pro}$ at concentrations of 10, 1, 0.1, 0.01 and 0.001 nM.

Table S1. ADMET properties predictions by SwissModel.

Compound		Actinodaphine	Boldine	Coclaurine	Laurolitsine	Assimilobine	Reticuline	Bulbocapnine
Physicochemical properties	Formula Molecular	$C_{18}H_{17}NO_4$	$C_{20}H_{23}NO_3$	$C_{17}H_{19}NO_3$	$C_{18}H_{19}NO_4$	$C_{17}H_{17}NO_2$	$C_{19}H_{23}NO4$	$C_{19}H_{19}NO_4$
	Molecular Weight	311.33	325.4	285.34	313.35	267.32	329.39	325.36
	#Heavy atoms	23	24	21	23	20	24	24
	#Aromatic heavy atoms	12	12	12	12	12	12	12
	Fraction Csp3	0.33	0.4	0.29	0.33	0.29	0.37	0.37
	#Rotatable bonds	1	2	3	2	1	4	1
	#H-bond acceptors	5	4	4	5	3	5	5
	#H-bond donors	2	1	3	3	2	2	1
	MR	88.65	98.95	85.62	91.1	82.59	97.01	93.55
	$TPSA^2$	59.95	41.93	61.72	70.95	41.49	62.16	51.16
Lipophilicity	iLOGP	2.95	3.33	2.55	2.71	2.58	3.13	3.16
	XLOGP3	2.45	3.44	2.58	2.25	2.64	3.01	2.92

Table S1 (cont.) ADMET properties predictions by SwissModel.

Compound		Actinodaphine	Boldine	Coclaurine	Laurolitsine	Assimilobine	Reticuline	Bulbocapnine
Lipophilicity	WLOGP	1.83	2.76	1.83	1.82	2.11	2.18	2.18
	MLOGP	1.92	2.54	1.84	1.52	2.43	1.75	2.16
	Silicos-IT Log P	3.34	3.95	2.94	3.02	3.48	2.92	3.27
	Consensus Log P	2.5	3.2	2.35	2.26	2.65	2.6	2.74
Water solubility	ESOL Log S	-3.63	-4.26	-3.46	-3.45	-3.54	-3.88	-4
	ESOL Solubility (mg/ml)	7.23e-02	1.78e-02	9.91e-02	1.10e-01	7.73e-02	4.30e-02	3.25e-02
	ESOL Solubility (mol/l)	2.32e-04	5.46e-05	3.47e-04	3.51e-04	2.89e-04	1.30e-04	9.98e-05
	ESOL Class	S[3]	MS[4]	S	S	S	S	MS
	Ali Log S	-3.35	-4	-3.52	-3.38	-3.16	-3.98	-3.66
	Ali Solubility (mg/ml)	1.38e-01	3.24e-02	8.53e-02	1.32e-01	1.84e-01	3.45e-02	7.19e-02
	Ali Solubility (mol/l)	4.44e-04	9.97e-05	2.99e-04	4.21e-04	6.89e-04	1.05e-04	2.21e-04
	Ali Class	S	MS	S	S	S	S	S

Table S1 (cont.) ADMET properties predictions by SwissModel.

Compound		Actinodaphine	Boldine	Coclaurine	Laurolitsine	Assimilobine	Reticuline	Bulbocapnine
Water solubility	Silicos-IT LogSw	-5.13	-5.55	-4.94	-4.93	-5.39	-4.72	-4.79
	Silicos-IT Solubility (mg/ml)	2.32e-03	9.11e-04	3.25e-03	3.72e-03	1.09e-03	6.25e-03	5.26e-03
	Silicos-IT Solubility (mol/l)	7.46e-06	2.80e-06	1.14e-05	1.19e-05	4.06e-06	1.90e-05	1.62e-05
	Silicos-IT class	MS	MS	MS	MS	MS	MS	MS
Pharmacokinetic properties	GI[5] absorption	High	High	High	High	High	High	High
	BBB[6] permeant	Yes	Yes	Yes	Yes	Yes	Yes	Yes
	Pgp[7] substrate	Yes	Yes	Yes	Yes	Yes	Yes	Yes
	CYP1A2 inhibitor	Yes	Yes	No	Yes	Yes	No	Yes
	CYP2C19 inhibitor	No	No	No	No	No	No	Yes
	CYP2C9 inhibitor	No	No	No	No	No	No	Yes

Table S1 (cont.) ADMET properties predictions by SwissModel.

Compound		Actinodaphine	Boldine	Coclaurine	Laurolitsine	Assimilobine	Reticuline	Bulbocapnine
Pharmacokinetic properties	CYP2D6 inhibitor	Yes	Yes	Yes	Yes	Yes	Yes	Yes
	CYP3A4 inhibitor	Yes	Yes	No	Yes	Yes	No	Yes
	log Kp (cm/s)	-6.46	-5.84	-6.21	-6.61	-6.06	-6.17	-6.21
Druglikeness	Lipinski #violations	0	0	0	0	0	0	0
	Ghose #violations	0	0	0	0	0	0	0
	Veber #violations	0	0	0	0	0	0	0
	Egan #violations	0	0	0	0	0	0	0
	Muegge #violations	0	0	0	0	0	0	0
	Bioavailability Score	0.55	0.55	0.55	0.55	0.55	0.55	0.55

Table S1 (cont.) ADMET properties predictions by SwissModel.

Compound		Actinodaphine	Boldine	Coclaurine	Laurolitsine	Assimilobine	Reticuline	Bulbocapnine
Medicinal Chemistry	PAINS #alerts	0	0	0	0	0	0	0
	Brenk #alerts	0	0	0	0	0	0	0
	Leadlikeness #violations	0	0	0	0	0	0	0
	Synthetic Accessibility	3.56	3.65	2.78	3.46	3.24	3.07	3.77
Toxicity	Mutagenic	none	none	none	none	none	none	none
	Tumorigenic	none	none	high	none	none	none	none
	Reproductive Effective	none	none	none	none	none	none	none
	Irritant	none	none	none	none	none	none	none

Table S2: Score values and probability of activity of the test compounds on the target $3CL^{pro}$ (PDB: 6M2N).

Compound	Moldock Score	(*p*) Moldock Score	Rerank Score	(*p*) Rerank Score	PLANTS Score	(*p*) PLANTS Score	(*p*) Total
actinodaphine	-110.452	0.85	-87.5808	0.88	-495.574	0.88	0.87
boldine	-114.959	0.88	-91.2593	0.92	-497.582	0.88	0.89
coclaurine	-114.653	0.88	-92.7533	0.93	-479.268	0.85	0.89
laurolitsine	-115.519	0.88	-89.944	0.90	-488.491	0.87	0.89
assimilobine	-88.7997	0.68	-64.2278	0.64	-451.941	0.80	0.71
reticuline	**-129.865**	**1**	**-98.8927**	**1**	-460.433	0.82	**0.94**
bulbocapnine	-110.315	0.84	-83.281	0.84	-495.129	0.88	0.85
Lig PDB/ positive Control	-97.7095	0.75	-79.639	0.80	**-559.57**	**1**	0.85

Legend: In bold is the lowest score.

Table S3: Score values and probability of activity of the test compounds on the target $3CL^{pro}$ (PDB: 7B3E).

Compound	Moldock Score	(*p*) Moldock Score	Rerank Score	(*p*) Rerank Score	PLANTS Score	(*p*) PLANTS Score	(*p*) Total
actinodaphine	-84.0975	0.89	-30.5719	0.50	-419.077	0.79	0.72
boldine	-84.3368	0.89	**-60.9568**	**1**	-416.924	0.78	**0.89**
coclaurine	-78.2785	0.82	-34.228	0.56	-419.069	0.79	0.72
laurolitsine	-81.0543	0.85	-45.3966	0.74	-420.503	0.79	0.79
assimilobine	-70.4253	0.74	7.80961	-0.12	-402.672	0.76	0.45
reticuline	-93.9823	0.99	-50.4015	0.82	-426.781	0.80	0.87
bulbocapnine	**-94.3855**	**1**	-50.0182	0.82	-445.505	0.84	0.88
Lig PDB/ positive Control	-78.5492	0.83	1.72583	-0.02	**-528.57**	**1**	0.60

Legend: In bold is the lowest score.

Table S4: Score values and probability of activity of the test compounds on the target PL^{pro} (PDB: 7LBR).

Compound	Moldock Score	(*p*) Moldock Score	Rerank Score	(*p*) Rerank Score	PLANTS Score	(*p*) PLANTS Score	(*p*) Total
actinodaphine	-119.994	0.67	-95.1362	0.69	-300.432	0.50	0.62
boldine	-109.138	0.61	-72.0945	0.52	-295.071	0.49	0.54
coclaurine	-106.26	0.59	-78.2978	0.57	-315.275	0.53	0.56
laurolitsine	-112.807	0.63	-81.642	0.59	-289.608	0.48	0.57
assimilobine	-106.279	0.59	-78.6753	0.57	-284.505	0.47	0.54
reticuline	-118.242	0.66	-21.3136	0.15	-321.294	0.54	0.45
bulbocapnine	-123.147	0.68	-88.5518	0.64	-298.235	0.50	0.61
Lig PDB/ positive Control	**-178.71**	**1**	**-136.949**	**1**	**-592.812**	**1**	**1**

Legend: In bold is the lowest score.

Table S5: Score values and probability of activity of the test compounds on the target PL^{pro} (PDB: 7TZJ).

Compound	Moldock Score	(*p*) Moldock Score	Rerank Score	(*p*) Rerank Score	PLANTS Score	(*p*) PLANTS Score	(*p*) Total
actinodaphine	-103.473	0.83	-79.2322	0.77	-403.972	0.67	0.76
boldine	-96.5568	0.78	-61.6073	0.59	-371.097	0.62	0.66
coclaurine	-103.549	0.83	-79.0817	0.76	-401.086	0.67	0.76
laurolitsine	-97.008	0.78	-56.4308	0.54	-363.582	0.61	0.64
assimilobine	-84.8215	0.68	-67.0917	0.65	-370.901	0.62	0.65
reticuline	-123.467	1	-87.3236	0.84	-412.378	0.69	0.84
bulbocapnine	-119.546	0.96	-56.4875	0.54	-392.416	0.69	0.72
Lig PDB/ positive Control	**-123.096**	**0.99**	**-102.81**	**1**	**-594.722**	**1**	**0.99**

Legend: In bold is the lowest score.

Table S6: Score values and probability of activity of the test compounds on the target Spike (PDB: 3SCI).

Compound	Moldock Score	(*p*) Moldock Score	Rerank Score	(*p*) Rerank Score	PLANTS Score	(*p*) PLANTS Score	(*p*) Total
actinodaphine	-101.755	0.59	-59.4184	0.55	-62.6934	0.88	0.68
boldine	-108.076	0.63	-84.8481	0.79	-54.9883	0.77	0.73
coclaurine	-103.13	0.60	-80.0076	0.75	-62.9042	0.88	0.74
laurolitsine	-107.169	0.62	-84.9237	0.79	-53.1883	0.75	0.72
assimilobine	-86.2089	0.50	-69.1342	0.64	-55.0889	0.77	0.64
reticuline	-117.652	0.69	-79.3336	0.74	-58.0239	0.82	0.75
bulbocapnine	-112.808	0.66	-88.9631	0.83	-58.1751	0.82	0.77
Lig PDB/ positive Control	**-170.128**	**1**	**-106.666**	**1**	**-70.7053**	**1**	**1**

Legend: In bold is the lowest score.

Table S7: Score values and probability of activity of the test compounds on the target Spike (PDB: 6M0J).

Compound	Moldock Score	(*p*) Moldock Score	Rerank Score	(*p*) Rerank Score	PLANTS Score	(*p*) PLANTS Score	(*p*) Total
actinodaphine	-107.117	0.59	-85.5649	0.68	**-67.5166**	1	0.76
boldine	-101.282	0.56	-81.4506	0.65	-52.0767	0.77	0.66
coclaurine	-100.287	0.55	-68.1878	0.54	-65.7778	0.97	0.69
laurolitsine	-105.687	0.58	-80.1244	0.64	-58.3808	0.86	0.69
assimilobine	-85.3583	0.47	-64.8527	0.52	-61.7834	0.91	0.63
reticuline	-125.626	0.69	-95.6976	0.76	-60.9201	0.90	0.78
bulbocapnine	-107.579	0.59	-65.3193	0.52	-64.0248	0.94	0.69
Lig PDB/ positive Control	**-180.188**	**1**	**-124.414**	**1**	-61.688	**0.91**	**0.97**

Legend: In bold is the lowest score.